

ON QUANTUM EFFECTS IN THE DYNAMICS OF MACROSCOPIC TEST MASSES

Von der Fakultät für Mathematik und Physik
der Gottfried Wilhelm Leibniz Universität Hannover

zur Erlangung des Grades

Doktor der Naturwissenschaften

— Dr. rer. nat. —

genehmigte Dissertation

von

Dipl. Phys. Helge Müller-Ebhardt

geboren am 16.05.1979 in Hannover

(2009)

Referent: Prof. Dr. R. Schnabel
Korreferent: Prof. Dr. K. Danzmann
Tag der Promotion: 16.12.2008

Kurzfassung

Im letzten Jahrhundert haben zwei revolutionäre Theorien die Physik bereichert: die Quantenmechanik und die allgemeine Relativitätstheorie. Letztere hat die Existenz von Gravitationswellen vorhergesagt, die von massereichen astrophysikalischen Objekten emittiert werden können. Der wohl vielversprechendste Detektortyp für den ersten direkten Nachweis von Gravitationswellen ist durch große Laserinterferometer gegeben. Diese Interferometer sind in zweierlei Hinsicht groß: zum einen in der Spannweite ihrer Arme sowie in Größe und Gewicht ihrer verspiegelten Testmassen. Durch eine Fülle technischer Verbesserungen wird die Sensitivität der Interferometer mehr und mehr gesteigert werden, so dass erwartet wird, dass bereits die nächste Generation solcher Detektoren durch Quanteneffekte im Messprozess limitiert sein wird. Das stellt natürlich die Frage nach der Existenz von Quanteneffekten in der Dynamik der Testmassen des Detektors. Diese theoretische Arbeit möchte eine Verbindung herstellen zwischen der Sensitivitätssteigerung von Gravitationswellendetektoren und der Möglichkeit makroskopische Quantenzustände in den Detektoren zu generieren.

Im ersten Teil dieser Arbeit wird das Quantenrauschen in einem Sagnac Interferometer, das mit einem zusätzlichen verstimmten Resonator in seinem Ausgang ausgestattet ist, theoretisch untersucht. Diese Technik des verstimmten Signal-Recyclings wurde bereits in Zusammenhang mit einem Michelson Interferometer untersucht und findet im Gravitationswellendetektor GEO600 Anwendung. Zusammen mit der Analyse des Quantenrauschens in einem einfachen Sagnac Interferometer legt dies die Grundlage für diesen Teil der Arbeit: Wir werden die Sensitivität des Sagnac Interferometers bezüglich der Detektion einer bestimmten Gravitationswellenquelle und in Hinblick auf ein realistisches klassisches Rauschen optimieren. Da ein Michelson Interferometer mit verstimmtem Signal-Recycling die Gravitationswellendehnung in echte Spiegelbewegung umwandeln kann, vergleichen wir diese Umwandlung mit der bei einem Sagnac Interferometer. Dann setzen wir die Untersuchungen über den ponderomotiven Squeezer fort und untersuchen das konditionierte Ausgangssqueezing eines Resonators, der sowohl für sein Hauptlaserfeld als auch für ein zweites Unterlaserfeld verstimmt ist.

Ausgestattet mit dem Wissen über den Quantenmessprozess in Interferometern aus dem ersten Teil besteht der zweite Teil dieser Arbeit aus einer theoretischen Analyse, die sich mit dem konditionierten Zustand von Ort und Impuls der Testmassen beschäftigt. Wir werden begründen, warum es einfacher ist, die so genannte Wiener Filter Methode zu benutzen, um den konditionierten Zustand zu erhalten als stochastische Mastergleichungen aufzustellen. Mit der Hilfe von Wiener Filtern werden wir den allgemeinsten Ausdruck für die konditionierte Kovarianzmatrix eines gaussischen Zustands unter einem linearen markovischen Messprozess errechnen. Dann werden wir auf die Interferometrie zurückkommen und theoretisch nachweisen, unter welchen Umständen die konditionierten Zustände der Testmassen in einem Michelson Interferometer nahe an reine Quantenzustände kommen und Quanteneigenschaften wie Squeezing und Verschränkung zeigen können. Dies hängt natürlich vom Niveau des klassischen Rauschens ab. Wir werden dies aber quantifizieren, indem wir eine notwendige Beziehung zwischen dem Spektrum des klassischen Rauschens und einer Standardreferenz in der Interferometrie, dem Standardquantenlimit, herstellen werden.

Stichworte: Gravitationswellendetektor, Laserinterferometrie, makroskopische Quantenmechanik

Abstract

In the last century two revolutionary new concepts have enriched the field of theoretical physics: the theory of quantum mechanics and the general theory of relativity. The latter one has predicted the existence of gravitational waves, which can be emitted from massive astrophysical objects. The most promising detector design for the first direct observation of gravitational waves is given by large-scale laser interferometers. These interferometers are large in terms of the extension of their arms as well as in terms of the size and the weight of their mirror-endowed test masses. Due to a vast choice of possible technological improvements the sensitivity of those interferometers will be increased more and more. It is expected that the sensitivity of the planned next generation of laser interferometer gravitational-wave detectors already becomes limited by quantum effects in the measurement process. This certainly raises the question about the existence of quantum effects in the dynamics of the test masses of the detector. This thesis will theoretically provide a link between the increase of the sensitivity of gravitational-wave detectors and the possibility of preparing macroscopic quantum states in such detectors.

In the first part of this thesis, we theoretically explore the quantum measurement noise of an optical speed meter topology, the Sagnac interferometer, equipped with an additional detuned cavity at the output port. This detuned signal-recycling technique was already investigated when applying it to a Michelson interferometer and is used in the gravitational-wave detector GEO600. Together with the quantum noise analysis of the simple Sagnac interferometer, it is the basis of our study: we optimize the Sagnac interferometer's sensitivity towards the detection of a certain gravitational-wave source in the vicinity of a realistic classical noise environment. Motivated by the fact that the Michelson interferometer, as a position meter, with detuned signal-recycling can transduce the gravitational-wave strain into real mirror motion, we compare the transducer effect in a speed and in a position meter. Furthermore, we theoretically investigate the conditional output squeezing of a cavity which is detuned with respect to its carrier and its subcarrier. Therewith we pursue the theoretical analysis of the ponderomotive squeezer.

With the knowledge gained in the first part about the quantum measurement process in laser interferometers, the second part of this thesis comprises a theoretical analysis of the conditional state in position and momentum of the interferometer's test masses. We motivate not to obtain the conditional states from a stochastic master equation but with the help of the so-called Wiener filtering method. Using this method, we calculate the most general expression for the conditional covariance matrix of the Gaussian state of a test mass under any linear Markovian measurement process. Then we specify to the interferometry and theoretically show under which circumstances the conditional states of the test masses in a Michelson interferometer become close to pure quantum states, showing quantum features as squeezing or even entanglement. This certainly depends on the level of the classical noise. But we quantify this by giving a necessary relation between the spectrum of the classical noise and a standard reference in interferometric experiments, the standard quantum limit.

Keywords: Gravitational-wave detector, laser interferometry, macroscopic quantum mechanics

Contents

1	Introduction	3
1.1	Quantum mechanics and the measurement process	6
1.1.1	Measurement's back action and the standard quantum limit	9
1.1.2	Quantum non-demolition measurements	10
1.1.3	Collapse of the wave function	11
1.2	Quantum dynamical interaction between a mechanical oscillator and light . .	12
1.2.1	Quantum Langevin equations	13
1.2.2	Travelling waves approach	15
1.2.3	Susceptibilities	18
1.2.4	Optical spring effect	20
1.3	Quantum Brownian motion of a mechanical harmonic oscillator	22
1.4	Quantum entanglement	23
1.4.1	Separability of bipartite two-mode Gaussian states	24
1.4.2	Bipartite two-mode Gaussian Einstein-Podolsky-Rosen states	26
2	Part I: Quantum non-demolition gravitational-wave detectors	27
2.1	Signal-recycled Michelson interferometer	28
2.1.1	Test-mass dynamics and measurement output	30
2.1.2	Sensitivity towards gravitational waves	32
2.2	Signal-recycled Sagnac interferometer	33
2.2.1	Free resonant structure	36
2.2.2	Test-mass dynamics and measurement output	37
2.2.3	Sensitivity to gravitational waves	40
2.2.4	Classical noise budget and sensitivity to a specific astrophysical gravitational-wave source	42
2.2.5	Sensitivity to inspiraling neutron star binaries assuming a third- generation classical noise budget	46
2.3	Transducer schemes	47
2.3.1	Signal-recycled interferometers as transducers	48
2.3.2	Double readout configurations	53
2.4	Double-optical-spring ponderomotive squeezer	55
2.4.1	Double optical spring	56
2.4.2	Output squeezing versus entanglement	59
2.4.3	Conditional covariance matrix	61
2.4.4	Conditional quantum output squeezing	62
2.4.5	Conditional output squeezing with classical noise	64

3	Part II: Macroscopic quantum mechanics	67
3.1	Conditional quantum states	68
3.1.1	Stochastic master equation	69
3.1.2	Wiener filtering	72
3.1.3	Two-dimensional Wiener filter	75
3.2	Preparation of conditional macroscopic quantum states using the Wiener filter	75
3.2.1	General linear Markovian measurement process	76
3.2.2	Quantum measurement noise versus classical noise	79
3.2.3	Very low finesse cavity with quantum vacuum noise	82
3.2.4	Very low finesse cavity with vacuum input and classical noise	84
3.2.5	Very low finesse cavity with squeezed input and classical noise	89
3.2.6	Cavity with finite bandwidth	90
3.2.7	Detuned cavity	94
3.2.8	Double carrier cavity	95
3.2.9	Speed meter	95
3.3	Verification of macroscopic quantum states	96
3.3.1	Free-evolution stage	97
3.3.2	Verification stage using back-action-noise evasion	99
3.4	Preparation of feedback-controlled macroscopic quantum states	100
3.4.1	Optimal controller	101
3.4.2	Very low finesse cavity with vacuum input and classical noise	104
3.5	Macroscopic entanglement	107
3.5.1	Michelson interferometer produces test-mass entanglement	107
3.5.2	Test-mass entanglement using conditional states	110
3.5.3	Lifetime of test-mass entanglement after preparation	114
3.5.4	Test-mass Einstein-Podolsky-Rosen entanglement	115
3.5.5	Test-mass entanglement using controlled states	115
4	Summary and conclusion	117

1 Introduction

One of the most popular theories in physics was celebrating its 100th birthday at the beginning of this century: the theory of *quantum mechanics*. Quantum mechanics is usually understood as a purely non-deterministic theory. That means that it can only make statistical predictions on the outcome of an experiment: the absolute square of the so-called *wave function* represents the probability for observing one of the possible results. And indeed, the predictions which can be obtained from the theory match perfectly all experimental observations. As long as one accepts the statistical nature of the quantum mechanical measurement theory – although it does not always follow the laws of probability theory – and does not raise the question about the actual situation of the observed object itself before and at the instant of the measurement, no problems arise. But many people had and still have problems with the sense or the interpretation of quantum mechanics [133]. Different interpretations actually co-exist, which can not be distinguished experimentally. One of them is the *Bohmian mechanics*. David Bohm suggested in the 50's that particles are guided by their wave function and follow certain trajectories which are not specified until the boundary conditions are known [8, 9]. This concept had already been developed by Louis de Broglie in the 20's. There is also the *many-worlds interpretation* [51] introduced by Hugh Everett also in the 50's, who proposed that all possible results of a measurement process could in principle exist – but in its own world. This means that there is a perhaps infinite number of different universes, where each possible measurement result that does not occur in our universe appears in another universe. But interestingly the interpretation which is probably most far away from common sense has become accepted: the *Copenhagen interpretation*. Its name actually comes from Niels Bohr and Werner Heisenberg's collaboration in Copenhagen around 1927. They have proposed that the measurement itself causes the wave function to collapse to a certain value exactly at the instant when the measurement takes place. This raises the very interesting question which is still open, namely about which one of the following two concepts is forced to be violated by the theory of quantum mechanics: locality or realism, or even both. This question which is important for the interpretation of quantum mechanics, is currently under experimental tests [61].

Quantum measurement effects in the context of macroscopic and heavy objects [20] became interesting probably for the first time when people started to hunt for the first direct detection of *gravitational waves*. Gravitational waves are often nicely described as ripples in space-time propagating at the speed of light. They are in fact a direct consequence of the *general theory of relativity*, which was founded by Albert Einstein in 1916 and is the other popular theory of the last century. In the framework of general relativity, gravitational waves are described by a weak metric perturbation on an otherwise static background metric. This can result in a vacuum wave equation for this metric perturbation. Note that the wave equation can be written in a frame independent way but is usually given in the so-called transverse-traceless coordinate gauge. The gravitational wave's amplitude is given by the dimensionless quantity $h = 2\delta L/L$, which is a relative length change of the distance L and therefore it is often referred to as a strain. The gravitational-wave field is of quadrupole nature, having two degrees of freedom which are its two polarizations. An incident gravitational wave (in z-direction) would periodically deform a ring of free falling test masses (in the x-y-plane) to ellipses, depending on the polarization of the gravitational wave: for the

plus-polarization the circle will be stretched in x-direction and simultaneously squeezed in y-direction and then after half a period this process is reversed. For the cross-polarization this squeezing and stretching will happen in exactly 45° between x-direction and y-direction. Gravitational waves are emitted from massive astrophysical objects if they cause a change in the quadrupole momentum of the mass distribution. Examples are: burst signals from supernovae explosions; signals from inspiraling or merging binary systems (consisting of e.g. two neutron stars, two black holes or a system of a neutron star and a black hole); periodic signals from pulsars; or finally the stochastic background signal from for instance the inflational stage of the early universe. A good introduction to the general theory of relativity and the theory of gravitational waves can be found in many different textbooks as e.g. in Refs. [7, 65, 111, 129].

The first attempts towards the direct observation of gravitational waves were carried out by Joseph Weber starting in the late 50's. He used large metal cylinders, so-called resonant bar detectors [128]. Today the efforts on the direct detection of gravitational waves additionally rely on large-scale laser interferometers as it was proposed by Gerstenshtein and Pustovoi in the 60's (cf. Ref. [58]). These detectors maximize the response to the plus-polarization of a gravitational wave but are insensitive to its cross-polarization. Due to several advantages of using laser-interferometric detectors compared to using resonant bar detectors, the direct search for gravitational waves concentrates more on laser interferometers. The major advantage is probably that with a laser interferometer it is much easier to realize long detector arms which certainly are more effected by the gravitational-wave strain. Another advantage is the interferometer's broadband detection ability in the frequency space. There is a large network of operating ground-based laser interferometer gravitational-wave detectors spanned all over the world: the three LIGO detectors [48, 112] located in the USA; the VIRGO detector [52] located in Italy; the GEO600 detector [50] located in Germany; and the TAMA project [5] located in Japan. All of these detectors are realized by large Michelson-type interferometers – having extensions of 300 m up to 4 km in arm length – with suspended, but due to a low eigenfrequency of the pendulum approximately free falling, macroscopic, mirror-endowed test masses ranging from 1 kg to 21 kg. The next generation of such detectors, such as Advanced LIGO [1], will even exceed the first generation, for example in terms of its test masses' weight of 40 kg and the available laser power. It has been planned from the bottom up and is now virtually ready for its construction. Moreover, there is much effort in investigating even more advanced technologies. The noise contaminating the detection of gravitational waves – as a quantum measurement – is usually classified into two main categories: *(i)* the fundamental quantum noise which in interferometric experiments arises from the light; and *(ii)* the rest which comes from so-called classical noise sources. Remarkably, the sensitivity of the first generation of detectors is already limited by quantum noise at high frequencies. Furthermore, it is expected that already the next generation of detectors will be quantum-noise limited at almost all frequencies within their detection band (~ 10 Hz – some kHz). Therefore, the quantum noise in gravitational-wave detection becomes more and more an important factor. With clever optical designs of the detector, it is possible to shape the quantum noise spectral densities: different optical topologies show different so-called optomechanical properties, which in turn is reflected in different quantum noise behavior. The challenge is to lower the quantum noise in the frequency band, where on the one hand the theoretically predicted gravitational-wave forms provide with highest possibility the strongest signal and on the other hand the quan-

tum noise also dominates the total noise. Early in this decade an important observation has given a great opportunity in shaping the quantum noise, namely the fact that a certain interferometer configuration shows the so-called *optical spring effect* [22]. Note that this effect can also help in the production of squeezed light which originates from the coupling between the light and the motion of the test-mass mirrors [37]. Because a single optical spring usually transforms a device into an unstable system [22], it will probably be replaced by the so-called double optical spring in future experiments.

The question arises whether the macroscopic objects themselves, such as the test masses of a gravitational-wave detector, can also start to behave quantum mechanically in their degree of freedom which is subject to a quantum-noise limited measurement. This question is related to a big issue in modern physics, namely to the question whether macroscopic objects are in principle able to show quantum behavior or not. In the microscopic regime, quantum physics is probably the most successful area of natural science: An exceptional consistency between theoretical and experimental research has been found. But at macroscopic scales considering heavy objects none of these effects have ever been verified. There are even theories predicting that quantum mechanics of macroscopic and heavy objects fundamentally fails due to, for instance, the gravity decoherence [95] or the spontaneous reduction model [59]. This would directly lead to the question where exactly to draw the line between the microscopic and the macroscopic world which could be answered by those theories. Throughout this thesis we will use the term 'macroscopic' to be a synonym for a macroscopic and heavy object larger than a single molecule if not otherwise stated. Macroscopic and heavy objects if they are explicitly considered in this thesis are usually mirrors weighing between 1 g and several kg. But the discussion about macroscopic quantum states will be held independent of the actual mass of the object.

This thesis is divided into two parts: the first one can be found in Sec. 2 and is strongly related to gravitational waves and their detection. Here we will deal with advanced interferometer configurations which allow to manipulate the arising quantum noise. Therefore, as they are used as a laser interferometer gravitational-wave detector, they allow to increase the sensitivity at the relevant frequencies. Whereas the second part of this thesis, in Sec. 3, is only related to the detectors themselves. It is especially concerned with the test masses in such a detector: we will be interested in the states of these test masses. We hope that gravitational-wave detectors will not only open a new window to the universe in the sense of detecting astrophysical sources but also to open a window to the world of macroscopic quantum mechanics. Both parts of this thesis have a big overlap: in both of them we will deal with the same quantum measurement process and we are required to have a low classical noise floor. At the beginning of each part, we will give a brief introduction to the specific subject. In Sec. 4 we will then summarize our conclusions on both parts of this thesis by highlighting the main results of this work.

In this first chapter we will start with reviewing some important theoretical basics from quantum mechanics and quantum measurement theory which will be used throughout both parts of this thesis. In Sec. 1.1 we will remind the reader of some principles of quantum mechanics and generally describe characteristics of quantum measurement processes. Then we will describe the dynamics of a concrete quantum measurement process in Sec. 1.2 using two different approaches. In Sec. 1.3 we will motivate a simple model for the quantum Brownian motion. Finally, in Sec. 1.4 we will briefly introduce the theory of quantum entanglement.

1.1 Quantum mechanics and the measurement process

Whenever measurements are as precise as up to the quantum scale which means that they are of such an accuracy that terms of the order of the *reduced Planck constant* $\hbar \approx 1.05457 \cdot 10^{-34}$ Js cannot be neglected, fundamental quantum effects become of major importance and we can speak of a *quantum measurement*. Later on in Sec. 3.2.1 we will give an explicit definition of this quantum measurement process. One, or probably even the most important statements of quantum mechanics in this context is the so-called *Heisenberg uncertainty principle* [67]. In 1927, Werner Heisenberg formulated this inequality for the measurement uncertainty of two non-commuting observables. Mathematically speaking, the Heisenberg uncertainty principle results from the commutation relation of the operators which are associated with the observables. As an example, the operator of the position

time-domain susceptibility	$C_{o_1 o_2}^-(t, t') = [\hat{o}_1^{(0)}(t), \hat{o}_2^{(0)}(t')]$
frequency-domain susceptibility	$R_{o_1 o_2}(\Omega) = \frac{i}{\hbar} \int_0^\infty dt e^{i\Omega t} C_{o_1 o_2}^-(0, -t)$
time-domain correlation function	$C_{o_1 o_2}(t - t') = \langle \hat{o}_1(t) \hat{o}_2(t') \rangle_{\text{sym}}$
single-sided cross-spectral density	$\pi \delta(\Omega - \Omega') S_{o_1 o_2}(\Omega) = \langle \hat{o}_1(\Omega) \hat{o}_2^\dagger(\Omega') \rangle_{\text{sym}}$
the latter two satisfying	$C_{o_1 o_2}(t - t') = 2 \int_0^\infty \frac{d\Omega}{2\pi} S_{\hat{o}_1 \hat{o}_2}(\Omega) e^{-i\Omega(t-t')}$
frequency-domain transform	$\hat{o}_1(t) = \int_{-\infty}^\infty \frac{d\Omega}{2\pi} e^{-i\Omega t} \hat{o}_1(\Omega)$

Table 1: Collection of specific functions among any two linear Heisenberg operators $\hat{o}_1(t)$ and $\hat{o}_2(t)$, as used throughout this thesis. The brackets $\langle \dots \rangle$ denote the quantum-mechanical expectation value and the subscript 'sym' stand for symmetrization of the operators within the brackets. The time-domain functions depend only $(t - t')$ if the Hamiltonian of the system does not explicitly depend on time.

observable \hat{x} and the one of the momentum \hat{p} fulfill the canonical commutation relation

$$[\hat{x}, \hat{p}] \equiv \hat{x} \hat{p} - \hat{p} \hat{x} = i \hbar. \quad (1.1)$$

From the *Schwarz inequality*, one can derive the Heisenberg uncertainty principle for the second-order moments of position and momentum to give

$$V_{xx} V_{pp} - V_{xp}^2 \geq \frac{\hbar^2}{4}, \quad (1.2)$$

by making also use of Eq. (1.1). Here we have defined the second-order moments of the state which are often also called variances by

$$V_{xx} \equiv \langle (\hat{x} - \langle \hat{x} \rangle)^2 \rangle, \quad (1.3)$$

$$V_{pp} \equiv \langle (\hat{p} - \langle \hat{p} \rangle)^2 \rangle, \quad (1.4)$$

$$V_{xp} \equiv \frac{1}{2} \langle (\hat{x} - \langle \hat{x} \rangle) (\hat{p} - \langle \hat{p} \rangle) + (\hat{p} - \langle \hat{p} \rangle) (\hat{x} - \langle \hat{x} \rangle) \rangle, \quad (1.5)$$

where the quantum-mechanical expectation value $\langle \dots \rangle$ has to be taken. Note that a Gaussian state is completely determined by its first- and second-order moments. Eq. (1.2) tells us now that the position and the momentum can never be measured or even defined – this depends on the interpretation of quantum mechanics – simultaneously to arbitrary precision.

For Gaussian states the Heisenberg *uncertainty product* becomes minimal, that means equal sign in Eq. (1.2), if and only if the system is pure. A pure system is the first candidate among all Gaussian systems which should be considered as a real quantum system because it cannot be described as a mixture of different states. This is in contrast to a thermally excited system described by a highly mixed state which should definitively be considered as classical. The probability to find a pure system in its eigenstate is actually equal to one. Another intrinsic feature of a pure state is that its density matrix operator is given by a projection operator which is idempotent. Furthermore, the ground state of a harmonic oscillator as an example is always represented by a pure state.

Since throughout this thesis we will only deal with Gaussian states, we will use the value of the uncertainty product which is given by $(V_{xx} V_{pp} - V_{xp}^2)$ as a measure of the *purity* and therefore to describe the *quantum-ness* of the state of an object under linear observation. This seems to be reasonable because trying to reconstruct, as commonly done, the number of quanta, the so-called *occupation number*, may not always be the most fundamental figure of merit in this context: squeezed states, for example, can have high occupation numbers, yet they should be considered as quantum – probably even more quantum than vacuum states. Moreover, the definition of an occupation number requires a well-defined, real-valued eigenfrequency, which is not always given, as for example in the case of a free mass or in other examples as given in the second part of this thesis. On the other hand, if a state has no correlation in position and momentum, i.e. $V_{xp} = 0$, its Heisenberg uncertainty product can be converted back into an *effective occupation number* by using the relation

$$\mathcal{N}_{\text{eff}} = \frac{1}{\hbar} \sqrt{V_{xx} V_{pp}} - \frac{1}{2}. \quad (1.6)$$

This effective occupation number should be interpreted as follows: suppose that the variances in position and momentum are given and produced by a perfect harmonic oscillator in a quadratic potential having an arbitrary but real-valued eigenfrequency ω_{eff} . Then the effective occupation number is obtained by minimizing the total energy divided by the energy of each quanta with respect to that eigenfrequency ω_{eff} . This strategy reads

$$\mathcal{N}_{\text{eff}} = \min_{\omega_{\text{eff}}} \left\{ \frac{1}{\hbar \omega_{\text{eff}}} \left(\frac{V_{pp}}{2m} + \frac{m \omega_{\text{eff}}^2 V_{xx}}{2} \right) - \frac{1}{2} \right\}, \quad (1.7)$$

where the minimum is achieved at

$$\omega_{\text{eff}} = \sqrt{\frac{V_{pp}}{m^2 V_{xx}}}. \quad (1.8)$$

Thus, the effective occupation number is the minimal occupation number one could obtain when assuming to have a harmonic oscillator with no correlation in position and momentum and an effective eigenfrequency as given in Eq. (1.8). It might be worth noting that the effective occupation number in fact also determines the *von Neumann entropy* of a state [134] given by

$$\mathcal{S} = (\mathcal{N}_{\text{eff}} + 1) \log(\mathcal{N}_{\text{eff}} + 1) - \mathcal{N}_{\text{eff}} \log \mathcal{N}_{\text{eff}}. \quad (1.9)$$

But this should just be regraded as an interesting fact which we will not further stress in the course of this thesis.

Furthermore, it is advisable to gather the second-order moments of position and momentum of the Gaussian state into the so-called *covariance matrix* which is given by

$$\mathbf{V} = \begin{pmatrix} V_{xx} & V_{xp} \\ V_{xp} & V_{pp} \end{pmatrix}. \quad (1.10)$$

Then the uncertainty product is given by the determinant of the covariance matrix and Heisenberg uncertainty principle simply reads $\det \mathbf{V} \geq \hbar^2/4$. In general, the squeezing of the Gaussian state is given by the smaller eigenvalue of its covariance matrix \mathbf{V} , and is therefore equal to $(\sqrt{\det \mathbf{V}} e^{-r})$, where the quantity r is the squeezing factor given by

$$r = \text{arccosh} \frac{\text{tr} \mathbf{V}}{2 \sqrt{\det \mathbf{V}}}. \quad (1.11)$$

Note that the factor $(-20 r / \ln 10)$ provides the squeezing strength in dB. Furthermore, we say that the state represented by the covariance matrix \mathbf{V} is squeezed at the angle φ given by

$$\varphi = \arctan \left(\frac{V_{xx} - V_{pp} - \sqrt{(\text{tr} \mathbf{V})^2 - 4 \det \mathbf{V}}}{2 V_{xp}} \right) + \frac{\pi}{2}, \quad (1.12)$$

where φ actually defines the angle between the position and the squeezed quadrature and determines the rotation into the eigensystem. With these definitions we are able to draw a *squeezing ellipse* corresponding to the covariance matrix into a coordinate system of position and momentum. This ellipse has the eigenvalues $(\sqrt{\det \mathbf{V}} e^{\pm r})$ as its semi-major and semi-minor axis, respectively, where the angle between its semi-minor axis and the position axis is given by φ . Then the area of the squeezing ellipse is equal to π times the uncertainty product.

Note that the Heisenberg uncertainty product together with the squeezing factor and angle form another complete set which determines the Gaussian state – apart from the first-order moments. This set often becomes even more important in order to characterize the quantum states than the set of second-order moments, i.e. the covariance matrix. As we will see, all the equations which transform between the two sets – Eqs. (1.2), (1.11) and (1.12) – are used throughout this thesis.

A commonly used distribution to describe a quantum mechanical state is the so-called *Wigner function*. In general, this function is a quasi-probability distribution in phase space. But for Gaussian states the Wigner function is also always positive and is moreover totally given in terms of the covariance matrix as

$$W(x, p) = \frac{1}{2\pi \sqrt{\det \mathbf{V}}} e^{-\frac{1}{2} (x, p) \mathbf{V}^{-1} (x, p)^T}. \quad (1.13)$$

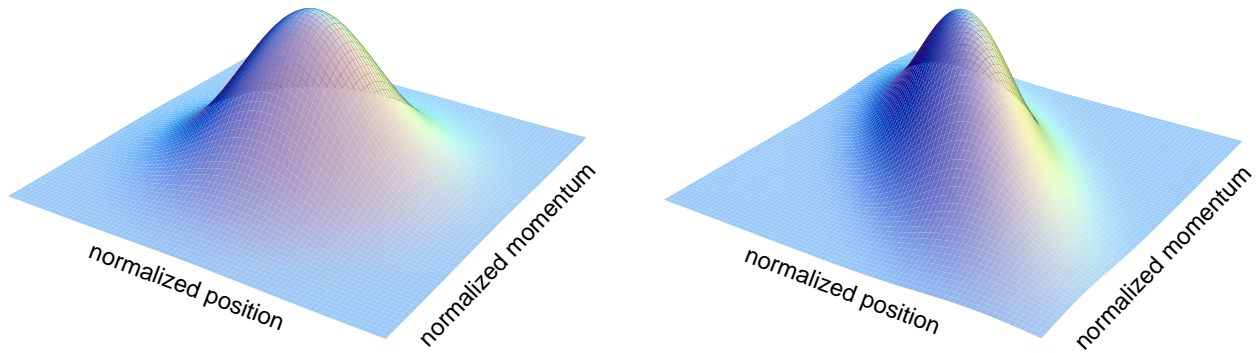


Figure 1: Wigner function of the ground state (left panel) of a mechanical harmonic oscillator in normalized position and momentum coordinates. Wigner function of a squeezed state (right panel) of an oscillator: squeezed by the factor of $r = \operatorname{arccosh} \sqrt{2}$ and in 45° between normalized position and normalized momentum quadrature.

Fig. 1 shows two characteristic Wigner functions of a mechanical harmonic oscillator in a pure Gaussian state: the ground state and a specially squeezed ground state. We will encounter the first one of these two states again in Sec.1.3 as the unconditional ground state of a mechanical harmonic oscillator and the other one in the second part of this thesis as the conditional ground state of a free mass.

1.1.1 Measurement's back action and the standard quantum limit

Let us say we have a system with two non-commuting observables, such as position and momentum as in the previous section. Following the Copenhagen interpretation of quantum mechanics, a measurement collapses the wave function of the measured object into a state with a certain uncertainty in these two observables. In other words, if we perform a quantum measurement with a certain precision in one of these observables the uncertainty in the other observable might have to increase in order to save the Heisenberg uncertainty principle. Therefore the measurement has to act back onto the measured object. This effect is usually called *quantum back action*. A typical example is the diffraction in single slit experiments, which occurs if the wavelength of the light, or the de Broglie wavelength of a non-massless particle as an electron or even an atom, is of the order of the size of the slit. One can think about such an experiment in the following way: the slit measures the position of the particle at the instance when passing through the slit which simultaneously perturbs the momentum causing on the one hand the natural extension of the beam and on the other hand prohibits certain positions in a second measurement on a screen which causes the interference pattern.

In repeated quantum measurement processes, where the back-action perturbed observable couples into the measured observable via free evolution, the back action causes additional noise. This was first realized by Braginsky in the 60's, where he had shown that the *back-action noise* together with the measurement noise can result into the so-called *standard quantum limit* [12, 18] for the measurement's sensitivity, if both back-action noise and measurement noise are uncorrelated. Here the measurement noise, which is also often called *shot noise*, is a necessary result of the fact that the measurement can collect only a finite amount of information in a finite amount of time. Note that the standard quantum limit always arises in measurement processes where the Heisenberg operators of the measured observable

do not commute at different times.

At this stage, we shall consider the example of measuring the position of a free falling object with rest mass m . The Heisenberg operator of the object's position under free evolution can be written as

$$\hat{x}(t) = \hat{x} + \frac{\hat{p}}{m} (t - t_0). \quad (1.14)$$

Using the commutation relation between position and momentum as given in Eq. (1.1), it is easy to show that the Heisenberg position operators at different times do not commute but obey the relation

$$[\hat{x}(t), \hat{x}(t')] = \frac{i\hbar}{m} (t' - t). \quad (1.15)$$

A measurement of the position at time $t = 0$ reduces the wave function of the free mass into a state with position and momentum widths $V_{xx} = \langle \hat{x}(0) \hat{x}(0) \rangle - \langle \hat{x}(0) \rangle^2$ and $V_{pp} = \langle \hat{p}(0) \hat{p}(0) \rangle - \langle \hat{p}(0) \rangle^2$, respectively. Here V_{xx} represents the error of the measurement, or the measurement noise, showing us how precisely we can know the position, while $V_{pp} \geq \hbar^2 / (4V_{xx})$ gives us the momentum uncertainty due to the measurement's back action, lower limited by the Heisenberg uncertainty principle. Assuming no correlation between position and momentum, i.e. $V_{xp} = 0$, one has, right before a next measurement at time τ , the position width

$$\langle \hat{x}(\tau) \hat{x}(\tau) \rangle - \langle \hat{x}(\tau) \rangle^2 = V_{xx} + \frac{V_{pp}}{m^2} \tau^2 \geq \frac{\hbar \tau}{m}, \quad (1.16)$$

which limits the accuracy of the second position measurement. The right hand side of the inequality in Eq. (1.16) is obtained by finding the right balancing between measurement noise and back action noise and it represents the standard quantum limit. Repeating the measurement many times and taking the continuous limit, we can convert Eq. (1.16) into a limit of the noise spectral density in a continuous position measurement process by understanding it as the mean-squared noise on the measurement's bandwidth $\Omega = 1/\tau$. Then the single-sided spectral density – which is basically equal to two times the mean-squared noise over the bandwidth – of the free-mass standard quantum limit in a continuous position measurement is given by

$$S^{\text{SQL}}(\Omega) = \frac{2\hbar}{m\Omega^2}, \quad (1.17)$$

having units of m^2/Hz . The standard quantum limit has been established as a standard reference in quantum measurement processes. Aiming at the precision of a measurement, as in gravitational-wave detection, definitely requires a low standard quantum limit which can be achieved by increasing the mass. But in the last years the interest in reaching the standard quantum limit with the objective of actually seeing and experimentally proving it has increased, which in turn requires a high standard quantum limit. Note that we will encounter Eq. (1.17) in nearly all sections within this thesis – sometimes in a slightly different format. In Sec. 3.2.1 we will give a more rigorous derivation of Eq. (1.17) for an arbitrary linear Markovian measurement process in terms of the measurement's spectral densities.

1.1.2 Quantum non-demolition measurements

When people started to think about the standard quantum limit as a limit [120] in the 60's, certain people really insisted on the free-mass standard quantum limit to provide a

real limit to continuous quantum measurements which can never be circumvented [28]. But after a rather controversial debate it was eventually realized that the standard quantum limit can in principle be surpassed [72]. Today we know that a measurement can surpass the standard quantum limit if (i) the measurement is made through monitoring of a *quantum non-demolition* observable [16], or (ii) the quantum mechanics of the measuring device is taken into account and quantum correlations in back-action and shot noise are used, for instance by using *back-action-noise evasion* techniques [117].

A quantum non-demolition observable is a conserved quantity of the system such as its conjugated momentum or its energy. If a quantity is conserved it cannot be altered – not even by the measurement’s back action. Usually the term ‘quantum non-demolition’ in the context of measurement processes was introduced for a measurement which totally does not affect the probe. But instead of totally suppressing the back-action simply removing its noise from the measurement output also allows to surpass the standard quantum limit. Today the term ‘quantum non-demolition’ is usually used in a more broader sense and each device for which its measurement noise just beats the standard quantum limit – or in a continuous measurement process its spectrum – at a certain level, bears this name. Furthermore, the term ‘quantum non-demolition’ is still used even if the spectral density of the standard quantum limit is only beaten within a certain frequency range. We will also use this modern convention. In this thesis, especially in the first part, we will become acquainted with some of those quantum non-demolition devices.

1.1.3 Collapse of the wave function

The measurement device back-acting on the measured object is not the only quantum measurement effect we have to consider. Following again the Copenhagen interpretation of quantum mechanics, a measurement reduces the wave function of an object and collapses it into a certain state. The reality of such a wave function collapse was, and is still today, under strong debate. The question has always been whether it is a fundamental physical phenomenon or it just emerges due to some other process, such as decoherence. As an example, Roger Penrose suggested that the state reduction could be caused by gravity [95]: a quantum superposition of a macroscopic and heavy object as an example would lead to an ambiguity in defining the space-time. If only one version of the space-time exists this would cause a gravitationally induced collapse of the wave function. Other models rely on a spontaneous reduction of the wave function from an unknown origin such as the Ghirardi-Rimini-Weber model [59]. These models would also account for the – in my opinion only very small – possibility that quantum states of macroscopic and heavy objects are fundamentally banned.

Is a rose still red if we stop looking at it? No question, it is hard to believe that an observer really can influence the measured object’s state. The common sense would prefer that there is the passive observer and an object, which is in some state independent from the fact whether the observer notice it or not. Furthermore, Erwin Schrödinger’s famous gedanken experiment with the cat that may be in a superposition of dead or alive [109] somehow also calls the attention to the question of what an observer, which can cause a state reduction actually has to be composed of. Is it obliged to be a human being? All these questions really challenge realism. But for this thesis they should be only considered as philosophical questions and we do not want to go too much into the details. For us it should

be enough to assume that the state of a measured quantum object is what the observer knows about this object. In a continuous measurement, the wave function is continuously reduced and a certain trajectory of the measured object can be observed. This follows the concept of *a posteriori* [6] states. Such kind of states are also called *conditional states* and we will mainly deal with them in the second part of this thesis.

1.2 Quantum dynamical interaction between a mechanical oscillator and light

A well-known example of a realistic quantum measurement process is borrowed from quantum optics: the high-precision position measurement with laser light, on which we will concentrate our discussion throughout this thesis. In this example, the coupling between the measured object, a suspended high-reflective mirror, and the meter, the laser light, is via radiation pressure. Note that we will always consider the linear regime of this coupling. For such an interaction, both parts of the wave-particle dualism, which is strongly manifested in quantum mechanics, are essential: the laser light becomes phase-shifted due to the motion of the mirror – wave interpretation – and on the other hand the radiation pressure of the photons – particle interpretation – is in turn exciting the mirror motion. Here the measurement’s back action is clearly the laser light’s fluctuating radiation pressure which imposes a force onto the mirror and causes the *radiation-pressure noise* in the measurement output. In the end, the measurement process consists of counting the number of photons by recording the photo current of the photo diode. The photons of a coherent beam arrive according to a Poissonian distribution. The photon counting error represents the measurement noise, which is in this case also called *photon shot noise*. If these two quantum noise sources are uncorrelated they result in the standard quantum limit of this measurement with a spectral density as given by Eq. (1.17), if the mirror can be approximated as a free falling mass in the direction of incident laser beam – due to a very low eigenfrequency of the pendulum created by the mirror’s suspension.

In this section, we will briefly review two different approaches dealing with the dynamical interaction via radiation pressure between the quantum fluctuations in laser light and movable mirrors. Then we will show, by means of an example, that they yield equivalent results. Note that we will not go too much into the details here because both of the approaches are described and used throughout the literature. The first approach is based on a Hamiltonian from which linearized quantum Langevin equations are derived. For further reading see e.g. Refs. [56, 57, 93, 125, 126]. The second approach is based on travelling waves. The term ‘travelling’ may be somehow misleading and should be understood more in the way that we will evaluate the laser field at different locations. The laser field under free evolution is at a certain position and a certain time equal to the field at some displacement Δx at the time $\Delta x/c$ the wave needed to propagate to this displacement, where $c \equiv 299792458$ m/s is the speed of light in vacuum. From this fact we are able to obtain matrix relations which tell us how the field operators transform. For further reading please refer to e.g. Refs. [22, 29, 37, 78, 110].

As an example, we will consider – in Sec. 1.2.1 using linearized quantum Langevin equations and in Sec. 1.2.2 using the travelling waves approach – the quantum dynamics of a Fabry-Pérot cavity which has a movable end mirror and is not resonant for the frequency of the driving laser field. This *detuning* of the cavity makes the power inside the interferometer

dependent on the motion of the mirror, creating an *optical spring*. The general principle underlying this effect has already been explained by Braginsky and colleagues, namely in the 70's in their works in the context of microwave resonators, and later in the 90's in connection with optical fields [13, 17]. In Sec. 1.2.4, we will spend some time on reviewing this effect.

Note that this section is mostly intended to give a pedagogical introduction to the topic. We will carry out some example calculations to show how the things work. The advanced reader may want to skip this section.

1.2.1 Quantum Langevin equations

The first way of describing the dynamics of radiation-pressure interaction starts, as promised, with a Hamiltonian [93]

$$\hat{H} = \underbrace{\hbar\omega_c \hat{c}^\dagger \hat{c}}_{\hat{H}_{\text{cavity}}} + \underbrace{\frac{\hat{p}^2}{2m} + \frac{m\omega_m^2 \hat{x}^2}{2}}_{\hat{H}_{\text{mirror}}} - \underbrace{\frac{\hbar\omega_c}{L} \hat{c}^\dagger \hat{c} \hat{x}}_{\hat{H}_{\text{int}}} + \underbrace{i\hbar \sqrt{\frac{P_{\text{in}} \gamma_c}{\hbar\omega_0}} e^{i\vartheta} (\hat{c}^\dagger e^{-i\omega_0 t} - \hat{c} e^{i\omega_0 t})}_{\hat{H}_{\text{driving}}}. \quad (1.18)$$

In \hat{H}_{cavity} , \hat{c} denotes the annihilation operator of the resonant mode of the laser field in the cavity with the eigenfrequency ω_c . Here the cavity has a bandwidth γ_c and a length L . The coherent laser input field drives the cavity at the frequency ω_0 , at the phase ϑ and with an optical power of P_{in} . The cavity's movable end mirror of mass m is assumed to be a simple harmonic oscillator with the eigenfrequency $\omega_m \ll c/(2L)$, having a position operator \hat{x} and a momentum operator \hat{p} . Here the interaction of mirror and cavity mode works via the light's radiation pressure and is described by the interaction Hamiltonian \hat{H}_{int} . The radiation-pressure force at the mirror in \hat{H}_{int} is motivated by the fact that classically it would correspond to the energy of the cavity mode divided by the cavity length.

Recall that in the quantum mechanical Heisenberg picture, operators, instead of states, evolve in time. The equations of motion for an arbitrary operator \hat{o} under any Hamiltonian \hat{H} , which does not explicitly depend on time, is obtained from

$$\frac{d}{dt} \hat{o}(t) = \frac{i}{\hbar} [\hat{H}, \hat{o}(t)]. \quad (1.19)$$

Using the commutation relations $[\hat{x}, \hat{p}] = i\hbar$ (cf. Eq. (1.1)) and $[\hat{c}, \hat{c}^\dagger] = 1$ as well as Eq. (1.19) and the input-output theory for quantum damping [56, 57], we obtain the following set of coupled quantum Langevin equations in the interaction picture with respect to $(\hbar\omega_0 \hat{c}^\dagger \hat{c})$ (cf. e.g. Refs. [93, 125, 126])

$$m \frac{d^2}{dt^2} \hat{x}(t) = -m\omega_m^2 \hat{x}(t) + \hbar \frac{\omega_c}{L} \hat{c}^\dagger(t) \hat{c}(t), \quad (1.20)$$

$$\frac{d}{dt} \hat{c}(t) = \left(-i\omega_c + i\omega_0 - \frac{\gamma_c}{2} + i \frac{\omega_c}{L} \hat{x}(t) \right) \hat{c}(t) + \sqrt{\gamma_c} \hat{a}(t) + \sqrt{\frac{P_{\text{in}} \gamma_c}{\hbar\omega_0}} e^{i\vartheta}, \quad (1.21)$$

where we have already inserted $d/dt \hat{x}(t) = \hat{p}(t)/m$. Furthermore, \hat{a} represents the annihilation operator associated with the vacuum fluctuations of the continuum of modes outside the cavity having the only non-vanishing two-point time-domain correlation function

$$\langle \hat{a}(t) \hat{a}^\dagger(t') \rangle = \delta(t - t'). \quad (1.22)$$

In the next step, we will linearize Eqs. (1.20) and (1.21) around the steady state of the system which is given by

$$\tilde{x}_{\text{ss}} = \frac{\hbar \omega_c}{L m \omega_m^2} |\tilde{c}_{\text{ss}}|^2, \quad (1.23)$$

$$\tilde{p}_{\text{ss}} = 0, \quad (1.24)$$

$$\tilde{c}_{\text{ss}} = \sqrt{\frac{P_{\text{in}} \gamma_c}{\hbar \omega_0}} \frac{e^{i\vartheta}}{\gamma_c/2 - i\Delta}, \quad (1.25)$$

where the cavity is detuned with respect to ω_0 by

$$\Delta = \omega_0 + \frac{\hbar \omega_c^2}{L^2 m \omega_m^2} |\tilde{c}_{\text{ss}}|^2 - \omega_c. \quad (1.26)$$

Note that now \tilde{c}_{ss} is implicitly given when inserting Eq. (1.26) into Eq. (1.25). Without any loss of generality we can choose the phase ϑ of the coherent driving field in such a way that \tilde{c}_{ss} becomes real. Introducing the hermitian amplitude field quadrature operator $\hat{c}_1(t) = (\hat{c}(t) + \hat{c}^\dagger(t))/\sqrt{2}$ and phase field quadrature operator $\hat{c}_2(t) = i(\hat{c}^\dagger(t) - \hat{c}(t))/\sqrt{2}$, the linearized quantum Langevin equations read

$$m \frac{d^2}{dt^2} \hat{x}(t) = -m\omega_m^2 \hat{x}(t) + \sqrt{\frac{2 P_{\text{in}} \omega_c^2 \gamma_c \hbar}{\omega_0 L^2 (\Delta^2 + (\gamma_c/2)^2)}} \hat{c}_1(t), \quad (1.27)$$

$$\frac{d}{dt} \hat{c}_1(t) = -\frac{\gamma_c}{2} \hat{c}_1(t) - \Delta \hat{c}_2 + \sqrt{\gamma_c} \hat{a}_1(t), \quad (1.28)$$

$$\frac{d}{dt} \hat{c}_2(t) = -\frac{\gamma_c}{2} \hat{c}_2(t) + \Delta \hat{c}_1 + \sqrt{\gamma_c} \hat{a}_2(t) + \sqrt{\frac{2 P_{\text{in}} \omega_c^2 \gamma_c}{\omega_0 L^2 \hbar (\Delta^2 + (\gamma_c/2)^2)}} \hat{x}(t). \quad (1.29)$$

Here $\hat{a}_1(t) = (\hat{a}(t) + \hat{a}^\dagger(t))/\sqrt{2}$ and $\hat{a}_2(t) = i(\hat{a}^\dagger(t) - \hat{a}(t))/\sqrt{2}$ are the incoming amplitude and phase field quadrature operators, respectively. Since Eqs. (1.27)–(1.29) are given in the interaction picture with respect to $(\hbar \omega_0 \hat{c}^\dagger \hat{c})$, switching into frequency domain turns the operators into a function of the modulation frequency Ω around ω_0 . Throughout this thesis we will use the convention for frequency-domain transformation as given in Tab. 1. If we assemble Eqs. (1.28) and (1.29) into vector notation, we can easily solve them in the frequency domain for the cavity mode quadrature vector $(\hat{c}_1(\Omega), \hat{c}_2(\Omega))$ and obtain the decoupled equation

$$\begin{pmatrix} \hat{c}_1(\Omega) \\ \hat{c}_2(\Omega) \end{pmatrix} = \begin{pmatrix} \frac{\gamma_c/2 - i\Omega}{\Delta^2 + (\gamma_c/2 - i\Omega)^2} & -\frac{\Delta}{\Delta^2 + (\gamma_c/2 - i\Omega)^2} \\ \frac{\Delta}{\Delta^2 + (\gamma_c/2 - i\Omega)^2} & \frac{\gamma_c/2 - i\Omega}{\Delta^2 + (\gamma_c/2 - i\Omega)^2} \end{pmatrix} \times \left[\sqrt{\gamma_c} \begin{pmatrix} \hat{a}_1(\Omega) \\ \hat{a}_2(\Omega) \end{pmatrix} + \sqrt{\frac{2 P_{\text{in}} \omega_0 \gamma_c}{L^2 \hbar (\Delta^2 + (\gamma_c/2)^2)}} \begin{pmatrix} 0 \\ \hat{x}(\Omega) \end{pmatrix} \right], \quad (1.30)$$

where we have approximated $\omega_c^2/\omega_0^2 \approx 1$. Furthermore, we have assumed a steady state where the initial values of $\hat{c}_{1,2}(t)$ can be neglected. The output field quadrature operators are given by the input-output relation [56, 57]

$$\hat{b}_i(\Omega) = \sqrt{\gamma_c} \hat{c}_i(\Omega) - \hat{a}_i(\Omega), \quad (1.31)$$

for $i = 1, 2$. Eq. (1.31) together with the equation

$$-m\Omega^2 \hat{x}(\Omega) = -m\omega_m^2 \hat{x}(\Omega) + \sqrt{\frac{2 P_{\text{in}} \omega_0 \gamma_c \hbar}{L^2 (\Delta^2 + (\gamma_c/2)^2)}} \hat{c}_1(\Omega) \quad (1.32)$$

give us then the linearized equations of motion of the system in the frequency domain, where initial values are neglected. Finally, we can insert Eq. (1.30) into Eq. (1.31) as well as the first component of the vector from Eq. (1.30) into Eq. (1.32).

1.2.2 Travelling waves approach

In the framework of the *two-photon formalism* [29,110], the quantized electric field of the light wave at a certain location in or outside the cavity can be written in terms of its quadrature fields $\hat{E}_{1,2}(t)$ which describe modulations around the carrier frequency ω_0 varying at a much longer timescale than $1/\omega_0$ (cf. e.g. Refs. [22,37,78]). This fact reads

$$\hat{E}(t) = \hat{E}_1(t) \cos(\omega_0 t) + \hat{E}_2(t) \sin(\omega_0 t). \quad (1.33)$$

The quadrature fields read in a suitable normalization

$$\hat{E}_i(t) = \sqrt{\frac{8\pi P}{\mathcal{A} c}} \left[\begin{pmatrix} \cos \vartheta \\ \sin \vartheta \end{pmatrix} \right]_i + \sqrt{\frac{4\pi \hbar \omega_0}{\mathcal{A} c}} \int_0^\infty \frac{d\Omega}{2\pi} \left(\hat{a}_i(\Omega) e^{-i\Omega t} + \hat{a}_i^\dagger(\Omega) e^{i\Omega t} \right), \quad (1.34)$$

for $i = 1, 2$ and with the effective beam area \mathcal{A} . Here the first term denotes the quadrature fields of the monochromatic carrier light with optical power P and phase ϑ , while $\hat{a}_1(\Omega)$ and $\hat{a}_2(\Omega)$ are the amplitude and phase quadrature operators, respectively, of the fluctuating fields at a modulation frequency which we will usually call the *sideband frequency* Ω , having the only non-vanishing commutators

$$[\hat{a}_1(\Omega), \hat{a}_2^\dagger(\Omega')] = -[\hat{a}_2(\Omega), \hat{a}_1^\dagger(\Omega')] = 2\pi i \delta(\Omega - \Omega') \delta_{ij} \quad (1.35)$$

and the only non-vanishing vacuum correlation functions

$$\langle \hat{a}_i(\Omega) \hat{a}_j^\dagger(\Omega') \rangle_{\text{sym}} \equiv \frac{1}{2} \langle \hat{a}_i(\Omega) \hat{a}_j^\dagger(\Omega') + \hat{a}_j^\dagger(\Omega') \hat{a}_i(\Omega) \rangle = \pi \delta(\Omega - \Omega') \delta_{ij}, \quad (1.36)$$

where throughout this thesis the subscript 'sym' will stand for symmetrization. It is convenient to assemble the two quadrature operators into vector notation $\vec{a}(\Omega) = (\hat{a}_1(\Omega), \hat{a}_2(\Omega))^T$ and assign different vectors to different locations by giving them different names. The simplest transformation certainly is propagating such a quadrature vector $\vec{a}(\Omega)$ through a free space of length L , where the fluctuating quadrature fields at L are described by $\vec{b}(\Omega)$. Then we have $\hat{E}^{\vec{a}}(t) = \hat{E}^{\vec{b}}(t - L/c)$ and this transforms the vector $\vec{a}(\Omega)$ into a vector $\vec{b}(\Omega)$ as

$$\vec{b}(\Omega) = e^{i\Omega L/c} \begin{pmatrix} \cos(\omega_0 L/c) & -\sin(\omega_0 L/c) \\ \sin(\omega_0 L/c) & \cos(\omega_0 L/c) \end{pmatrix} \vec{a}(\Omega). \quad (1.37)$$

The coupling between mirror motion and in-coming and out-going quadrature vectors at the mirror is slightly more complicated. On the one hand, the momentum flow of the optical field induces a force on the mirror and on the other hand, the mirror's motion phase

modulates the carrier field. Thus, we are firstly interested in the fluctuating part of the total momentum flow of the optical field at the mirror. The total momentum flow carried by each field incident on the mirror is

$$\hat{\Pi}(t) = \frac{\mathcal{A}}{c} \left(\hat{E}_1(t) \cos(\omega_0 t) + \hat{E}_2(t) \sin(\omega_0 t) \right)^2. \quad (1.38)$$

After time averaging and removing the static parts, we obtain in the frequency domain

$$\hat{\Pi}_{\text{fluc}}^{\vec{a}}(\Omega) = \sqrt{\frac{2P\omega_0\hbar}{c^2}} (\cos\vartheta, \sin\vartheta) \vec{a}(\Omega). \quad (1.39)$$

Using momentum conservation at the mirror we can write down the equations of motion of the mirror motion in the frequency domain

$$-m\Omega^2 \hat{x}(\Omega) = -m\omega_m^2 \hat{x}(\Omega) + \sum_{\vec{a}} \left(\pm \hat{\Pi}_{\text{fluc}}^{\vec{a}}(\Omega) \right), \quad (1.40)$$

where the summation is done over all fields entering and exiting the mirror and ω_m is the mechanical eigenfrequency of the mirror. Note that the sign of $\hat{\Pi}_{\text{fluc}}^{\vec{a}}(\Omega)$ belonging to each field depends on the direction of propagation relative to the mirror's direction of propagation. In turn, a displacement $\hat{x}(t)$ of the mirror produces a phase change of $2\hat{x}(t)\omega_0/c$ in the reflected field, where we have

$$\hat{E}_i(t \pm \frac{2\hat{x}(t)}{c}) \approx \hat{E}_i(t) \pm \frac{2\hat{x}(t)\omega_0}{c} \left[\begin{pmatrix} \sin\vartheta \\ -\cos\vartheta \end{pmatrix} \right]_i, \quad (1.41)$$

in leading order of $\hat{x}(t)$. The sign accounts for whether the mirror moves in or against the direction of field propagation. Therefore, a quadrature vector $\vec{a}(\Omega)$ incident on the mirror transforms into a reflected quadrature vector $\vec{b}(\Omega)$ as

$$\vec{b}(\Omega) = \vec{a}(\Omega) \pm \sqrt{\frac{8P\omega_0}{c^2\hbar}} \begin{pmatrix} \sin\vartheta \\ -\cos\vartheta \end{pmatrix} \hat{x}(\Omega). \quad (1.42)$$

This formulation turn calculating the quantum fields in complex optical devices into simple matrix algebra.

Now we will come back to the Fabry-Pérot cavity of length L which is detuned from the driving input laser field by Δ and use the above formulation to get the equations of motion. The coherent input laser field has again an optical power P_{in} at the frequency ω_0 . The input mirror is fixed and has a power reflectivity ρ_{ITM}^2 and a power transmissivity $\tau_{\text{ITM}}^2 = 1 - \rho_{\text{ITM}}^2$. The movable end mirror is assumed to be highly reflective. In Fig. 2 the relevant locations of the quadrature fields are labeled by their quadrature vector. Here we understand L as the total length of the cavity where the end mirror is already moved due to the steady state radiation-pressure force of the light and we have

$$\omega_0 = \frac{2\pi c}{L} + \Delta. \quad (1.43)$$

We can easily put up the following coupled set of equations in the frequency domain for the

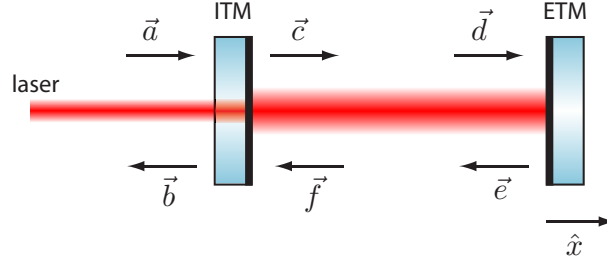


Figure 2: Schematic plot of a Fabry-Pérot cavity. It is formed by two parallel mirrors: the partly-transparent input mirror (ITM) and the high-reflective end mirror (ETM). The ETM is movable in \hat{x} direction. The vectors \vec{a} to \vec{f} are quadrature vectors representing the modulation fields at different locations.

quadrature vectors and the end mirror's displacement operator \hat{x}

$$\vec{b} = -\rho_{\text{ITM}} \vec{a} + \tau_{\text{ITM}} \vec{f}, \quad (1.44)$$

$$\vec{c} = \rho_{\text{ITM}} \vec{f} + \tau_{\text{ITM}} \vec{a}, \quad (1.45)$$

$$\vec{d} = e^{i\Omega L/c} \begin{pmatrix} \cos(\Delta L/c) & -\sin(\Delta L/c) \\ \sin(\Delta L/c) & \cos(\Delta L/c) \end{pmatrix} \vec{c}, \quad (1.46)$$

$$\vec{e} = \vec{d} - \sqrt{\frac{8 P_{\text{in}} \omega_0 \tau_{\text{ITM}}^2}{c^2 \hbar (1 + \rho_{\text{ITM}}^2 - 2 \rho_{\text{ITM}} \cos(2\Delta L/c))}} \begin{pmatrix} 0 \\ -1 \end{pmatrix} \hat{x}(\Omega), \quad (1.47)$$

$$\vec{f} = e^{i\Omega L/c} \begin{pmatrix} \cos(\Delta L/c) & -\sin(\Delta L/c) \\ \sin(\Delta L/c) & \cos(\Delta L/c) \end{pmatrix} \vec{e}, \quad (1.48)$$

$$\hat{x}(\Omega) = -\frac{1}{m(\Omega^2 - \omega_m^2)} \sqrt{\frac{8 P_{\text{in}} \omega_0 \hbar \tau_{\text{ITM}}^2}{c^2 (1 + \rho_{\text{ITM}}^2 - 2 \rho_{\text{ITM}} \cos(2\Delta L/c))}} (1, 0) (\vec{d} + \vec{e}), \quad (1.49)$$

where we have chosen ϑ without loss of generality. Eqs. (1.45)–(1.48) can be solved for \vec{c} to dependent only on \vec{a} and \hat{x} . Then we rewrite Eqs. (1.44)–(1.49) as

$$\vec{b} = -\frac{1}{\rho_{\text{ITM}}} \vec{a} + \frac{\tau_{\text{ITM}}}{\rho_{\text{ITM}}} \vec{c}, \quad (1.50)$$

$$\vec{c} = \left(\mathbb{1} - \rho_{\text{ITM}} e^{2i\Omega L/c} \begin{pmatrix} \cos(2\Delta L/c) & -\sin(2\Delta L/c) \\ \sin(2\Delta L/c) & \cos(2\Delta L/c) \end{pmatrix} \right)^{-1} \times \left(\tau_{\text{ITM}} \vec{a} - \sqrt{\frac{8 P_{\text{in}} \omega_0 \tau_{\text{ITM}}^2 \rho_{\text{ITM}}^2 e^{2i\Omega L/c}}{c^2 \hbar (1 + \rho_{\text{ITM}}^2 - 2 \rho_{\text{ITM}} \cos(2\Delta L/c))}} \begin{pmatrix} \sin(\Delta L/c) \\ -\cos(\Delta L/c) \end{pmatrix} \hat{x}(\Omega) \right), \quad (1.51)$$

$$\hat{x}(\Omega) = -\frac{1}{m(\Omega^2 - \omega_m^2)} \sqrt{\frac{8 P_{\text{in}} \omega_0 \hbar \tau_{\text{ITM}}^2 e^{2i\Omega L/c}}{c^2 (1 + \rho_{\text{ITM}}^2 - 2 \rho_{\text{ITM}} \cos(2\Delta L/c))}} (\cos(\Delta L/c), -\sin(\Delta L/c)) \vec{c}. \quad (1.52)$$

Now we first need to insert Eq. (1.51) into Eqs. (1.50) and (1.52). Then we expand simultaneously in τ_{ITM}^2 and $1/c$ up to the zeroth order which is here a special kind of linearization. When we then additionally use the definition of the cavity bandwidth $\gamma_c = c \tau_{\text{ITM}}^2 / (2L)$, we find that Eq. (1.52) is totally equivalent to Eq. (1.32) and Eq. (1.50) to Eq. (1.31).

1.2.3 Susceptibilities

Note that all equations of motion for the different optical-mechanical coupled – we will often also use the term ‘optomechanically coupled’ – systems analyzed in this thesis are obtained by using the above method of propagating modulation fields through the optical device. As outlined in Ref. [23], we can go one step further and in turn put this formulation back into a formulation governed by a perturbed Hamiltonian and express the equations of motion in terms of so-called *susceptibilities*. In fact, as shown in Ref. [18], any linear quantum measurement can be described in this way.

First of all, we will gather the functions in front of \vec{a} and \hat{x} in Eq. (1.32) which is equal to the linearized Eq. (1.52), as well as in Eq. (1.31) which is equal to the linearized Eq. (1.50) and give names to them – at this stage still without any meaning. Then we have

$$\begin{aligned} \hat{y}_\zeta(\Omega) &\equiv \hat{b}_1(\Omega) \sin \zeta + \hat{b}_2(\Omega) \cos \zeta \\ &= \underbrace{\hat{Y}_1^{(0)}(\Omega) \sin \zeta + \hat{Y}_2^{(0)}(\Omega) \cos \zeta}_{\hat{Y}_\zeta^{(0)}(\Omega)} + \underbrace{\left(R_{Y_1 F}^{\text{cav}}(\Omega) \sin \zeta + R_{Y_2 F}^{\text{cav}}(\Omega) \cos \zeta \right)}_{R_{Y_\zeta F}^{\text{cav}}(\Omega)} \hat{x}(\Omega), \end{aligned} \quad (1.53)$$

$$\hat{x}(\Omega) = R_{xx}^{\text{cav}}(\Omega) \left(\hat{F}_{\text{RP}}^{(0)}(\Omega) + R_{FF}^{\text{cav}}(\Omega) \hat{x}(\Omega) \right). \quad (1.54)$$

Here we have additionally assumed to perform a perfect balanced homodyne detection on the output field at a certain frequency-independent angle ζ . Therefore the output field needs to become superposed with another high-power light field, which has the same frequency as the carrier field and is usually called the *local oscillator*, on a beam splitter. Then each of the two outputs of the beam splitter is measured via a photo detection and the two photocurrents are subtracted from each other. By adjusting the phase of the local oscillator, the homodyne detection enables us to observe a specific quadrature of the output field given by the homodyne angle. Then the measurement-output operator is given by \hat{y}_ζ in Eq. (1.53). In that equation we can already see that the operators

$$\hat{Y}_1^{(0)}(\Omega) = y_1^{\text{cav}}(\Omega) \hat{a}_1(\Omega) + y_2^{\text{cav}}(\Omega) \hat{a}_2(\Omega), \quad (1.55)$$

$$\hat{Y}_2^{(0)}(\Omega) = -y_2^{\text{cav}}(\Omega) \hat{a}_1(\Omega) + y_1^{\text{cav}}(\Omega) \hat{a}_2(\Omega), \quad (1.56)$$

account for the output quadrature operators in the case of a fixed end mirror, where we have the coefficients

$$y_1^{\text{cav}}(\Omega) = \frac{\Omega^2 - \Delta^2 + (\gamma_c/2)^2}{\Delta^2 + (\gamma_c/2 - i\Omega)^2}, \quad (1.57)$$

$$y_2^{\text{cav}}(\Omega) = -\frac{\Delta\gamma_c}{\Delta^2 + (\gamma_c/2 - i\Omega)^2}, \quad (1.58)$$

while the operator

$$\hat{F}_{\text{RP}}^{(0)} = f_1^{\text{cav}}(\Omega) \hat{a}_1(\Omega) + f_2^{\text{cav}}(\Omega) \hat{a}_2(\Omega), \quad (1.59)$$

in Eq. (1.54) describes the radiation-pressure forces which would act on the fixed end mirror.

The remaining functions are given by

$$R_{xx}^{\text{cav}}(\Omega) = -\frac{1}{m(\Omega^2 - \omega_m^2)}, \quad (1.60)$$

$$R_{Y_1F}^{\text{cav}}(\Omega) = \frac{1}{\hbar} f_2^{\text{cav}}(\Omega) = \sqrt{\frac{2 P_{\text{in}} \omega_0 \gamma_c^2}{L^2 \hbar (\Delta^2 + (\gamma_c/2)^2)}} \frac{-\Delta}{\Delta^2 + (\gamma_c/2 - i\Omega)^2}, \quad (1.61)$$

$$R_{Y_2F}^{\text{cav}}(\Omega) = \frac{1}{\hbar} f_1^{\text{cav}}(\Omega) = \sqrt{\frac{2 P_{\text{in}} \omega_0 \gamma_c^2}{L^2 \hbar (\Delta^2 + (\gamma_c/2)^2)}} \frac{\gamma_c/2 - i\Omega}{\Delta^2 + (\gamma_c/2 - i\Omega)^2}, \quad (1.62)$$

$$R_{FF}^{\text{cav}}(\Omega) = \frac{2 P_{\text{in}} \omega_0 \gamma_c}{L^2 (\Delta^2 + (\gamma_c/2)^2)} \frac{-\Delta}{\Delta^2 + (\gamma_c/2 - i\Omega)^2}, \quad (1.63)$$

which have been obtained by comparing Eq. (1.31) with Eq. (1.53) as well as Eq. (1.32) with Eq. (1.54).

Now we will clarify the meaning of Eqs. (1.53) and (1.54), and especially the meaning of the functions given in Eqs. (1.60)–(1.63). For this purpose, let us consider the following Hamiltonian [23]

$$\hat{H} = \hat{H}_M + \hat{H}_L \underbrace{-\hat{x} \hat{F}_{\text{RP}}}_{\hat{H}_I}. \quad (1.64)$$

This should actually represent the Hamiltonian on a product Hilbert space $\mathcal{H} = \mathcal{H}_M \otimes \mathcal{H}_L$ of two linear independent systems on the two different Hilbert spaces \mathcal{H}_M and \mathcal{H}_L which are coupled by an explicitly given – in terms of the Schrödinger operators \hat{x} acting only on the Hilbert space \mathcal{H}_M and \hat{F}_{RP} acting only on the Hilbert space \mathcal{H}_L – interaction Hamiltonian \hat{H}_I . We can treat the interaction Hamiltonian as a perturbation of the total Hamiltonian. The Heisenberg evolution of any observable \hat{o} can be written as a perturbation series of the interaction Hamiltonian in the interaction picture $\hat{H}_I(t) = -\hat{x}^{(0)}(t) \hat{F}_{\text{RP}}^{(0)}(t)$ as

$$\begin{aligned} \hat{o}(t) &= \hat{o}^{(0)}(t) + \frac{i}{\hbar} \int_{-\infty}^t dt_1 \left[\hat{H}_I(t_1), \hat{o}^{(0)}(t) \right] \\ &+ \left(\frac{i}{\hbar} \right)^2 \int_{-\infty}^t dt_1 \int_{-\infty}^{t_1} dt_2 \left[\hat{H}_I(t_2), \left[\hat{H}_I(t_1), \hat{o}^{(0)}(t) \right] \right] + \dots \end{aligned} \quad (1.65)$$

where the superscript '(0)' denotes free evolution under \hat{H}_M or \hat{H}_L , respectively. For a linear observable in a linear system having c-number commutators together with all other operators of its Hilbert space, this perturbation series breaks down after the first order. Thus, the linear operator \hat{x} acting only on \mathcal{H}_M as well as the linear operators \hat{y}_ζ and \hat{F}_{RP} acting only on \mathcal{H}_L , evolve as

$$\hat{y}_\zeta(t) = \hat{y}_\zeta^{(0)}(t) + \frac{i}{\hbar} \int_{-\infty}^t dt' C_{Y_\zeta F}^-(t, t') \hat{x}(t), \quad (1.66)$$

$$\hat{F}_{\text{RP}}(t) = \hat{F}_{\text{RP}}^{(0)}(t) + \frac{i}{\hbar} \int_{-\infty}^t dt' C_{FF}^-(t, t') \hat{x}(t), \quad (1.67)$$

$$\hat{x}(t) = \hat{x}^{(0)}(t) + \frac{i}{\hbar} \int_{-\infty}^t dt' C_{xx}^-(t, t') \hat{F}_{\text{RP}}(t). \quad (1.68)$$

Here the time-domain susceptibilities $C_{Y_\zeta F}^-(t, t')$, $C_{FF}^-(t, t')$ and $C_{xx}^-(t, t')$ are defined as shown in Tab. 1 and depend only on the difference $(t - t')$ since \hat{H}_M and \hat{H}_L do not depend

explicitly on time. Since the frequency-domain susceptibility is specially related to the time-domain susceptibility, it is also given in Tab. 1. Then, in the frequency domain, Eqs. (1.66)–(1.68) read

$$\hat{y}_\zeta(\Omega) = \hat{Y}_\zeta^{(0)}(\Omega) + R_{Y_\zeta F}(\Omega) \hat{x}(\Omega), \quad (1.69)$$

$$\hat{F}_{\text{RP}}(\Omega) = \hat{F}_{\text{RP}}^{(0)}(\Omega) + R_{FF}(\Omega) \hat{x}(\Omega), \quad (1.70)$$

$$\hat{x}(\Omega) = \hat{x}^{(0)}(\Omega) + R_{xx}(\Omega) \hat{F}_{\text{RP}}(\Omega). \quad (1.71)$$

Inserting Eq. (1.70) into Eq. (1.71) and with $R_{xx}(\Omega) = R_{xx}^{\text{cav}}(\Omega)$ and $R_{FF}(\Omega) = R_{FF}^{\text{cav}}(\Omega)$ the equivalence to Eq. (1.54) is not hard to spot. This also applies to Eq. (1.69) and Eq. (1.53) which when using $R_{Y_\zeta F}(\Omega) = R_{Y_\zeta F}^{\text{cav}}(\Omega)$ are also totally equivalent.

Let us pause for the moment and recall what we have actually done. In particular, what can we learn from this? We have shown that the equations of motion for the measurement output (cf. Eq. (1.53)) and the mirror motion (cf. Eq. (1.54)) could have originated from the Hamiltonian given in Eq. (1.64), where \hat{H}_M is the Hamiltonian of the free mirror and \hat{H}_L the one of the free light. Free in the sense of before the coupling of the mirror and the light. Furthermore, we can use a linearized version of the interaction Hamiltonian in Eq. (1.18). As we have already seen right after setting up Eqs. (1.53) and (1.54), $\hat{Y}_\zeta^{(0)}$ and $\hat{F}_{\text{RP}}^{(0)}$ describe the free evolution of the measurement output and the radiation-pressure force, respectively. Furthermore, it has turned out that the functions in Eqs. (1.60)–(1.63) are the susceptibilities of the system.

1.2.4 Optical spring effect

A closer look at Eq. (1.54) reveals that $\hat{x}(\Omega)$ is subject to a frequency-dependent restoring force $R_{FF}^{\text{cav}}(\Omega) \hat{x}(\Omega)$ which is usually called the optical spring [17]. A possible way of explaining this phenomenon is by looking at the optical power inside the cavity and how it depends on the detuning (cf. Fig. 3). The optical power has a maximum when the carrier is resonant

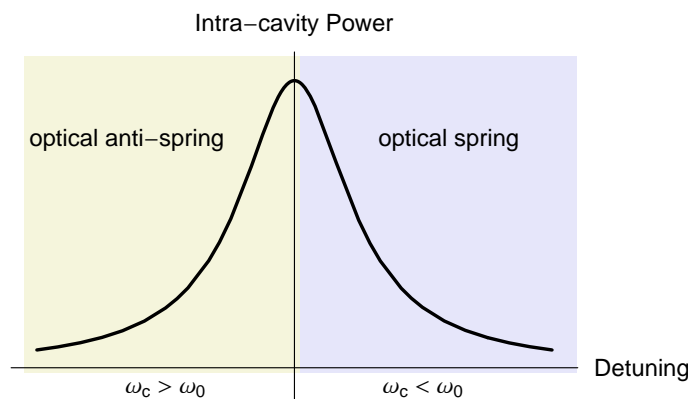


Figure 3: Intra-cavity power depending on the detuning of the cavity with respect to the light. This function is called Airy peak. The differently shaded regions mark either optical spring or optical anti-spring regimes.

in the cavity. When the cavity is detuned in such a way that it is too long for the carrier to be able to resonate, i.e. $\omega_c < \omega_0$, we have the following situation: when the cavity

length increases even more, the optical power decreases. Less optical power imposes a weaker radiation-pressure force onto the mirror. But as the cavity becomes shorter, the carrier frequency fits better into the cavity and the optical power increases. Therefore, the radiation-pressure force also increases. A restoring force! Because the optical power lags behind the cavity motion, the dynamics is anti-damped. Although this model provides a very nice way of understanding the optical spring effect, it is not the whole story.

The similarity to a mechanical spring becomes more apparent when expanding $R_{FF}^{\text{cav}}(\Omega)$ up to first order in Ω

$$R_{FF}^{\text{cav}}(\Omega) \approx -\frac{2 P_{\text{in}} \omega_0 \gamma_c \Delta}{L^2 (\Delta^2 + (\gamma_c/2)^2)^2} \left(1 + i \Omega \frac{\gamma_c}{\Delta^2 + (\gamma_c/2)^2} \right) \equiv -K + i \Omega \Gamma, \quad (1.72)$$

where K and Γ are real constants. This *weakly coupled* approximation requires that optical frequency scales, such as detuning Δ and bandwidth γ_c , are dominating the dynamics. Note that converting the equations of motion of a velocity-damped mechanical spring with a spring constant K and a damping rate Γ as given by

$$m \ddot{x}(t) = -K x(t) - \Gamma \dot{x}(t) + F(t), \quad (1.73)$$

into frequency domain, it just yields

$$-m \Omega^2 x(\Omega) = -K x(\Omega) + i \Omega \Gamma x(\Omega) + F(\Omega). \quad (1.74)$$

Therefore, Eq. (1.72) gives rise to a damped spring term in the equations of motion of the mirror (cf. Eq. (1.54)) which is not of mechanical but of optical origin. Often, a $R_{FF}^{\text{cav}}(\Omega) \neq 0$ is also called *ponderomotive* rigidity. In the approximation given in Eq. (1.72), $R_{FF}^{\text{cav}}(\Omega)$ either introduces a restoring force ($K > 0$) with an anti-damping ($\Gamma < 0$) or an anti-restoring force ($K < 0$) with a damping ($\Gamma > 0$). This depends on the sign of the detuning Δ , i.e. on whether the cavity is red or blue detuned with respect to the carrier. It is a peculiar feature that the viscous damping does not introduce additional thermal fluctuation (higher than \hbar) as one would expect from the fluctuation-dissipation theorem. This is simply because the spring is established by ground state fields. One is therefore usually tempted to say that the optical spring can introduce a non-dissipative damping force.

Another fact is that the optical spring modifies the resonant structure of the system. The system has still two resonance frequencies but usually both, the mechanical ω_m and the optical $\omega_0 - \Delta - i \gamma_c/2$, are shifted due to the coupling of mirror and light. The new resonance frequency which originates from the mechanical resonance is usually called *optomechanical resonance* frequency. Note that in the weakly coupled regime (cf. Eq. (1.72)) the optical resonance is not shifted and the optomechanical resonance is just a sum, where $m \omega_m^2 \rightarrow m \omega_m^2 + K$ and a mechanical damping γ_m would be shifted as $m \gamma_m \rightarrow m \gamma_m + \Gamma$. Since also the imaginary part of the resonances is shifted, the system can become unstable, i.e. the damping turns into a positive build up. We have found that starting with a damped system, it remains stable as long as the input power fulfills

$$P_{\text{in}} < \begin{cases} -\frac{L^2 \omega_m^2 (\Delta^2 + (\gamma_c/2)^2)^2}{8 \omega_0 \gamma_c \Delta} & \text{if } \Delta < 0 \\ \frac{L^2 \gamma_m (\Delta^2 + (\gamma_c/2)^2) (\omega_m^4 + 2 \omega_m^2 (\gamma_c/2 (\gamma_c/2 + \gamma_m) - \Delta^2) + ((\gamma_c/2)^2 + \Delta^2) (\Delta^2 + (\gamma_c/2 + \gamma_m)^2))}{8 \omega_0 \Delta (\gamma_c + \gamma_m)^2} & \text{if } \Delta > 0 \end{cases}. \quad (1.75)$$

Note that a free mass, with $\omega_m, \gamma_m \rightarrow 0$, is turned inescapably into an unstable system. For an oscillator, there does exist a stable optical spring regime where an increase in mechanical resonant frequency is associated with an increase in damping. But this regime requires that the optical frequency scales are much lower than the mechanical frequency. Such a regime was experimentally investigated e.g. in Ref. [107].

1.3 Quantum Brownian motion of a mechanical harmonic oscillator

A harmonic oscillator, even in its quantum-mechanical ground state, is never at rest due to Heisenberg's uncertainty principle (cf. Sec. 1.1). This fact requires the equal-time commutator among the oscillator's position and momentum to vanish. But using Eq. (1.54) and $\hat{p}(\Omega) = -i m \Omega \hat{x}(\Omega)$ we calculate $[\hat{x}(t), \hat{p}(t)] = 0$. This tells us that Eq. (1.54) cannot completely describe the Gaussian quantum dynamics of the harmonic oscillator.

One easy way out of this problem which takes the zero-point motion of an oscillator being in a Gaussian state into account, is using the following strategy: let us introduce a small loss – i.e. a damping γ_m which is small with respect to the oscillator's eigenfrequency ω_m – into the center-of-mass dynamics of the mechanical harmonic oscillator and couple it to some thermal bath which becomes quantum at the temperature of absolute zero. In this way we obtain a Gaussian state in center-of-mass position and momentum of the oscillator at temperatures greater zero, but with zero-point fluctuations at zero temperature. Note that this formulation can of course not cover the regime of non-Gaussian number states with occupation number unequal to zero.

Practically speaking, we will introduce an operator $\hat{\xi}(t)$ which acts as a force onto the oscillator. Then we will appropriately design its two-point correlation function as well as its commutator such as it is shown in Refs. [25, 26, 57, 60]. Therefor we need to modify the Langevin equations of motion of the oscillator's position – here as an example without coupling to the light – to

$$m \frac{d^2}{dt^2} \hat{x}(t) + m \omega_m^2 \hat{x}(t) + \gamma_m \hat{p}(t) = \hat{\xi}(t), \quad (1.76)$$

where the momentum can be obtained from $\hat{p}(t) = m d/dt \hat{x}(t)$. If we turn into frequency domain and assign the following artificial commutator and correlation function to $\hat{\xi}(\Omega)$

$$\left[\hat{\xi}(\Omega), \hat{\xi}^\dagger(\Omega') \right] = 2 m \gamma_m \hbar \Omega 2\pi \delta(\Omega - \Omega'), \quad (1.77)$$

$$\langle \hat{\xi}(\Omega) \hat{\xi}^\dagger(\Omega') \rangle_{\text{sym}} = 2 m \gamma_m \hbar \omega_m \coth \left(\frac{\hbar \omega_m}{2 k_B T} \right) 2\pi \delta(\Omega - \Omega'), \quad (1.78)$$

where $k_B \approx 1.3806504 \cdot 10^{-23} \text{ J/K}$ is the Boltzmann constant, the equal-time commutator between position and momentum yields $[\hat{x}(t), \hat{p}(t)] = i \hbar$ (cf. Eq. (1.1)) as it is required from quantum mechanics. Moreover, in Ref. [25] it has been proven that the above formulation and using Eqs. (1.77) and (1.78) provides an adequate and consistent description of the quantum Brownian motion of a weakly damped oscillator, i.e. with $\gamma_m \ll \omega_m$. Note that Eqs. (1.77) and (1.78) become in turn inconsistent with this formulation in a strongly damped system. But throughout this thesis we will only consider weakly damped oscillators. At high

temperatures with $k_B T \gg \hbar \omega_m$, the state, which is usually called a *classical* or a *thermal* state, is determined by

$$V_{xx}^{\text{thermal}} = \frac{k_B T}{m \omega_m^2}, \quad V_{pp}^{\text{thermal}} = m k_B T, \quad (1.79)$$

and no correlation between position and momentum $V_{xp}^{\text{thermal}} = 0$. Whereas in the limit of temperature around the absolute zero, the oscillator reaches its ground state with position and momentum width of

$$V_{xx}^{\text{ground}} = \frac{\hbar}{2 m \omega_m}, \quad V_{pp}^{\text{ground}} = \frac{\hbar m \omega_m}{2}, \quad (1.80)$$

and again $V_{xp}^{\text{ground}} = 0$. Let us introduce the *ground-state normalized operators*

$$\hat{x}^{\text{norm}} = \sqrt{\frac{2 m \omega_m}{\hbar}} \hat{x}, \quad \hat{p}^{\text{norm}} = \sqrt{\frac{2}{m \omega_m \hbar}} \hat{p}, \quad (1.81)$$

for the position and the momentum, respectively. With these operators we obtain a coordinate system in which the oscillator's ground-state squeezing ellipse becomes a circle. The Wigner function of the oscillator's ground state in such normalized coordinates can be found in the left panel of Fig. 1. In the *free-mass limit* of the oscillator, i.e. with $\omega_m \rightarrow 0$, it becomes ambiguous to define a ground state, since here the state is totally fuzzy in position with $V_{xx}^{\text{ground}} \rightarrow \infty$ and simultaneously infinitely sharp in momentum with $V_{pp}^{\text{ground}} \rightarrow 0$.

Note that both, the ground and the thermal state, are independent of γ_m . In the limit of a strong measurement present, which exerts a strong back-action force on the oscillator, its zero-point motion can be neglected. In the same manner other classical forces acting onto the oscillator allow to disregard the quantum Brownian motion.

1.4 Quantum entanglement

Deep-seated in the theory of quantum mechanics is the phenomenon that the state of two or more objects may be linked together in such a way that each object can lose some individual properties. Even when the objects are spatially separated, the quantum correlations are so strong that one cannot describe one object without fully mentioning the other. This situation is called quantum entanglement [109] – the term was chosen by Erwin Schrödinger in 1935 – and the objects are said to be in an entangled state. At first glance this situation seems to be incomprehensible and it caused the physicists Albert Einstein, Boris Podolsky and Nathan Rosen to doubt whether quantum mechanics is complete at the time when quantum mechanics was developed. They realized that the sum of the positions of two objects commutes with the difference in their momenta. Therefore, these two degrees of freedom do not need to fulfil any Heisenberg uncertainty relation and can both be measured with arbitrary precision. Using the measurement performed at one of the objects to infer the position or momentum onto the other, one could think that in principle one object can have simultaneously well-defined position and momentum. This is strictly forbidden by the Heisenberg uncertainty principle. Today this gedanken experiment is known as the Einstein-Podolsky-Rosen paradox [47] which is in fact not a paradox with our current understanding

of quantum physics. It is broadly accepted that the objects are not defined individually in the entangled quantities but only with respect to each other.

Entanglement is simply a consequence of coherence and the superposition principle. The characteristic nature of an entangled state is always its inseparability which also applies to its density matrix. Probably the most well-known example of a maximally entangled state in discrete variables is the Bell state

$$|\Psi\rangle = \frac{1}{\sqrt{2}} (|0\rangle |0\rangle + |1\rangle |1\rangle) , \quad (1.82)$$

which is obviously non-separable. But it is not always so evident whether a state is entangled or not – especially in the case of continuous variables. A famous criterion for the separability of a density matrix is the positive partial transpose criterion proposed by Asher Peres [96] and proved by the Horodeckis [69]. Most of the subsequent entanglement criteria are based on this criterion.

Generally, entanglement could arise either when the two or more objects have a common origin, when they have been in a strong quantum interacting or when they share a strong common quantum force. The entanglement gets always lost again when the systems interact with their environment. As an example, the mirror-light interaction from the previous section certainly produces entanglement between mirror and output field variables. This entanglement vanishes if for example the mirror is subject to too much thermal noise. In Sec. 3.5 we will learn that the two end mirrors of a Michelson interferometer can be entangled due to the fact that they share the common and differential mode radiation-pressure force.

In the following we will briefly review the condition for the non-separability of bipartite two-mode Gaussian states and the condition for having bipartite two-mode Gaussian Einstein-Podolsky-Rosen states. Note that we specify our discussion to the entanglement between two mechanical objects in position and momentum. With slight modifications the following discussion also applies to the entanglement in any other two conjugate variables by taking the commutator among these variables into account. Then we can also describe the entanglement between mechanical system variables and coherent laser beam variables as used in Sec. 3.2.6 or between variables of two coherent laser beams as used in Sec. 2.4.2.

1.4.1 Separability of bipartite two-mode Gaussian states

For Gaussian states, things simplify a lot and entanglement can be discovered just by looking at the corresponding covariance matrix which consists of the state's second-order moments. This is sufficient because two Gaussian states with the same covariance matrix but different first-order moments are locally equivalent. Let us consider two Gaussian systems each with position and momentum operator fulfilling $[\hat{x}^{(i)}, \hat{p}^{(j)}] = i\hbar \delta_{ij}$ with $i, j = 1, 2$ (cf. Eq. (1.1)). The total (4×4) covariance matrix of the composed system can be written in block matrix form as

$$\mathbf{V}_{\text{total}} = \begin{pmatrix} \mathbf{V}_{11} & \mathbf{V}_{12} \\ \mathbf{V}_{12}^T & \mathbf{V}_{22} \end{pmatrix} . \quad (1.83)$$

The Heisenberg uncertainty relation appears in the form of the requirement that the matrix $(\mathbf{V}_{\text{total}} + i\hbar/2 \mathbf{J})$ has to be positive definite, where we have defined

$$\mathbf{J} = \begin{pmatrix} 0 & 1 & 0 & 0 \\ -1 & 0 & 0 & 0 \\ 0 & 0 & 0 & 1 \\ 0 & 0 & -1 & 0 \end{pmatrix}. \quad (1.84)$$

By applying so-called local linear unitary Bogoliubov operations, every (4×4) covariance matrix can be transformed into its standard form

$$\mathbf{V}_{\text{total}} \rightarrow \begin{pmatrix} V_a & 0 & V_{c_1} & 0 \\ 0 & V_a & 0 & V_{c_2} \\ V_{c_1} & 0 & V_b & 0 \\ 0 & V_{c_2} & 0 & V_b \end{pmatrix}. \quad (1.85)$$

These local linear unitary Bogoliubov operations are elements of the four dimensional symplectic group. The transformation in Eq. (1.85) is done by a set of (2×2) rotation and squeezing matrices applied separately on each Gaussian subsystem. Eq. (1.83) and Eq. (1.85) are further connected by the relations

$$\det \mathbf{V}_{11} = V_a^2, \quad (1.86)$$

$$\det \mathbf{V}_{22} = V_b^2, \quad (1.87)$$

$$\det \mathbf{V}_{12} = V_{c_1} V_{c_2}, \quad (1.88)$$

$$\det \mathbf{V}_{\text{total}} = (V_a V_b - V_{c_1}^2) (V_a V_b - V_{c_2}^2). \quad (1.89)$$

Note that such a composed Gaussian state is pure if and only if $\det \mathbf{V}_{\text{total}} = \hbar^4/16$ as well as $\det \mathbf{V}_{11} = \det \mathbf{V}_{22}$ and $\Sigma_+ = \hbar^2/2$, where we have defined

$$\Sigma_{\pm} = \det \mathbf{V}_{11} + \det \mathbf{V}_{22} \pm 2 \det \mathbf{V}_{12}. \quad (1.90)$$

The quantities Σ_{\pm} are invariant under any transformation within the two single subsystems if the transformation matrix has a determinate equal to one.

As shown in Refs. [46, 113], a bipartite Gaussian state is separable if and only if the total covariance matrix after partial transposition still fulfils the Heisenberg uncertainty relation. Here partial transpose is equivalent to the matrix operation with $\mathbf{\Lambda} = \text{diag}(1, 1, 1, -1)$, where the partially transposed covariance matrix is given by $\mathbf{\Lambda} \mathbf{V}_{\text{total}} \mathbf{\Lambda}$. Therefore, our state is separable if and only if the matrix $(\mathbf{\Lambda} \mathbf{V}_{\text{total}} \mathbf{\Lambda} + i\hbar/2 \mathbf{J})$ is positive definite. As this is equivalent to demand that $(\mathbf{V}_{\text{total}} + i\hbar/2 \mathbf{\Lambda} \mathbf{J} \mathbf{\Lambda})$ is positive definite, and since $\mathbf{\Lambda} \mathbf{J} \mathbf{\Lambda}$ is invariant under local linear unitary Bogoliubov operations, it is sufficient to care only about the total covariance matrix in its standard form given in Eq. (1.85). As then calculated in Refs. [46, 113] the partially transposed total covariance matrix still fulfils the Heisenberg uncertainty relation if and only if the following relation is true:

$$\frac{\hbar^2}{4} + \frac{4}{\hbar^2} \det \mathbf{V}_{\text{total}} - \Sigma_- \geq 0, \quad (1.91)$$

Thus, a pure state is entangled if and only if $\det \mathbf{V}_{12} < 0$ which is equivalent to $\det \mathbf{V}_{11} > \hbar^2/4$. In other words, if we have a pure bipartite two-mode Gaussian state, entanglement

becomes unveiled by the fact that the Gaussian subsystems are not pure. The 'purity' of each subsystem is lost due to the correlation among these two subsystems.

A widely used quantitative measure for the strength of the entanglement within an arbitrary bipartite system, the *logarithmic negativity*, was introduced in Ref. [123]. It is an upper bound for distillable entanglement and because it is possible to convert it into a bit rate for entanglement channels, it becomes very important in quantum information theory. For a bipartite two-mode Gaussian state the logarithmic negativity reads

$$E_{\mathcal{N}} = \max[0, -\log_2 \sigma^-], \quad (1.92)$$

where

$$\sigma^- = \sqrt{\frac{1}{2\hbar^2} \left(\Sigma_- - \sqrt{\Sigma_-^2 - 4 \det \mathbf{V}_{\text{total}}} \right)}. \quad (1.93)$$

The higher the value of $E_{\mathcal{N}}$, the stronger the state is entangled.

1.4.2 Bipartite two-mode Gaussian Einstein-Podolsky-Rosen states

A stronger requirement on the correlations between the two parts of a bipartite two-mode Gaussian state gives the request for the state not only being non-separable but also representing an Einstein-Podolsky-Rosen-paradox. Let us again consider two Gaussian systems each with position and momentum operator and define the common mode operators by $\hat{x}^c \equiv \hat{x}_1 + \hat{x}_2$ and $\hat{p}^c \equiv (\hat{p}_1 + \hat{p}_2)/2$ as well as the differential mode operators by $\hat{x}^d \equiv \hat{x}_1 - \hat{x}_2$ and $\hat{p}^d \equiv (\hat{p}_1 - \hat{p}_2)/2$. Then we have the commutation relations $[\hat{x}^c, \hat{p}^c] = [\hat{x}^d, \hat{p}^d] = i\hbar$ and $[\hat{x}^c, \hat{p}^d] = [\hat{x}^d, \hat{p}^c] = 0$. The condition for an Einstein-Podolsky-Rosen state simply reads

$$V_{xx}^c V_{pp}^d < \frac{\hbar^2}{4} \quad \text{or} \quad V_{xx}^d V_{pp}^c < \frac{\hbar^2}{4}. \quad (1.94)$$

It is easy to accept that a bipartite two-mode Gaussian state fulfilling Eq. (1.94) violates Heisenberg uncertainty relation after partial transposition – recall that partial transposition causes $V_{pp}^c \leftrightarrow V_{pp}^d$. Furthermore, a state fulfilling Eq. (1.94) exactly meets the condition for the gedanken experiment as proposed by Einstein, Podolsky and Rosen.

Note that there is a generalization of the condition for an Einstein-Podolsky-Rosen state by Reid [105]. He suggested to look at two arbitrary orthogonal quadratures within the two subsystems. This concept is commonly used in optics [11], where the amplitude and the phase quadrature of a coherent laser beam are not naturally defined as the position and the momentum of a mechanical system usually are. Other people have suggested to extend the concept of Einstein-Podolsky-Rosen entanglement to something which they refer to as steering [73].

2 Part I: Quantum non-demolition gravitational-wave detectors

Laser interferometer gravitational-wave detectors are probably the most sensitive devices to the displacement of a macroscopic and heavy object the human mankind has ever built. There is an enormous effort to increase the quality of the technical components of these detectors even more – such as the mirror and beam splitter materials, the suspension systems, the stability of the laser source, etc. – in order to decrease the amount of classical noise. Already in the next generation of gravitational-wave detectors, such classical noise sources will have taken a back seat at almost all frequencies. Then the new goal will be to reduce the quantum noise which is introduced by the light’s quantum nature into the test-mass motion. This can be achieved by using different quantum non-demolition [16, 20] methods. Such methods have been discussed in many works where either the currently used topology, the Michelson interferometer, is proposed to be extended – for a subtotal list see Tab. 2 – or on the other hand completely new optical configurations have been introduced.

It is well-known that the accuracy of observing the differential mode of motion between the two end mirrors in a simple Michelson interferometer via the modulation fields leaking out at the dark port is limited by the free-mass standard quantum limit – as given in Eq. (1.17), where m has to be replaced by the reduced mass $m/2$. But the quantum noise can already surpass this limit when using a conventional balanced homodyne detection scheme instead of a standard photo detection (cf. e.g. Ref. [78]). Recall that the quantum noise of a gravitational-wave detector is composed of radiation-pressure noise dominating the spectrum at low frequencies and photon shot noise which dominates at high frequencies. The radiation-pressure noise is caused by amplitude fluctuations of the light. These fluctuations can in turn be observed via the homodyne detection at the dark port. Choosing the homodyne phase appropriately, the radiation-pressure noise can be completely removed from the output – at least at a single sideband frequency. In Ref. [78] it has been further proposed to filter the output light with the help of appropriately designed filter cavities before performing the homodyne detection. The authors have shown that two lossless filter cavities are sufficient to completely remove the radiation-pressure noise from the output. The remaining quantum noise, the photon shot noise, can then be lowered by increasing the optical power. Another idea is to inject squeezed (vacuum) states into the interferometer’s dark port [27]. Again in Ref. [78] it was shown that when filtering the squeezing before sending it into the interferometer, the total quantum noise spectrum can be reduced by the squeezing factor. It has already been successfully experimentally demonstrated that this can improve the displacement sensitivity of a power- and signal-recycled table-top Michelson interferometer as reported in Ref. [121]. There are a number of other interesting ideas to further increase the sensitivity of quantum-noise limited gravitational-wave detectors such as: using intra-cavity readout schemes [13, 15, 76]; realizing time-domain back-action evasion techniques by either performing a stroboscopic measurement [19] or a quantum variational measurement [127]; reading out the test-mass speed [14]; developing optical speed-meter topologies [77] by either adding a sloshing cavity [99, 100] to a Michelson interferometer or by using a Sagnac topology [31, 92]; inventing double readout schemes [103, 104]; constructing displacement noise free interferometers [32, 33, 74]; and finally inserting a nonlinear Kerr media into the arm cavities [102].

In this chapter, we will start in Sec. 2.1 with reviewing one of the quantum non-demolition

scheme	benefit	frequency band	Refs.
balanced homodyne detection	push quantum noise down to shot noise level	at a certain frequency in radiation-pressure dominated regime	e.g. [78]
variational output	push quantum noise down to shot noise level	in radiation-pressure dominated regime	e.g. [78]
squeezed input at fixed squeeze angle	reduce quantum noise by the squeezing factor	at certain frequency	e.g. [27, 78]
squeezed input with frequency-dependent squeeze angle	reduce quantum noise by the squeezing factor	overall frequencies	e.g. [63, 78]
signal recycling	increase sensitivity	around resonances	[22–24]
speed meter	quantum noise parallel to SQL	in radiation-pressure dominated regime	[14, 77, 99] [31, 92, 100]
double carrier	increase sensitivity	at low frequencies and around resonances	[103, 104]

Table 2: Examples of quantum non-demolition add-ons for a simple Michelson interferometer. Note that combinations among the rows of this table are also possible.

techniques from Tab. 2, namely the signal-recycled Michelson interferometer configuration where the signal-recycling cavity is detuned. In Sec. 2.2 we will explore a completely different optical topology, the Sagnac interferometer as one representative of the group of speed-meter topologies, also equipped with a detuned signal-recycling cavity. Then in Sec. 2.3 we will recall the transducer configuration, an interesting application to an interferometer with a closed signal-recycling port, and compare the position-meter with the speed-meter topology. In Sec. 2.4 we will explore a special version of a ponderomotive squeezer, namely the double-optical-spring ponderomotive squeezer. This device is intended to provide a quite unorthodox way of generating squeezed vacuum input for a gravitational-wave detector.

2.1 Signal-recycled Michelson interferometer

Let us now start our discussion with reviewing the extensively theoretically [22–24] as well as experimentally [87, 114] investigated Michelson interferometer with resonant cavities in the arms but a detuned signal-recycling cavity as depicted in Fig. 4. The signal-recycling

topology was originally proposed by Meers in Ref. [85]. An additional mirror, the so-called signal-recycling mirror, is placed at the dark output port of the interferometer, reflecting parts of the signal modulation fields back into the interferometer and forming a signal-recycling cavity together with the input mirrors of the interferometer's arm cavities. The signal, which is the arm cavity mirror's differential displacement, becomes recycled which means that it is basically amplified due to an increase in interaction time between the light and the mirrors. When the signal-recycling cavity is neither resonant nor anti-resonant with respect to the carrier frequency, the optical configuration is called detuned signal-recycling. Even though the circulating optical power in the arm cavities of a Michelson interferometer with detuned signal-recycling is not modified, Buonanno and Chen have shown that the detuned signal-recycling technique also induces an optical spring effect on the differential motion of the arm cavities mirrors [22]. The signal-recycling technique in a Michelson

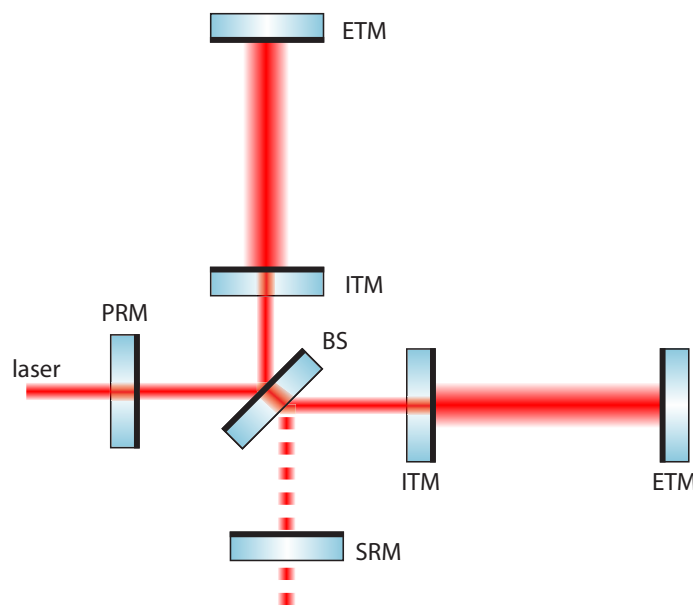


Figure 4: Schematic plot of a power- and signal-recycled Michelson interferometer with arm cavities. The laser light is split at the beam splitter (BS) which has become enhanced by the power-recycling cavity which is formed by the power-recycling mirror (PRM) and the input mirrors (ITM). The ITMs direct each of the beams into the north and the east arm cavity, respectively, which they form together with the high-reflective end mirrors (ETM). The signal-recycling mirror (SRM) is placed behind the dark port and reflects parts of the output back into the interferometer.

interferometer without arm cavities, was already successfully tested in the 30 m prototype gravitational-wave detector in Garching, Germany [54,66]. Furthermore, the optical spring effect has been demonstrated in the 40 m prototype gravitational-wave detector [87] located on the campus of the California Institute of Technology, Pasadena. Note that also the GEO600 detector – located near Hanover, Germany – as the only first generation detector already has implemented a signal-recycling cavity which can in principle be detuned. But here, it is much harder to see the optical spring effect probably because the GEO600 detector, just like the 30 m prototype detector in Garching, is not equipped with arm cavities. Motivated by the good results obtained at the 40 m prototype, the signal-recycling technique is planned to be installed in the next generation of detectors such as the Advanced LIGO detectors in

order to make use of the optical spring effect. The Advanced LIGO detectors are planned to replace the two long – out of the three existing – LIGO detectors in 2013. One of these long initial LIGO detectors is located in Hanford, Washington and the other one is located in Livingston, Louisiana. While the delivery of the first components to the two sites will already start next year in 2009, the decommissioning of initial LIGO and simultaneously the start of installation of Advanced LIGO is planned to be in 2011 [2]. Throughout this chapter we will

mirror mass	m	40 kg
circulating carrier power	P	800 kW
laser wavelength	$2\pi c/\omega_0$	1064 nm
cavity length	L	4 km
cavity half bandwidth	γ	2π 15 Hz

Table 3: Advanced LIGO baseline-design parameter values used for the numerical calculations.

use Advanced LIGO parameters [1]: the baseline design envisages 4 km long arm cavities – the vacuum tubes are borrowed from the current operating initial LIGO detectors – with a half-bandwidth of 2π 15 Hz, producing a circulating laser beam with an optical power of 800 kW at a wavelength of 1064 nm incident on 40 kg heavy test-mass mirrors which form the arm cavities. These parameters are also listed in Tab. 3.

Buonanno and Chen have shown theoretically in Ref. [24] that it is possible to find a simple map between the following two systems: *(i)* the differential motion of the arm cavity mirrors in a Michelson interferometer with detuned signal-recycling and the dark port output fields and *(ii)* the motion of the end mirror in a single cavity with only this end mirror movable and the cavity output fields. Furthermore, it was shown in Ref. [64] that an arm-cavity equipped interferometer’s output is only negligible influenced by the motion of the beam splitter. This is due to the fact that the carrier light incident on the beam splitter is weak and the arm cavities prevent fluctuations from building up. In the Michelson interferometer with detuned signal-recycling, the optical spring can shift the mechanical eigenfrequency of the test masses’ differential motion from the pendulum frequency to the optomechanical resonance frequency. This optomechanical resonance and the optical resonance appear both as dips in the noise spectral density of the interferometer. Therefore, the sensitivity towards gravitational waves can be increased dramatically around these resonances, even allowing to surpass the free-mass standard quantum limit. The price one has to pay is that the sensitivity is lost at frequencies lower and higher than these two resonances.

2.1.1 Test-mass dynamics and measurement output

Let us recall that the Heisenberg equations of motion in the frequency domain for the total differential mode of motion

$$\hat{x} = (\hat{x}_{\text{ETM}}^{\text{N}} - \hat{x}_{\text{ITM}}^{\text{N}}) - (\hat{x}_{\text{ETM}}^{\text{E}} - \hat{x}_{\text{ITM}}^{\text{E}}) \quad (2.1)$$

between the mirrors in the north and the east arm, as well as for the measurement-output quadrature operator \hat{y}_ζ at a homodyne detection angle ζ , read as follows

$$\hat{y}_\zeta = \hat{Y}_1^{(0)}(\Omega) \sin \zeta + \hat{Y}_2^{(0)}(\Omega) \cos \zeta + [R_{Y_1 F}^{\text{Mich}}(\Omega) \sin \zeta + R_{Y_2 F}^{\text{Mich}}(\Omega) \cos \zeta] \hat{x}, \quad (2.2)$$

$$\hat{x} = R_{xx}^{\text{Mich}}(\Omega) \left[\hat{F}_{\text{RP}}^{(0)}(\Omega) + R_{FF}^{\text{Mich}}(\Omega) \hat{x} \right] + h L. \quad (2.3)$$

Here the operators $\hat{Y}_1^{(0)}(\Omega) = y_1^{\text{Mich}}(\Omega) \hat{a}_1 + y_2^{\text{Mich}}(\Omega) \hat{a}_2$ and $\hat{Y}_2^{(0)}(\Omega) = -y_2^{\text{Mich}}(\Omega) \hat{a}_1 + y_1^{\text{Mich}}(\Omega) \hat{a}_2$ account for the shot noise in case of fixed mirrors, where we have (cf. Ref. [24])

$$y_1^{\text{Mich}}(\Omega) = \frac{\lambda^2 - (\epsilon^2 - \Omega^2)}{(\Omega - \lambda + i\epsilon)(\Omega + \lambda + i\epsilon)}, \quad (2.4)$$

$$y_2^{\text{Mich}}(\Omega) = \frac{2\lambda\epsilon}{(\Omega - \lambda + i\epsilon)(\Omega + \lambda + i\epsilon)}, \quad (2.5)$$

while the operator $\hat{F}_{\text{RP}}^{(0)} = f_1^{\text{Mich}}(\Omega) \hat{a}_1 + f_2^{\text{Mich}}(\Omega) \hat{a}_2$ describes the radiation-pressure forces which would act on fixed mirrors caused by the incoming vacuum fields at the dark port. Here \hat{a}_1 and \hat{a}_2 are the amplitude and phase quadrature operators, respectively, of the incoming vacuum fields at the dark port [78] obeying the correlation as given in Eq. (1.36). Furthermore, we have assumed the gravitational wave is incident with an amplitude described by the function of sideband frequency, $h(\Omega)$, from right above the interferometer plane with a polarization that maximizes the response of the Michelson interferometer, the plus polarization.

The susceptibilities of the system are given by [24]

$$R_{Y_1 F}^{\text{Mich}}(\Omega) = \frac{1}{\hbar} f_2^{\text{Mich}}(\Omega) = \sqrt{\frac{\epsilon\theta m}{2\hbar}} \frac{\lambda}{(\Omega - \lambda + i\epsilon)(\Omega + \lambda + i\epsilon)}, \quad (2.6)$$

$$R_{Y_2 F}^{\text{Mich}}(\Omega) = \frac{1}{\hbar} f_1^{\text{Mich}}(\Omega) = -\sqrt{\frac{\epsilon\theta m}{2\hbar}} \frac{\epsilon - i\Omega}{(\Omega - \lambda + i\epsilon)(\Omega + \lambda + i\epsilon)}, \quad (2.7)$$

$$R_{FF}^{\text{Mich}}(\Omega) = \frac{\theta m}{4} \frac{\lambda}{(\Omega - \lambda + i\epsilon)(\Omega + \lambda + i\epsilon)}, \quad (2.8)$$

where $\theta = 8P\omega_0/(mLc)$ has units of frequency cubed. Here P refers to the circulating optical power in each arm cavity and L is the length of these arm cavities. The carrier with angular frequency ω_0 is resonant in the arm cavities and when the mirrors are held fixed, the optical resonant frequency of the differential optical mode that is closest to the carrier frequency is given by $\omega_0 - \lambda - i\epsilon$, where, in terms of interferometer parameters, λ and ϵ are determined by (cf. Ref. [24])

$$\lambda = \gamma \frac{2\rho_{\text{SR}} \sin 2\phi}{1 + \rho_{\text{SR}}^2 + 2\rho_{\text{SR}} \cos 2\phi} \quad \text{and} \quad \epsilon = \gamma \frac{1 - \rho_{\text{SR}}^2}{1 + \rho_{\text{SR}}^2 + 2\rho_{\text{SR}} \cos 2\phi}. \quad (2.9)$$

Here ρ_{SR} is the signal-recycling mirror's amplitude reflectivity, ϕ the detuning phase of the carrier frequency with respect to the signal-recycling cavity and γ the half-bandwidth of the arm cavities. When fixing the characteristic frequency $\sqrt[3]{\theta}$, this half-bandwidth γ determines how much optical power has to pass the beam splitter which is actually equal to the optical input power multiplied by the power-recycling gain.

In the free-mass limit assuming a very low eigenfrequency of the suspension-induced pendulum, the mechanical susceptibility of the differential motion with an effective mass $m/4$ is given by

$$R_{xx}^{\text{Mich}} = \frac{4}{m \Omega^2}. \quad (2.10)$$

Recall that the mechanical as well as the the optical resonances are shifted due to the optical spring and the differential motion of the arm cavity mirrors turns inescapably into an unstable system. Thus, this degree of freedom needs to be stabilized. But as Buonanno and Chen have shown in Ref. [23], one can cope with the instability by incorporating a linear feedback control system which ideally would not modify the interferometer's sensitivity towards gravitational waves.

2.1.2 Sensitivity towards gravitational waves

The equations of motion Eqs. (2.2) and (2.3) can be gathered into an input-output relation. Namely, if we revert to the quadrature vector notation from Sec. 1.2.2 and define the input quadrature vector $\vec{a} = (\hat{a}_1, \hat{a}_2)^T$, the equations of motion can be put into the following form

$$\hat{y}_\zeta = (\sin \zeta, \cos \zeta) \left(\mathbf{T}_{\text{quant}}^{\text{Mich}} \vec{a} + \bar{t}_h^{\text{Mich}} h L \right). \quad (2.11)$$

The Michelson interferometer's quantum-noise-transfer matrix $\mathbf{T}_{\text{quant}}^{\text{Mich}}$ linearly transforms the quantum noise into the output, while the signal-transfer vector \bar{t}_h^{Mich} linearly transforms the gravitational-wave signal ($h L$) into the output. Both can be deduced from Eqs. (2.2) and (2.3) as

$$\mathbf{T}_{\text{quant}}^{\text{Mich}} = \begin{pmatrix} y_1^{\text{Mich}} & y_2^{\text{Mich}} \\ -y_2^{\text{Mich}} & y_1^{\text{Mich}} \end{pmatrix} + \frac{R_{xx}^{\text{Mich}}}{1 - R_{xx}^{\text{Mich}} R_{FF}^{\text{Mich}}} \begin{pmatrix} R_{Y_1 F}^{\text{Mich}} \\ R_{Y_2 F}^{\text{Mich}} \end{pmatrix} (f_1^{\text{Mich}}, f_2^{\text{Mich}}), \quad (2.12)$$

$$\bar{t}_h^{\text{Mich}} = \frac{1}{1 - R_{xx}^{\text{Mich}} R_{FF}^{\text{Mich}}} \begin{pmatrix} R_{Y_1 F}^{\text{Mich}} \\ R_{Y_2 F}^{\text{Mich}} \end{pmatrix}. \quad (2.13)$$

Then the Michelson interferometer's quantum-noise limited sensitivity to gravitational waves can be inferred from its single-sided noise spectral density given by

$$S_h^{\text{Mich}}(\Omega) = \frac{(\sin \zeta, \cos \zeta) \mathbf{T}_{\text{quant}}^{\text{Mich}} \left(\mathbf{T}_{\text{quant}}^{\text{Mich}} \right)^\dagger (\sin \zeta, \cos \zeta)^T}{L^2 (\sin \zeta, \cos \zeta) \bar{t}_h^{\text{Mich}} \left(\bar{t}_h^{\text{Mich}} \right)^\dagger (\sin \zeta, \cos \zeta)^T}. \quad (2.14)$$

Turning out the signal-recycling technique by setting $\rho_{\text{SR}} = \phi = 0$ which causes $\lambda = 0$ and $\epsilon = \gamma$ (cf. Eq. (2.9)) and performing a phase quadrature detection with $\zeta = 0$, then $S_h^{\text{Mich}}(\Omega)$ is limited from below by the spectral density of the Michelson interferometer's free-mass standard quantum limit which is given by

$$S_h^{\text{SQL}}(\Omega) = \frac{8 \hbar}{m \Omega^2 L^2}. \quad (2.15)$$

Note that Eq. (2.15) is equal to Eq. (1.17) – but at the Michelson interferometer's reduced mass $m/4$ and divided by L^2 due to the h -referredness.

If we plot $S_h^{\text{Mich}}(\Omega)$ versus sideband frequency – as done for two example configurations in Fig. 5 – one can clearly spot the resonance frequencies as dips in the noise curves: at

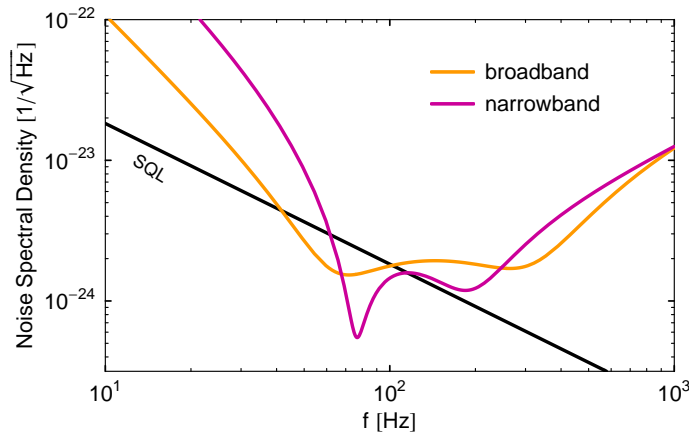


Figure 5: Example quantum noise spectral densities for a Michelson interferometer with detuned signal-recycling versus frequency $f = \Omega/(2\pi)$. Here basically Advanced LIGO parameters are used (cf. Tab. 3). The free optical resonance frequency for broadband configuration is at $\lambda = 2\pi 290$ Hz and $\epsilon = 2\pi 120$ Hz while the homodyne detection angle is $\zeta = 0.7\pi$. The narrowband configuration has $\lambda = 2\pi 197$ Hz and $\epsilon = 2\pi 51$ Hz and the phase quadrature is detected, i.e. $\zeta = 0$. The black line denotes the free-mass standard quantum limit (SQL).

lower frequencies the optomechanical resonance and at higher frequencies the shifted optical resonance. The position of these resonances in the frequency band depends especially on the free optical resonances from Eq. (2.9) and the characteristic frequency $\sqrt[3]{\theta}$ which is proportional to the cubic root of the optical power. The depth of the optomechanical resonance frequency additionally depends on the homodyne detection angle. Varying these parameters can shape the quantum noise curves differently: the broadband configuration in Fig. 5 is good for the detection of sources emitting a gravitational-wave spectrum which is spread over a wide frequency band while the narrowband configuration is highly sensitive in a specific frequency band, namely around the optomechanical resonance frequency, and loses sensitivity especially in the low frequency regime. Note that the deep dip in the narrowband noise curve, produced by the optomechanical resonance, is usually covered by classical noise anyway. However, the broadband configuration as plotted in Fig. 5 is actually the optimal choice – if a realistic classical noise budget is included – for the detection of inspiraling neutron star binaries which produce an analytically well-known and intense gravitational-wave signal following the power law of $h(f) \propto f^{-7/6}$. Full particulars about the optimization towards the signal of inspiraling neutron star binaries and the classical noise budget used can be found in Sec. 2.2.4. The broadband configuration is usually also called the Advanced LIGO configuration.

2.2 Signal-recycled Sagnac interferometer

Originally, the interferometric experiment performed by Georges Sagnac in 1913 has been intended to observe the correlation of angular momentum and phase-shift [106]. Today, such an experiment has become a standard interferometer setup which is still mainly used to sense rotations, for example as the reference for modern inertial guidance systems. Until now, a Sagnac interferometer has never been rigorously employed experimentally as a large-scale detector for gravitational waves. Using a Sagnac interferometer as a large-scale gravitational-

wave detector can only be considered as a third-generation detector because it requires to change the optical layout – the next generation of gravitational-wave detectors are already planned to use the Michelson topology. People in the gravitational-wave community are probably discouraged of the Sagnac design because of the following reasons: on the one hand this configuration might be more difficult to realize due to more optical components involved; people have much more experiences using Michelson interferometers; and there are some disadvantageous noise properties present as its low tolerance to the beam splitter reflectivity error and the beam splitter tilt and a slightly higher sensitivity to optical losses [43] than in a Michelson interferometer. On the other hand, several clever designs on how to realize a Sagnac interferometer with a simpler optical layout have been proposed recently: for example how to turn a Michelson interferometer into a Sagnac by using polarizing optics [84]. And it is nevertheless always advisable to theoretically explore other configurations such as the Sagnac interferometer. In Ref. [92], we have extended the analysis carried out in Ref. [31] by adding a detuned signal-recycling cavity to a Sagnac interferometer and have studied first its ideal quantum noise performance while then introducing classical noise and optimizing the quantum noise towards the detection of specific gravitational-wave sources. Note that our analysis is quite general and can also be applied to the whole group of so-called *speed-meter* configurations (cf. Tab. 2).

Fig. 6 shows a Sagnac interferometer as we will consider it in this section: it has two arms which are folded in order to make the Sagnac interferometer sensitive to length changes which is indispensable for the detection of gravitational waves [115]. The two arms are formed by

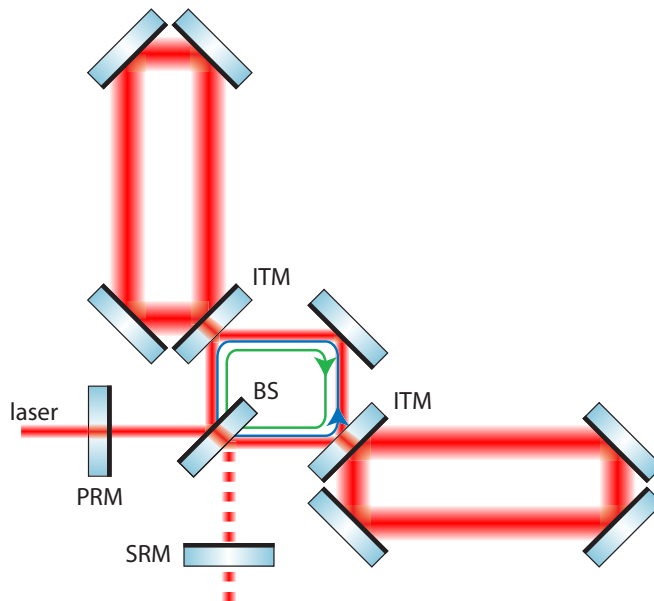


Figure 6: Schematic plot of a power- and signal-recycled Sagnac interferometer with folded ring-cavity arms. The laser light, coming from the left, passes the power-recycling mirror (PRM) and then becomes split into two beams at the beam splitter (BS), where the right circulating (green) part gets inducted through the input mirror (ITM) into the north arm first and then travels through the east arm while a left circulating (blue) part travels the other way round. The signal-recycling mirror (SRM) reflects back parts of the output into the interferometer.

ring cavities consisting each of four suspended mirrors: the input mirror and the mirror

located nearby as well as two far end mirrors. Therefore, the north (east) arm cavity is basically spanned in south-north (west-east) direction with an arm length L . One could also think about even fixing the small distance of the input mirror and the mirror located nearby as well as the distance between the two far end mirrors. This could for example be realized by bounding them on a common suspended platform. Ring cavities can also be realized in an triangular shape as considered in Ref. [31]. The light is split into two beams at the beam splitter and travels through the ring cavities in opposite order and opposite direction. The mirror placed at the dark port realizes the signal-recycling technique just as for the Michelson interferometer (cf. Sec. 2.1).

The signal-recycled Sagnac interferometer has two optical resonances which are shifted with increasing laser power due to the stronger optomechanical coupling. It has turned out that in the free test-mass limit, i.e. with a low eigenfrequency of the mechanical pendulum created by the suspension of the mirrors, this mechanical resonance frequency is not shifted. That means that we do not find an optomechanical resonance produced by an optical spring effect as it is the case in a Michelson interferometer with detuned signal-recycling (cf. Sec. 2.1). The test masses' dynamics is therefore not modified – they remain approximately free but are subject to an *optical inertia* which increases the dynamical reduced mass of the mirrors [92]. This is due to the fact that a Sagnac interferometer configuration as depicted in Fig. 6 is at low frequencies sensitive to the speed of its test-masses [31] – exactly as in a speed meter [77, 99, 100]. The idea of using speed meters in the context of quantum measurements was to totally avoid the quantum back action and to build a real quantum non-demolition device. At first glance it seemed to be very promising to reach this goal by measuring the speed because usually the momentum as a conserved quantity is proportional to speed. Measuring a conserved quantity does not introduce back-action noise (cf. Sec. 1.1.2). But if the detector couples to speed, one can show that the conjugate momentum is actually not proportional to speed [75]. Nevertheless, a speed meter is able to surpass the standard quantum limit by removing parts of the radiation-pressure noise from the measurement output. Therefore, using a speed-meter topology we are actually not able to avoid the back action itself but can lower the back-action noise.

The optical inertia effect can easily be understood by following the next three hand-waving arguments: The phase gained by a laser beam is proportional to the time-dependent displacement in the cavity. The right circulating beam in the Sagnac interferometer feels the total length change of the north arm cavity first and then – after some time delay $t_{\text{arm}} \approx 1/\gamma = \tau_{\text{ITM}}^2 c/(4L)$, where τ_{ITM} is the amplitude transmissivity of the input mirror and L the cavity length – the one of the east arm cavity, while the right circulating beam travels through the arm cavities in opposite direction. These facts read

$$\delta a_2^{\text{R}} \sim \delta x^{\text{N}}(t) + \delta x^{\text{E}}(t + t_{\text{arm}}), \quad \delta a_2^{\text{L}} \sim \delta x^{\text{E}}(t) + \delta x^{\text{N}}(t + t_{\text{arm}}). \quad (2.16)$$

If we take the difference between these two phase changes and expand in powers of t_{arm} , we find that at first order the output phase at the beam splitter is proportional to the speed of the differential displacement in the two arms

$$\delta a_2 = \delta a_2^{\text{L}} - \delta a_2^{\text{R}} \sim \delta \dot{x}^{\text{N}}(t) - \delta \dot{x}^{\text{E}}(t) + \dots, \quad (2.17)$$

which is simply the speed-meter effect. Similarly, the fluctuating part of the radiation-pressure force in the north arm is caused by amplitude fluctuations in the right circulating

beam and additionally by amplitude fluctuations in the left circulating beam which has already traveled through the east arm and is therefore time delayed by t_{arm} . And again vice versa for the radiation-pressure force in the east arm. Therefore, we have

$$\delta F_{\text{RP}}^{\text{N}} \sim \delta a_1^{\text{R}}(t) + \delta a_1^{\text{L}}(t + t_{\text{arm}}), \quad \delta F_{\text{RP}}^{\text{E}} \sim \delta a_1^{\text{L}}(t) + \delta a_1^{\text{R}}(t + t_{\text{arm}}). \quad (2.18)$$

Again, after Taylor expansion, the difference of the radiation-pressure force in both arms is also at first order proportional to the time derivatives of the amplitude fluctuations in right and left circulating beams

$$\delta F_{\text{RP}}^{\text{N}} - \delta F_{\text{RP}}^{\text{E}} \sim \delta \dot{a}_1^{\text{L}}(t) - \delta \dot{a}_1^{\text{R}}(t) + \dots \quad (2.19)$$

In the detuned signal-recycling cavity, the amplitude and the phase quadrature of the modulation fields become mixed and then together with Eq. (2.17) and with Eq. (2.19) we learn that the radiation pressure depends on the acceleration of the mirrors. But on the other hand the radiation-pressure force itself drives together with other (external) forces the mirror motion. The equations of motion becomes

$$m (\delta \ddot{x}^{\text{N}} - \delta \ddot{x}^{\text{E}}) \sim \delta F_{\text{RP}}^{\text{N}} - \delta F_{\text{RP}}^{\text{E}} + F_{\text{external}} \sim m_{\text{opt}} (\delta \ddot{x}^{\text{N}} - \delta \ddot{x}^{\text{E}}) + F_{\text{external}}. \quad (2.20)$$

Thus, the radiation pressure introduces the extra mass term m_{opt} . Since the above treatment was quite general, it shows that the optical inertia effect is common to all detuned speed-meter topologies. Note that this effect will be stronger at time-scales much higher than the arm-cavity storage time t_{arm} or equivalently in the frequency domain, at frequencies much lower than the arm cavity half-bandwidth γ . Otherwise the higher order terms in t_{arm} become more significant in the dynamics. Therefore, increasing γ will certainly facilitate the observation of the optical inertia effect. Later on in this section, we will prove this optical inertia effect in the signal-recycled Sagnac interferometer more rigorously.

2.2.1 Free resonant structure

The signal-recycled Sagnac interferometer consists of two coupled resonators. Thus we can expect to find two optical resonance frequencies in the differential optical mode. The condition for such an optical resonance is simply that the field, which has been propagated through the whole interferometer plus signal-recycling cavity, interferes constructively with the in-coming field. We find that for a carrier with frequency ω_0 the differential optical mode without optomechanical coupling – corresponding to fixed mirrors – is resonant at the frequencies (that are closest to the carrier frequency) of $\omega_0 + \lambda_{1,2} - i\epsilon_{1,2}$ with

$$\lambda_{1,2} = \gamma \frac{\pm 2 \sqrt{\rho_{\text{SR}}} \cos \phi}{1 + \rho_{\text{SR}} \pm 2 \sqrt{\rho_{\text{SR}}} \sin \phi} \quad \text{and} \quad \epsilon_{1,2} = \gamma \frac{1 - \rho_{\text{SR}}}{1 + \rho_{\text{SR}} \pm 2 \sqrt{\rho_{\text{SR}}} \sin \phi}, \quad (2.21)$$

where ρ_{SR} is the signal-recycling mirror amplitude reflectivity, $\phi = \omega_0 l / c$ stands for the detuning phase of the signal-recycling cavity of length l with respect to the carrier frequency ω_0 . Furthermore, γ denotes the ring cavity's half-bandwidth. Note that the two real and the two imaginary parts of the two resonance frequencies are related by

$$\lambda_2 = -\gamma^2 \frac{\lambda_1}{\lambda_1^2 + \epsilon_1^2} \quad \text{and} \quad \epsilon_2 = \gamma^2 \frac{\epsilon_1}{\lambda_1^2 + \epsilon_1^2}, \quad (2.22)$$

which is still true when exchanging '1' and '2' in the subscripts. The relations in Eq. (2.22) become for instance important when optimizing the interferometer's sensitivity with respect to certain gravitational-wave sources. As we will see later on, the noise spectral density of the interferometer can be expressed in terms of these resonance frequencies. A grid search over the parameter space (ρ_{SR}, ϕ) is much less efficient than over the resonance frequencies themselves because an equally spaced ϕ gives a strongly weighted $(\lambda_1, \epsilon_1, \lambda_2, \epsilon_2)$ space. With the help of Eq. (2.22), we can perform a grid search over the parameter space (λ_1, ϵ_1) . But keep in mind that there is a third independent parameter, namely the cavity half-bandwidth γ , which crucially influences the relative position of the two resonances if we have fixed λ_1 and ϵ_1 .

We can infer two extreme examples from Eq. (2.22): the *degenerated resonance* case, where

$$\lambda_2 = -\lambda_1 \quad \text{and} \quad \epsilon_2 = \epsilon_1, \quad (2.23)$$

exists only if $\lambda_1^2 + \epsilon_1^2 = \gamma^2$ which is in turn only true for $\sin \phi = 0$, i.e. for a non-detuned signal-recycling cavity. Whereas the *well-separated resonance* case

$$|\lambda_1| \gg |\lambda_2| \quad \text{and} \quad \epsilon_1 \gg \epsilon_2, \quad (2.24)$$

is available for $|\lambda_1|, \epsilon_1 \gg \gamma$, i.e. for a *strong signal-recycling* with a high reflectivity of the signal-recycling mirror and $\sin \phi \approx -1$.

2.2.2 Test-mass dynamics and measurement output

Let us have a look at the Heisenberg equations of motion in the frequency domain obtained by using the method introduced in Sec. 1.2.2. After performing the relevant calculations we have found that it can be written exactly in the same format as in the case of a detuned cavity (cf. Eqs. (1.53) and (1.54)). Here we consider the total differential mode of motion $\hat{x} = \hat{x}_{\text{breath}}^{\text{N}} - x_{\text{breath}}^{\text{E}}$ between all the mirrors which is the difference in north and east arm cavity's breathing mode. The breathing mode gives the total expansion of the cavity: here all mirrors move in normal direction with respect to their surface, either all inwards or all outwards with respect to the cavity's geometry. Then we have

$$\hat{y}_\zeta = \hat{Y}_1^{(0)}(\Omega) \sin \zeta + \hat{Y}_2^{(0)}(\Omega) \cos \zeta + \left(R_{Y_1 F}^{\text{Sag}}(\Omega) \sin \zeta + R_{Y_2 F}^{\text{Sag}}(\Omega) \cos \zeta \right) \hat{x}, \quad (2.25)$$

$$\hat{x} = R_{xx}^{\text{Sag}}(\Omega) \left(\hat{F}_{\text{RP}}^{(0)}(\Omega) + R_{FF}^{\text{Sag}}(\Omega) \hat{x} + \hat{F}_{\text{external}} \right), \quad (2.26)$$

where the first equation describes the measurement-output operator \hat{y}_ζ at a homodyne detection angle ζ . In the language of Sec. 1.2.3, the operators

$$\hat{F}_{\text{RP}}^{(0)} = f_1^{\text{Sag}}(\Omega) \hat{a}_1 + f_2^{\text{Sag}}(\Omega) \hat{a}_2, \quad (2.27)$$

$$\hat{Y}_1^{(0)}(\Omega) = y_1^{\text{Sag}}(\Omega) \hat{a}_1 + y_2^{\text{Sag}}(\Omega) \hat{a}_2, \quad (2.28)$$

$$\hat{Y}_2^{(0)}(\Omega) = -y_2^{\text{Sag}}(\Omega) \hat{a}_1 + y_1^{\text{Sag}}(\Omega) \hat{a}_2, \quad (2.29)$$

are free quantities, i.e. before mirrors and light are coupled. Here \hat{a}_1 and \hat{a}_2 are the amplitude and phase quadrature operators, respectively, of the incoming vacuum fields at the dark port [78] obeying the correlation as given in Eq. (1.36). As Buonanno and Chen have done

for the signal-recycled Michelson interferometer in Ref. [24], we have also managed to express each coefficient function in Eqs. (2.27)–(2.29), i.e. y_1^{Sag} , y_2^{Sag} , f_1^{Sag} and f_2^{Sag} , as well as the susceptibilities R_{FF}^{Sag} , $R_{Y_1F}^{\text{Sag}}$ and $R_{Y_2F}^{\text{Sag}}$ from Eqs. (2.25) and (2.26) totally in terms of the optical resonances as given in Eq. (2.21) and the characteristic frequency $\sqrt[3]{\theta}$ which is defined below. Then the coefficient functions and the susceptibilities read as follows

$$y_1^{\text{Sag}}(\Omega) = -\frac{(\Omega^2 + \epsilon_1^2 - \lambda_1^2)(\Omega^2 + \epsilon_2^2 - \lambda_2^2) + 2(\epsilon_2^2\lambda_1^2 + \epsilon_1^2\lambda_2^2)}{(\Omega + i\epsilon_1 - \lambda_1)(\Omega + i\epsilon_1 + \lambda_1)(\Omega + i\epsilon_2 - \lambda_2)(\Omega + i\epsilon_2 + \lambda_2)}, \quad (2.30)$$

$$y_2^{\text{Sag}}(\Omega) = -\frac{2\Omega^2(\epsilon_1 + \epsilon_2)(\lambda_1 + \lambda_2)}{(\Omega + i\epsilon_1 - \lambda_1)(\Omega + i\epsilon_1 + \lambda_1)(\Omega + i\epsilon_2 - \lambda_2)(\Omega + i\epsilon_2 + \lambda_2)}, \quad (2.31)$$

$$f_1^{\text{Sag}}(\Omega) = \hbar R_{Y_2F}^{\text{Sag}}(\Omega) = \frac{-i\Omega\sqrt{m\theta\hbar}(\epsilon_1 + \epsilon_2)/2((\epsilon_1 - i\Omega)(\epsilon_2 - i\Omega) - \lambda_1\lambda_2)}{(\Omega + i\epsilon_1 - \lambda_1)(\Omega + i\epsilon_1 + \lambda_1)(\Omega + i\epsilon_2 - \lambda_2)(\Omega + i\epsilon_2 + \lambda_2)}, \quad (2.32)$$

$$f_2^{\text{Sag}}(\Omega) = \hbar R_{Y_1F}^{\text{Sag}}(\Omega) = \frac{-\Omega^2\sqrt{m\theta\hbar}(\epsilon_1 + \epsilon_2)/2(\lambda_1 + \lambda_2)}{(\Omega + i\epsilon_1 - \lambda_1)(\Omega + i\epsilon_1 + \lambda_1)(\Omega + i\epsilon_2 - \lambda_2)(\Omega + i\epsilon_2 + \lambda_2)}, \quad (2.33)$$

$$R_{FF}^{\text{Sag}}(\Omega) = -\frac{m\theta\Omega^2(\lambda_1 + \lambda_2)}{4(\Omega + i\epsilon_1 - \lambda_1)(\Omega + i\epsilon_1 + \lambda_1)(\Omega + i\epsilon_2 - \lambda_2)(\Omega + i\epsilon_2 + \lambda_2)}. \quad (2.34)$$

Since there are eight movable mirrors involved we have a mechanical susceptibility of

$$R_{xx}^{\text{Sag}}(\Omega) = -\frac{8}{m\Omega^2} \quad (2.35)$$

in the free-mass limit with a very low pendulum eigenfrequency and damping. The characteristic frequency is identical to the one of a Michelson interferometer, i.e. $\theta = 8P\omega_0/(mLc)$ having units of frequency cubed. Here ω_0 is the carrier's angular frequency and P refers to the carrier power of each circulating beam inside the ring cavities which corresponds to the circulating power of the carrier in one arm of a Michelson interferometer when assuming the same optical power for Sagnac and Michelson before the beam splitter. Furthermore, L is the arm length which is given by the length of the long edge of the ring cavities.

Interestingly, in the real limit of the well-separated resonance case (cf. Sec. 2.2.1), i.e. with $\lambda_2, \epsilon_2 \rightarrow 0$ while λ_1, ϵ_1 then become both infinitely large, Eqs. (2.30)–(2.34) analytically coincides with the corresponding functions of the signal-recycled Michelson interferometer, i.e. with Eqs. (2.4)–(2.8), when setting $\lambda_1 \rightarrow -\lambda$ and $\epsilon_1 \rightarrow \epsilon$. In other words, for certain signal-recycling parameters a Sagnac can become very similar to a Michelson interferometer. But in the weakly coupled approximation, where $\lambda_1, \epsilon_1, \lambda_2$ and ϵ_2 are all reasonably large, we can power expand R_{FF}^{Sag} in terms of the sideband frequency Ω and find

$$R_{FF}^{\text{Sag}}(\Omega) \approx -\Omega^2 \underbrace{\frac{m\theta(\lambda_1 + \lambda_2)}{4(\epsilon_1^2 + \lambda_1^2)(\epsilon_2^2 + \lambda_2^2)}}_{m_{\text{opt}}}, \quad (2.36)$$

being real and having neither a constant part nor a part which is linear in sideband frequency, just in contrast to an optical rigidity (cf. Eq. (1.72)). The series starts with a term quadratic in sideband frequency as given in Eq. (2.36) which introduces a dynamical mass term into the equations of motion. This gives rise to the optical inertia effect which we have already

mentioned above. Finally, in the degenerated resonance case we obtain $R_{FF}^{\text{Sag}} \rightarrow 0$, and we can recover the formulas as discussed in Ref. [31].

Eq. (2.26) shows that the optomechanical coupling can strongly change the dynamics – or it is better to say the dynamical mass – of the mirror. The optomechanically coupled system has new resonance frequencies which are given by the roots of the following characteristic equation:

$$0 = \frac{1}{R_{xx}^{\text{Sag}}(\Omega)} - R_{FF}^{\text{Sag}}(\Omega) = -\frac{m\Omega^2}{8} \left(\frac{(\Omega + i\epsilon_1 - \lambda_1)(\Omega + i\epsilon_1 + \lambda_1)(\Omega + i\epsilon_2 - \lambda_2)(\Omega + i\epsilon_2 + \lambda_2) - 2\theta(\lambda_1 + \lambda_2)}{(\Omega + i\epsilon_1 - \lambda_1)(\Omega + i\epsilon_1 + \lambda_1)(\Omega + i\epsilon_2 - \lambda_2)(\Omega + i\epsilon_2 + \lambda_2)} \right). \quad (2.37)$$

We can say that the optical resonances (cf. Eq. (2.21)) become shifted with increasing power (cf. Fig. 7), i.e. with stronger optomechanical coupling, while the mechanical resonance in the free-mass limit at 0 Hz is not shifted. This rigorously proves what we have already argued

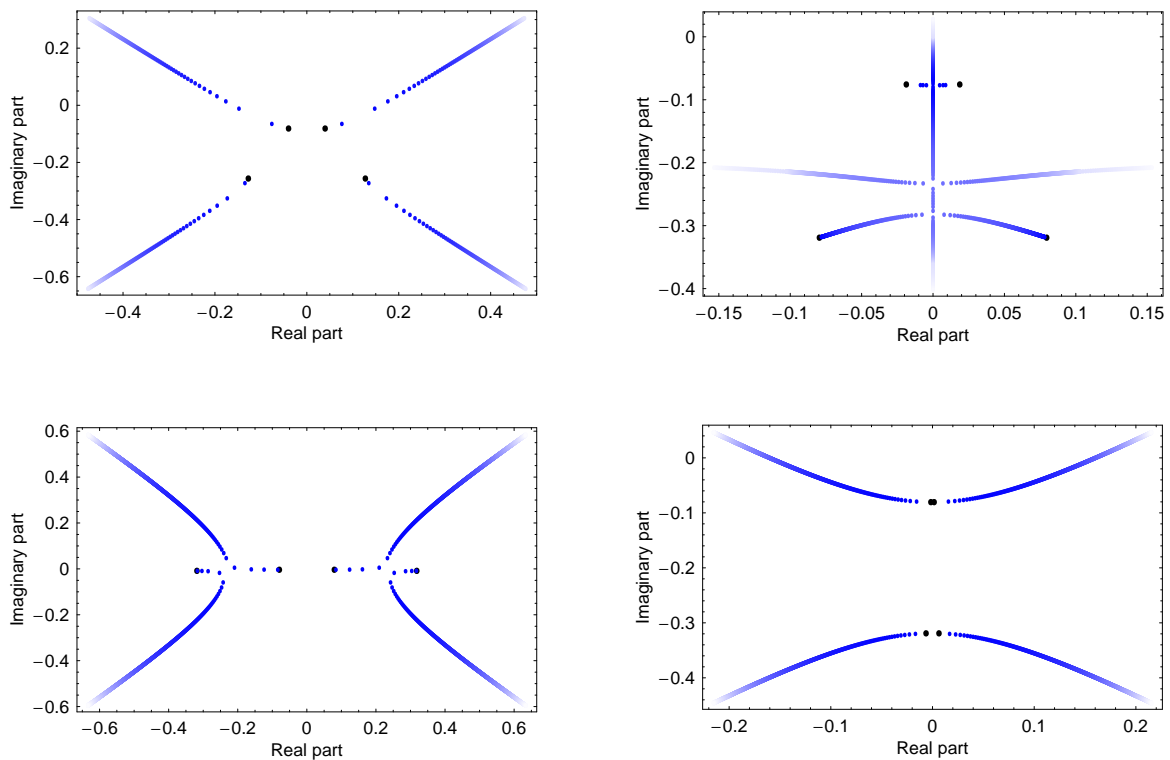


Figure 7: Four different examples of the optomechanical induced shift in the optical resonances (obtained numerically solving Eq. (2.37)) of a Sagnac interferometer with detuned signal-recycling and of Advanced LIGO scale (cf. Tab. 3): therefor the normalized characteristic frequency $\sqrt[3]{\theta}/\gamma$ is increased from zero (fat black dot) to 6.6 (bright blue dot) – corresponding to Advanced LIGO parameters as arm cavity bandwidth and circulating power from Tab. 3. The free optical resonance frequencies are chosen at $\lambda_1/\gamma = 0.25$ and $\epsilon_1/\gamma = 0.5$ (upper left panel); $\lambda_1/\gamma = 0.5$ and $\epsilon_1/\gamma = 2$ (upper right panel); $\lambda_1/\gamma = 0.5$ and $\epsilon_1/\gamma = 0.01$ (lower left panel); $\lambda_1/\gamma = 0.01$ and $\epsilon_1/\gamma = 0.5$ (lower right panel). Note that the axes are also scaled with the arm cavity bandwidth.

above, namely, that in the resonant structure of the signal-recycled Sagnac, there does not

appear an optomechanical resonance induced by an optical spring effect. A linear shift in the imaginary parts of the optical resonances is given by $\epsilon_{1,2} + \delta\epsilon_{1,2}$ with

$$\begin{aligned}\delta\epsilon_{1,2} &= \mp \frac{2\theta\epsilon_1\lambda_1}{\gamma^4 - 2(\epsilon_1^2 - \lambda_1^2)\gamma^2 + (\epsilon_1^2 + \lambda_1^2)^2} \\ &= \mp 2\theta \frac{(1 - \rho_{\text{SR}})\cos\phi}{8\gamma^2\sqrt{\rho_{\text{SR}}}}.\end{aligned}$$

That means that the imaginary part of one of the optical resonances indeed decreases – which one of them actually depends on whether the signal-recycling cavity is blue or red detuned. But at the same time the other one increases and thus, the system can become unstable. A precise statement regarding the stability of the system is given by the condition that all roots of the characteristic equation (cf. Eq. (2.37)) must have negative imaginary parts. We find that the system remains stable as long as the optical power is restricted to the constraint

$$\begin{aligned}\frac{\theta}{\gamma^3} < \frac{\theta_{\text{crit}}}{\gamma^3} &\equiv \max \left\{ -\frac{\gamma(\epsilon_1^2 + \lambda_1^2)}{2\lambda_1(\gamma^2 - \epsilon_1^2 - \lambda_1^2)}, \frac{\gamma^4 + 2(\epsilon_1^2 - \lambda_1^2)\gamma^2 + (\epsilon_1^2 + \lambda_1^2)^2}{2\gamma\lambda_1(\gamma^2 - \epsilon_1^2 - \lambda_1^2)} \right\} \\ &= \max \left\{ -\frac{1 + \rho_{\text{SR}}^2 + 2\rho_{\text{SR}}\cos(2\phi)}{8\rho_{\text{SR}}\sin(2\phi)}, \frac{1 + \rho_{\text{SR}}^2 - 2\rho_{\text{SR}}\cos(2\phi)}{2\rho_{\text{SR}}\sin(2\phi)} \right\}.\end{aligned}\quad (2.38)$$

Since $(1 - \rho_{\text{SR}})^2 \leq 1 + \rho_{\text{SR}}^2 \pm 2\rho_{\text{SR}}\cos(2\phi) \leq (1 + \rho_{\text{SR}})^2$, the system remains stable for higher circulating optical power, i.e. θ_{crit} increases, when the signal-recycling mirror's reflectivity is small and when the carrier is more resonant or more anti-resonant in the signal-recycling cavity, i.e. for a *weak signal-recycling*. Such a weak signal-recycling configuration can be found in the lower right panel of Fig. 7, where $\lambda_1/\gamma = 0.01$ and $\epsilon_1/\gamma = 0.5$ and thus $\theta_{\text{crit}}/\gamma^3 \approx 104$. For devices with optical power scales as high as planned for the next generation gravitational-wave detectors and a strong signal-recycling, the system becomes inescapably unstable as depicted in the three other panels of Fig. 7. Thus, a Sagnac interferometer of Advanced LIGO scale could also have the need for a control system in the detection band. The behavior of the optical resonances in the upper right panel of Fig. 7 probably needs some more explanation: both optical resonances become purely imaginary while each of them has two parts, one travelling up the imaginary axis and the other one down. When two of the resonances meet on the imaginary axis, they both move again away from the imaginary axis in opposite directions.

2.2.3 Sensitivity to gravitational waves

Exactly as in Sec. 2.1, the equations of motion in Eqs. (2.25) and (2.26) can be gathered into an input-output relation. Recall that we have

$$\hat{y}_\zeta = (\sin\zeta, \cos\zeta) \left(\mathbf{T}_{\text{quant}}^{\text{Sag}} \vec{a} + \bar{t}_h^{\text{Sag}} R_{xx}^{\text{Sag}} \hat{F}_{\text{external}} \right), \quad (2.39)$$

where $\vec{a} = (\hat{a}_1, \hat{a}_2)^T$ is the input quadrature vector and

$$\mathbf{T}_{\text{quant}}^{\text{Sag}} = \begin{pmatrix} y_1^{\text{Sag}} & y_2^{\text{Sag}} \\ -y_2^{\text{Sag}} & y_1^{\text{Sag}} \end{pmatrix} + \frac{R_{xx}^{\text{Sag}}}{1 - R_{xx}^{\text{Sag}} R_{FF}^{\text{Sag}}} \begin{pmatrix} R_{Y_1F}^{\text{Sag}} \\ R_{Y_2F}^{\text{Sag}} \end{pmatrix} \begin{pmatrix} f_1^{\text{Sag}} \\ f_2^{\text{Sag}} \end{pmatrix}, \quad (2.40)$$

$$\bar{t}_h^{\text{Sag}} = \frac{1}{1 - R_{xx}^{\text{Sag}} R_{FF}^{\text{Sag}}} \begin{pmatrix} R_{Y_1F}^{\text{Sag}} \\ R_{Y_2F}^{\text{Sag}} \end{pmatrix}. \quad (2.41)$$

When we do the following replacement in the equations of motion (cf. Eq. (2.26))

$$R_{xx}^{\text{Sag}} \hat{F}_{\text{external}} \rightarrow h/2 L + \hat{\xi}_{\text{cl}}, \quad (2.42)$$

we have assumed the gravitational wave with amplitude h as incident from right above the interferometer with a polarization that maximizes the response of a L-shaped interferometer. Furthermore, we have included classical noise sources which are described by the operator $\hat{\xi}_{\text{cl}}$ obeying the correlation

$$\langle \hat{\xi}_{\text{cl}}(\Omega) (\hat{\xi}_{\text{cl}}^\dagger(\Omega'))_{\text{sym}} \rangle = 2\pi \frac{S_{\text{cl}}(\Omega)}{2} \delta(\Omega - \Omega'). \quad (2.43)$$

For the detection of gravitational waves it is advisable to fix the small distance of the input mirror and the mirror located nearby for each cavity as well as the small distance between the two far end mirrors of each cavity. Then each ring cavity is prohibited to expand or shrinking in direction of its small edge, i.e. perpendicular to the edge with arm length L . The gravitational wave as quadrupole radiation shrinks a ring cavity in one direction while at the same time expanding it in the perpendicular direction. But since gravitational waves causes only relative length changes, the length of the small edge of each ring cavity is hardly influenced by the gravitational wave. What is more important is the fact that the radiation-pressure noise and the classical noise are actually causing the cavity to expand in all directions. Fixing the small edges of each ring cavity reduces R_{xx}^{Sag} by a factor of two which makes it equal to R_{xx}^{Mich} . Then we can replace

$$R_{xx}^{\text{Sag}} \hat{F}_{\text{external}} \rightarrow h L + \hat{\xi}_{\text{cl}} \quad (2.44)$$

in Eq. (2.26). Then (similar to Sec. 2.1), the total sensitivity to gravitational waves can be inferred from the h -referred noise spectral density

$$S_h^{\text{Sag}}(\Omega) = \frac{(\sin \zeta, \cos \zeta) \mathbf{T}_{\text{quant}}^{\text{Sag}} \left(\mathbf{T}_{\text{quant}}^{\text{Sag}} \right)^\dagger (\sin \zeta, \cos \zeta)^T}{L^2 (\sin \zeta, \cos \zeta) \bar{t}_h^{\text{Sag}} \left(\bar{t}_h^{\text{Sag}} \right)^\dagger (\sin \zeta, \cos \zeta)^T} + \frac{S_{\text{cl}}(\Omega)}{L^2}. \quad (2.45)$$

It turns out that if the extra degree of freedom of the ring cavities is removed, the Sagnac interferometer has the same h -referred standard quantum limit as the Michelson interferometer (cf. Eq. (2.15)).

If the optical power is high such that $\theta > \theta_{\text{crit}}$ (cf. Eq. (2.38)), the system becomes unstable and needs to be controlled. It has been shown that an ideal feedback control system does not give rise to any fundamental change in the sensitivity to gravitational waves [22–24], intuitively because the signal and the noise are fed back with the same proportion onto the mirrors. When linearly feeding back the output \hat{y}_ζ onto the differential motion \hat{x} with an arbitrary filter kernel $K_C(\Omega)$ and without introducing extra noise, the quantum-noise-transfer matrix and the signal-transfer vector both become multiplied by the same frequency-dependent factor

$$\mathbf{T}_{\text{quant}}^{\text{Sag}} \rightarrow \frac{1 - R_{xx}^{\text{Sag}}(\Omega) R_{FF}^{\text{Sag}}(\Omega)}{1 - R_{xx}^{\text{Sag}}(\Omega) R_{FF}^{\text{Sag}}(\Omega) - R_{Y_\zeta F}^{\text{Sag}}(\Omega) K_C(\Omega)} \mathbf{T}_{\text{quant}}^{\text{Sag}}, \quad (2.46)$$

$$\bar{t}_h^{\text{Sag}} \rightarrow \frac{1 - R_{xx}^{\text{Sag}}(\Omega) R_{FF}^{\text{Sag}}(\Omega)}{1 - R_{xx}^{\text{Sag}}(\Omega) R_{FF}^{\text{Sag}}(\Omega) - R_{Y_\zeta F}^{\text{Sag}}(\Omega) K_C(\Omega)} \bar{t}_h^{\text{Sag}}. \quad (2.47)$$

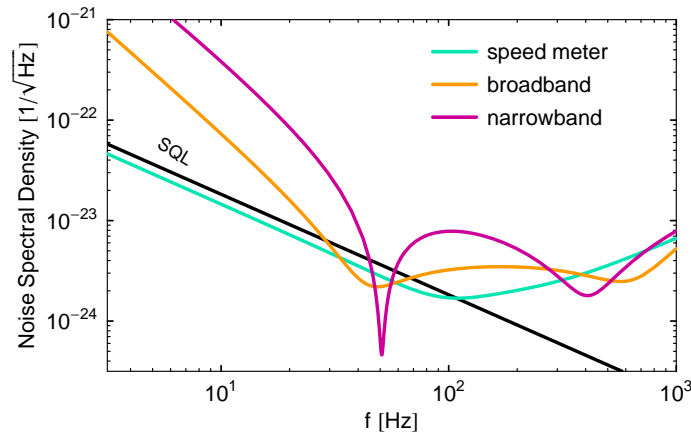


Figure 8: Example quantum noise spectral densities for a Sagnac interferometer with detuned signal-recycling. Here basically Advanced LIGO-like parameter are used (Tab. 3). For the speed-meter configuration we have chosen $\gamma = 2\pi 150$ Hz, $\lambda_1 = 2\pi 50$ Hz, $\epsilon_1 = 2\pi 90$ Hz and $\zeta = 0.18\pi$; the broadband configuration has $\gamma = 2\pi 15$ Hz, $\lambda_1 = -2\pi 600$ Hz, $\epsilon_1 = 2\pi 250$ Hz and $\zeta = 0.7\pi$; while the narrowband configuration has $\gamma = 2\pi 15$ Hz, $\lambda_1 = -2\pi 400$ Hz, $\epsilon_1 = 2\pi 100$ Hz and $\zeta = 0$. Note that broadband and narrowband configurations have to be stabilized, while the speed-meter configuration is self-stable. The black line denotes the free-mass standard quantum limit (SQL).

It is easy to see that the noise spectral density (cf. Eq. (2.45)) is indeed invariant under this transformation.

Even though the dynamical interaction between mirrors and light in the Sagnac interferometer is quite different from the one in a Michelson interferometer, their quantum noise behavior can become very similar as shown in Fig. 8. This is not the case around the degenerated resonance case, i.e. with a signal-recycling cavity close to resonance or anti-resonance (such as discussed in Ref. [31]), where we can clearly spot the speed-meter feature: the noise curve follows the standard quantum limit at low frequencies, and can even beat it in a wide frequency range when using appropriately high optical power and bandwidth. But abandoning this regime, the speed-meter feature becomes more and more lost and entering the well-separated resonance case the noise curves are more and more similar to the one of a signal-recycled Michelson interferometer (compare Fig. 8 with Fig. 5).

2.2.4 Classical noise budget and sensitivity to a specific astrophysical gravitational-wave source

The most popular gravitational-wave forms are probably those emitted from inspiraling binary systems composed of compact objects which are always used when designing the sensitivity of gravitational-wave detectors. This may be due to the fact that they are in fact one of the few analytically known wave forms. Moreover, in 1993, Russell Hulse and Joe Taylor were awarded the Nobel Prize in Physics for the first indirect evidence of gravitational-wave emission by observing a system of two inspiraling neutron stars [71, 116]. Only a handful of binary neutron star systems have been detected yet but the existence of many other systems is predicted. The waveform of such compact binary inspirals is given in the

lowest Post-Newtonian approximation by (cf. e.g. Ref. [40])

$$|h(f)| = \frac{G^{5/6}(M/2)^{1/2}(2M)^{1/3}}{\sqrt{30}\pi^{2/3}c^{3/2}D} f^{-7/6} \Theta(f_{\max} - f), \quad (2.48)$$

where a single neutron star has a mass of $M \approx 1.4 M_{\odot}$ and D is the distance from the source to the detector. $M_{\odot} \approx 1.9891 \cdot 10^{30}$ kg stands for the solar mass. There is an upper cut-off frequency, $f_{\max} \approx 1570$ Hz, in Eq. (2.48), beyond which the system undergoes a transition from adiabatic inspiral into non-adiabatic merger, and Eq. (2.48) is no longer a valid approximation. Then the optimal signal-to-noise ratio [53]

$$\frac{S}{N} \propto \int_{f_{\min}}^{f_{\max}} \frac{f^{-7/3}}{S_h(f)} df, \quad (2.49)$$

is achievable by correlating the data with a known template from Eq. (2.48), where seismic noise defines a lower bound of $f_{\min} \approx 7$ Hz. One can either calculate the achievable range D of a detector with a fixed signal-to-noise ratio or conversely, calculate the achievable signal-to-noise ratio for a detector observing an astrophysical object at fixed distance D . The event rate is roughly the cube of the radius of detectable range D and is therefore at a fixed radius proportional to signal-to-noise ratio cubed.

Now we assume a standard noise budget which was simulated with the software *Bench* [3] for the current Advanced LIGO classical noise budget: each contribution to the total classical noise budget $S_{\text{cl}}(\Omega)$ – consisting of suspension thermal noise, seismic noise, thermal fluctuations in the coating and gravity gradient noise – are gathered in Fig. 9. Including this classical noise budget, we are able to perform a grid search on the signal-to-noise ratio over a parameter space spanned by variable parameters such as those from the signal-recycling and the homodyne detection, in order to optimize the signal-recycled Sagnac interferometer's sensitivity towards specific astrophysical gravitational-wave sources as neutron star binary inspirals. For all grid searches performed in this thesis we have used the commercial simulation software *Matlab*[®].

Note that due to the weighting factor of $f^{-7/3}$ in Eq. (2.49), the optimization strategy tends to focus more on the low frequency regime at the expense of the sensitivity at higher frequencies. Therefore, the detection of gravitational-wave sources with a high frequency periodical signal, such as the millisecond pulsars, becomes hindered with that optimization strategy. To compensate for that fact, we can conduct an additional sub-optimization in order to achieve a better sensitivity in the high frequency regime [80, 103]: it can be accomplished by first picking out all configurations obeying a sensitivity which is at least a certain fraction of the optimal sensitivity. In a second step these configurations are explored in the high frequency regime using the same power law but considering a smaller frequency integration interval, as e.g. [150 Hz, 1570 Hz], and selecting the optimal signal-to-noise ratio on this interval.

A signal-recycled Sagnac interferometer of Advanced LIGO scale can produce a noise curve which is really congruent with the noise curve of the Advanced LIGO configuration – therefore compare the yellow curve in Fig. 5 with the red curve in Fig. 9. This is due to the fact that $\lambda_1 = -2\pi \cdot 290$ Hz and $\epsilon_1 = 2\pi \cdot 120$ Hz as used for the red curve in Fig. 9 lie within the regime of well-separated resonances (cf. Sec. 2.2.1), i.e. they are much larger than $\gamma = 2\pi \cdot 15$ Hz. Recall that in that regime the signal-recycled Sagnac and Michelson

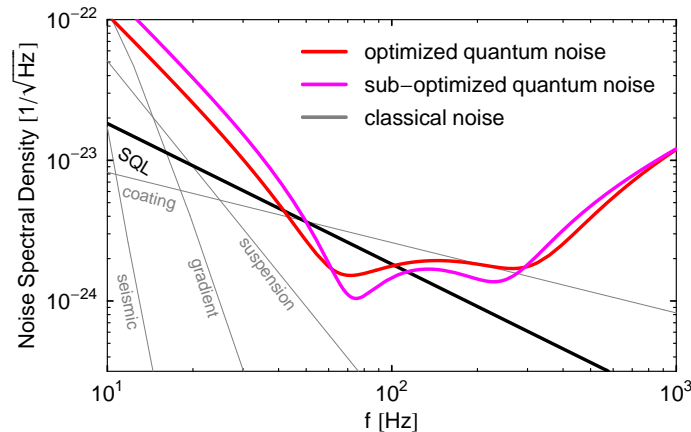


Figure 9: Noise spectral densities of a Sagnac interferometer with detuned signal-recycling of Advanced LIGO scale (cf. Tab. 3). Configurations have optimized (red) and sub-optimized (pink) sensitivity towards neutron star binary inspirals if the arm cavity half-bandwidth is fixed to $\gamma = 2\pi 15$ Hz. We have $\lambda_1 = -2\pi 290$ Hz, $\epsilon_1 = 2\pi 120$ Hz and $\zeta = 0.7\pi$ for the optimized configuration and $\lambda_1 = -2\pi 243$ Hz, $\epsilon_1 = 2\pi 76$ Hz and $\zeta = 0.8\pi$ for the sub-optimized configuration. Standard Advanced LIGO classical noise budget is given: the single contributions are labeled in the plot.

interferometers are approximately equivalent in terms of their quantum noise. Therefore, it does not come as a big surprise that for the Sagnac configuration with $\gamma = 2\pi 15$ Hz, $\lambda_1 = -2\pi 290$ Hz and $\epsilon_1 = 2\pi 120$ Hz and $\zeta = 0.7\pi$, we obtain the same signal-to-noise ratio as for the Advanced LIGO configuration represented by the yellow curve in Fig. 5 which has been obtained by optimizing a signal-recycled Michelson interferometer – assuming the classical noise budget as given by the gray curves in Fig. 9 – towards the signal of neutron star binary inspirals. It has turned out that the red curve in Fig. 9 gives also the best sensitivity of a signal-recycled Sagnac interferometer to neutron star binary inspirals for the given noise budget if the Sagnac interferometer’s arm cavity half-bandwidth is fixed to $\gamma = 2\pi 15$ Hz. The sub-optimized configuration in Fig. 9 has still 98% of the signal-to-noise ratio of the Advanced LIGO configuration on the whole frequency range [7 Hz, 1570 Hz], but a much better sensitivity on the restricted frequency interval [150 Hz, 1570 Hz]. For both configurations, the optimal and the sub-optimal, we find $\theta > \theta_{\text{crit}}$ and thus, they are required to be stabilized by a feedback control system within the detection band. One could think about optimizing the signal-recycled Sagnac configuration with the constraint of a stable system in order to circumvent relying on the control scheme in the detection band.

In contrast to the signal-recycled Michelson interferometer, in the signal-recycled Sagnac interferometer the arm cavity half-bandwidth γ not only has influence on technical parameter but also becomes a quite important factor when optimizing the sensitivity. Let us fix θ but increase the half-bandwidth γ – assuming a higher power-recycling factor which results in more optical power at the beam splitter. Note that in order to maintain θ , the power-recycling factor has to be multiplied by actually the same factor as it is used for the assumed increase in arm cavity bandwidth. Therefore, the optical power which has to pass the beam splitter is also increased by this factor. Then we can optimize the sensitivity to neutron star binary inspirals again, but using different values for γ . The results of this optimization are presented in the first part of Tab. 4.

	γ in Hz	λ_1 in Hz	ϵ_1 in Hz	ζ in radian	improvement
standard classical noise	$2\pi 15$	$-2\pi 290$	$2\pi 120$	0.7π	0 %
	$2\pi 75$	$-2\pi 58$	$2\pi 32$	0.5π	13 %
	$2\pi 88$	$-2\pi 70$	$2\pi 38$	0.4π	29 %
	$2\pi 100$	$-2\pi 74$	$2\pi 39$	0.4π	40 %
	$2\pi 113$	$-2\pi 75$	$2\pi 39$	0.4π	44 %
	$2\pi 125$	$-2\pi 78$	$2\pi 43$	0.3π	45 %
	$2\pi 138$	$-2\pi 76$	$2\pi 45$	0.3π	41 %
	$2\pi 150$	$-2\pi 74$	$2\pi 48$	0.3π	34 %
	$2\pi 163$	$-2\pi 72$	$2\pi 53$	0.3π	25 %
	$2\pi 175$	$-2\pi 69$	$2\pi 59$	0.2π	16 %
	$2\pi 188$	$-2\pi 67$	$2\pi 66$	0.2π	7 %
low classical noise	$2\pi 38$	$-2\pi 31$	$2\pi 19$	0.5π	85 %
	$2\pi 50$	$-2\pi 38$	$2\pi 27$	0.5π	170 %
	$2\pi 63$	$-2\pi 49$	$2\pi 36$	0.5π	230 %
	$2\pi 75$	$-2\pi 12$	$2\pi 110$	0.45π	10 %
	$2\pi 88$	$-2\pi 11$	$2\pi 142$	0.4π	15 %
	$2\pi 100$	$-2\pi 0.1$	$2\pi 150$	0.4π	31 %
	$2\pi 113$	$-2\pi 0.1$	$2\pi 150$	0.35π	29 %
	$2\pi 125$	$-2\pi 0.1$	$2\pi 148$	0.3π	19 %
	$2\pi 138$	$-2\pi 0.1$	$2\pi 148$	0.25π	4 %

Table 4: Resulting parameters of the optimization towards the signal of inspiraling neutron star binaries assuming different values for the cavity half-bandwidth γ . Advanced LIGO parameters are used (cf. Tab. 3) and the circulating power is fixed to $P = 800$ kW. The last column gives the improvement in event rate for the signal-recycled Sagnac interferometer compared to the optimized Michelson interferometer of the same scale. For the upper part we adopted the current Advanced LIGO noise budget and for the lower part the gravity gradient noise and the suspension thermal noise are reduced by a factor of ten and the coating thermal by a factor of three.

As an example, for $\gamma = 2\pi 125$ Hz we find that the optimal choice is a configuration far outside the regime of well-separated resonances (cf. Fig. 10 and sixth row of Tab. 4), increasing the sensitivity to neutron star binary inspirals by $\sim 13\%$ compared to the Advanced LIGO configuration, which corresponds to an improvement of $\sim 45\%$ in the event rate. This configuration requires a moderate signal-recycling with $\rho_{\text{SR}} = 0.38$ and $\phi = 0.88\pi$. Note that a moderate signal-recycling is common to all the configurations from Tab. 4 with $\gamma \geq 2\pi 75$ Hz. In Fig. 10 we can recover the speed-meter feature at low frequencies, where the quantum noise beats the standard quantum limit over a large frequency band by a big factor while the sensitivity is not degraded too much at high frequencies. Note that all optimized configuration from Tab. 4 with $\gamma \geq 2\pi 88$ Hz are even self-stable, i.e. have a $\theta < \theta_{\text{crit}}$. The sub-optimized Sagnac configuration as plotted in Fig. 10 has still a comparable sensitivity to Advanced LIGO on the full frequency interval but is much more sensitive at higher frequencies – to be precise about $\sim 28\%$ in the event rate. After adding up all noise contribution shown e.g. in Fig. 10, it turns out that the total noise spectral density of the optimized signal-recycled Sagnac interferometer almost follows the borderline set by the classical noise

in the low frequency regime. Furthermore, we can see in Fig. 10 that at low frequencies, i.e.

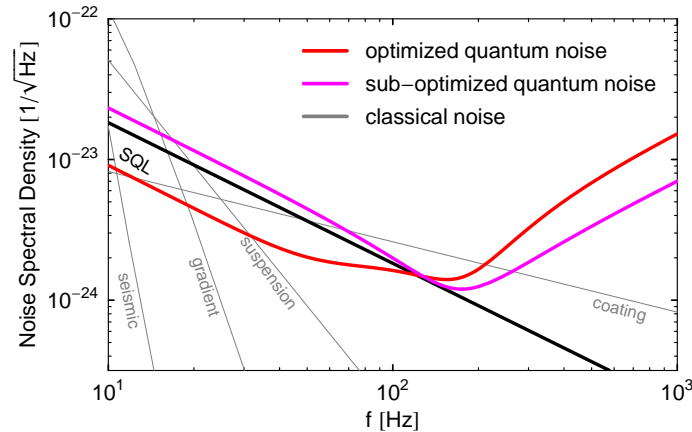


Figure 10: Optimized noise spectral densities with respect to neutron star binary inspirals for a signal-recycled Sagnac interferometer of Advanced LIGO scale (cf. Tab. 3) including a standard Advanced LIGO classical noise budget. We have $\gamma = 2\pi 125$ Hz, $\lambda_1 = -2\pi 78$ Hz, $\epsilon_1 = 2\pi 43$ Hz and $\zeta = 0.3\pi$ for the optimized configuration and $\gamma = 2\pi 175$ Hz, $\lambda_1 = -2\pi 171$ Hz, $\epsilon_1 = 2\pi 95$ Hz and $\zeta = 0.025\pi$ for the sub-optimized configuration.

below ~ 150 Hz, the quantum noise is already much below the classical noise. That actually suggests that lowering the quantum noise in the low frequency regime further cannot significantly improve the sensitivity. This fact motivates to assume a lower classical noise floor and investigate the Sagnac interferometer's sensitivity performance again.

2.2.5 Sensitivity to inspiraling neutron star binaries assuming a third-generation classical noise budget

Because a detuned signal-recycled Sagnac interferometer may be considered as a real candidate design for third-generation gravitational-wave detectors, it would be advisable to consider a plausible noise budget for interferometers right beyond the second generation. One can already presage that technical improvements will reduce the classical noise floor significantly in the remote future. In order to explore the real potential of the signal-recycled Sagnac interferometer, we analyze its performance on such a reduced classical noise budget. A limiting factor at lower frequencies is, for instance, the gravity gradient noise. As suggested in Ref. [70], this effect can be removed from the recorded data by performing an independent measurement of the ground's density fluctuations near each test-mass. We assume it to be 1/10 (in amplitude) the current estimation for Advanced LIGO [4]. Another limiting factor is given by the thermal noise in the suspension system and in the mirrors. We assume that the suspension thermal noise can be lowered by a factor of 10 in amplitude, while the internal thermal noise of the mirrors can be lowered by a factor of 3 in amplitude [4]. Such improvements may possibly be realized by *(i)* optimizing the design of the mirror coating structure and the suspension wires, *(ii)* improving the mechanical quality factors of mirror coating, substrate and suspension materials, and *(iii)* applying cryogenic techniques [10, 21, 62, 118, 119].

The results of the optimization – if different arm cavity bandwidths are given at a fixed circulating power – with respect to inspiraling neutron star binaries against such an opti-

mistic classical noise budget are presented in the second part of Tab. 4. Fig. 11 shows an example where the quantum noise nicely blends with the gap between the standard quantum limit and the classical noise floor at low frequencies. Remarkably, this configuration improves

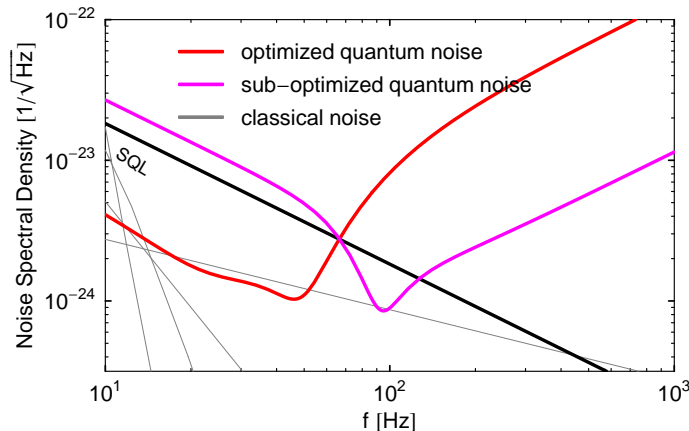


Figure 11: Optimized noise spectral densities with respect to neutron star binary inspirals for a signal-recycled Sagnac interferometer of Advanced LIGO scale (cf. Tab. 3) including a more optimistic classical noise budget. We have $\gamma = 2\pi 63$ Hz, $\lambda_1 = -2\pi 49$ Hz, $\epsilon_1 = 2\pi 36$ Hz and $\zeta = 0.5\pi$ for the optimized configuration and $\gamma = 2\pi 75$ Hz, $\lambda_1 = -2\pi 82$ Hz, $\epsilon_1 = 2\pi 80$ Hz and $\zeta = 0.2\pi$ for the sub-optimized configuration.

the event rate by 230 %, when comparing it to the sensitivity of a Michelson topology which is also optimized against the low classical noise budget – such a Michelson configuration can be found in Ref. [103]. The parameters of the optimized configuration plotted in Fig. 11 are quite close to the degenerate resonance case and are given in the third row of the second part of Tab. 4. Converting them into signal-recycling parameters, we obtain $\rho_{\text{SR}} = 0.3$ and $\phi = 0.99\pi$ corresponding to a weak signal-recycling. Note that the optomechanical configuration is again self-stable. Other configurations, which are optimal assuming different arm cavity bandwidths, are summarized in Tab. 4. The sub-optimized Sagnac configuration as plotted in Fig. 11 has still a comparable sensitivity on the full frequency interval as the – against the low classical noise budget – optimized Michelson configuration. We can see, however, that this sub-optimized Sagnac configuration retains the Advanced LIGO sensitivity at higher frequencies, which is not true for the optimized Sagnac configuration and totally hopeless for an optimized Michelson configuration.

2.3 Transducer schemes

In the mid 90's, Braginsky, Khalily and colleagues introduced a number of quantum non-demolition configurations for the detection of gravitational waves which involved an alternative way of readout, namely the so-called *intra-cavity readout* schemes [13, 15, 76]. These configurations were able to beat the free-mass standard quantum limit. The idea of such schemes is not to measure the phase shift of the light, induced by the gravitational wave, via monitoring the outgoing modulations fields outside the interferometer but to measure the redistribution of optical energy directly inside the interferometer. All these schemes consist of a L-shaped cavity as depicted in Fig. 12. The measurement can either be done by inserting a nonlinear meter into this cavity or by converting the gravitational-wave strain via

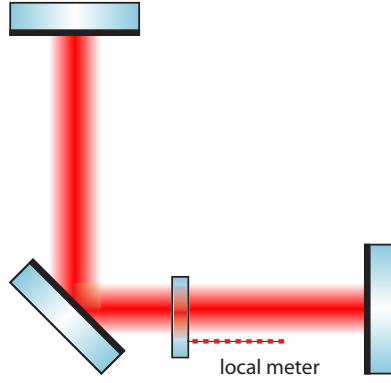


Figure 12: Schematic plot of one example of an intra-cavity readout scheme: the optical bar. A partly-transmissive, tiny mirror is placed into a L-shaped cavity. Its motion can be observed by a local meter.

radiation pressure into real motion of a tiny extra mirror placed in the cavity (cf. Fig. 12). This motion can then be sensed by some additional readout, a so-called *local meter*, which is attached to the extra mirror. Braginsky and Khalily have called the configuration having this second readout method implemented the *optical bar* because it really behaves like its mechanical analog, the resonant bar detectors [128]. The underlying principle of the optical bar is actually the optical spring effect. The two end mirrors of the cavity are each rigidly connected with the tiny extra mirror via optical springs. In the local inertial frame of the extra mirror the effect of gravitational waves can be described completely as a tidal force field, which induces forces only on the end mirrors. Since the mirrors are rigidly connected, they will all move together and we can say that the end mirrors *transduce* their motion onto the tiny extra mirror. This enables us to measure the real motion of the extra mirror using the additional local meter.

2.3.1 Signal-recycled interferometers as transducers

Closing the signal-recycling port by making the signal-recycling mirror high-reflective can convert every interferometer topology with arm cavities and detuned signal-recycling into a transducer. Here the optical field connects the input mirror with the end mirror in each arm. And while in the co-local frame of beam splitter and input mirrors a gravitational-wave induces forces only on the end mirrors, it could be converted by the optomechanical coupling into real motion of the input mirrors. Realizing a transducer in this way automatically solves a practical problem: the closed system of the L-shaped cavity (cf. Fig. 12) does not intuitively suggest how the light actually gets into the cavity.

After evaluating for the differential motion only between the two input mirrors $\hat{x}_{\text{ITM}}^{\text{diff}}$ as well as for the differential motion only between the two end mirrors $\hat{x}_{\text{ETM}}^{\text{diff}}$ of a Michelson interferometer by assuming that all mirrors have equal masses, it turns out that we can simply split Eq. (2.3) and write it into vector notation as

$$\begin{pmatrix} \hat{x}_{\text{ITM}}^{\text{diff}} \\ \hat{x}_{\text{ETM}}^{\text{diff}} \end{pmatrix} = \frac{R_{xx}^{\text{Mich}}}{2} \begin{pmatrix} -\hat{F}_{\text{ITM}}^{\text{diff}} \\ \hat{F}_{\text{ETM}}^{\text{diff}} \end{pmatrix} + \frac{R_{xx}^{\text{Mich}} R_{FF}^{\text{Mich}}}{2} \begin{pmatrix} 1 & -1 \\ -1 & 1 \end{pmatrix} \begin{pmatrix} \hat{x}_{\text{ITM}}^{\text{diff}} \\ \hat{x}_{\text{ETM}}^{\text{diff}} \end{pmatrix}. \quad (2.50)$$

Analogously, we can split Eq. (2.26) for the Sagnac interferometer. Here we assume again

that the small distance of the input mirror and the mirror located nearby for each cavity is fixed and treat this system as a single mirror. We assume the same for the end mirrors. Then we effectively reduce the number of moving mirrors and the Sagnac interferometer's mechanical susceptibility becomes reduce by a factor of two and therefore coincides with the one of the Michelson, i.e. $R_{xx}^{\text{Sag}}(\Omega) = R_{xx}^{\text{Mich}}(\Omega) = R_{xx}(\Omega)$. Then Eq. (2.50) hold also for the Sagnac interferometer when exchanging the corresponding susceptibilities.

Generally, we can express the differential motion of the input mirrors in terms of the forces acting on input and end mirrors by solving Eq. (2.50) for $\hat{x}_{\text{ITM}}^{\text{diff}}$ which gives

$$\hat{x}_{\text{ITM}}^{\text{diff}} = - \frac{2}{\underbrace{\frac{1 - R_{xx}(\Omega) R_{FF}(\Omega)}{1 - R_{xx}(\Omega)/2 R_{FF}(\Omega)}}_{\mathcal{M}(\Omega)}} \frac{\hat{F}_{\text{ITM}}^{\text{diff}}}{m \Omega^2} \underbrace{\frac{R_{xx}(\Omega)/2 R_{FF}(\Omega)}{1 - R_{xx}(\Omega) R_{FF}(\Omega)}}_{\mathcal{T}(\Omega)} \frac{R_{xx}(\Omega)}{2} \hat{F}_{\text{ETM}}^{\text{diff}}, \quad (2.51)$$

where $R_{FF}(\Omega)$ could either stand for $R_{FF}^{\text{Mich}}(\Omega)$ or for $R_{FF}^{\text{Sag}}(\Omega)$. Here we have defined the frequency depended transducer mass $\mathcal{M}(\Omega)$ and the transducer function $\mathcal{T}(\Omega)$. As mentioned above, the effect of a gravitational wave in the co-inertial frame of beam splitter and input mirrors can be described as a force on the end mirrors contributing to $\hat{F}_{\text{ETM}}^{\text{diff}}$. Both differential motions are driven by the free radiation-pressure force $\hat{F}_{\text{RP}}^{(0)}$ – given in Sec. 2.1 for the case of a Michelson interferometer and in Sec. 2.2 for the case of a Sagnac interferometer – which therefore contributes to both $\hat{F}_{\text{ITM}}^{\text{diff}}$ and $\hat{F}_{\text{ETM}}^{\text{diff}}$. But note that in the limit of a closed output port of the interferometer, the free radiation-pressure force vanishes. On the input mirrors, the back-action force of the local meter acts additionally – contributing to $\hat{F}_{\text{ITM}}^{\text{diff}}$. Then the spectral density of the standard quantum limit of a standard local meter would read

$$S_{\text{LM}}^{\text{SQL}} = \frac{2 \hbar}{\mathcal{M}(\Omega) \Omega^2} \frac{1}{(\mathcal{T}(\Omega))^2 L^2}, \quad (2.52)$$

assuming a linear continuous position measurement with no correlation in the back-action and the shot noise.

Let us summarize some interesting effects [92] for specific values of the optomechanical susceptibility $R_{xx}(\Omega)/2 R_{FF}(\Omega)$ at a certain sideband frequency (cf. Tab. 5). In the case of a very rigid spring as in the first row of Tab. 5, the transducer function becomes equal to one half and the transducer mass becomes twice as big as the initial mass. This is actually the optical bar regime. Since the input mirrors are rigidly connected to the end mirrors, they all move by one half the amount the end mirrors would have moved if there were no optical spring present. If $R_{FF}(\Omega) = 2/R_{xx}(\Omega)$ at a certain sideband frequency just as in the second row of Tab. 5, the transducer function is equal to one but the transducer mass becomes infinitely heavy. At first glance this seems to be a very unexpected situation since the input mirrors do not respond to any forces which act directly on them because such a force will totally be canceled by the radiation-pressure force. They are only driven by the force acting on the end mirror. But recalling classical mechanics we recollect that such a situation can always appear in the case of two coupled oscillators. Nevertheless, this situation seems to be a very interesting regime for the case of a transducer since the spectral density of the standard quantum limit of the local meter goes to zero. That means that around that sideband frequency for which $R_{FF}(\Omega) = 2/R_{xx}(\Omega)$ has been realized, a local meter is able to measure without introducing any quantum back-action noise and making a real quantum

$R_{xx}(\Omega)/2 R_{FF}(\Omega)$	$\mathcal{M}(\Omega)$	$\mathcal{T}(\Omega)$	$S_{LM}^{\text{SQL}}(\Omega)$
$\rightarrow \infty$	$2m$	$\frac{1}{2}$	$\frac{1}{2} S_h^{\text{SQL}}$
1	$\rightarrow \infty$	1	$\rightarrow 0$
$\frac{1}{2}$	$\rightarrow 0$	$\rightarrow \infty$	$\rightarrow 0$
$\frac{1}{4}$	$\frac{2}{3}m$	$-\frac{1}{2}$	$\frac{3}{2} S_h^{\text{SQL}}$
$\rightarrow 0$	m	$\rightarrow 0$	$\rightarrow \infty$

Table 5: Different regimes of a transducer generated by different values of $R_{xx}/2 R_{FF}$ each at a certain frequency.

non-demolition measurement. Here the back action is really eliminated at a certain sideband frequency and the measured object is not influenced by the measurement. This is in contrast to the case of an homodyne detection at a certain quadrature (cf. Tab. 2) which can only remove the radiation-pressure noise from the measurement output: the measurement still acts back onto the measured object, but the noise induced is removed from the measurement output by adjusting the homodyne phase. Finally, in the third row of Tab. 5, we have the resonant case when $R_{FF}(\Omega) = 1/R_{xx}(\Omega)$. Here the transducer mass becomes infinitely light but the transducer function goes to infinity. Therefore, the spectral density of the standard quantum limit of the local meter still goes to zero. This regime becomes very interesting when the local meter performs a weak measurement which is shot noise limited and therefore produces not much back action. For the sake of completeness we have listed two more cases in Tab. 5 which are interesting – but which are actually no useful transducer regimes.

Let us re-scale our parameters with the arm cavity half-bandwidth, such as the sideband frequency $\Omega \rightarrow \gamma \Omega_\gamma$ and the characteristic frequency $\theta \rightarrow \gamma^3 \theta_\gamma$, in order to obtain dimensionless parameters. Then we obtain for the detuned signal-recycled Michelson interferometer with closed output port, i.e. $\rho_{\text{SR}} \rightarrow 1$, the following relations: $\lambda \rightarrow \gamma \tan \phi$ and $\epsilon \rightarrow 0$ (cf. Eq. (2.9)) and thus

$$R_{xx}(\Omega)/2 R_{FF}^{\text{Mich}}(\Omega) \rightarrow \frac{-\theta_\gamma \tan \phi}{2 \Omega_\gamma^2 (\Omega_\gamma^2 - \tan^2 \phi)}. \quad (2.53)$$

Together with this relation, the transducer function and the transducer mass are then given by

$$\mathcal{T}^{\text{Mich}}(\Omega_\gamma) = \frac{\theta_\gamma \tan \phi}{2 (\Omega_\gamma^2 (\Omega_\gamma^2 - \tan^2 \phi) + \theta_\gamma \tan \phi)}, \quad (2.54)$$

$$\mathcal{M}^{\text{Mich}}(\Omega_\gamma) = \frac{2 (\Omega_\gamma^2 (\Omega_\gamma^2 - \tan^2 \phi) + \theta_\gamma \tan \phi)}{2 \Omega_\gamma^2 (\Omega_\gamma^2 - \tan^2 \phi) + \theta_\gamma \tan \phi} m, \quad (2.55)$$

respectively. Similarly, for the detuned signal-recycled Sagnac interferometer with closed output port we find that $\lambda_1 \rightarrow \gamma \lambda_0 \equiv \gamma \tan(\pi/4 - \phi/2)$, $\lambda_2 \rightarrow -\gamma/\lambda_0$ and $\epsilon_{1,2} \rightarrow 0$ (cf.

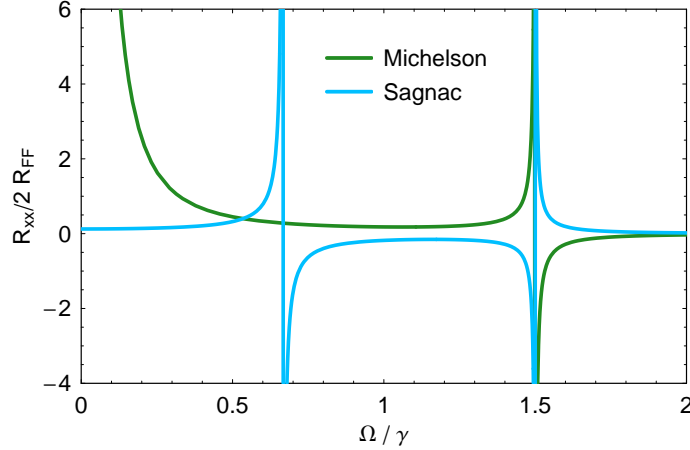


Figure 13: Examples for the frequency behavior of the optomechanical susceptibility $R_{xx}(\Omega)/2 R_{FF}(\Omega)$, comparing a position with a speed meter topology. For the Michelson interferometer we have chosen $\theta/\gamma^3 = 0.3$ and $\tan \phi = 1.5$ and also for the Sagnac interferometer $\theta/\gamma^3 = 0.3$ and $\lambda_0 = 1.5$.

Eq. (2.21)) and thus

$$R_{xx}(\Omega)/2 R_{FF}^{\text{Sag}}(\Omega) \rightarrow \frac{\theta_\gamma (\lambda_0 - 1/\lambda_0)}{2 (\Omega_\gamma^2 - \lambda_0^2) (\Omega_\gamma^2 - 1/\lambda_0^2)}. \quad (2.56)$$

Then the signal-recycled Sagnac transfer function and output mass read

$$\mathcal{T}^{\text{Sag}}(\Omega_\gamma) = \frac{-\theta_\gamma (\lambda_0 - 1/\lambda_0)}{2 ((\Omega_\gamma^2 - \lambda_0^2) (\Omega_\gamma^2 - 1/\lambda_0^2) - 2\theta_\gamma (\lambda_0 - 1/\lambda_0))}, \quad (2.57)$$

$$\mathcal{M}^{\text{Sag}}(\Omega_\gamma) = \frac{2 ((\Omega_\gamma^2 - \lambda_0^2) (\Omega_\gamma^2 - 1/\lambda_0^2) - \theta_\gamma (\lambda_0 - 1/\lambda_0))}{2 (\Omega_\gamma^2 - \lambda_0^2) (\Omega_\gamma^2 - 1/\lambda_0^2) - \theta_\gamma (\lambda_0 - 1/\lambda_0)} m, \quad (2.58)$$

respectively.

Now we can analyze the frequency dependence of the quantity $R_{xx}(\Omega)/2 R_{FF}(\Omega)$, as shown in Fig. 13, for both, a position meter in the form of the Michelson interferometer and a speed meter in the form of the Sagnac interferometer. In a relatively flat regime, where $R_{xx}(\Omega)/2 R_{FF}(\Omega)$ remains constant over some bandwidth around a certain frequency, one can always try to tune the optical power and the cavity half-bandwidth in such a way that $R_{xx}(\Omega)/2 R_{FF}(\Omega)$ reaches one of the interesting values from Tab. 5 around that frequency and turns the interferometer into some fancy transducer.

As shown in Fig. 13, in the Michelson case $R_{xx}(\Omega)/2 R_{FF}^{\text{Mich}}(\Omega)$ has a relatively flat regime around $\Omega = \Omega_{\text{Mich}} \equiv (\gamma/\sqrt{2} \tan \phi)$ which is below the optical resonance at $\Omega = \gamma \tan \phi$. This happens before at low frequencies $R_{xx}(\Omega)/2 R_{FF}^{\text{Mich}}(\Omega)$ diverges due to the optical spring effect and turns the Michelson transducer inescapably into an optical bar (cf. first row of Tab. 5). In the flat regime we find

$$R_{xx}(\Omega_{\text{Mich}})/2 R_{FF}^{\text{Mich}}(\Omega_{\text{Mich}}) = \frac{2\theta_\gamma}{\tan^3 \phi}. \quad (2.59)$$

In order to increase the bandwidth of the flat regime around Ω_{Mich} , we need to push the optical resonance frequency to higher frequencies by increasing $\tan \phi$ or the arm cavity bandwidth.

In the Sagnac case, there is not only a relatively flat regime of $R_{xx}(\Omega)/2 R_{FF}^{\text{Sag}}(\Omega)$ around $\Omega = \Omega_{\text{Sag}} \equiv \gamma \sqrt{(\lambda_0^2 + 1/\lambda_0^2)}/2$ which is exactly between the two optical resonances (cf. Fig. 13) at $\Omega = \gamma \lambda_0$ and $\Omega = \gamma/\lambda_0$, respectively. Here we obtain

$$R_{xx}(\Omega_{\text{Sag}})/2 R_{FF}^{\text{Sag}}(\Omega_{\text{Sag}}) = \frac{2\theta_\gamma \lambda_0^3}{(1 - \lambda_0^2)(1 + \lambda_0^2)^2}. \quad (2.60)$$

Furthermore, at low frequencies much below the optical resonances, $R_{xx}(\Omega)/2 R_{FF}^{\text{Sag}}(\Omega)$ does not increase as in the Michelson case but becomes constant due to the optical inertia effect. But unfortunately in that regime, $R_{xx}(\Omega)/2 R_{FF}^{\text{Sag}}(\Omega)$ reaches another level than in the regime around Ω_{Sag} , namely

$$R_{xx}(0)/2 R_{FF}^{\text{Sag}}(0) = \frac{\theta_\gamma}{2} \left(\lambda_0 - \frac{1}{\lambda_0} \right). \quad (2.61)$$

If we want to increase the bandwidth of the flat regime below the optical resonances, the two optical resonances have to be equal, i.e. $\lambda_0 = 1$, and the arm cavity bandwidth γ has to be increased. The increase of λ_0 and also the increase of γ pushes the two resonances further apart which increases the bandwidth of flat regime between the two optical resonances.

Fig. 14 shows the standard quantum limits of a local meter (cf. Eq. (2.52)) in comparison to reading out a Michelson and reading out a Sagnac interferometer. Here both interferome-

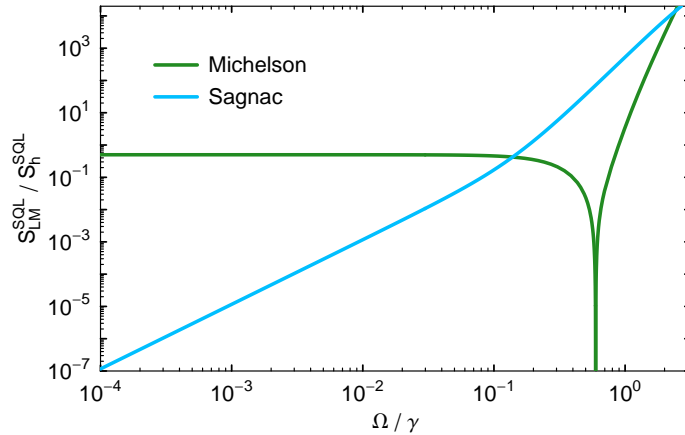


Figure 14: Examples for the standard quantum limit of a local meter (cf. Eq. (2.52)) when reading out a Michelson and a Sagnac interferometer, respectively. The standard quantum limit is normalized with the one of the Michelson and Sagnac interferometer, when conventionally reading out at the dark port, which is given in Eq. (2.15). We have chosen again $\theta/\gamma^3 = 0.3$ and the detuning in such a way that $\mathcal{M}^{\text{Mich}}(\Omega_{\text{Mich}}/\gamma) \rightarrow \infty$ and $\mathcal{M}^{\text{Sag}}(0) \rightarrow \infty$ (cf. Tab. 5).

ters have the same optical power, while the detuning of the signal-recycling cavity is chosen in such a way that $\mathcal{M}^{\text{Mich}}(\Omega_{\text{Mich}}/\gamma) \rightarrow \infty$ and $\mathcal{M}^{\text{Sag}}(0) \rightarrow \infty$ (cf. second row of Tab. 5). For the Michelson interferometer this means $\tan \phi = \sqrt[3]{2\theta_\gamma}$ and the Sagnac interferometer should be detuned satisfying $\lambda_0 = 1/\theta_\gamma + \sqrt{1 + 1/\theta_\gamma^2}$. We can see very nicely that at low frequencies the Michelson becomes an optical bar while the Sagnac becomes a real quantum non-demolition transducer.

2.3.2 Double readout configurations

Even when the signal-recycling mirror is partly transparent, the transducer effect is still present in an interferometer with detuned signal-recycling. But usually it is unwanted since, as an example, the optical bar effect which is always present in a detuned signal-recycled Michelson interferometer at low frequencies weakens the sensitivity of the interferometer with a conventional readout. In Ref. [104] we have suggested a configuration which on the one hand cures this problem and on the other hand also offers a practical realization of the local meter by actually combining two interferometers into one scheme. A secondary laser is injected into the bright port of an ordinary Michelson interferometer with arm cavities and detuned signal-recycling, establishing the local readout possibility. The secondary laser can have much less optical power than the first one. It could be resonant for the signal-recycling cavity but must not resonate in the arm cavities. The arm cavities should be even anti-resonant for this secondary carrier in order to ban the secondary carrier from entering the arm cavities. Therefore, we have obtained a second Michelson interferometer which has the input mirrors of the large-scale interferometer as its end mirrors. Note that because this secondary interferometer does not have arm cavities, we are automatically forced to take the beam splitter motion into account [64]. Furthermore, the two carriers should have preferably opposite polarizations in order to make it easy to separate their outputs at the dark port. The instability introduced by the optical spring of the large-scale interferometer has to be stabilized using a feedback control system. Even though the double-readout system is quite complex, we have been able to show that an ideal feedback control system does not give rise to any fundamental change in the sensitivity to gravitational waves.

The two outputs at the dark port of the double interferometer, corresponding each to one of the two carriers, have to be optimally filtered: we have found out that at frequencies below the optomechanical resonance frequency, the filter should use mainly the local readout's output. This is actually the optical bar regime (cf. first row of Tab. 5) in which the large-

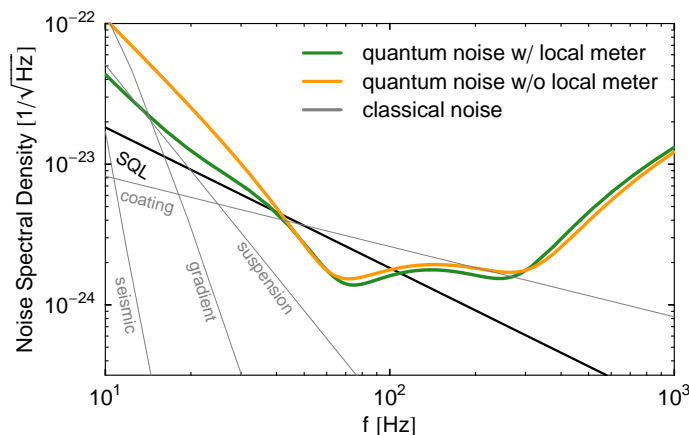


Figure 15: Optimized noise spectral densities with respect to neutron star binary inspirals for a local readout scheme (of Advanced LIGO scale including a standard Advanced LIGO classical noise budget) compared to the Advanced LIGO configuration. The secondary laser establishing the local meter has an optical power of 4 kW at the beam splitter, the bandwidth of the local meter's signal-recycling cavity is 2π 4 kHz and the phase quadrature is detected. The large-scale interferometer in the local readout scheme has $\lambda = 2\pi$ 220 Hz and $\epsilon = 2\pi$ 64 Hz and a homodyne detection angle of 0.7π . For other parameters see Tab. 3.

scale Michelson interferometer converts the gravitational-wave strain into real motion of its arm cavity mirrors and weakens in fact the sensitivity of its own output. But on the other hand this real mirror motion can be sensed by the second carrier. At frequencies around and above the optomechanical resonance in turn, the filter prefers the output of the large-scale interferometer. In order to find this optimal situation, we have analytically minimized the combined h -referred noise spectral density at each sideband frequency by varying the two filter functions. Each of these two filter function has been applied to one of the two outputs which are then summed up to give the combined output.

Taking into account the current classical noise budget of Advanced LIGO as well as constraints on the optical power, we have performed an extensive parameter optimization of our local readout scheme towards the detection of compact binary inspirals [104]. We have shown that the addition of the local meter with an optical power of 4 kW can improve the sensitivity at low frequencies significantly while it can also indirectly improve the sensitivity at high frequencies. The improvement at low frequencies can be seen very well in Fig. 15 which compares the optimized quantum noise of an Advanced LIGO configuration with and without a local meter. The optimization is here towards the signal of inspiraling neutron star binaries, when the standard classical noise budget as also shown in in Fig. 15 is assumed. We have found that the local meter can increase the sensitivity of Advanced LIGO to neutron star binary inspirals by 29% in the event rate. Moreover, we have shown that the local meter

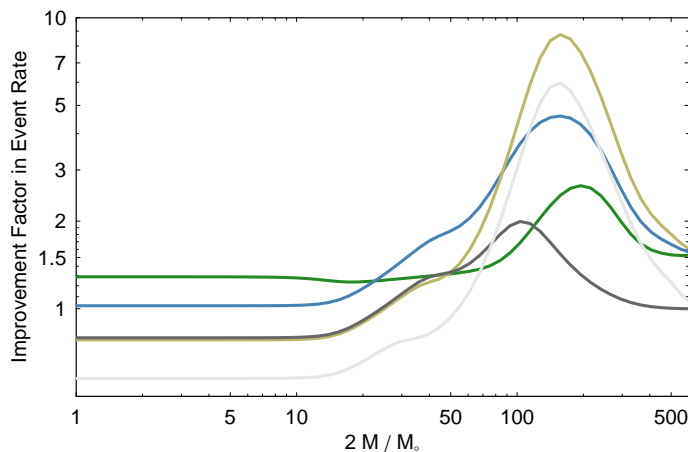


Figure 16: Improvement in the event rate compared to the Advanced LIGO detector (a Michelson interferometer with detuned signal-recycling which is optimized for the signal of inspiraling neutron star binaries) versus total binary mass. The signal-recycled interferometer with (colored curves) and without (gray curves) local meter are optimized for three different binary masses: neutron star with $M = 1.4 M_{\odot}$ (green curve); intermediate-mass black holes with $M = 20 M_{\odot}$ (blue and dark gray curve) and with $M = 60 M_{\odot}$ (khaki and bright gray curve). Note that each curve has fixed optimization parameters. The secondary laser establishing the local meter has an optical power of 4 kW at the beam splitter.

can broaden the detection band of Advanced LIGO which will allow the interferometer to search for multiple sources simultaneously as well as to examine a wider frequency range of the same source. As an example, we have explored how the increase in detection bandwidth can allow us to detect more efficiently the population of compact binary objects with a broad range of masses – from neutron stars to intermediate-mass black holes – and hence a broad signal frequency band. Fig. 16 compares the ability of the local readout scheme with the one

of an ordinary signal-recycled Michelson interferometer to detect different binary inspirals once the optimization parameters such as the signal-recycling detuning and the homodyne detection angle are fixed.

We must have come to the conclusion that this scheme should be further investigated as a low-cost add-on for the Advanced LIGO detector. Or in possible conjunction with other quantum non-demolition techniques – such as input squeezing (cf. Tab. 2) probably even for both, the local meter and the large-scale interferometer – it could even be considered as a real candidate design for a third-generation detector. For further reading and more details about our used optimization parameters and results we refer the reader to the very detailed Refs. [101, 104]. Note that it is also possible to strongly detune the local meter in the local readout scheme which is explored in Ref. [81]. But in that reference the aim is only at beating the standard quantum limit around the optomechanical resonance frequency of the large-scale interferometer such as in mechanical resonant bar detectors.

Another idea for a real third-generation detector is to construct a local readout scheme where the large-scale interferometer has a speed-meter topology with detuned signal-recycling (cf. Sec. 2.2) and the local meter a Michelson topology. A practical realization of this scheme could be to construct the large-scale interferometer by taking a Michelson interferometer with an added sloshing cavity [99, 100] and adding the detuned signal-recycling technique to that. The local meter is then realized by a secondary laser injected into the Michelson interferometer which does not enter the sloshing cavity. It might also be possible to realize such a scheme by using polarizing optics. This speed meter local readout scheme will probably be even more interesting because of the advantageous transducer properties of the speed-meter interferometer at low frequencies: the transducer function is not restricted to one half but can become much larger (cf. third row of Tab. 5). Even though the transducer mass decreases then which causes an increase in the radiation-pressure noise, the signal-to-noise ratio of a weak local meter could be really high – much higher than reading out a Michelson interferometer. Another option is that the transducer function could become close to one (cf. second row of Tab. 5) while the transducer mass increases and suppresses radiation pressure. The question is how good the sensitivity of the large-scale interferometer with the conventional readout at high frequencies can be in such optimal transducer situations. This has to be explored in details. We have planned to rigorously investigate such a scheme and perform an extensive parameter search as it was done for the local readout scheme in Ref. [104].

2.4 Double-optical-spring ponderomotive squeezer

The ponderomotive squeezer suggested in Refs. [36, 37] is intended to provide a quite unorthodox way of generating a squeezed vacuum input for a gravitational-wave detector. Inserting squeezed vacuum states into the dark port of a laser interferometer gravitational-wave detector increases its quantum limited sensitivity (cf. Tab. 2) as it was first shown in Ref. [27]. The conventional method of preparing optical squeezed states is to make use of the $\chi^{(2)}$ -nonlinearity in optical media as employed for example in Refs. [30, 122]. But it is also well-known that the fluctuating radiation-pressure force generates squeezed optical states inside an interferometer and the idea is to make use of the squeezed vacuum fields leaking out at the dark port. The advantage of using the optical spring effect in this context is that in this case the strength of the generated quantum squeezing is frequency independent up to

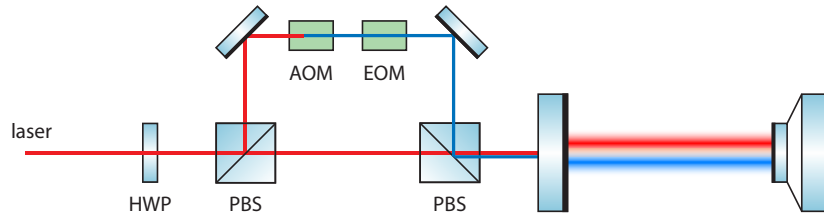


Figure 17: Schematic plot of the double-optical-spring ponderomotive squeezer experiment as located at the MIT [35]. The laser light is split into two paths by a combination of a half wave plate (HWP) and a polarizing beam splitter (PBS). In one of the paths the light is frequency shifted using an acousto-optic modulator (AOM) and phase modulated by an electro-optic modulator (EOM). Carrier and subcarrier are recombined on a second PBS before being injected into the cavity with a tiny end mirror.

the optomechanical resonance frequency. Moreover, up to that frequency the squeezing angle is fixed and the squeezing ellipse does not rotate with the sideband frequency. Furthermore, the optical spring is also able to suppress classical noise. On the other hand, one has to deal with the instability introduced by the optical spring [22] and this issue is also important in the theoretical calculations since every stabilizing control system influences the squeezing: one effect of a feedback control system for instance is that it requires a detection on the output which certainly decreases the amount of available squeezing.

It seems to be the ideal solution to employ a second optical spring which removes the instability introduced by the first optical spring. Note that such a scheme should be regarded as an ideal and practical realization of a quantum control system. The stable optomechanical resonance has already been demonstrated experimentally in Ref. [35] and its direct benefits regarding gravitational-wave detectors was theoretically explored in Ref. [103]. In Ref. [89] we have investigated the output of a stable double-optical-spring ponderomotive squeezer which will be described in the following.

2.4.1 Double optical spring

In general, a second optical spring can easily be realized by inserting a frequency-looked secondary carrier laser field or a subcarrier field which is some frequency-shifted fraction of the carrier laser field into the bright port of a detuned interferometer or a detuned cavity, respectively. The carrier and the secondary carrier or the carrier and the subcarrier should preferably have opposite polarization. In the following we will adopt our formulation to match the real experimental setup described in Ref. [35] which is located at the Massachusetts Institute of Technology, Cambridge, and which is depicted in Fig. 17: a laser field is detuned with respect to a single small-scale cavity formed by a heavy input mirror and a tiny end mirror. Before being inserted into that cavity, some fraction of the carrier light has become frequency-shifted using an acousto-optic modulator and phase-modulated by an electro-optic modulator to form a subcarrier which can further be detuned from resonance to create the second optical spring. The parameter values of this experiment which are used for the numerical calculations are listed in Tab. 6. We would like to emphasize that all following equations are of course also applicable to describe a Michelson interferometer with detuned arm cavities – when using the reduced mass of the mirrors. With slight modifications (cf.

Sec. 2.1), they are even applicable to describe a Michelson interferometer with a detuned signal-recycling cavity. The advantage of using a Michelson interferometer compared to a

mirror mass	m	1 g
carrier input power	$P_{\text{in}}^{(1)}$	2.85 W
subcarrier input power	$P_{\text{in}}^{(2)}$	0.15 W
laser wavelength	$2\pi c/\omega_0^{(1)}$	1064 nm
cavity length	L	0.9 m
cavity half bandwidth	γ	2π 10 kHz

Table 6: Double optical spring ponderomotive squeezer parameter values used for the numerical calculations are based on the experimental setup located at the MIT [35].

single cavity is that then the output squeezing is less susceptible to laser noise.

If we denote the amplitude and phase quadrature operators of the incoming sideband fields by $\hat{a}_1^{(i)}$ and $\hat{a}_2^{(i)}$ and the one of the outgoing sideband fields by $\hat{b}_1^{(i)}$ and $\hat{b}_2^{(i)}$ – associated with the carrier ($i = 1$) and the subcarrier ($i = 2$) field, respectively – we can define an input double quadrature vector by $\vec{a}_d = (\hat{a}_1^{(1)}, \hat{a}_2^{(1)}, \hat{a}_1^{(2)}, \hat{a}_2^{(2)})^T$ and a corresponding output vector by $\vec{b}_d = (\hat{b}_1^{(1)}, \hat{b}_2^{(1)}, \hat{b}_1^{(2)}, \hat{b}_2^{(2)})^T$. Note that in contrast to the usual quadrature vector these vectors are now 4-dimensional. The vacuum correlations of the input quadrature operators can be gathered into one equation as

$$\langle \hat{a}_k^{(i)}(\Omega) (\hat{a}_l^{(j)})^\dagger(\Omega') \rangle_{\text{sym}} = \pi \delta(\Omega - \Omega') \delta_{ij} \delta_{kl}, \quad (2.62)$$

and the input-output relation can be written as

$$\vec{b}_d = \mathbf{T}_{\text{quant}}^{\text{DOS}} \vec{a}_d + \vec{t}_{\text{cl}}^{\text{DOS}} \hat{\xi}_{\text{cl}}, \quad (2.63)$$

where the (4×4) matrix $\mathbf{T}_{\text{quant}}^{\text{DOS}}$ linearly transforms the quantum noise into the output channels while $\vec{t}_{\text{cl}}^{\text{DOS}}$ transforms the classical noise $\hat{\xi}_{\text{cl}}$ into the outputs. The quantum-noise-transfer matrix is given by

$$\mathbf{T}_{\text{quant}}^{\text{DOS}} = \begin{pmatrix} \mathbf{Y}^{(1)} & \mathbf{0} \\ \mathbf{0} & \mathbf{Y}^{(2)} \end{pmatrix} + \frac{R_{xx}^{\text{cav}}}{1 - R_{xx}^{\text{cav}}(R_{FF}^{\text{cav}(1)} + R_{FF}^{\text{cav}(2)})} \times \begin{pmatrix} R_{Y_1F}^{\text{cav}(1)} \\ R_{Y_2F}^{\text{cav}(1)} \\ R_{Y_1F}^{\text{cav}(2)} \\ R_{Y_2F}^{\text{cav}(2)} \end{pmatrix} \left(f_1^{\text{cav}(1)}, f_2^{\text{cav}(1)}, f_1^{\text{cav}(2)}, f_2^{\text{cav}(2)} \right), \quad (2.64)$$

where the coefficient matrices read

$$\mathbf{Y}^{(i)} = \begin{pmatrix} y_1^{\text{cav}(i)} & y_2^{\text{cav}(i)} \\ -y_2^{\text{cav}(i)} & y_1^{\text{cav}(i)} \end{pmatrix}. \quad (2.65)$$

Furthermore, the classical-noise-transfer vector is given by

$$\vec{t}_{\text{cl}}^{\text{DOS}} = \frac{1}{1 - R_{xx}^{\text{cav}}(R_{FF}^{\text{cav}(1)} + R_{FF}^{\text{cav}(2)})} \begin{pmatrix} R_{Y_1F}^{\text{cav}(1)} \\ R_{Y_2F}^{\text{cav}(1)} \\ R_{Y_1F}^{\text{cav}(2)} \\ R_{Y_2F}^{\text{cav}(2)} \end{pmatrix}. \quad (2.66)$$

The susceptibilities are given in Eqs. (1.60)–(1.63), where here the superscript '(1)' always denotes carrier quantities and '(2)' subcarrier quantities. Then the characteristic equation of the double optical spring reads

$$0 = \frac{1}{R_{xx}^{\text{cav}}(\Omega)} - R_{FF}^{\text{cav}(1)}(\Omega) - R_{FF}^{\text{cav}(2)}(\Omega). \quad (2.67)$$

The stabilization process of the double optical spring is nicely explained in great details and with the help of many pictures in our Ref. [103] and will not be stressed here.

For our analytic calculations, we will consider the input-output relation at sideband frequencies much below the optical bandwidth ($\Omega \ll \gamma^{(1)} = \gamma^{(2)} = \gamma$) and therefore also much below the optomechanical resonance frequencies. This is actually the regime in which the experiment suggested in Ref. [36, 37] is supposed to be carried out and, furthermore, it is the regime in which the quantum squeezing is constant in its strength and angle. In this approximation, the quantum-noise-transfer matrix simplifies to

$$\mathbf{T}_{\text{quant}}^{\text{DOS}} = \begin{pmatrix} 1 & 0 & 0 & 0 \\ 2(\alpha_{\text{os}}^{(1)})^2 & 1 & 2\alpha_{\text{os}}^{(1)}\alpha_{\text{os}}^{(2)} & 0 \\ 0 & 0 & 1 & 0 \\ 2\alpha_{\text{os}}^{(1)}\alpha_{\text{os}}^{(2)} & 0 & 2(\alpha_{\text{os}}^{(2)})^2 & 1 \end{pmatrix}, \quad (2.68)$$

where the coefficients

$$(\alpha_{\text{os}}^{(i)})^2 = \frac{\gamma}{|\Delta^{(i)}|} \frac{(\Omega_{\text{os}}^{(i)})^2}{(\Omega_{\text{os}}^{(1)})^2 - (\Omega_{\text{os}}^{(2)})^2} \quad (2.69)$$

are the coupling constants between the mirror and the carrier ($i = 1$) and subcarrier ($i = 2$), respectively. Furthermore, we have defined the quantities

$$\Omega_{\text{os}}^{(i)} = \sqrt{\frac{4|\Delta^{(i)}|P_{\text{in}}^{(i)}\omega_0^{(i)}\gamma}{L^2((\Delta^{(i)})^2 + (\gamma)^2)}}. \quad (2.70)$$

From Sec. 1.2.4 we know that in the weakly coupled approximation, $\Omega_{\text{os}}^{(i)}$ is equal to the absolute value of the real part of the optomechanical resonance frequency – for $i = 1$ produced by the carrier and for $i = 2$ produced by the subcarrier. Note that in the following we suppose the carrier to be always positively detuned and the subcarrier to be always negatively detuned as well as $\Omega_{\text{os}}^{(1)} > \Omega_{\text{os}}^{(2)}$ which guarantees for a total restoring force induced by the light. Then the stability condition simply reads

$$\frac{(\Omega_{\text{os}}^{(2)})^2}{\gamma^2 + (\Delta^{(2)})^2} \geq \frac{(\Omega_{\text{os}}^{(1)})^2}{\gamma^2 + (\Delta^{(1)})^2}. \quad (2.71)$$

In the low frequency approximation ($\Omega \ll \gamma$) the classical-noise-transfer vector simplifies to

$$\vec{t}_{\text{cl}} = \frac{1}{R_{xx}^{\text{cav}}} \sqrt{\frac{2}{\hbar}} \left(0, \frac{\alpha_{\text{os}}^{(1)}}{\sqrt{(\Omega_{\text{os}}^{(1)})^2 - (\Omega_{\text{os}}^{(2)})^2}}, 0, \frac{\alpha_{\text{os}}^{(2)}}{\sqrt{(\Omega_{\text{os}}^{(1)})^2 - (\Omega_{\text{os}}^{(2)})^2}} \right)^T. \quad (2.72)$$

Keep in mind that, as we can see in Eq. (2.72), the classical noise is suppressed with a larger difference in the two optomechanical resonance frequencies.

2.4.2 Output squeezing versus entanglement

Let us start with considering only the quantum noise of the light. It is obvious that the radiation-pressure fluctuations arising from the modulation fields around the subcarrier's frequency will also move the mirror, therefore causing an additional radiation-pressure noise on the carrier's sideband fields. Of course the same is true vice versa. Because of this additional noise, the output states corresponding to the carrier and those corresponding to the subcarrier turn into mixed states even when we consider only the quantum noise. But the combined system of the two output states still gives a pure state. Recall from Sec. 1.4 that for a composite system, where the total system is in a pure state, the existence of entanglement is equivalent to having mixed states when the individual systems are observed. This simply

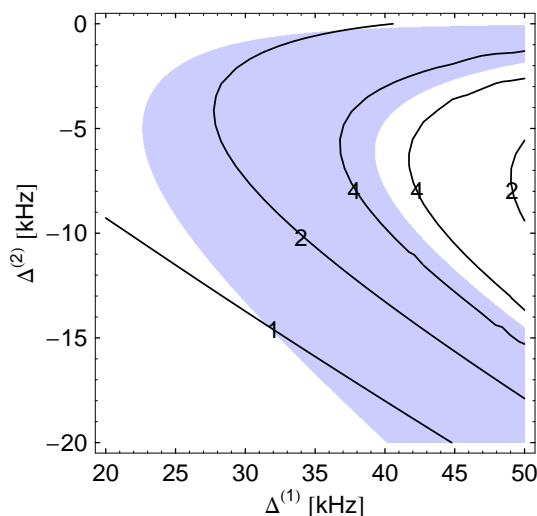


Figure 18: Logarithmic negativity values of the carrier-subcarrier output quantum entanglement at low frequencies and versus carrier and subcarrier detuning. Other parameter values are taken from Tab. 6. The shaded region marks the stable double-optical-spring regime.

means that the output states around the carrier frequency and those around the subcarrier frequency are entangled. In Ref. [132] it is outlined that this fact could be used to generate ponderomotive entanglement. We can characterize the entanglement between the outputs corresponding to the carrier and the subcarrier, respectively, with the logarithmic negativity – as introduced in Sec. 1.4 – at a given sideband-frequency, which is constant in the low frequency approximation ($\Omega \ll \gamma$) and reads

$$E_{\mathcal{N}}(\Omega) = \frac{1}{2 \ln 2} \operatorname{arccosh} \left(2 \left(1 + 4 (\alpha_{\text{os}}^{(1)} \alpha_{\text{os}}^{(2)})^2 \right) - 1 \right). \quad (2.73)$$

This result has independently been derived in Ref. [132]: compare our Eq. (2.73) to Eq. (7) of that reference. Recall that $E_{\mathcal{N}}(\Omega) = 0$ corresponds to no carrier-subcarrier output entanglement which is only true for $\alpha_{\text{os}}^{(1)} = 0$ or $\alpha_{\text{os}}^{(2)} = 0$. This simply tells us that as long as we have a detuned carrier and a detuned subcarrier in a cavity sharing the same end mirror, their output states are always entangled at sideband frequencies below the total optomechanical resonance frequency and in the absence of classical noise. Fig. 18 shows this carrier-subcarrier output entanglement for quantum noise only and for parameter values taken from Tab. 6. In the stable regime, the output of the carrier can be remarkably

strong entangled with the output corresponding to the subcarrier, where the logarithmic negativity can theoretically reach values of about $E_{\mathcal{N}}(\Omega) \sim 8$ for $\Omega \ll \gamma$. In Fig. 19 the

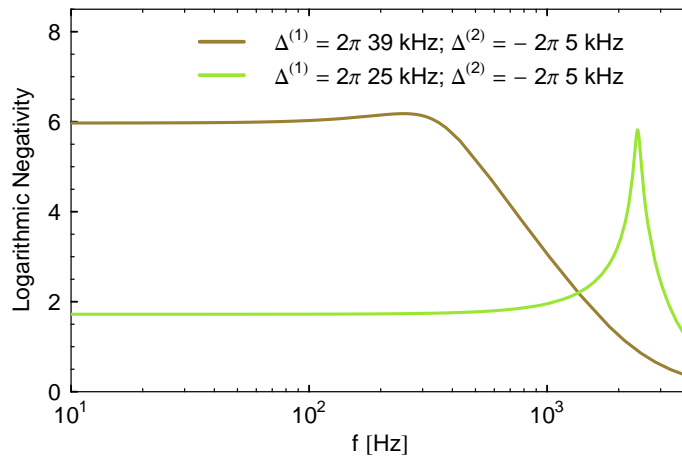


Figure 19: Logarithmic negativity of the carrier-subcarrier output quantum entanglement versus sideband frequency and for two different sets of carrier and subcarrier detuning. Other parameter values are taken from Tab. 6.

carrier-subcarrier output quantum entanglement is plotted versus sideband frequency. Here the situation for two stable optical springs is shown: one with a high total optomechanical eigenfrequency produced by $\Delta^{(1)} = 2\pi 25$ kHz and $\Delta^{(2)} = -2\pi 5$ kHz and one with a low total optomechanical eigenfrequency produced by $\Delta^{(1)} = 2\pi 39$ kHz and $\Delta^{(2)} = -2\pi 5$ kHz. We can see that at frequencies below the total optomechanical eigenfrequency, the entanglement is frequency independent. In that regime, the optical spring with the lower optomechanical eigenfrequency produces more entanglement.

In this section we will describe the output squeezing by deriving the minimal noise spectrum with respect to the quadrature angle which in turn is then equal to the squeezed quadrature. As an example, the minimal quantum noise spectrum associated to the carrier is given in the low frequency approximation ($\Omega \ll \gamma$) by

$$\begin{aligned}
 S_{\min}^{(1)}(\Omega) &\equiv \min_{\zeta^{(1)}} \left\{ (\sin \zeta^{(1)}, \cos \zeta^{(1)}, 0, 0) \mathbf{T}_{\text{quant}}^{\text{DOS}} (\mathbf{T}_{\text{quant}}^{\text{DOS}})^{\dagger} \begin{pmatrix} \sin \zeta^{(1)} \\ \cos \zeta^{(1)} \\ 0 \\ 0 \end{pmatrix} \right\} \\
 &= \frac{1 + 4(\alpha_{\text{os}}^{(1)} \alpha_{\text{os}}^{(2)})^2}{1 + 2(\alpha_{\text{os}}^{(1)})^2 e^{\text{arcsinh}((\alpha_{\text{os}}^{(1)})^2 + (\alpha_{\text{os}}^{(2)})^2)}} \geq e^{-2 \text{arcsinh} \frac{\gamma}{\Delta^{(1)}}}. \quad (2.74)
 \end{aligned}$$

Eq. (2.74) becomes minimized at $\alpha_{\text{os}}^{(2)} = 0$ which corresponds to a vanishing subcarrier. Therefore, the strongest output squeezing is realized in the single optical spring case. With increasing subcarrier strength, the squeezing strength decreases but recall that at the same time the carrier-subcarrier output entanglement increases. Here we can already see that entanglement between the two output fields seems to be unwanted if our aim is to generate squeezed vacuum. We obtain the output squeezing around the subcarrier frequency by exchanging '(1)' and '(2)' in the result of Eq. (2.74). Since we choose our detunings such that $\alpha_{\text{os}}^{(2)} > \alpha_{\text{os}}^{(1)}$ is realized almost everywhere – and especially in the stable regime, we

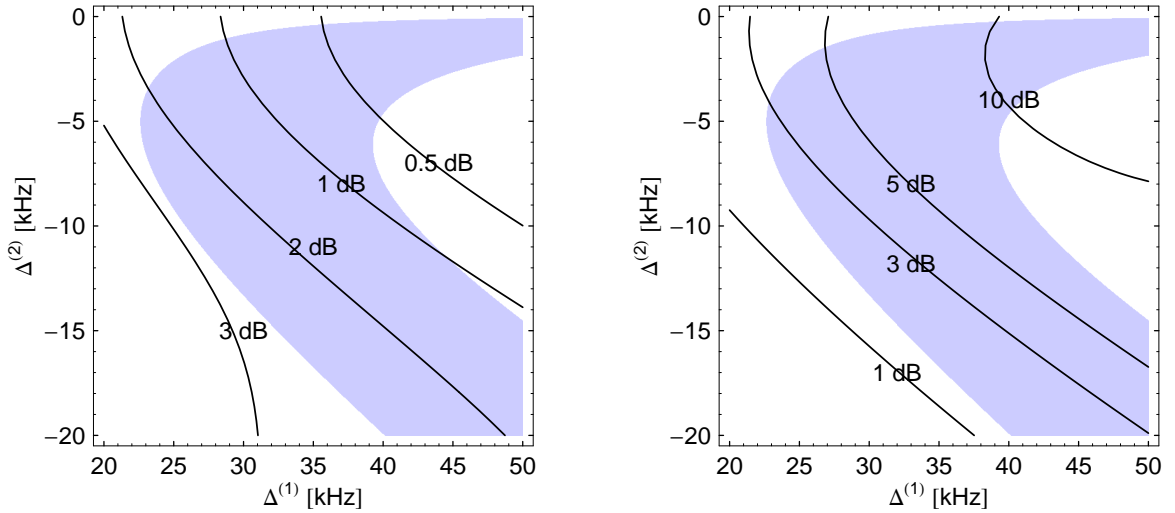


Figure 20: Contour plot of the quantum squeezing produced by the carrier (left panel) and by the subcarrier (right panel) at low frequencies and versus the two different detunings. Other parameter values are taken from Tab. 6. The shaded region marks again the stable regime.

produce a subcarrier output squeezing which is usually stronger than the carrier output squeezing as it can also be seen in Fig. 20. Note that the double-optical-spring stable regime as marked by the shaded region in e.g. Fig. 20 has actually not been obtained by considering the simplified stability condition in Eq. (2.71), but by demanding that the imaginary parts of all roots of the double optical spring's characteristic equation from Eq. (2.67) are smaller than zero.

However, the fact that the additional noise is due to quantum entanglement allows us to remove that noise coherently, because the other partner in the entangled pair is available for a measurement. The output squeezing corresponding to the carrier can therefore be made conditioned onto the measurement result of the output field corresponding to the subcarrier or vice versa. Please note that it is easy to verify that it will make no difference in the final noise spectrum of some device with an arbitrary linear transfer-function – such as a laser interferometer gravitational-wave detector – whether: *(i)* one injects one of the unconditional squeezer output into that device first and then condition the device's output onto the second squeezer output or *(ii)* one just injects the conditional squeezing – suppose that there is a squeezing-source which has exactly the noise spectrum of the conditional squeezing – into the device. The first procedure would be more what can be implemented into real experimental situations but the second one is how we will treat the problem theoretically.

2.4.3 Conditional covariance matrix

The most obvious way to recover a stronger squeezing of the out-going field corresponding to the carrier is to measure the amplitude quadrature of the out-going field around the subcarrier, i.e. to measure $\hat{b}_1^{(2)}$. By doing so, we can obtain information about the additional radiation-pressure fluctuations coming from the subcarrier field. When we then condition the measurement of the carrier's output-squeezing at each sideband frequency on the result

of measuring the subcarrier's radiation-pressure noise, we can remove the effect of the second optical spring completely.

But it has turned out that the amplitude quadrature is not even the optimal one to observe. In order to find the optimal conditional squeezing, we need to know – at every sideband frequency – the covariance matrix among $(b_1^{(1)}, b_2^{(1)})$ conditioned on measuring $\hat{b}_1^{(2)} \cos \zeta^{(2)} + \hat{b}_2^{(2)} \sin \zeta^{(2)}$ with an arbitrary quadrature $\zeta^{(2)}$. This can be easily accomplished by the following mathematical procedure: first apply a rotation to the vector \vec{b}_d , rotating the detected quadrature to the last element of the (4×4) covariance matrix $\langle \vec{b}_d \vec{b}_d^\dagger \rangle$. This is achieved by applying $\mathbf{R} \vec{b}_d$ with the rotation matrix given by

$$\mathbf{R} = \begin{pmatrix} \mathbb{1} & \mathbf{0} \\ \mathbf{0} & \begin{pmatrix} \sin \zeta^{(2)} & -\cos \zeta^{(2)} \\ \cos \zeta^{(2)} & \sin \zeta^{(2)} \end{pmatrix} \end{pmatrix}. \quad (2.75)$$

Then the covariance matrix among $(b_1^{(1)}, b_2^{(1)})$ conditioned on measuring $\hat{b}_1^{(2)} \cos \zeta^{(2)} + \hat{b}_2^{(2)} \sin \zeta^{(2)}$ at a given sideband frequency is simply equal to the first (2×2) block of the conditional covariance matrix $\mathbf{R} \langle \vec{b}_d \vec{b}_d^\dagger \rangle \mathbf{R}^T$ which is conditioned on its last element. As it can be found in many textbooks on multivariate statistics (cf. e.g. Ref. [82]), a Gaussian covariance matrix conditioned on its last element is equal to the Schur complement of that matrix with respect to its last element. The Schur complement is well-known from linear algebra. For a general (4×4) matrix \mathbf{V} the first (2×2) block of the Schur complement with respect to the last element V_{44} reads

$$\begin{pmatrix} V_{11} & V_{12} \\ V_{21} & V_{22} \end{pmatrix} - \frac{1}{V_{44}} \begin{pmatrix} V_{14} V_{41} & V_{14} V_{42} \\ V_{24} V_{41} & V_{24} V_{42} \end{pmatrix}, \quad (2.76)$$

where first indices indicate the rows of \mathbf{V} and second indices the columns. Quite important for us is the fact that as long as a (4×4) matrix represents a pure bipartite Gaussian state, the first (2×2) block of the Schur complement with respect to the last element also represents a pure Gaussian state. Here this fact means that for quantum noise only, any homodyne detection on the subcarrier light would project the carrier output into a pure state.

2.4.4 Conditional quantum output squeezing

The optimal conditional output squeezing is always stronger than the unconditional squeezing. For quantum noise only, it is given for one of the outputs in the low frequency approximation ($\Omega \ll \gamma$) by

$$S_{\min}^{\text{cond}(i)}(\Omega) = \frac{S_{\min}^{(i)}(\Omega)}{1 + 4(\alpha_{\text{os}}^{(1)} \alpha_{\text{os}}^{(2)})^2}, \quad (2.77)$$

requiring a detection of the other output at the homodyne detection angle given by

$$\tan \zeta^{(j)} = -e^{-\text{arcsinh}((\alpha_{\text{os}}^{(1)})^2 + (\alpha_{\text{os}}^{(2)})^2)}, \quad (2.78)$$

where $i = 1, 2$ and $j = 2, 1$. Eq. (2.77) tells us that the conditional output squeezing simply increases with higher $\alpha_{\text{os}}^{(1)}$ and $\alpha_{\text{os}}^{(2)}$. Recall that these coefficients increase with higher optomechanical resonance frequencies and with a smaller separation among the two optomechanical resonance frequencies. Note that the factor $S_{\min}^{(i)}/S_{\min}^{\text{cond}(i)}$ as given in Eq. (2.77)

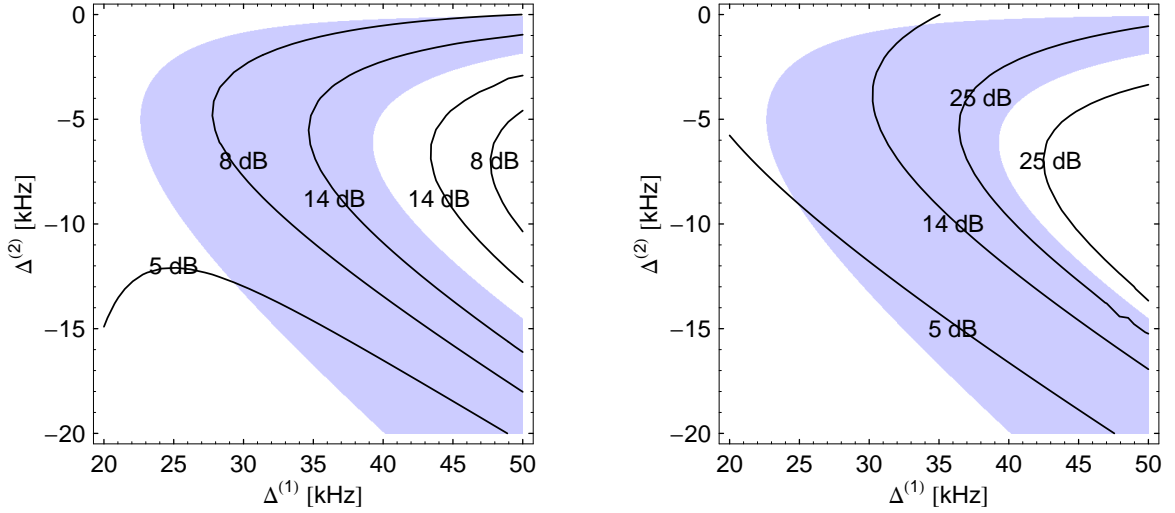


Figure 21: Contour plot of the carrier squeezing conditioned on the subcarrier output (left panel), subcarrier squeezing conditioned on the carrier output (right panel) at low frequencies and versus the two different detunings. Other parameter values are taken from Tab. 6. The shaded region marks the stable regime.

describes how much the conditioning is able to improve the squeezing. On the other hand this factor is also equal to the argument of the function from Eq. (2.73) giving the carrier-subcarrier output entanglement. We have mentioned this interdependence between output squeezing and output entanglement already before. But here we can explicitly see that it is due to the fact that the correlations between carrier and subcarrier – which are responsible for the carrier-subcarrier output entanglement – can be removed by the conditioning in order to improve the output squeezing. Comparing Fig. 21 with Fig. 20 we find that the condi-

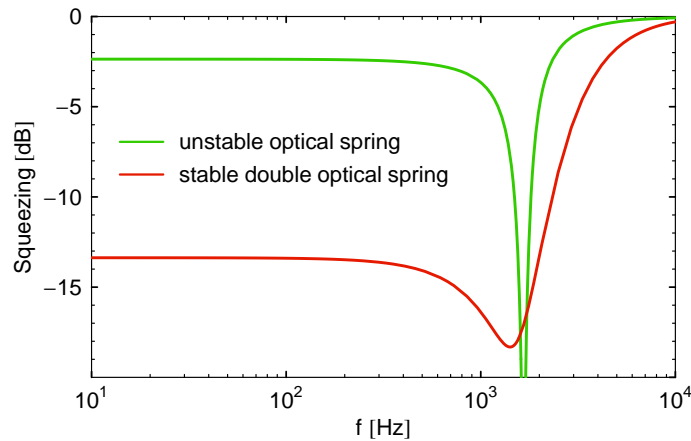


Figure 22: Single optical spring and double optical spring (subcarrier conditioned on the carrier) quantum output squeezing versus sideband frequency. For the single optical spring the full carrier ($P_{\text{in}}^{(1)} = 3 \text{ W}$, $P_{\text{in}}^{(2)} = 0$) is injected into the cavity and detuned by $\Delta = 2\pi 38.5 \text{ kHz}$. The double optical spring has $\Delta^{(1)} = 2\pi 30 \text{ kHz}$ and $\Delta^{(2)} = -2\pi 5 \text{ kHz}$. All other parameters are taken from Tab. 6.

tioning can reveal a strong subcarrier output squeezing of the stable double-optical-spring ponderomotive squeezer. Including Fig. 18 into this comparison, we can actually see that

the conditioning is indeed able to reveal more squeezing in regions of high carrier-subcarrier output entanglement.

Fig. 22 compares the frequency dependence of the quantum output squeezing of an unstable single and a stable double optical spring. We have chosen the detunings in such a way that the real part of the double optical spring's total optomechanical resonance frequency coincides with the real part of the single optical spring's optomechanical resonance frequency. The quantum noise spectral densities for the carrier and the subcarrier in this special situation can be found in Fig. 23. Fig. 22 shows that in the quantum noise case the conditional quantum output squeezing is indeed constant up to the optomechanical resonance frequency.

2.4.5 Conditional output squeezing with classical noise

Until now we have considered only quantum noise. But in a real experiment the squeezing

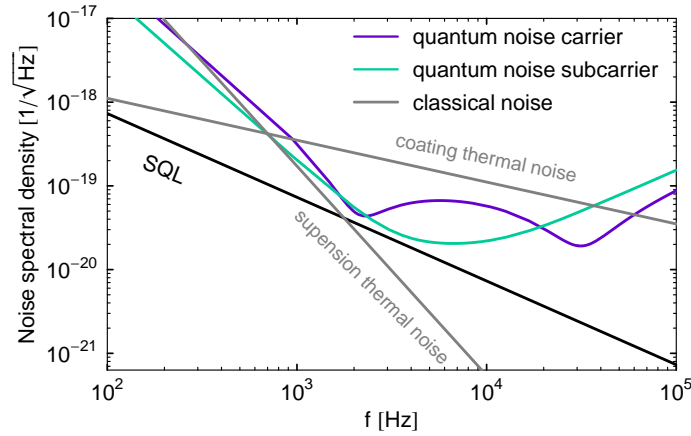


Figure 23: Example quantum noise spectral densities for the carrier and the subcarrier with $\Delta^{(1)} = 2\pi 30$ kHz and $\Delta^{(2)} = -2\pi 5$ kHz and all other parameters are taken from Tab. 6. Two classical noise sources at a certain level as given in Ref. [36] are used: suspension thermal noise and coating thermal noise.

will become weaker with classical noise. In the low frequency approximation, the optimal minimal conditional noise spectrum of the subcarrier reads

$$S_{\min}^{\text{cond}(2)}(\Omega) = \frac{1 + \left((\alpha_{\text{os}}^{(1)})^2 + (\alpha_{\text{os}}^{(2)})^2 \right) \frac{2 S_{\text{cl}}(\Omega)}{\hbar |R_{xx}(\Omega)|^2 \left((\Omega_{\text{os}}^{(1)})^2 - (\Omega_{\text{os}}^{(2)})^2 \right)}}{1 + \frac{2 (\alpha_{\text{os}}^{(1)})^2 S_{\text{cl}}(\Omega)}{\hbar |R_{xx}(\Omega)|^2 \left((\Omega_{\text{os}}^{(1)})^2 - (\Omega_{\text{os}}^{(2)})^2 \right)} + 2 (\alpha_{\text{os}}^{(2)})^2 e^{\text{arcsinh} \left((\alpha_{\text{os}}^{(1)})^2 + (\alpha_{\text{os}}^{(2)})^2 + \frac{S_{\text{cl}}(\Omega)}{2 \hbar |R_{xx}(\Omega)|^2 \left((\Omega_{\text{os}}^{(1)})^2 - (\Omega_{\text{os}}^{(2)})^2 \right)} \right)}}, \quad (2.79)$$

where the optimal detection angle becomes frequency-dependent and reads

$$\tan \zeta^{(2)} = -e^{-\text{arcsinh} \left((\alpha_{\text{os}}^{(1)})^2 + (\alpha_{\text{os}}^{(2)})^2 + \frac{S_{\text{cl}}(\Omega)}{2 \hbar |R_{xx}(\Omega)|^2 \left((\Omega_{\text{os}}^{(1)})^2 - (\Omega_{\text{os}}^{(2)})^2 \right)} \right)}. \quad (2.80)$$

Recall that the classical noise is suppressed with a larger difference in the two optomechanical resonance frequencies, which is completely the other way round compared to the strength of conditional squeezing. One therefore has to balance between high quantum squeezing and

high classical noise suppression. Fig. 24 compares the output squeezing of an unstable single and a stable double optical spring, both in the vicinity of frequency dependent classical noise as given in Fig. 23. Here only the dominating classical noise sources are considered at a level as it is expected for the experimental parameters given in Tab. 6 at room temperature [36]: the spectrum of the suspension thermal noise dominates at low frequencies and the one of the coating thermal noise at intermediate and high frequencies – both are combined in $S_{\text{cl}}(\Omega)$. For the configurations as plotted in Fig. 24 we have again made sure that the double

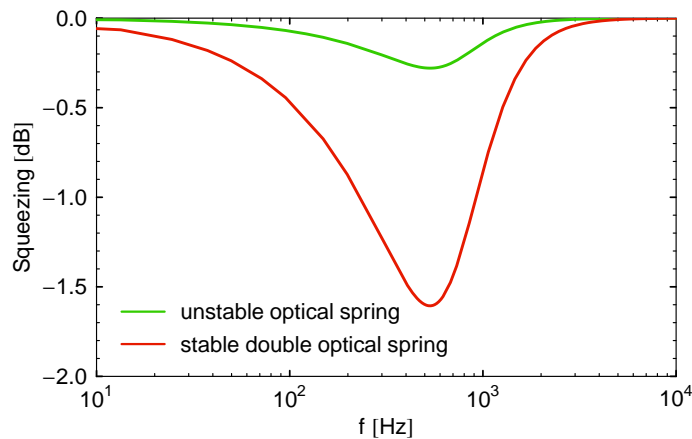


Figure 24: Single optical spring and conditional double optical spring (subcarrier conditioned on the carrier) output squeezing in the vicinity of classical noise as shown in Fig. 23. For the single optical spring the full carrier ($P_{\text{in}}^{(1)} = 3 \text{ W}$, $P_{\text{in}}^{(2)} = 0$) is injected into the cavity and detuned by $\Delta = 2\pi 38.5 \text{ kHz}$. The double optical spring has $\Delta^{(1)} = 2\pi 30 \text{ kHz}$ and $\Delta^{(2)} = -2\pi 5 \text{ kHz}$. All other parameters are taken from Tab. 6.

optical spring has the same total optomechanical resonance frequency as the single optical spring. For these two configurations the stable double optical spring still produces more ponderomotive squeezing than the unstable single optical spring. Due to the frequency dependence of the classical noise the output squeezing becomes also frequency dependent as shown in Fig. 24. But even though the classical noise dominates almost the entire noise spectrum, the stable double optical spring can produce remarkably strong ponderomotive output squeezing.

Note that we have not included the laser noise into our theoretical discussion. Technical laser noise will significantly perturb the production of the ponderomotive output squeezing from a single cavity. This is actually the limiting factor which has prevented the experimental setup from Ref. [35] to produce ponderomotive squeezing until now. But as we have already mentioned above, this problem could be circumvented by using a Michelson interferometer topology instead of a single cavity.

3 Part II: Macroscopic quantum mechanics

Since the foundation of quantum mechanics, people have been fascinated by the quantum mechanics of macroscopic and heavy objects. Initially, the considerations were confined to pure thought experiments as Erwin Schrödinger's famous gedanken experiment with the macroscopic cat that may be put into a quantum superposition [109]. But in the last years it has become more and more likely that quantum effects of macroscopic and heavy objects could be seen in real experiments. Especially in the gravitational-wave community, a big effort has been made in building very well-isolated macroscopic and heavy test masses, namely the end mirrors of large-scale laser interferometers used as prototypes as well as real detectors, in order to make them less susceptible to thermal noise. Even though the aim in this community is the lowering of the total noise arising in the detection of gravitational waves, the classical as well as the quantum noise, the detectors can also provide an ideal device to study the quantum mechanics of macroscopic objects as we will see in this chapter.

It seems to be a very good assumption to treat the center-of-mass position and momentum of a macroscopic mechanical oscillator always as being in Gaussian states. This is due to the fact that a macroscopic object is not a point mass but consists of many atoms which are of course bonded in a solid state but still can move which then can in turn influence the center of mass. Due to the well-known *central limit theorem* from mathematics, a large number of independent random processes will be approximately Gaussian. Nevertheless, under certain conditions also Gaussian states should be considered as quantum states and they can show quantum features such as squeezing and entanglement. If one identifies also a coherent laser

	massless particle	non-massless particle
microscopic object	single photon	single electron or atom
discrete variable	polarization	spin
macroscopic object	coherent laser beam	test-mass
continuous variables	amplitude and phase quadrature	position and momentum

Table 7: Comparison between the microscopic and the macroscopic world of massless and non-massless particles.

beam as a macroscopic object, we find a nice analogy between the microscopic world and the macroscopic world of massless and non-massless particles as shown in Tab. 7. Note that quantum states have been experimentally found in all cells of Tab. 7 except in the lower right one if the object is larger than a single molecule.

A macroscopic object is in close contact to its environment which is already unavoidable just because of its size and its high number of degrees of freedom. This coupling causes on the one hand dissipation and simultaneously fluctuations, as described by the well-known *dissipation-fluctuation theorem*. In the previous chapter we have sometimes completely neglected the coupling of the center-of-mass motion of the mirrors to any additional environment than the light. At most we have considered the mirrors coupled to a highly thermal bath, i.e. to classical noise sources such as the noise arising from the dissipation in the mirrors' suspension. But even at zero temperatures the free mirrors are still subject to a zero-point motion (cf. Sec. 1.3).

An experiment producing a macroscopic quantum state should be divided into different stages separated in time: a preparation stage, an optional free-evolution stage and a verification stage. During the preparation the test mass will be observed and either a conditional or a controlled state will be produced. This state could freely evolve for some time and should then be verified. Here one needs to collect statistics from a huge number of identical trials as it is required from quantum mechanics.

In this chapter we will start by recalling the theory of conditional states in Sec. 3.1. In Sec. 3.2 we will then discuss the preparation of conditional macroscopic quantum states in various situations. Afterwards, we will treat the problem of verifying such conditional quantum states in Sec. 3.3. In Sec. 3.4 we will consider the preparation of feedback-controlled macroscopic quantum states. Finally, we will investigate the generation of macroscopic entanglement in position and momentum between the two end mirrors of a Michelson interferometer in Sec. 3.5.

3.1 Conditional quantum states

The conventional way of describing the state of a quantum system undergoing a continuous quantum measurement is to construct a *stochastic master equation* [45, 57, 68, 86]. For a Gaussian system, which is totally characterized by its first- and second-order moments, the first-order moments of the state will totally depend on measurement results in the past and therefore, the state is called *a posteriori* [6] or *conditional* state. These first-order moments undergo a random walk in time as depicted in Fig. 25, while the covariance matrix of the second-order moments usually results in a so-called Riccati matrix differential equation. One can solve this equation for the second-order moments. It then turns out that the second-order moments reach a steady state in time if the system is stable. We will start this section by describing how to obtain such a stochastic master equation for an explicit example: the quantum measurement of a mirror's position with light.

If one is only interested in the steady state of the quantum system, a much simpler way of revealing the conditional state is by introducing *Wiener filtering* [131] in the context of Gaussian quantum systems, which, compared with the approach involving a stochastic master equation, allows us to determine the conditional state directly from the spectral densities of the system [90, 91]. Another advantage is that the Wiener filtering method is aimed directly at experimental efforts. By knowing the right Wiener filter, which has to be calculated assuming a certain model, one is able to extract the conditional quantum state from a set of measurement data as a kind of post-processing.

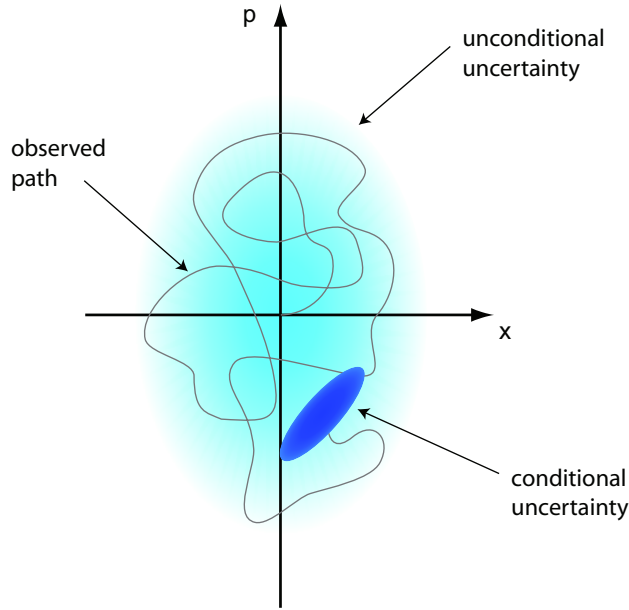


Figure 25: Illustrative picture of a conditional state. The path of the conditional first-order moments in phase-space is revealed by a measurement. The conditional second-order moments leave out some rest uncertainty described by squeezing ellipse (deep-blue). It is embedded in the large ellipse representing the unconditional uncertainty about the state.

After presenting the derivation of a concrete stochastic master equation, we will continue with recalling more generally the theory of Wiener filtering which is a well-known result from classical, linear optimal control theory. We will start with the one-dimensional Wiener filter and continue with the two-dimensional Wiener filter. We will need the two-dimensional Wiener filter whenever we have two independent measurement outputs on which we want to conditioning the measured state. Note that throughout this thesis, we will only use the Wiener filtering method in order to obtain our results about conditional states. We will not present how to obtain the steady state conditional variances from a stochastic master equation even though we have gone through the calculations.

3.1.1 Stochastic master equation

Let us again consider the Hamiltonian from Sec. 1.2.3 which describes an optical field in a cavity and the cavity's movable end mirror

$$\hat{H} = \hat{H}_M + \hat{H}_L + \hat{H}_I. \quad (3.1)$$

But for simplicity we will omit the cavity mode here because then the coupling between the mirror and the light simplifies to

$$\hat{H}_I = -\alpha \hat{x} \hat{a}_1 \quad (3.2)$$

with a coupling constant given by

$$\alpha = \sqrt{\frac{8 P \omega_0 \hbar}{c^2}}, \quad (3.3)$$

where P is the circulating laser power and ω_0 the laser angular frequency. Adiabatically eliminating the cavity mode is always possible if the cavity bandwidth is reasonably high. In Eq. (3.2), \hat{a}_1 denotes as usual the amplitude quadrature operator of the optical field and \hat{x} the position operator of the mirror. Different to what has been done in Sec. 1.2.3, we will treat the problem by setting up an equation for the density matrix operator of the system. In the interaction picture with respect to \hat{H}_L , the free time evolution of the optical field is suppressed, and the density matrix operator of the total system evolves as

$$\frac{d}{dt} \hat{\rho}(t) = -\frac{i}{\hbar} \left[\hat{H}_M, \hat{\rho}(t) \right] - \frac{i}{\hbar} \left[\hat{H}_I(t), \hat{\rho}(t) \right], \quad (3.4)$$

where $\hat{H}_I(t) = -\alpha \hat{x} \hat{a}_1(t)$. Suppose that at each time instant t the density matrix operator is disentangled in mirror and light system, i.e. $\hat{\rho}(t) = \hat{\rho}_M(t) \otimes \hat{\rho}_L$. This is true because at each time instant another light portion is incident on the mirror – remember that there is no cavity which could store the light. Then we can expand the solution to Eq. (3.4) for $\hat{\rho}$ at time $t + dt$ as

$$\begin{aligned} \hat{\rho}(t + dt) &= \hat{\rho}(t) - \frac{i}{\hbar} \left[\hat{H}_M, \hat{\rho}(t) \right] dt - \frac{i}{\hbar} \int_t^{t+dt} dt' \left[\hat{H}_I(t'), \hat{\rho}(t) \right] \\ &\quad + \left(-\frac{i}{\hbar} \right)^2 \int_t^{t+dt} dt' \int_t^{t+dt} dt'' \left[\hat{H}_I(t''), \left[\hat{H}_I(t'), \hat{\rho}(t) \right] \right] + \mathcal{O}(dt^2) \\ &= \hat{\rho}(t) - \frac{i}{\hbar} \left[\hat{H}_M, \hat{\rho}(t) \right] dt + \frac{i\alpha}{\hbar} \left[\hat{x} \hat{A}_1, \hat{\rho}(t) \right] \\ &\quad - \frac{\alpha^2}{2\hbar^2} \left[\hat{x} \hat{A}_1, \left[\hat{x} \hat{A}_1, \hat{\rho}(t) \right] \right] + \mathcal{O}(dt^2), \end{aligned} \quad (3.5)$$

where we have defined

$$\hat{A}_1 \equiv \int_t^{t+dt} dt' \hat{a}_1(t'). \quad (3.6)$$

Note that the second equality sign in Eq. (3.5) is justified when defining \hat{A}_1 as in Eq. (3.6), because of $[\hat{a}_1(t'), \hat{a}_1(t'')] = [\hat{x}, \hat{a}_1(t')] = 0$. Suppose that we perform a homodyne detection on the phase quadrature, the measurement-output operator is \hat{y} , if we define

$$\hat{y} \equiv \int_t^{t+dt} dt' \hat{a}_2(t'), \quad (3.7)$$

where \hat{a}_2 denotes the phase quadrature operator of the optical field. Note that we can easily extend this concept to the case when observing an arbitrary quadrature.

Now we project with the projection operator $\mathbb{1} \otimes \hat{P}_{y dt}$ the density matrix operator onto the space where the measurement-output operator takes the measured value ($y dt$). Every projection of that form disentangles the mirror system again from the light. Thus, we can partially trace over the optical field to obtain the conditional density matrix operator of the

system which is then given by

$$\begin{aligned} \hat{\rho}_M(t + dt | \hat{y} = y dt) \propto & \int_{-\infty}^{\infty} \frac{dk}{2\pi} e^{-ik y dt} \left(\langle e^{ik \hat{y}} \rangle \hat{\rho}_M(t) - \frac{i}{\hbar} \langle e^{ik \hat{y}} \rangle \left[\hat{H}_M, \hat{\rho}_M(t) \right] dt \right. \\ & - \frac{i\alpha}{\hbar} \left(\langle e^{ik \hat{y}} \hat{A}_1 \rangle \hat{x} \hat{\rho}_M(t) - \langle \hat{A}_1 e^{ik \hat{y}} \rangle \hat{\rho}_M(t) \hat{x} \right) \\ & - \frac{\alpha^2}{2\hbar^2} \left(\langle e^{ik \hat{y}} \hat{A}_1^2 \rangle \hat{x}^2 \hat{\rho}_M(t) - 2 \langle \hat{A}_1 e^{ik \hat{y}} \hat{A}_1 \rangle \hat{x} \hat{\rho}_M(t) \hat{x} + \langle \hat{A}_1^2 e^{ik \hat{y}} \rangle \hat{\rho}_M(t) \hat{x}^2 \right) \\ & \left. + \mathcal{O}(dt^2) \right). \end{aligned} \quad (3.8)$$

With the commutation relation $[\hat{a}_1(t), \hat{a}_2(t')] = i \delta(t - t')$ we obtain $\langle [\hat{A}_1, \hat{y}] \rangle = i dt$ and when we assume the following Gaussian first- and second-order moments for the optical field

$$\langle \hat{A}_1 \rangle = \langle \hat{y} \rangle = 0 \quad \text{and} \quad \langle \hat{A}_1^2 \rangle = \langle \hat{y}^2 \rangle = dt/2, \quad (3.9)$$

we obtain

$$\begin{aligned} \hat{\rho}_M(t + dt | \hat{y} = y dt) \propto & \frac{e^{-(y dt)^2/dt}}{\sqrt{\pi dt}} \left(\hat{\rho}_M(t) - \frac{i}{\hbar} \left[\hat{H}_M, \hat{\rho}_M(t) \right] dt - \frac{\alpha}{\hbar} \{ \hat{x}, \hat{\rho}_M(t) \} y dt \right. \\ & \left. - \frac{\alpha^2}{2\hbar^2} \left((\hat{x}^2 \hat{\rho}_M(t) + \hat{\rho}_M(t) \hat{x}^2) (dt - (y dt)^2) - 2 \hat{x} \hat{\rho}_M(t) \hat{x} (y dt)^2 \right) \right). \end{aligned} \quad (3.10)$$

In order to obtain the probability density of $(y dt)$, we have to trace over the mirror system

$$\mathcal{P}(y dt) = \frac{e^{-(y dt)^2/dt}}{\sqrt{\pi dt}} \left(1 - 2 \frac{\alpha}{\hbar} \langle \hat{x} \rangle y dt - \frac{\alpha^2}{2\hbar^2} \langle \hat{x}^2 \rangle (2 dt - 4 (y dt)^2) \right). \quad (3.11)$$

Therefore, we have

$$\langle y dt \rangle = \frac{\alpha}{\hbar} \langle \hat{x} \rangle dt \quad \text{and} \quad \langle (y dt)^2 \rangle = \frac{dt}{2} + \mathcal{O}(dt^2). \quad (3.12)$$

Basically, this means that we can write

$$y dt = \frac{\alpha}{\hbar} \langle \hat{x} \rangle dt + dW/\sqrt{2}, \quad (3.13)$$

where $dW^2 = dt$ is called Wiener increment. Normalizing Eq. (3.10) with Eq. (3.11) and expanding up to linear order in dt , we obtain the conditional covariance matrix (cf. e.g. Refs. [57, 86])

$$\begin{aligned} \hat{\rho}_M^{\text{cond}}(t + dt) = & \hat{\rho}_M(t) - \frac{i}{\hbar} \left[\hat{H}_M, \hat{\rho}_M(t) \right] dt - \frac{\alpha^2}{4\hbar^2} [\hat{x}, [\hat{x}, \hat{\rho}_M(t)]] dt \\ & + \frac{\alpha}{\sqrt{2}\hbar} (\{ \hat{x}, \hat{\rho}_M \} - 2 \langle \hat{x} \rangle \hat{\rho}_M) dW. \end{aligned} \quad (3.14)$$

The third term on the right hand side of Eq. (3.14) describes the well-known back action of the measurement, while the last term, which actually is of stochastic nature, gives rise to conditioning the state onto the measurement result.

At this stage we will stop even though we have not obtained the conditional variances yet. Note that as a good exercise we have actually gone through the whole calculation of constructing as well as solving the Riccati matrix differential equation for the conditional covariance matrix in position and momentum from Eq. (3.14). This Riccati matrix differential equation as well as its solution can be found in Ref. [45]. One can imagine that the stochastic master equation method becomes much more complicated when analyzing more complex measurement devices. Remember that we usually already know the equations of motion in the frequency domain and that we are usually only interested in the steady state solution of the conditional variances. This leads to a much more convenient method which we will describe in the following.

3.1.2 Wiener filtering

Let us assume that we already know the equations of motion describing the measured system as well as the one of the quantum measurement process. Then we generally define $\hat{y}(t)$ to be the Heisenberg operator of any linear quantum measurement output and $\hat{x}(t)$ and $\hat{p}(t)$ the Heisenberg operators of position and momentum, respectively, of the system being measured. What we want to do is to use the knowledge obtained from the measurement results or, in other words, we want to estimate $\langle \hat{x}(t) \rangle^{\text{cond}}$ and $\langle \hat{p}(t) \rangle^{\text{cond}}$ using the output data of $\hat{y}(t)$ which, in terms of classical dynamics, is a very common problem in engineering. In order to reconstruct the quantum-mechanical operators $\hat{x}(t)$, $\hat{p}(t)$ by linearly filtering the operator $\hat{y}(t)$ with the demand of giving the best estimation, we have to make sure that the commutation relations

$$0 = [\hat{y}(t), \hat{y}(t')] \quad \forall t, t' \quad \text{and} \quad (3.15)$$

$$0 = [\hat{x}(t), \hat{y}(t')] = [\hat{p}(t), \hat{y}(t')] \quad \forall t > t' \quad (3.16)$$

hold. Usually we are saved, since Eq. (3.15) is satisfied by all *simultaneously measurable* variables such as the output of any quantum measurement device [23], while Eq. (3.16) has to be satisfied due to *causality*: the measurement-output operator should of course be not influenced by any future system observable. This means that all $\hat{y}(t')$ for $0 < t' < t$ can be regarded as classical quantities, as long as we consider the state of the system at time t .

The optimal filter function for the displacement $K_x(t)$ is determined by the condition that the quantity

$$\hat{R}_x(t) \equiv \hat{x}(t) - \int_{-\infty}^t dt' K_x(t-t') \hat{y}(t') \quad (3.17)$$

must be uncorrelated with the past output, i.e. $\langle \hat{R}_x(t) \hat{y}(t') \rangle = 0$ for all $t' < t$. Please do not confuse $\hat{R}_x(t)$ with the frequency-domain susceptibility $R_{xx}(\Omega)$. After rearranging, Eq. (3.17) can also be understood in the way that we split $\hat{x}(t)$ into two independent parts, where one of them reveals what we know about $\hat{x}(t)$ from the measurement result, while $\hat{R}_x(t)$ denotes the unknown content of $\hat{x}(t)$, which is not accessible by the measurement. Inserting Eq. (3.17) into $\langle \hat{R}_x(t) \hat{y}(t') \rangle = 0$ leads to the Wiener-Hopf equation which can be found in many textbooks on classical linear optimal control theory (cf. e.g. Refs. [94,97,98]) and which reads

$$C_{xy}(t-t'') - \int_{-\infty}^t dt' K_x(t-t') C_{yy}(t'-t'') = 0 \quad \forall t'' \leq t. \quad (3.18)$$

Here $C_{xy}(t-t')$ and $C_{yy}(t-t')$ stand for the (symmetric) time-domain, two-point correlation functions (cf. Tab. 1) between two Heisenberg operators. If we suppose that $K_x(t) = 0$ for $t < 0$, which makes sure that the filter is a causal function, we can rewrite Eq. (3.18) as

$$C_{xy}(t) - \int_{-\infty}^{\infty} dt' K_x(t') C_{yy}(t-t') = 0 \quad \forall t \geq 0. \quad (3.19)$$

In the frequency domain the condition Eq. (3.19) is satisfied if the function

$$L(\Omega) = S_{xy}(\Omega) - K_x(\Omega) S_{yy}(\Omega) \quad (3.20)$$

is analytic in the lower-half complex plane while the Fourier transform of the filter function $K_x(\Omega)$ is analytic in the upper-half complex plane. Furthermore, $L(\Omega)$ has to vanish at plus and minus infinity. We have denoted with $S_{xy}(\Omega)$ and $S_{yy}(\Omega)$ the single-sided (cross-) spectral density (cf. Tab. 1) among the two operators \hat{x} and \hat{y} . The obvious solution for $K_x(\Omega)$ is given by

$$K_x(\Omega) = \frac{1}{s_y^+(\Omega)} \left[\frac{S_{xy}(\Omega)}{s_y^-(\Omega)} \right]_+, \quad (3.21)$$

where we have split $S_{yy}(\Omega) = s_y^+(\Omega) s_y^-(\Omega)$ in such a way that $s_y^+(\Omega)$ and its inverse are analytic functions in the upper-half complex plane while $s_y^-(\Omega)$ and its inverse are analytic functions in the lower-half complex plane. Note that $[\dots]_+$ stands for taking the component of a function whose inverse Fourier transform has support only in positive times. Operationally, this could be realized by keeping only terms of the function's partial fraction expansion whose poles have negative imaginary parts. Note that the decomposition of a function into $[\dots]_- + [\dots]_+$ is only unique up to a polynomial in Ω . But the condition that $L(\Omega)$ has to vanish at plus and minus infinity uniquely defines $K_x(\Omega)$ in Eq. (3.21). Back in the time domain, this provides the causal Wiener filter function [131] for the position which is then given by

$$K_x(t-t') = \int_{-\infty}^{\infty} \frac{d\Omega}{2\pi} \frac{1}{s_y^+(\Omega)} \left[\frac{S_{xy}(\Omega)}{s_y^-(\Omega)} \right]_+ e^{-i\Omega(t-t')}. \quad (3.22)$$

Analogously we find the optimal filter function, i.e. the causal Wiener filter function, for the momentum by exchanging x with p .

Let us assume that we are in the steady state where \hat{x} and \hat{p} both have unconditionally zero mean values. As we have motivated in the appendix of Ref. [90], the first-order moments of the conditional state are totally determined by the measurement results and can be written as

$$\langle \hat{x}(t) \rangle^{\text{cond}} = \int_{-\infty}^t dt' K_x(t-t') y(t'), \quad (3.23)$$

$$\langle \hat{p}(t) \rangle^{\text{cond}} = \int_{-\infty}^t dt' K_p(t-t') y(t'), \quad (3.24)$$

where $y(t)$ is the measurement result of $\hat{y}(t)$ at each time instant. Furthermore, we have shown in the appendix of Ref. [90] that the conditional second-order moments depend only on the operators which are uncorrelated with the measurement-output operator, since they

correspond to the remaining fluctuations if taking the measurement result into account. This fact reads

$$V_{xx}^{\text{cond}} = \langle (\hat{x}(t))^2 \rangle^{\text{cond}} - (\langle \hat{x}(t) \rangle^{\text{cond}})^2 = \langle \hat{R}_x(t) \hat{R}_x(t) \rangle, \quad (3.25)$$

$$V_{pp}^{\text{cond}} = \langle \hat{p}^2 \rangle^{\text{cond}} - (\langle \hat{p} \rangle^{\text{cond}})^2 = \langle \hat{R}_p(t) \hat{R}_p(t) \rangle, \quad (3.26)$$

$$\begin{aligned} V_{xp}^{\text{cond}} &= \frac{1}{2} \langle \hat{x}(t) \hat{p}(t) + \hat{p}(t) \hat{x}(t) \rangle^{\text{cond}} - \langle \hat{x}(t) \rangle^{\text{cond}} \langle \hat{p}(t) \rangle^{\text{cond}} \\ &= \frac{1}{2} \langle \hat{R}_x(t) \hat{R}_p(t) + \hat{R}_p(t) \hat{R}_x(t) \rangle. \end{aligned} \quad (3.27)$$

Because the measurement output spectrum $S_{yy}(\Omega)$ is in general a rational function of Ω^2 with real coefficients, we can further use the fact that $s_y^-(\Omega) = (s_y^+)^*(\Omega)$. Then together with Eq. (3.17) and with Eq. (3.21), we can derive the conditional second-order moments to result in

$$\begin{aligned} V_{xx}^{\text{cond}} &= \int_0^\infty \frac{d\Omega}{2\pi} (S_{xx}(\Omega) - 2K_{\hat{x}}(\Omega) S_{xy}^*(\Omega) + K_{\hat{x}}(\Omega) K_{\hat{x}}^*(\Omega) S_{yy}(\Omega)) \\ &= \int_0^\infty \frac{d\Omega}{2\pi} \left(S_{xx}(\Omega) - \left[\frac{S_{xy}}{s_y^-} \right]_+ \left[\frac{S_{xy}}{s_y^-} \right]_+^* \right), \end{aligned} \quad (3.28)$$

and similarly we find

$$V_{pp}^{\text{cond}} = \int_0^\infty \frac{d\Omega}{2\pi} \left(S_{pp}(\Omega) - \left[\frac{S_{py}}{s_y^-} \right]_+ \left[\frac{S_{py}}{s_y^-} \right]_+^* \right), \quad (3.29)$$

$$V_{xp}^{\text{cond}} = \int_0^\infty \frac{d\Omega}{2\pi} \Re \left\{ S_{xp}(\Omega) - \left[\frac{S_{xy}}{s_y^-} \right]_+ \left[\frac{S_{py}}{s_y^-} \right]_+^* \right\}. \quad (3.30)$$

Now we are in principle able to deduce the conditional variances from the spectral densities $S_{yy}(\Omega)$, $S_{xy}(\Omega)$ and $S_{py}(\Omega)$ obtained from real measurement data together with the predicted spectral densities $S_{xx}(\Omega)$ and $S_{pp}(\Omega)$ from the theory.

We can see that the conditional variances in Eqs. (3.28)–(3.30) are actually composed of the unconditional variance from which a certain contribution due to the observation is subtracted. This contribution depends on the correlation between the measured quantity and the measurement output operator. Note that the unconditional cross-variance V_{xp} always vanishes because $\Re \{S_{xp}(\Omega)\} = 0$. Furthermore, it is probably worth mentioning that, as we can see from Eqs. (3.28)–(3.30), the conditional variances are invariant under multiplying the measurement output operator \hat{y} by any constant real factor.

Note that we have written a package for the commercial software *Mathematica*[®] in order to numerically calculate conditional states resulting from any noise spectrum consisting of broken-rational functions in Ω^2 . The package numerically calculates the lists of zeros and poles of the spectra and derives by only modifying these lists the conditional variances. Therefore the routine is quite fast, even for long lists of poles and zeros.

In the following sections we will mostly consider conditional states and will therefore omit the superscript 'cond' for the sake of convenience unless it can cause confusions.

3.1.3 Two-dimensional Wiener filter

Imagine that two or even more independent linear quantum measurements are made on one and the same object. In this case the conditional state depends on all measurement outputs. Let us restrict the discussion to the two-dimensional case. Then Eq. (3.17) becomes

$$\hat{R}_x(t) \equiv \hat{x}(t) - \int_{-\infty}^t dt' \vec{K}_x^T(t-t') \vec{y}(t'), \quad (3.31)$$

where the vector $\vec{y}^T(t) = (\hat{y}_1(t), \hat{y}_2(t))$ is composed of the two measurement-output operators and the optimal filter functions corresponding to these outputs are gathered in $\vec{K}_x(t)$. Now the condition that $\langle \hat{R}_x(t) \hat{y}_i(t') \rangle = 0$ for all $t' < t$ and $i = 1, 2$ results in a Wiener-Hopf matrix equation which in turn requires that both entries of the vector function

$$\vec{L}(\Omega) = \begin{pmatrix} S_{xy_1}(\Omega) \\ S_{xy_2}(\Omega) \end{pmatrix} - \underbrace{\begin{pmatrix} S_{y_1y_1}(\Omega) & S_{y_2y_1}(\Omega) \\ S_{y_1y_2}(\Omega) & S_{y_2y_2}(\Omega) \end{pmatrix}}_{\mathbf{S}_{yy}} \begin{pmatrix} K_x^{(1)}(\Omega) \\ K_x^{(2)}(\Omega) \end{pmatrix} \quad (3.32)$$

are analytic in the lower-half complex plane and vanish at plus and minus infinity. The aim is to factorize the rational matrix $\mathbf{S}_{yy} = \Phi_- \Phi_+$ which can certainly be achieved, as we have eventually realized, using the method of symmetric factors extraction, suggested by Davis in Ref. [44]. But here we will not go into the details of the Davis factorization. Having obtained this factorization, the vector of optimal filter function is given by

$$\begin{pmatrix} K_x^{(1)}(\Omega) \\ K_x^{(2)}(\Omega) \end{pmatrix} = \Phi_+^{-1} \left[\Phi_-^{-1} \begin{pmatrix} S_{xy_1}(\Omega) \\ S_{xy_2}(\Omega) \end{pmatrix} \right]_+ . \quad (3.33)$$

We have written another *Mathematica*[®] package which numerically Davis-factorizes rational matrices and then numerically calculates the conditional second-order moments of a double measured system. This two-dimensional concept can easily be extended to the case with more dimensions.

3.2 Preparation of conditional macroscopic quantum states using the Wiener filter

We will start our discussion about the preparation of a conditional quantum state of a macroscopic and heavy object under continuous measurement with a very general treatment. Then we will specify more and more to concrete examples: *(i)* measuring the position of the end mirror of a cavity with infinitely large bandwidth which is theoretically equivalent to measuring the differential motion between the end mirrors of a simple Michelson interferometer which is totally balanced in arm length as well as in end mirror weight; *(ii)* measuring the position of the end mirror of a cavity with finite bandwidth which is equivalent to measuring the differential motion between the end mirrors of a Michelson interferometer with arm cavities; *(iii)* measuring the position of the end mirror of a detuned cavity which is equivalent to measuring the differential motion between the end mirrors of a Michelson interferometer with arm cavities and detuned signal-recycling; *(iv)* and finally measuring the differential motion between the mirrors of a speed meter.

3.2.1 General linear Markovian measurement process

Let us start our discussion as promised generally with an abstract continuous linear Markovian measurement process, which monitors the position of a simple harmonic oscillator [42, 90]. The Heisenberg equations of motion in the frequency domain can be written as

$$\hat{y} = \hat{Z} + \hat{x}, \quad (3.34)$$

$$\hat{x} = R_{xx}(\Omega) \hat{F}, \quad (3.35)$$

where the two measurement noise operators \hat{Z} and \hat{F} have both a white spectrum. This accounts for the Markovian measurement process: \hat{Z} and \hat{F} in the time domain are subject to a stochastic first order Markov-chain, where at each time instant, they are independent of their entire history. We assume that \hat{Z} and \hat{F} have the single-sided (cross-) spectral densities $S_{ZZ} \geq 0$, $S_{FF} \geq 0$ and S_{ZF} , which are supposed to be real constants satisfying the Heisenberg relation of the measurement process [18]

$$S_{ZZ}S_{FF} - S_{ZF}^2 \geq \hbar^2, \quad (3.36)$$

which is imposed by the measurement's back action. If the measurement process is pure, which turns the inequality sign in Eq. (3.36) for the measurement noise into an equal sign, i.e. $S_{ZZ}^q S_{FF}^q - (S_{ZF}^q)^2 \equiv \hbar^2$, we call it a *quantum measurement process*. Note that the two noise operators \hat{Z} and \hat{F} , may also contain additional noise that does not directly come from the operators \hat{Z} and \hat{F} . In Eq. (3.34), \hat{y} denotes the measurement-output operator and \hat{x} is the quantity being measured. Recall that the mechanical susceptibility of a damped harmonic oscillator is given by

$$R_{xx}(\Omega) = -\frac{1}{m(\Omega^2 + i\gamma_m\Omega - \omega_m^2)}, \quad (3.37)$$

with the eigenfrequency ω_m , the damping rate $\gamma_m \ll \omega_m$ and the mass m . Note that if $\gamma_m \neq 0$, S_{FF} has to contain at least the zero-point fluctuations of the oscillator (cf. Sec. 1.3) in addition to the noise coming from the measurement. Then we can easily assemble the single-sided spectral densities of the measurement process as

$$\begin{aligned} S_{yy}(\Omega) &= S_{ZZ} + 2\Re\{R_{xx}(\Omega)\} S_{ZF} + |R_{xx}(\Omega)|^2 S_{FF} \\ &\equiv m^2 |R_{xx}(\Omega)|^2 \left(\Omega^4 - 2\left(q_1 - \frac{\gamma_m^2}{2}\right)\Omega^2 + q_2^2 \right) S_{ZZ}, \end{aligned} \quad (3.38)$$

$$\begin{aligned} S_{xy}(\Omega) &= |R_{xx}(\Omega)|^2 S_{FF} + R_{xx}(\Omega) S_{ZF} \\ &= -m |R_{xx}(\Omega)|^2 \left(\Omega^2 - i\gamma_m\Omega - \omega_m^2 - \frac{S_{FF}}{S_{ZF}} \right) S_{ZF}, \end{aligned} \quad (3.39)$$

$$S_{xx}(\Omega) = |R_{xx}(\Omega)|^2 S_{FF}, \quad (3.40)$$

where we have defined the coefficients

$$q_1 \equiv \omega_m^2 + \frac{S_{ZF}}{m S_{ZZ}}, \quad (3.41)$$

$$q_2 \equiv \sqrt{\omega_m^4 + 2\omega_m^2 \frac{S_{ZF}}{m S_{ZZ}} + \frac{S_{FF}}{m^2 S_{ZZ}}}. \quad (3.42)$$

Note that we always have $q_2^2 \geq 0$, i.e. q_2 is a positive real number, since the two coefficients fulfil

$$q_2^2 - q_1^2 = \frac{S_{ZZ}S_{FF} - S_{ZF}^2}{m^2 S_{ZZ}^2} \geq \frac{\hbar^2}{m^2 S_{ZZ}^2} \geq 0, \quad (3.43)$$

which implies that $q_2 \geq |q_1|$. From Eq. (3.38) we can recover a quantum limit of the measurement process: if we have $S_{ZF} = 0$ and use Eq. (3.36), the spectral density of the measurement noise is restricted to

$$\begin{aligned} S_{yy}(\Omega) &= S_{ZZ} + |R_{xx}(\Omega)|^2 S_{FF} \geq 2 |R_{xx}(\Omega)| \sqrt{S_{ZZ} S_{FF}} \\ &\geq 2 \hbar |R_{xx}(\Omega)| \equiv S^{\text{SQL}}(\Omega). \end{aligned} \quad (3.44)$$

Compare the right hand side of Eq. (3.44) – when we have $|R_{xx}(\Omega)| = 1/(m\Omega^2)$ for a free mass and $S_{ZZ} S_{FF} = S_{ZZ}^q S_{FF}^q \equiv \hbar$ for a pure measurement – with the free mass standard quantum limit in Eq. (1.17). Note that for the free mass the first inequality sign in Eq. (3.44) becomes an equality sign at $\Omega = \Omega_q$, where the measurement frequency is defined by

$$\Omega_q^2 \equiv \sqrt{\frac{S_{FF}^q}{m^2 S_{ZZ}^q}}. \quad (3.45)$$

Therefore, the measurement frequency Ω_q is by definition the frequency at which the noise spectral density of any Markovian quantum measurement process with no correlation in \hat{Z} and \hat{F} touches its free mass standard quantum limit, i.e. $S_{yy}(\Omega_q) = S^{\text{SQL}}(\Omega_q) = 2 S_{ZZ}^q$.

Now it is straightforward to derive the conditional variances assuming $\hat{p} = -i m \Omega \hat{x}$ and using the Wiener filter method as explained in Sec. 3.1.2. For this it has actually been crucial to first spectral factorize $S_{yy}(\Omega)$ as done in Eq. (3.38). Then we need to insert the spectral densities from Eqs. (3.38)–(3.40) into Eqs. (3.28)–(3.30) and evaluate the integrals. Here we require that $S_{ZF} > 0$ or at least $S_{FF} S_{ZZ} - S_{ZF}^2 > \gamma_m^2 m^2 S_{ZZ}^2$ ($\gamma_m^2/4 - \omega_m^2 - S_{ZF}/(m S_{ZZ})$). Then after several cumbersome calculational steps, we finally obtain the conditional variances which read

$$V_{xx} = \frac{S_{ZZ}}{\sqrt{2}} \left(\sqrt{q_2 - q_1 + \frac{\gamma_m^2}{2}} - \frac{\gamma_m}{\sqrt{2}} \right), \quad (3.46)$$

$$V_{pp} = m^2 \frac{S_{ZZ}}{\sqrt{2}} \left((q_2 + \gamma_m^2) \left(\sqrt{q_2 - q_1 + \frac{\gamma_m^2}{2}} - \frac{\gamma_m}{\sqrt{2}} \right) - (q_2 - q_1) \frac{\gamma_m}{\sqrt{2}} \right), \quad (3.47)$$

$$V_{xp} = m \frac{S_{ZZ}}{2} \left(\sqrt{q_2 - q_1 + \frac{\gamma_m^2}{2}} - \frac{\gamma_m}{\sqrt{2}} \right)^2. \quad (3.48)$$

Remember that these expressions are only valid in the weak-coupling regime, i.e. for $\gamma_m \ll \omega_m$. When the oscillator is coupled strongly to the thermal bath at such low temperatures where $k_B T$ is of the order of \hbar , the zero-point fluctuations of the oscillator become non-Markovian and turn S_{FF} into a frequency-dependent function. We can actually see when our formulation within the weak-coupling approximation breaks down: exactly when the

uncertainty product which is given by

$$\begin{aligned}
V_{xx} V_{pp} - V_{xp}^2 &= \frac{S_{FF} S_{ZZ} - S_{ZF}^2}{4} \frac{\sqrt{q_2 - q_1 + \frac{\gamma_m^2}{2}} - \frac{\gamma_m}{\sqrt{2}}}{\sqrt{q_2 - q_1 + \frac{\gamma_m^2}{2}} + \frac{\gamma_m}{\sqrt{2}}} \\
&\geq \left(\frac{\hbar^2}{4} + S_{ZZ} \underbrace{m \gamma_m \hbar \omega_m}_{\text{from Eq. (1.78)}} \right) \frac{\sqrt{q_2 - q_1 + \frac{\gamma_m^2}{2}} - \frac{\gamma_m}{\sqrt{2}}}{\sqrt{q_2 - q_1 + \frac{\gamma_m^2}{2}} + \frac{\gamma_m}{\sqrt{2}}}, \quad (3.49)
\end{aligned}$$

becomes for a certain γ_m smaller than the Heisenberg uncertainty principle allows.

In the perfect oscillator limit with $\gamma_m \rightarrow 0$, the Heisenberg uncertainty principle is always satisfied and the conditional covariance matrix is totally determined in terms of (S_{ZZ}, q_1, q_2, m) and we can put it into the following form

$$\mathbf{V} \equiv \begin{pmatrix} V_{xx} & V_{xp} \\ V_{xp} & V_{pp} \end{pmatrix} = m S_{ZZ} \frac{\sqrt{q_2^2 - q_1^2}}{2} \mathbf{D} \begin{pmatrix} \sqrt{\frac{2q_2}{q_1+q_2}} & \sqrt{\frac{q_2-q_1}{q_2+q_1}} \\ \sqrt{\frac{q_2-q_1}{q_2+q_1}} & \sqrt{\frac{2q_2}{q_1+q_2}} \end{pmatrix} \mathbf{D}^T, \quad (3.50)$$

where we have defined the matrix $\mathbf{D} = \text{diag}(1/\sqrt{m\sqrt{q_2}}, \sqrt{m\sqrt{q_2}})$. Note that Eq. (3.50) gives us now the most general covariance matrix of the conditional Gaussian state of a lossless harmonic oscillator under any linear Markovian position measurement. The form of that covariance matrix in Eq. (3.50) is reminiscent of an oscillator at an eigenfrequency represented by $\sqrt{q_2}$, where the matrix \mathbf{D} is then basically responsible for the re-scaling in that eigenfrequency. Here $\sqrt{q_2}$ actually coincides with ω_{eff} as defined in Eq. (1.8) if the conditional variances in position and momentum are considered. From Eq. (3.41) we can deduce that $\sqrt{q_2}$ is indeed equal to the shifted mechanical eigenfrequency and in the case of no correlation in \hat{Z} and \hat{F} , it even simplifies to $\omega_{\text{eff}} = \sqrt{q_2} = \omega_m \sqrt[4]{1 + \Omega_q^4/\omega_m^4}$.

Recall from Sec. 1.1 that a Gaussian state is pure if and only if its uncertainty product is Heisenberg-limited, i.e. for $\det \mathbf{V} = V_{xx} V_{pp} - V_{xp}^2 = \hbar^2/4$. In that section we have also argued why it makes sense to quantify the purity of the conditional state by its uncertainty product, here given by

$$\det \mathbf{V} = m^2 S_{ZZ}^2 \frac{q_2^2 - q_1^2}{4} = \frac{S_{FF} S_{ZZ} - S_{ZF}^2}{4} \geq \frac{\hbar^2}{4}, \quad (3.51)$$

which – as it has turned out when using the relation of Eq. (3.43) to produce the second equal sign in Eq. (3.51) – is identical to the purity of the measurement process. This simply shows that in the Markovian case, any measurement will produce a pure conditional state of a lossless harmonic oscillator if and only if it is a quantum measurement – that means that the measurement process has to be pure itself.

The covariance matrix in Eq. (3.50) becomes obviously diagonal and the correlation between \hat{x} and \hat{p} in the conditional state vanishes if and only if $q_1 = q_2$. But this is strictly forbidden due to the Heisenberg uncertainty principle as given in Eq. (3.51). The correlation in \hat{x} and \hat{p} increases – and in turn also the uncertainty product – with a higher difference in q_1 and q_2 . If we consider again the case of no correlation in \hat{Z} and \hat{F} , the difference in q_1

and q_2 is equal to the difference between the mechanical eigenfrequency and the new shifted mechanical eigenfrequency.

In order to realize the conditional state, as given in Eq. (3.50), the measurement data has to be filtered using the Wiener filter functions for position and momentum which are given in the frequency domain by

$$K_x(\Omega) = \sqrt{2} i \sqrt{q_2 - q_1} \frac{\Omega - \Omega_3}{(\Omega - \Omega_1)(\Omega - \Omega_2)}, \quad (3.52)$$

$$K_p(\Omega) = i m (q_2 - \omega_m^2) \frac{\Omega + \omega_m^2/\Omega_3}{(\Omega - \Omega_1)(\Omega - \Omega_2)}, \quad (3.53)$$

where $\Omega_{1,2} = (\pm\sqrt{q_2 + q_1} - i\sqrt{q_2 - q_1})/\sqrt{2}$ and $\Omega_3 = i/\sqrt{2}(\omega_m^2 - q_2)/\sqrt{q_2 - q_1}$. Note that the poles of the Wiener filter $\Omega_{1,2}$ are actually equal to the zeros of the measurement's output spectrum $S_{yy}(\Omega)$, which in turn correspond to the frequencies of maximal sensitivity and are therefore easy to find. Interestingly, we can find the relation $|\Omega_{1,2}| = \sqrt{q_2} = \omega_{\text{eff}}$, where ω_{eff} , as given in Eq. (1.8), minimizes the effective occupation number which can be obtained from the conditional variances.

3.2.2 Quantum measurement noise versus classical noise

Let us now have a closer look at the noise model which we will use throughout this chapter.

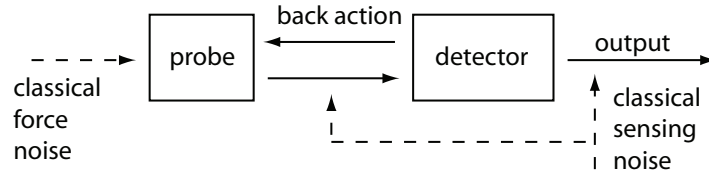


Figure 26: Schematic block diagram of a linear quantum measurement process. It is illustrated where the two different classical noise sources can couple into the measurement process. The probe could more concretely be the center-of-mass position of a test mass while the detector could consist of a coherent laser beam.

Note that from now on we will only consider quantum measurement processes. Generally, we will then categorize the noise of the quantum measurement process into two groups: (i) the one which is a result of the measurement process itself and is therefore pure, i.e. satisfies $S_{ZZ}^q S_{FF}^q - (S_{ZF}^q)^2 = \hbar^2$, will be denoted by *quantum noise*; and (ii) the noise on top of this quantum noise will be called *classical noise* which does not directly come from the measurement process (cf. Fig 26), usually has no correlation in \hat{Z} and \hat{F} , i.e. $S_{ZF}^{\text{cl}} = 0$, does not have to satisfy Eq. (3.36) and could further have $S_{FF}^{\text{cl}}, S_{xx}^{\text{cl}} \gg \hbar$. Then the two noise sources combine as $S_{FF} = S_{FF}^q + S_{FF}^{\text{cl}}$ and $S_{ZZ} = S_{ZZ}^q + S_{ZZ}^{\text{cl}}$.

As we know from Sec. 1.1, the noise of a quantum measurement – for instance with light – is dominated at high frequencies by shot noise which is covered by S_{ZZ}^q and at low frequencies by back-action noise which is covered by S_{FF}^q . The latter one is represented by the radiation-pressure noise in the case of a measurement with light. If both are uncorrelated, i.e. $S_{ZF}^q = 0$, they result in the standard quantum limit. Then the quantum noise spectral density $S^q(\Omega) = S_{ZZ}^q + |R_{xx}(\Omega)| S_{FF}^q$ (cf. Fig. 27) – describing the sensitivity of the measurement –

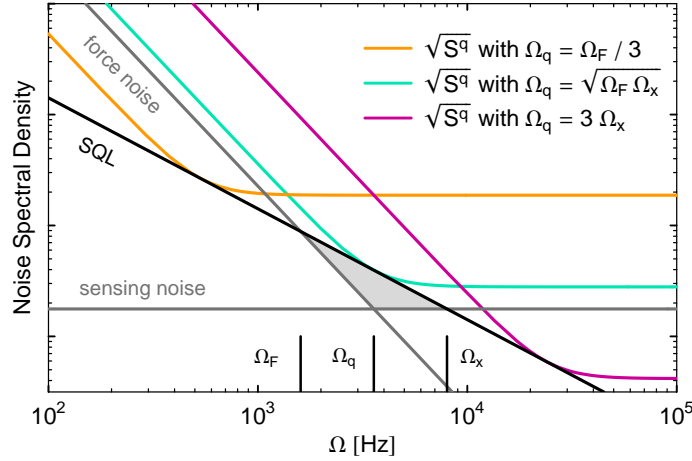


Figure 27: Example noise spectral densities (in arbitrary units) of a Markovian measurement process observing a free mass: the quantum noise spectral density (colored curves) with $S_{ZZ}^q S_{FF}^q = \hbar$ and $S_{ZF}^q = 0$ at different values of the measurement frequency Ω_q ; the free-mass standard quantum limit (black line) is denoted by SQL; as well as the spectral densities corresponding to a classical force noise (gray line) and a sensing noise (gray line) are marked in the plot. The gray shadowed region marks the classical noise standard quantum limit beating which we have chosen to have $\Omega_x/\Omega_F = 5$.

is limited from below by the free-mass standard quantum limit as shown in Eq. (3.44) and also in Fig. 27. The quantum noise touches the free-mass standard quantum limit at the frequency $\Omega = \Omega_q$ as defined in Eq. (3.45).

The other noise sources which usually have a classical origin can also be divided into two parts: a *classical force noise* S_{FF}^{cl} is added to S_{FF} which acts directly on the center of mass of the measured object, and is in real interferometric experiments due to for instance seismic noise or thermal noise in the suspension of the mirrors. The *classical sensing noise* S_{ZZ}^{cl} is only a pseudo motion of the measured object and may be due to the following reasons: (i) on the one hand due to thermal fluctuations of the mirror's shape as for example mirror internal thermal noise which makes only the mirror surface move with respect to its center of mass; or (ii) on the other hand be due to optical losses; or (iii) due to photo-detection inefficiency. Therefore, our sensing noise is somehow generalized from what is conventionally understood when using the term 'sensing noise'. Note that in the theoretical analysis of the sensitivity of gravitational-wave detectors – as we have dealt with in the first part of this thesis – there is usually no need to distinguish between the two classical noise sources, the force and the sensing noise. Moreover, in principle we did not need to distinguish even between quantum and classical noise. All of them are just noise sources which complicate the detection of gravitational waves. But in this part, where we consider conditional macroscopic quantum states, there is a strong need to distinguish between them because they are all differently integrated into these conditional states. It might even be misleading to call them 'noise' although we will do it due to historical reasons.

Throughout this second part we will assume both classical noise sources to have a white spectrum, that means that S_{FF}^{cl} and S_{ZZ}^{cl} are a constant with respect to the sideband frequency. Then they can be characterized by the frequencies, Ω_F for the force noise and Ω_x for the sensing noise, at which their noise spectral density intersects with the free-mass standard

quantum limit (cf. Fig. 27). These classical noise frequencies are defined by the following relations

$$S_{FF}^{\text{cl}} = 2 \hbar m \Omega_F^2, \quad (3.54)$$

$$S_{ZZ}^{\text{cl}} = \frac{2 \hbar}{m \Omega_x^2}. \quad (3.55)$$

As an example, the Markovian noise corresponding to the velocity damping of a harmonic oscillator with a damping rate γ_m can be described by

$$\Omega_F^2 = \frac{4 \gamma_m k_B T}{\hbar} \quad (3.56)$$

at a temperature T with $k_B T \gg \hbar \omega_m$ (compare Sec. 1.3). While in the limit of temperature around the absolute zero, i.e. with $T \rightarrow 0$, we obtain

$$\Omega_F^2 = 2 \gamma_m \omega_m. \quad (3.57)$$

But in the following we will usually not specify the type of classical noise and only consider its strength.

Note that the classical force noise together with the classical sensing noise can open a window in which both are completely below the free-mass standard quantum limit as indicated by the gray-shadowed region in Fig. 27. This is the case if and only if the classical noise sources satisfy

$$S_{FF}^{\text{cl}} S_{ZZ}^{\text{cl}} < \hbar^2 \quad \Leftrightarrow \quad \Omega_x / \Omega_F > 2, \quad (3.58)$$

which, as we have seen, turns into a constraint for the classical noise frequency ratio. If Eq. (3.58) holds, the classical noise is equal to a factor of $(2 \Omega_F / \Omega_x)$ times the free-mass standard quantum limit at the frequency $\Omega = \sqrt{\Omega_F \Omega_x}$. Since here the classical noise has the largest separation to the standard quantum limit, we can understand the factor $(2 \Omega_F / \Omega_x)$ as the *classical-noise-standard-quantum-limit-beating factor*.

Before we continue, we shall probably give some order-of-magnitude estimations on the quantum and the classical noise in real experimental situations: the initial LIGO detectors [48, 112] as examples of devices with really macroscopic and heavy test-masses are in their total noise roughly a factor of 10 away from their standard quantum limit [130]. In the planned Advanced LIGO detector [1], the measurement frequency is planned to reach $\Omega_q / (2\pi) \sim 100$ Hz. Note that here the measurement frequency is increased with the arm cavity bandwidth as shown in Sec. 3.2.6. Furthermore, people expect the suspension thermal noise to have a $\Omega_F / (2\pi) \sim 30 - 40$ Hz deducting the structural damping – but the coating thermal noise which will probably be the most challenging sensing noise source may provide a Ω_x that only coincides with Ω_F or is just marginally higher (cf. e.g. Fig. 15). Therefore, even this future detector will probably provide either no or only a very tiny frequency band in which the classical noise is completely below the standard quantum limit. In lab-scale experiments with tiny but still macroscopic test-masses, measurement frequencies of several kHz have already been realized [35, 36]. Here the classical noise is presumed to have $\Omega_F / (2\pi) \sim 1$ kHz but Ω_x is far below Ω_F (cf. e.g. Fig. 23). Therefore, such devices are definitely not yet beating the standard quantum limit with their current level of classical noise.

3.2.3 Very low finesse cavity with quantum vacuum noise

Let us come back to the example from Sec. 3.1.1, namely, to the simple theoretical situation of a laser beam incident on a suspended mirror. This corresponds to a mirror in a cavity (cf. Sec. 1.2) but tuned and with infinitely large bandwidth which allows to adiabatically eliminate the cavity mode. Then the spectral densities of the pure quantum measurement process are very simple and read

$$S_{ZZ}^q = \frac{\hbar^2}{\alpha^2}, \quad S_{FF}^q = \alpha^2, \quad S_{ZF}^q = 0, \quad (3.59)$$

with α as given in Eq. (3.3). In this example we have no correlation between the shot and the back-action noise of the quantum measurement.

In fact, the conditional variances for such a system have been solved by many previous works. Inserting Eq. (3.59) into Eq. (3.50), we obtain

$$V_{xx} = \frac{\hbar}{\sqrt{2} m \omega_m} \frac{1}{\sqrt{\sqrt{\frac{\Omega_q^4}{\omega_m^4} + 1} + 1}} \xrightarrow{\omega_m \rightarrow 0} \frac{\hbar}{\sqrt{2} m \Omega_q}, \quad (3.60)$$

$$V_{pp} = \frac{\hbar m \omega_m}{\sqrt{2}} \frac{\sqrt{\frac{\Omega_q^4}{\omega_m^4} + 1}}{\sqrt{\sqrt{\frac{\Omega_q^4}{\omega_m^4} + 1} + 1}} \xrightarrow{\omega_m \rightarrow 0} \frac{\hbar m \Omega_q}{\sqrt{2}}, \quad (3.61)$$

$$V_{xp} = \frac{\hbar}{2} \frac{\frac{\Omega_q^2}{\omega_m^2}}{\sqrt{\frac{\Omega_q^4}{\omega_m^4} + 1} + 1} \xrightarrow{\omega_m \rightarrow 0} \frac{\hbar}{2}, \quad (3.62)$$

where the measurement frequency is given by $\Omega_q = \alpha/\sqrt{\hbar m}$ which, as we know from Eq. (3.44), is the frequency at which the quantum noise touches the free mass standard quantum limit. Since the conditional variances from Eqs. (3.60)–(3.62) result from a pure quantum measurement process without any additional noise, they of course always represent a pure state, i.e. they satisfy $V_{xx} V_{pp} - V_{xp}^2 = \hbar^2/4$. We have found that the conditional variances completely coincide with those obtained from the stochastic master equation as given in Eq. (3.14). For that, compare also Eqs. (3.60)–(3.62) with Eqs. (2.8a)–(2.8c) from Ref. [45].

For $\omega_m \neq 0$ we can define the unconditional ground state of the oscillator as in Sec. 1.3. Then the conditional variances from Eqs. (3.60)–(3.62) represent a pure state which is squeezed in the oscillator's ground-state normalized coordinates which are defined in Eq. (1.81) with a squeezing factor given by (cf. Eq. (1.11))

$$r = \operatorname{arccosh} \left(\frac{1}{\sqrt{2}} \sqrt{\sqrt{\frac{\Omega_q^4}{\omega_m^4} + 1} + 1} \right), \quad (3.63)$$

and at a squeezing angle of (cf. Eq. (1.12))

$$\varphi = \arctan \left(\frac{\omega_m^2}{\sqrt{2} \Omega_q^2} \sqrt{\sqrt{\frac{\Omega_q^4}{\omega_m^4} + 1} + 1} \left(1 - \frac{\Omega_q^2}{\omega_m^2} - \sqrt{\frac{\Omega_q^4}{\omega_m^4} + 1} \right) \right) + \frac{\pi}{2}. \quad (3.64)$$

The test-mass squeezing increases with a faster measurement, i.e. with higher Ω_q , and

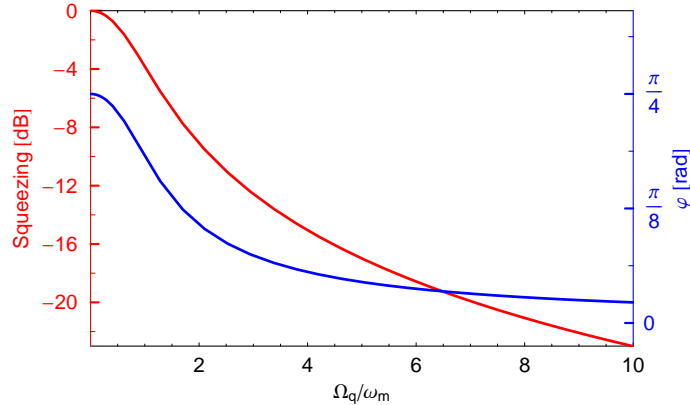


Figure 28: Test-mass squeezing in ground-state normalized coordinates with respect to the pendulum: squeezing strength ($-20 r/\ln 10$) with r as given in Eq. (3.63) (red curve) and squeezing angle φ as given in Eq. (3.64) (blue curve), both versus the dimensionless frequency ratio consisting of measurement frequency divided by mechanical resonance frequency. The conditional variances are produced by a pure quantum measurement. Note that $\varphi = 0$ corresponds to squeezing in (oscillator ground-state normalized) position and $\varphi = \pi/4$ to squeezing in exactly 45° between (oscillator ground-state normalized) position and (oscillator ground-state normalized) momentum.

with a lower mechanical eigenfrequency as shown in Fig. 28. Simultaneously, the squeezed quadrature turns from 45° between the oscillator's ground-state normalized position and momentum to the oscillator's ground-state normalized position quadrature. This is due to the fact that a higher measurement frequency corresponds to more optical power. With more optical power, the measurement is able to gain more information about the position of the test mass while it deteriorates the momentum with more back-action noise.

In the free-mass limit, where $\omega_m \rightarrow 0$, the conditional state spanned by the variances as given in Eqs. (3.60)–(3.62) is equal to a squeezed unconditional ground state of a mechanical harmonic oscillator but with an eigenfrequency Ω_q . In ground-state normalized coordinates with respect to an oscillator having the measurement frequency as its eigenfrequency, i.e. exchange ω_m by Ω_q in Eq. (1.81), we find a squeezing factor of $r = \text{arccosh } \sqrt{2}$ and squeezing angle of $\phi = \pi/4$, which means squeezing in exactly 45° between measurement-frequency ground-state normalized position and momentum. This defines the *conditional ground state of a free mass*. The Wigner function of such a state can be found in the right panel of Fig. 1.

For a free mass the Wiener filter functions for position and momentum become equal to simple decaying cosine functions at the measurement frequency and read

$$K_x(t) = \sqrt{2} \Omega_q e^{-\frac{\Omega_q t}{\sqrt{2}}} \cos\left(\frac{\Omega_q t}{\sqrt{2}}\right), \quad (3.65)$$

$$K_p(t) = \sqrt{2} m \Omega_q^2 e^{-\frac{\Omega_q t}{\sqrt{2}}} \cos\left(\frac{\Omega_q t}{\sqrt{2}} + \frac{\pi}{4}\right). \quad (3.66)$$

Now we can explicitly see why Ω_q is actually called measurement frequency: its inverse sets a timescale for the duration of the measurement which is needed in order to produce the conditional state. Fig. 29 shows that both filter functions sweep just once through the zero

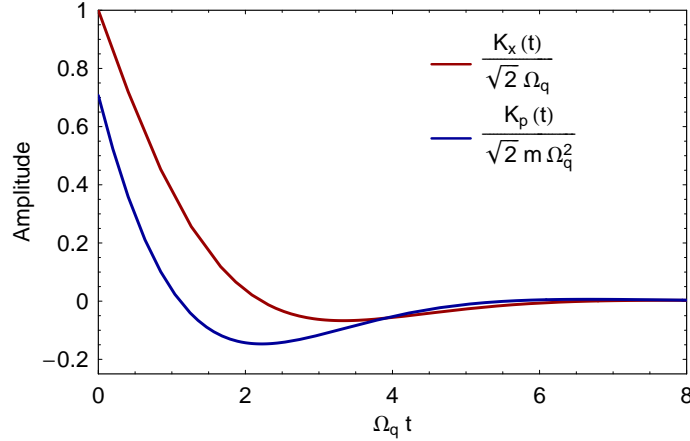


Figure 29: Normalized amplitudes of the Wiener filter functions for position and momentum in the free-mass limit versus normalized measurement time. A quantum measurement process with no correlation in shot and back-action noise is assumed. No additional noise is considered. These Wiener filter functions produce the conditional ground state of a free mass.

point as it is required for an optimal shock absorber. It shows further that in the absence of any classical noise the Wiener filter functions allow to stop measuring the free mass after $\sim 7/\Omega_q$ seconds in order to map it onto the conditional state.

3.2.4 Very low finesse cavity with vacuum input and classical noise

We shall extend our discussion by including classical noise in addition to the quantum-measurement noise. Furthermore, we will consider a perfect balanced homodyne detection on the output field which introduces correlations into the two quantum-measurement noise sources, the photon shot noise and the radiation-pressure noise, which gives $S_{ZF}^q \neq 0$. Then the form of the simplified Markovian quantum measurement process in Eqs. (3.34)–(3.35) still persists. But let us state here again the frequency-domain Heisenberg equations of motion, where \hat{F} and \hat{Z} have to be replaced accordingly, to give

$$\hat{y}(\Omega) = \sin \zeta \hat{a}_1 + \cos \zeta \left[\hat{a}_2 + \frac{\alpha}{\hbar} (\hat{x}(\Omega) + \hat{\xi}_x) \right], \quad (3.67)$$

$$\hat{x}(\Omega) = -\frac{1}{m(\Omega^2 + i\gamma_m\Omega - \omega_m^2)} (\alpha \hat{a}_1 + \hat{\xi}_F), \quad (3.68)$$

with α as given in Eq. (3.3). Here ω_m is as usual the pendulum angular eigenfrequency and γ_m the pendulum damping rate of the suspended test-mass mirror – a mechanical harmonic oscillator with mass m . The measurement output operator \hat{y} includes phase quadrature fluctuations of the in-going vacuum fields, the motion of the mirror's center of mass \hat{x} and classical sensing noise $\hat{\xi}_x$ obeying the frequency-domain correlation

$$\langle \hat{\xi}_x(\Omega) \hat{\xi}_x^\dagger(\Omega') \rangle_{\text{sym}} = 2\pi \frac{\hbar}{m\Omega_x^2} \delta(\Omega - \Omega'). \quad (3.69)$$

The angle ζ denotes the quadrature angle of the homodyne measurement performed on the output field. The motion of the test-mass's center of mass in turn is driven by radiation-

pressure fluctuations as well as by a classical force $\hat{\xi}_F$ having the correlation

$$\langle \hat{\xi}_F(\Omega) \hat{\xi}_F^\dagger(\Omega') \rangle_{\text{sym}} = 2\pi \hbar m \Omega_F^2 \delta(\Omega - \Omega'). \quad (3.70)$$

The amplitude \hat{a}_1 and the phase quadrature operator \hat{a}_2 of the in-going vacuum fields obey the correlation as given in Eq. (1.36). Note that Eqs. (3.67)–(3.68) and therefore the following analysis are also valid for the dark port fields entering and leaving an equal-arm Michelson interferometer with movable end mirrors and the differential motion between these mirrors – but then the mirror mass m in the following discussion has to be substituted by the effective mass $m/2$.

For this model we are still able to obtain quite simple analytic expressions for the conditional variances. We need to insert the spectral densities of the measurement process

$$S_{ZZ} = \frac{\hbar^2}{\alpha^2} \tan^2 \zeta + \frac{\hbar^2}{\alpha^2} + \frac{2\hbar}{m \Omega_x^2}, \quad S_{FF} = \alpha^2 + 2m \hbar \Omega_F^2, \quad S_{ZF} = \hbar \tan \zeta \quad (3.71)$$

into Eq. (3.50). Then we define the two scalars $\xi_F \equiv \Omega_F/\Omega_q$ and $\xi_x \equiv \Omega_q/\Omega_x$ with $\Omega_q = \alpha/\sqrt{\hbar m}$. Recall from Sec. 3.2.2 that the force and the sensing noise intersect the standard quantum limit at Ω_F and Ω_x , respectively, and for $\Omega_x/\Omega_F = 1/(\xi_F \xi_x) > 2$, we have a non-zero frequency band in between Ω_F and Ω_x in which the classical noise is completely below the standard quantum limit – maximally below with the classical-noise-standard-quantum-limit-beating factor of $(2 \xi_F \xi_x) = (2 \Omega_F/\Omega_x)$. In the free-mass limit, i.e. with $\omega_m \rightarrow 0$, the conditional variances from Eq. (3.50) simplify to

$$V_{xx} = \frac{\hbar \sqrt{1 + \tan^2 \zeta + 2 \xi_x^2}}{\sqrt{2} m \Omega_q} \left(\sqrt{(1 + 2 \xi_F^2)(1 + \tan^2 \zeta + 2 \xi_x^2)} - \tan \zeta \right)^{\frac{1}{2}}, \quad (3.72)$$

$$V_{pp} = \frac{\hbar m \Omega_q}{\sqrt{2}} \sqrt{1 + 2 \xi_F^2} \left(\sqrt{(1 + 2 \xi_F^2)(1 + \tan^2 \zeta + 2 \xi_x^2)} - \tan \zeta \right)^{\frac{1}{2}}, \quad (3.73)$$

$$V_{xp} = \frac{\hbar}{2} \left(\sqrt{(1 + 2 \xi_F^2)(1 + \tan^2 \zeta + 2 \xi_x^2)} - \tan \zeta \right), \quad (3.74)$$

while the purity of the state is given by

$$\begin{aligned} \det \mathbf{V} &= \frac{\hbar^2}{4} \left((1 + 2 \xi_F^2) (1 + 2 \xi_x^2) + 2 \xi_F^2 \tan^2 \zeta \right) \\ &\geq \frac{\hbar^2}{4} (1 + 2 \xi_F \xi_x)^2. \end{aligned} \quad (3.75)$$

Note that here the uncertainty product is actually independent of the mechanical eigenfrequency because it has turned out that in the case of an oscillator, i.e. for $\omega_m \neq 0$, Eq. (3.75) remains the same. It is clear from Eq. (3.75) that one should measure the phase quadrature with $\zeta = 0$ in order to minimize the uncertainty product. That means that in order to obtain a small uncertainty product, it is not required to remove the back-action noise from the measurement output – moreover, for that purpose it would be even destructive to do so. This fact is understandable, since here the aim is to learn as much as possible about the mirror motion. The back-action noise is an important content of the mirror motion encoded in the output.

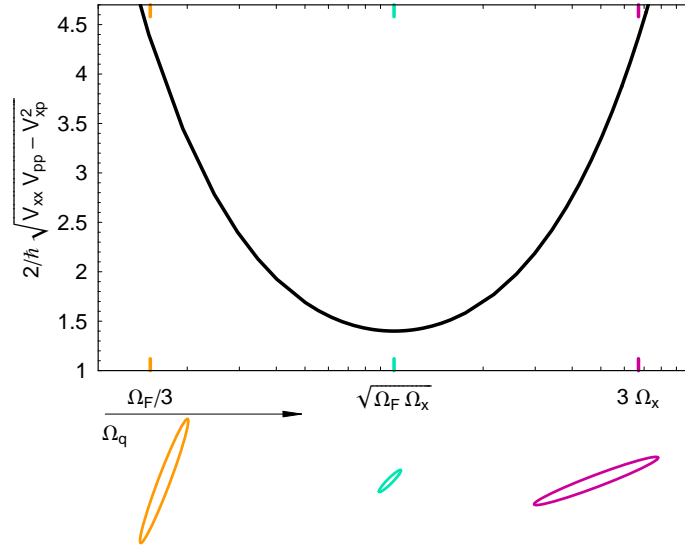


Figure 30: Conditional test-mass uncertainty product (in the free-mass limit and with phase quadrature detection) versus logarithmically spaced measurement frequency in arbitrary units. Here we have chosen a classical noise level satisfying $\Omega_x/\Omega_F = 5$. At three distinct points ($\Omega_q = \Omega_F/3$, $\Omega_q = \sqrt{\Omega_F \Omega_x}$ and $\Omega_q = 3\Omega_x$ – compare to Fig. 27) the test-mass squeezing ellipses in the conditional free-mass ground-state normalized position and momentum coordinates are shown. The horizontal axis corresponds to (ground-state normalized) position and the vertical axis to (ground-state normalized) momentum quadrature. Note that the area of each squeezing ellipse is here equal to a factor of π/\hbar times the uncertainty product.

We can learn from Eqs. (3.72)–(3.74) that the effect of the classical force noise in the conditional variances is suppressed with a higher measurement frequency while the classical sensing noise is suppressed with a lower measurement frequency – recall that the measurement frequency is proportional to the square root of the optical power and therefore describes the measurement strength. Moreover, in the absence of any classical sensing noise the test-mass state becomes even pure with an infinitely strong measurement. Then all classical forces acting on the test mass can be neglected in the vicinity of the strong back-action force and the test mass reaches the conditional ground state at the infinite measurement frequency. Contrary, in the theoretical absence of classical force noise, the test-mass state becomes pure in the limit of an infinitely weak measurement. This situation is also obvious: if the test-mass motion is only driven by the measurement’s back action but this motion is then unfortunately hidden in the measurement output because it is covered by the classical sensing noise, the best idea would be not to measure the test mass at all. Here we can see that the effects of classical force and sensing noise in the conditional variances are indeed – as stated in Sec. 3.2.2 – totally different. If both classical noise sources are present, the uncertainty product is minimized further with an optimal power which accomplishes a balancing between classical force and sensing noise, i.e. $\xi_F = \xi_x$. This produces an equal sign in the second line of Eq. (3.75) and is true for a measurement frequency of $\Omega_q = \sqrt{\Omega_F \Omega_x}$ (cf. also Fig. 30). This simply means that the quantum noise should touch the free-mass standard quantum limit at the frequency where the classical noise has the maximal separation to that limit (cf. Fig. 27). The expression of the minimal uncertainty product is then a function of the classical-noise-standard-quantum-limit-beating factor. We can easily see that the smaller

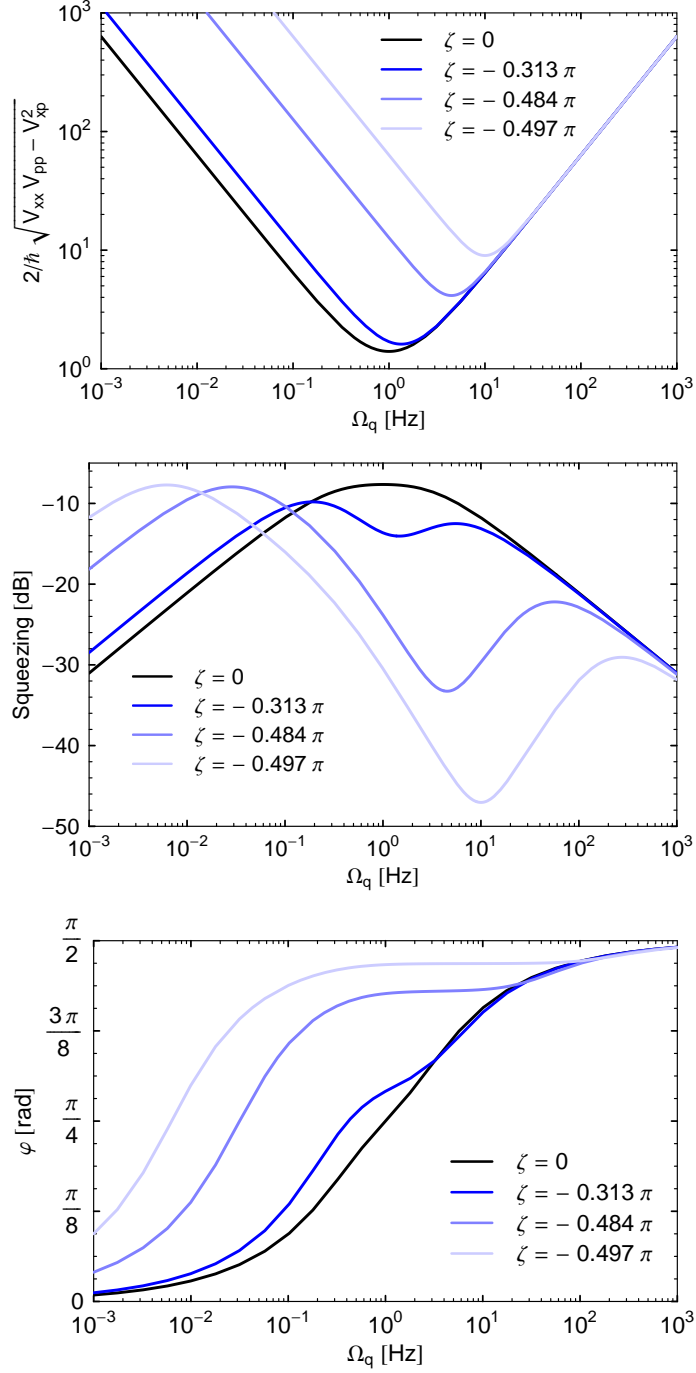


Figure 31: Conditional uncertainty produced (upper panel) as well as test-mass squeezing factor (middle panel) and squeezing angle (lower panel), where all quantities are in the free-mass limit and plotted versus measurement frequency including a certain classical noise budget: here we have chosen $\Omega_F = 1/\sqrt{5}$ and $\Omega_x = \sqrt{5}$. Examples for different homodyne detection angles are given. Both, squeezing factor and angle, are normalized with respect to the conditional ground state of a free mass.

the product $(\xi_F \xi_x)$ or equivalently, the bigger the ratio Ω_x/Ω_F , which both correspond to a broader frequency band in which the classical noise is completely below the standard quantum limit as well as a stronger classical noise beating the standard quantum limit, the more

pure the conditional state becomes. Of course, in the quantum-noise limit ($\xi_F = \xi_x = 0$ as in Sec. 3.2.3) the conditional state is always pure, which means it is Heisenberg-limited for any measurement frequency Ω_q and homodyne detection angle ζ .

We shall discuss the squeezing of the conditional free-mass state given by Eqs. (3.72)–(3.74) in coordinates which are normalized with respect to the conditional ground state of a free mass as defined in Sec. 3.2.3. Note that the conditional ground state of a free mass itself is already squeezed in position and momentum, where the squeezing depends on the measurement frequency. In this normalization the squeezing factor reads

$$r = \operatorname{arccosh} \left(\frac{1}{\sqrt{2}} \frac{\sqrt{1 + 2\xi_F^2} + \sqrt{1 + 2\xi_x^2}}{\sqrt{(1 + 2\xi_F^2)(1 + 2\xi_x^2)}} \right) \geq \operatorname{arccosh} \sqrt{2}, \quad (3.76)$$

when measuring the phase quadrature with $\zeta = 0$. This squeezing factor becomes minimal exactly when the uncertainty product is minimal, i.e. at $\xi_F = \xi_x$. With increasing measurement frequency, the squeezing angle turns smoothly from zero to $\pi/2$, crossing $\pi/4$ exactly at $\xi_F = \xi_x$. This means that for a slow measurement with a small Ω_q , the conditional state is squeezed in conditional free-mass ground-state normalized position, and anti-squeezed in conditional free-mass ground-state normalized momentum. For a fast measurement, i.e. with a high Ω_q , the situation is reversed and the state is squeezed in conditional free-mass ground-state normalized momentum, and anti-squeezed in conditional free-mass ground-state normalized position. Recall that increasing the measurement frequency, the conditional ground state itself becomes in turn more squeezed in position and more anti-squeezed in momentum (cf. Eqs. (3.60)–(3.62)). At the optimal measurement frequency satisfying $\xi_F = \xi_x$, the state is squeezed in 45° between conditional free-mass ground-state normalized position and momentum (cf. Fig. 30). Thus, for $\xi_F = \xi_x$, the conditional state of a free mass has always the same squeezing factor and angle as its conditional ground state, but a higher uncertainty product which depends on the level of classical noise.

With a variable homodyne detection angle, the situation becomes slightly more complicated. In the quantum-noise limit, i.e. with $\xi_F = \xi_x = 0$, the test-mass squeezing factor is not restricted to $r = \operatorname{arccosh} \sqrt{2}$ anymore but reads in the conditional free-mass ground-state normalized coordinates

$$r = \operatorname{arccosh} \left(\frac{1}{\sqrt{2}} \frac{\sqrt{1 + \tan^2 \zeta} + 1}{\sqrt{\sqrt{1 + \tan^2 \zeta} + \tan \zeta}} \right). \quad (3.77)$$

From Eq. (3.77) we can deduce that the test-mass squeezing becomes stronger for $\zeta \rightarrow \pi/2$ but the squeezing factor increases even faster for $\zeta \rightarrow -\pi/2$. We can see in the upper panel of Fig. 31 that for a fixed homodyne detection angle $\zeta \neq 0$ the uncertainty product is not minimized with $\xi_F = \xi_x$ anymore, but at a certain measurement frequency $\Omega_q \neq \sqrt{\Omega_F \Omega_x}$. This measurement frequency coincides with a local minimum of the squeezing factor – therefor compare the upper and the middle panel of Fig. 31. The squeezing factor diverges at small as well as at high measurement frequencies. At a fixed finite measurement frequency, approaching $\zeta = -\pi/2$ turns the squeezed quadrature from the conditional free-mass ground-state normalized position to the conditional free-mass ground-state normalized momentum quadrature (cf. lower panel of Fig. 31). This is actually no surprise because the amplitude quadrature at $\zeta = -\pi/2$ carries information about the past back action from

which the conditioning process can learn about the modified momentum. Note that here the aim is not at all at removing the back-action noise from the measurement output, which in contrast is achieved at a certain sideband frequency Ω when the homodyne detection angle satisfies $\tan \zeta = \Omega_q^2/\Omega^2$.

3.2.5 Very low finesse cavity with squeezed input and classical noise

Until now we have only treated in-going coherent vacuum states of the light $\hat{a}_{1,2}$ – but one could also think about optical squeezed vacuum states coupling to the mirror. This corresponds to inserting optical squeezed states into an interferometer's dark port. By doing so, the quantum limited sensitivity of an interferometer can be enhanced (cf. Tab. 2) as it was first shown in Ref. [27]. Instead of modifying the correlations of the in-going vacuum fields (cf. Eq. (1.36)), we can make the following replacement of the in-going amplitude and phase quadrature operators (as shown in Ref. [78]) in the equations of motion

$$\hat{a}_1 \rightarrow \hat{a}_1 (\cosh r_{\text{op}} + \cos 2\varphi_{\text{op}} \sinh r_{\text{op}}) + \hat{a}_2 \sin 2\varphi_{\text{op}} \sinh r_{\text{op}}, \quad (3.78)$$

$$\hat{a}_2 \rightarrow \hat{a}_1 \sin 2\varphi_{\text{op}} \sinh r_{\text{op}} + \hat{a}_2 (\cosh r_{\text{op}} - \cos 2\varphi_{\text{op}} \sinh r_{\text{op}}), \quad (3.79)$$

where the factor $-(20/\ln 10) r_{\text{op}} < 0$ gives the optical squeezing strength in dB and the squeezing angle is denoted by φ_{op} . Then the entries of the test-mass' conditional covariance matrix read in the free-mass approximation ($\omega_m = 0$)

$$V_{xx} = \frac{\hbar \sqrt{\lambda_-^2 + 2\xi_x^2}}{\sqrt{2} m \Omega_q} \left(\sqrt{(\lambda_+^2 + 2\xi_F^2)(\lambda_-^2 + 2\xi_x^2)} - \sin 2\varphi_{\text{op}} \sinh 2r_{\text{op}} \right)^{\frac{1}{2}}, \quad (3.80)$$

$$V_{pp} = \frac{\hbar m \Omega_q \sqrt{\lambda_+^2 + 2\xi_F^2}}{\sqrt{2}} \left(\sqrt{(\lambda_+^2 + 2\xi_F^2)(\lambda_-^2 + 2\xi_x^2)} - \sin 2\varphi_{\text{op}} \sinh 2r_{\text{op}} \right)^{\frac{1}{2}}, \quad (3.81)$$

$$V_{xp} = \frac{\hbar}{2} \left(\sqrt{(\lambda_+^2 + 2\xi_F^2)(\lambda_-^2 + 2\xi_x^2)} - \sin 2\varphi_{\text{op}} \sinh 2r_{\text{op}} \right). \quad (3.82)$$

Here we have defined $\lambda_{\pm}^2 = \cosh 2r_{\text{op}} \pm \cos 2\varphi_{\text{op}} \sinh 2r_{\text{op}}$. Then the purity of the conditional state can be inferred from

$$\begin{aligned} \det \mathbf{V} &= \frac{\hbar^2}{4} \left((\lambda_+^2 + 2\xi_F^2)(\lambda_-^2 + 2\xi_x^2) - \sin^2 2\varphi_{\text{op}} \sinh^2 2r_{\text{op}} \right) \\ &\geq \frac{\hbar^2}{4} \left(1 + 4\xi_F^2 \xi_x^2 + 2(\xi_F^2 + \xi_x^2) \cosh 2r_{\text{op}} - 2|\xi_F^2 - \xi_x^2| \sinh 2r_{\text{op}} \right) \\ &\geq \frac{\hbar^2}{4} (1 + 2\xi_F \xi_x)^2. \end{aligned} \quad (3.83)$$

The equality of the first inequality sign in Eq. (3.83) is achieved at $\varphi_{\text{op}} = 0$ for $\xi_F^2 > \xi_x^2$ and at $\varphi_{\text{op}} = \pi/2$ for $\xi_F^2 < \xi_x^2$, i.e. by squeezing either the phase or the amplitude quadrature, respectively. Note that in Eq. (3.83) for any Ω_q , the same minimum as in Eq. (3.75) is reached if $r_{\text{op}} = \text{arctanh}(|\xi_F^2 - \xi_x^2|/(\xi_F^2 + \xi_x^2))/2$ – even when having $\xi_F \neq \xi_x$. Therefore, even with input squeezing, the conditional state cannot become more pure than with coherent input, but the demands on the required measurement frequency – and with this the constraints on the optical power, which is needed in order to obtain a certain uncertainty product, can be relaxed. In real experiments the optical power is of course always limited and squeezed input becomes an very important tool.

It has turned out that the conditional variances are in principle even analytically equivalent in the following two cases: *(i)* input-squeezing at a flexible but frequency-independent angle or *(ii)* flexible amount of available optical power and a flexible but frequency-independent homodyne detection angle. This can easily be seen by replacing the homodyne detection angle $\tan \zeta \rightarrow \sin 2\varphi_{\text{op}} \sinh 2r_{\text{op}}$ and the measurement frequency $\Omega_q \rightarrow \lambda_+ \Omega_q$ in Eqs. (3.72)–(3.74). Then we simply end up with Eqs. (3.80)–(3.82). Here we can directly see that using input squeezing allows to change the parameters within Ω_q such as the optical power, the laser frequency and the mirror mass but by modifying the input squeezing parameter λ_+ we can at the same time maintain the measurement frequency. The above described equivalence justifies that from now on we will only treat the flexible homodyne detection angle and infinite amount of available optical power case in all following theoretical calculations but we will keep in mind that with the help of input squeezing we can meet the requirements on the technical parameters much easier.

Even though a homodyne detection different from the phase quadrature and input squeezing do both not help with increasing the purity of the conditional state, we will see in Sec. 3.5 that, since they increase the squeezing of the conditional test-mass state, they can help with entangling the two macroscopic test masses in a Michelson interferometer. Furthermore, with a certain homodyne detection angle or with a certain input squeezing it is possible to remove the position and momentum correlation in the conditional state, i.e. make sure that $V_{xp} = 0$. This becomes crucial for a quantum-noise limited feedback-controlled state as we will see in Sec. 3.4.

3.2.6 Cavity with finite bandwidth

If we consider a cavity of length L with a finite cavity half-bandwidth γ and a movable end mirror, the quantum measurement process becomes non-Markovian, since S_{ZZ} , S_{ZF} and S_{FF} are now frequency dependent functions. Therefore, we find that Eq. (3.50) is no longer the valid expression for the conditional covariance matrix. Here the Heisenberg equations of motion in the frequency domain modify to the Eqs. (1.53) and (1.54) with $\Delta = 0$ which read

$$\hat{y} = \sin \zeta \frac{\gamma + i\Omega}{\gamma - i\Omega} \hat{a}_1 + \cos \zeta \left(\frac{\gamma + i\Omega}{\gamma - i\Omega} \hat{a}_2 + \frac{\sqrt{c\gamma/L}}{\gamma - i\Omega} \frac{\alpha}{\hbar} (\hat{x}(\Omega) + \hat{\xi}_x) \right), \quad (3.84)$$

$$\hat{x} = -\frac{1}{m(\Omega^2 + i\gamma_m \Omega - \omega_m^2)} \left(\frac{\sqrt{c\gamma/L}}{\gamma - i\Omega} \alpha \hat{a}_1 + \hat{\xi}_F \right), \quad (3.85)$$

where the measurement frequency becomes $\Omega_q^{\text{cav}} = \sqrt{c/(m\hbar L\gamma)} \alpha$. We denote the eight different zeros of the measurement-output spectral density $S_{yy}(\Omega)$ by $\gamma(\pm a_1 \pm i b_1)$ and $\gamma(\pm a_2 \pm i b_2)$. These coefficients are for simplicity in the free-mass limit and at $\zeta = 0$ given by

$$a_{1,2} = \frac{1}{2} \sqrt{\sqrt{\varrho^2 \mp \sqrt{2}\varrho} \pm \frac{\varrho}{\sqrt{2}} - 1}, \quad (3.86)$$

$$b_{1,2} = \frac{1}{2} \sqrt{\sqrt{\varrho^2 \mp \sqrt{2}\varrho} \mp \frac{\varrho}{\sqrt{2}} + 1}, \quad (3.87)$$

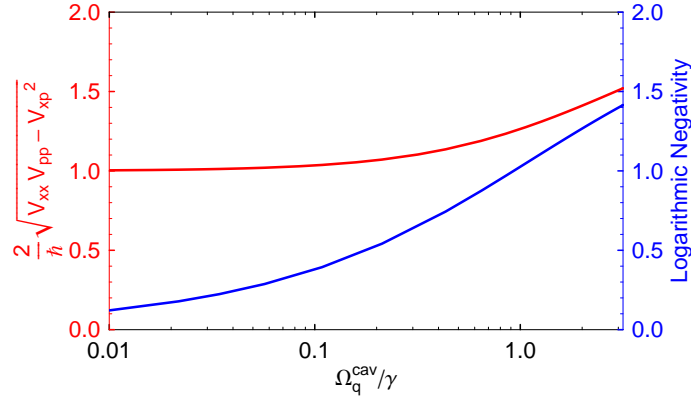


Figure 32: Test-mass uncertainty product (red line) compared to the entanglement (blue line) between the test mass and the tuned cavity mode both versus the dimensionless factor $\Omega_q^{\text{cav}}/\gamma$ which here determines both quantities. We have assumed that no classical noise is present. Free mass limit is used, i.e. $\omega_m = 0$, as well as phase quadrature detection $\zeta = 0$. Entanglement is quantified by the logarithmic negativity.

where we have defined $\varrho = \sqrt{\sqrt{(2\Omega_q^{\text{cav}}/\gamma)^4 + 1} + 1}$. Then we can write down the spectral density of the measurement output as

$$S_{yy} = \frac{\left(\gamma^4 a_1^4 + 2\gamma^2(\gamma^2 b_1^2 - \Omega^2) a_1^2 + (\Omega^2 + \gamma^2 b_1^2)^2\right) \left(\gamma^4 a_2^4 + 2\gamma^2(\gamma^2 b_2^2 - \Omega^2) a_2^2 + (\Omega^2 + \gamma^2 b_2^2)^2\right)}{(\gamma^2 + \Omega^2)^2 (\Omega^2 \gamma_m^2 + (\Omega^2 - \omega_m^2)^2)}. \quad (3.88)$$

Furthermore, we have the following relations among the (cross-) spectral densities

$$S_{xx}(\Omega) = \frac{\hbar}{m\gamma^2(\Omega_q^{\text{cav}})^2} (\gamma^2 + \Omega^2) (S_{yy}(\Omega) - 1), \quad (3.89)$$

$$S_{xy}(\Omega) = \frac{\sqrt{\hbar}}{\sqrt{m}\gamma\Omega_q^{\text{cav}}} (\gamma - i\Omega) (S_{yy}(\Omega) - 1), \quad (3.90)$$

which are helpful in the calculation of the conditional states.

If we then define the following coefficients from the zeros of the measurement-output spectral density as

$$c_1 = 2(b_1 + b_2 - 1), \quad (3.91)$$

$$c_3 = \frac{2}{3}(3a_1^2 b_1 - b_2^3 + 3a_2^2 b_2 - b_1^3 + 1), \quad (3.92)$$

$$c_5 = \frac{2}{5}(b_1^5 - 10a_1^2 b_1^3 + 5a_1^4 b_1 + b_2^5 - 10a_2^2 b_2^3 + 5a_2^4 b_2 - 1), \quad (3.93)$$

we can write down after cumbersome calculations the conditional variances in the free-mass

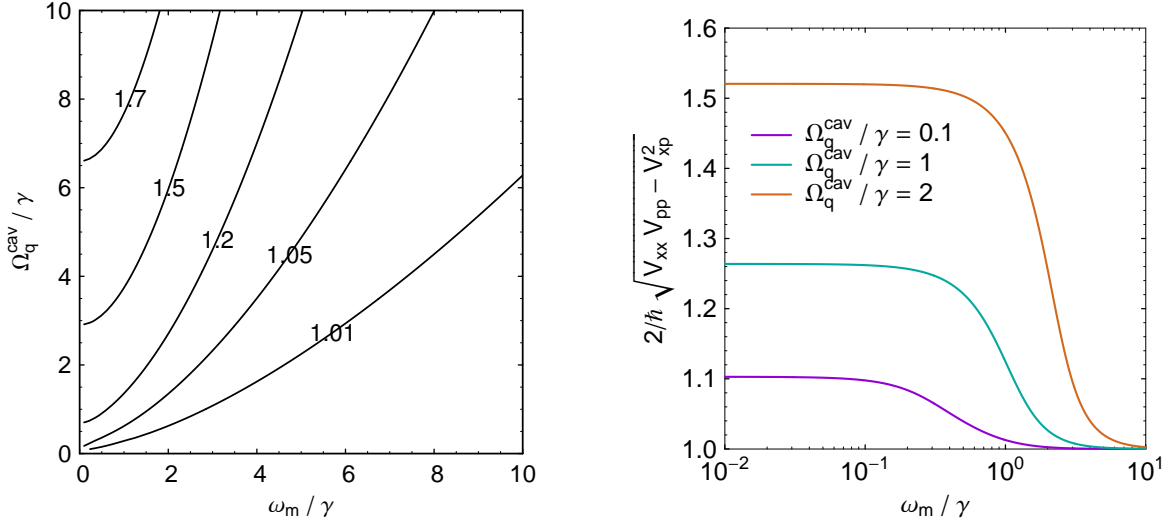


Figure 33: Contour plot (left panel) of the uncertainty product of a test-mass in a tuned cavity for quantum noise only versus two characteristic ratios: mechanical eigenfrequency over bandwidth ω_m/γ and measurement frequency over bandwidth $\Omega_q^{\text{cav}}/\gamma$. Example contour lines of $2/\hbar \sqrt{V_{xx} V_{pp} - V_{xp}^2}$ are marked in the plot. Phase quadrature detection $\zeta = 0$ is assumed. Uncertainty product in the same situation versus mechanical eigenfrequency over bandwidth for different examples of the ratio between measurement frequency and bandwidth (right panel).

approximation, in the quantum-noise limit and with phase quadrature detection as

$$V_{xx} = \frac{\hbar \gamma}{6 m (\Omega_q^{\text{cav}})^2} (c_1^3 + 3 c_1^2 + 3 c_1 + c_3), \quad (3.94)$$

$$V_{pp} = \frac{\hbar m \gamma^3}{120 (\Omega_q^{\text{cav}})^2} (3 c_1^5 + 15 c_1^4 + 20 c_1^3 + 60 c_3 + 60 c_5), \quad (3.95)$$

$$V_{xp} = \frac{\hbar \gamma^2}{16 (\Omega_q^{\text{cav}})^2} c_1^2 (c_1 + 2)^2. \quad (3.96)$$

Here we find for $\Omega_q^{\text{cav}}/\gamma > 0$ that even in the quantum-noise limit the conditional test-mass state is not Heisenberg-limited (cf. also Fig. 32) in contrast to the Markovian limit, i.e. with $\gamma \rightarrow \infty$, as discussed in Sec. 3.2.4 – compare especially the uncertainty product obtained from Eqs. (3.94)–(3.96) with Eq. (3.75). With a finite cavity bandwidth, the light is stored in the cavity for some time and information about the test-mass state is not able to leave the cavity instantaneously – which means that they are not accessible for the conditioning. Therefore, we inescapably need to factor the intra-cavity mode into our discussion. The Heisenberg equations of motion for the intra-cavity mode’s amplitude and phase quadrature operators are in the frequency domain given by (cf. Sec. 1.2)

$$\hat{c}_1(\Omega) = \frac{\sqrt{2c\gamma/L}}{\gamma - i\Omega} \hat{a}_1, \quad (3.97)$$

$$\hat{c}_2(\Omega) = \frac{\sqrt{2\gamma}}{\gamma - i\Omega} \hat{a}_2 + \frac{\sqrt{c/(2L)}}{\gamma - i\Omega} \frac{\alpha}{\hbar} \hat{x}. \quad (3.98)$$

From these equations we have obtained the conditional variances for the cavity mode which we will not report here. We have then constructed the total (4×4) conditional covariance

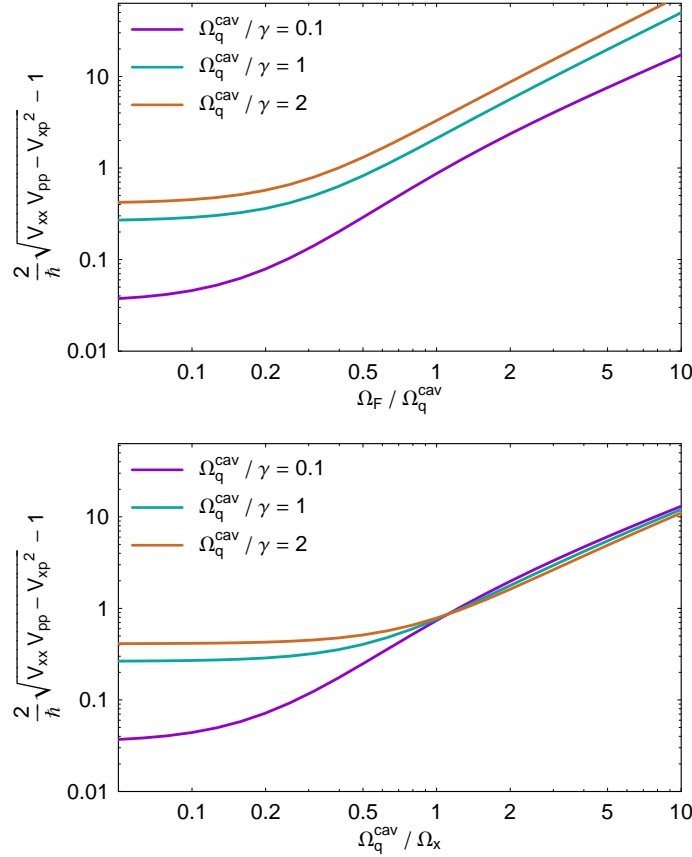


Figure 34: Uncertainty product of a test-mass in a tuned cavity versus classical force noise and without sensing noise (upper panel) as well as versus classical sensing noise without classical force noise (lower panel), both for different examples of ratios between measurement frequency and bandwidth. Free mass limit, i.e. with $\omega_m = 0$, as well as phase quadrature detection $\zeta = 0$ are assumed.

matrix of the composite system including test mass and cavity mode, and it has turned out that we actually have a covariance matrix fulfilling the condition of a pure bipartite state (cf. Sec. 1.4). Only if we look at one of the individual systems alone, each of them does not appear pure. This is clear evidence of entanglement between the test mass and the cavity mode, both conditioned on measuring the output field. We have plotted the logarithmic negativity of the entanglement between the conditional states of test mass and cavity mode in Fig. 32. In that figure we have also plotted the conditional uncertainty product of the test mass. We can see that the test-mass state's purity decreases and test-mass-light entanglement increases with smaller bandwidth and with higher measurement frequency Ω_q^{cav} . But as demonstrated in Fig. 32 and Fig. 33, as long as the cavity bandwidth is sufficiently larger than the measurement frequency, i.e. $\Omega_q^{\text{cav}} < \gamma$, we can neglect this effect and adiabatically eliminate the cavity mode, as we have done in the previous sections and will do in the following sections.

Fig. 33 further shows that in the oscillator case, i.e. with $\omega_m \neq 0$, the purity increases with higher mechanical eigenfrequency ω_m depending on the measurement frequency which in turn depends on the optical power. Let us consult the following hand-waving argument: with increasing ω_m the mechanical oscillator and the optical oscillator, which would resonate

at modulation-frequency zero, become more separated in the frequency space and therefore their entanglement decreases. And with decreasing entanglement the test-mass state becomes more pure.

Including the two classical noise sources from our simple model, the conditional state becomes more and more mixed but depending on the ratio between the measurement frequency and the optical bandwidth as shown in Fig. 34. Recall that the classical force noise increases with higher Ω_F while the classical sensing noise increases with lower Ω_x . The case of classical sensing noise in the absence of classical force noise shows the interesting feature that for $\Omega_q^{\text{cav}}/\Omega_x < 1$ a lower $\Omega_q^{\text{cav}}/\gamma$ produces a lower uncertainty product while at $\Omega_q^{\text{cav}}/\Omega_x > 1$ we need a high $\Omega_q^{\text{cav}}/\gamma$ in order to produce a small uncertainty product. For classical force noise in the absence of classical sensing noise, a lower $\Omega_q^{\text{cav}}/\gamma$ produces always a more pure state.

Note that we will not report here how the situation changes when observing the output of the cavity with finite bandwidth at another homodyne detection angle which is different from the phase quadrature.

3.2.7 Detuned cavity

As described in greater detail in Sec. 1.2.4, a cavity which is detuned with Δ from the carrier's frequency makes the power inside the cavity also dependent on the motion of the test-mass mirrors. This creates an optical spring or an optical anti-spring – depending on the sign of the detuning – both shifting the free mechanical and the free optical resonance frequency in the complex plane. Recall that the optical spring as well as the optical anti-

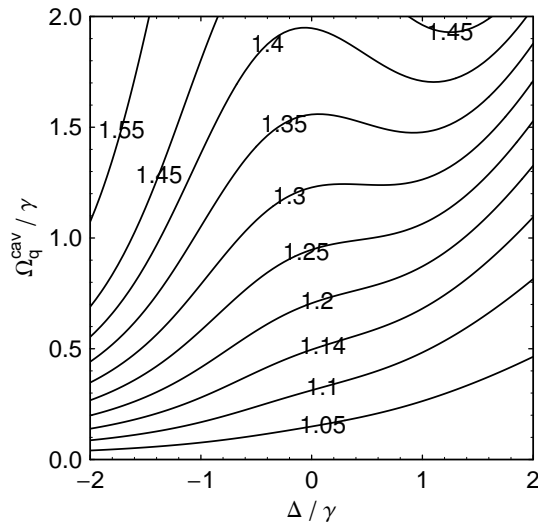


Figure 35: Contour plot of the test-mass uncertainty product in a detuned cavity versus two characteristic ratios: detuning over bandwidth Δ/γ and measurement frequency over bandwidth $\Omega_q^{\text{cav}}/\gamma$. Example contour lines of $2/\hbar \sqrt{V_{xx} V_{pp} - V_{xp}^2}$ are marked in the plot. We assume no classical noise and the free-mass limit, i.e. with $\omega_m = 0$, as well as phase quadrature detection $\zeta = 0$ are used.

spring usually introduces instability to the system which has to be cured with an appropriate linear feedback control [23]. But it is straightforward to show that the conditional covariance matrix does not change under any ideal, linear feedback control (cf. Sec. 3.4).

The Heisenberg equations of motion for such a system are given in Eqs. (1.53)–(1.54). Unfortunately, analytic expressions for the conditional covariance matrix are cumbersome. That is why we can only report numerical results here. Fig. 35 shows that detuning a cavity from the carrier frequency properly can also increase the purity and therefore decrease the quantum entanglement between test mass and cavity mode. In the regime of a blue detuned cavity ($\Delta > 0$) – producing an optical spring – and for $\Omega_q^{\text{cav}} < \Delta$, Fig. 35 simply agrees with Fig. 33. Here at fixed measurement frequency $\Omega_q^{\text{cav}} < \Delta$, a higher detuning Δ gives a lower optomechanical resonance frequency, while it corresponds to a higher optical resonance frequency. Therefore, again the two oscillators are more separated in the frequency space and their entanglement decreases. Interestingly, for higher Ω_q^{cav} the test-mass state could locally appear more pure in the red detuned cavity regime, i.e. at a certain $\Delta < 0$, which produces an optical anti-spring. Note that the uncertainty product diverges for an infinitely red detuned cavity ($\Delta \rightarrow -\infty$). For this fact we unfortunately do not have any intuitive explanation. We will again leave it at reporting only about the situation when observing the output of the detuned cavity at the phase quadrature.

3.2.8 Double carrier cavity

The double-optical-spring ponderomotive squeezer from Sec. 2.4 provides two measurement output channels with the carrier and the subcarrier. With the help of the two-dimensional Wiener filter (cf. Sec. 3.1.3), we have numerically derived the conditional variances of the end mirror in such a double-optical-spring cavity. We have theoretically investigated the conditional uncertainty product and have shown that it can be quite close to the Heisenberg limit – comparably close as a single optical spring. This has supported the investigation carried out in Ref. [35], where the unconditional state of the mirror in a double-optical-spring cavity is explored experimentally.

Furthermore, we have even been able to numerically construct the total (6×6) conditional covariance matrix of the composite system including the test mass as well as carrier and subcarrier cavity mode. Together with that covariance matrix, we have been able to verify that considering only quantum noise, the total state is pure. Since the conditional states of the single systems are not pure, this is a proof for various kinds of entanglement which cannot be removed by the conditioning: carrier cavity mode – subcarrier cavity mode; mirror mode – carrier cavity mode; mirror mode – subcarrier cavity mode.

3.2.9 Speed meter

Finally, we will consider an optical speed-meter configuration such as the Sagnac interferometer with finite arm cavity bandwidth γ from Sec. 2.2 without signal-recycling. Then the quantum measurement process is again non-Markovian and S_{ZZ} , S_{ZF} and S_{FF} are frequency dependent. The Heisenberg equations of motion in the frequency domain can be found in Eqs. (2.25) and (2.26) with signal-recycling parameter set to zero, i.e. $\rho_{\text{SR}} = \phi = 0$. Then we obtain together with $\lambda_1 = \lambda_2 = 0$ and $\epsilon_1 = \epsilon_2 = \gamma$ the Heisenberg equations of motion in the frequency domain of the measurement output operator and of the differential test-mass

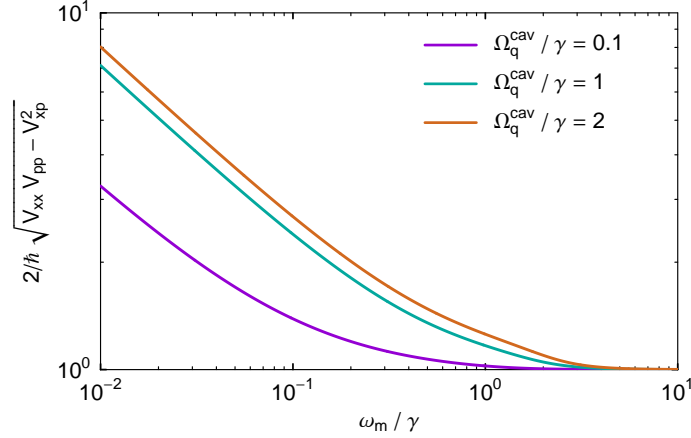


Figure 36: Uncertainty product of the differential test-mass motion in a speed-meter configuration for quantum noise only and versus mechanical eigenfrequency over bandwidth for different examples of the ratio between measurement frequency and bandwidth. Phase quadrature detection $\zeta = 0$ is assumed.

mode position operator, respectively, which read

$$\hat{y} = -\sin \zeta \frac{(\gamma + i\Omega)^2}{(\gamma - i\Omega)^2} \hat{a}_1 + \cos \zeta \left(-\frac{(\gamma + i\Omega)^2}{(\gamma - i\Omega)^2} \hat{a}_2 + \frac{i\Omega \sqrt{c\gamma/L}}{(\gamma - i\Omega)^2} \frac{\alpha}{\hbar} (\hat{x}(\Omega) + \hat{\xi}_x) \right), \quad (3.99)$$

$$\hat{x} = -\frac{4}{m(\Omega^2 + i\gamma_m\Omega - \omega_m^2)} \left(\frac{i\Omega \sqrt{c\gamma/L}}{(\gamma - i\Omega)^2} \alpha \hat{a}_1 + \hat{\xi}_F \right), \quad (3.100)$$

where the measurement frequency is again given by $\Omega_q^{\text{cav}} = \sqrt{c/(m\hbar L\gamma)} \alpha$. Note that here we have $\hat{p} = -im/4\Omega \hat{x}$.

We find that the uncertainty product considering only quantum noise is again totally described by the two characteristic ratios: mechanical eigenfrequency over bandwidth ω_m/γ and measurement frequency over bandwidth $\Omega_q^{\text{cav}}/\gamma$. We already know from Sec. 2.2 that a speed meter does not avoid the back action itself but removes the back-action from the measurement output. Because therefore important information about the test-mass motion is lost, we expect that a speed meter is not able to prepare a better quantum state than a conventional topology. And in fact we can see in Fig. 36 that the uncertainty product even formally diverges in the free-mass limit. This is probably due to the speed-meter effect which becomes more significant in the free-mass limit. Note that we will not consider the detuned speed meter as in Sec. 2.2 because we are not able to consider the uncertainty product in the free-mass limit and would therefore be forced to account for too many different parameters.

3.3 Verification of macroscopic quantum states

It is impossible to verify the conditional state from the output data used for the conditioning. The conditional second-order moments, V_{xx}^{cond} , V_{pp}^{cond} and V_{xp}^{cond} , are by definition the parts that are independent from the measurement data of previous times and are therefore the fluctuations which have not been directly measured in the stage when we collect data for the conditioning, the preparation stage. A verification could on the one hand justify the

model we have used and on the other hand it could test whether the wave function collapse really exists. We are actually left with two options: (i) we could characterize our device carefully or (ii) we could directly verify the remaining fluctuations after the conditioning by a second independent measurement in a so-called verification stage. Note that a verification is also impossible without a preparation stage. Actually, the whole procedure – consisting of state preparation and verification – has to be repeated several times in order to obtain the statistics from which the conditional quantum state can be proven. Furthermore, it may be useful to have an intermediate stage, where the test mass is not measured – or still measured, but the measurement result is neither used for the conditioning nor for the verification – and can freely evolve for some time. What we need to do is to give an estimation on how big the increase in the uncertainty product during the free evolution and the measurement error during the verification stage will be. We will touch on these issues in the following.

3.3.1 Free-evolution stage

How do the conditional variances look like at time $t + \tau$ when we have stopped looking at it at time t ? We have to go back into the construction of the Wiener filter and modify the requirements for the quantity $\hat{R}_x(t)$ from Eq. (3.17), namely to the requirement that at time $t + \tau$, it is only uncorrelated with past outputs up to time t , i.e. $\langle \hat{R}_x(t + \tau) \hat{y}(t') \rangle = 0$ for all $t' < t$. Then the conditional second-order moments become

$$V_{xx}(\tau) = \int_0^\infty \frac{d\Omega}{2\pi} \left(S_{xx} - \left[\frac{S_{xy} e^{-i\Omega\tau}}{s_y^-} \right]_+ \left[\frac{S_{xy} e^{-i\Omega\tau}}{s_y^-} \right]_+^* \right), \quad (3.101)$$

$$V_{pp}(\tau) = \int_0^\infty \frac{d\Omega}{2\pi} \left(S_{pp} - \left[\frac{S_{py} e^{-i\Omega\tau}}{s_y^-} \right]_+ \left[\frac{S_{py} e^{-i\Omega\tau}}{s_y^-} \right]_+^* \right), \quad (3.102)$$

$$V_{xp}(\tau) = \int_0^\infty \frac{d\Omega}{2\pi} \Re \left\{ S_{xp} - \left[\frac{S_{xy} e^{-i\Omega\tau}}{s_y^-} \right]_+ \left[\frac{S_{py} e^{-i\Omega\tau}}{s_y^-} \right]_+^* \right\}. \quad (3.103)$$

Let us come back to the example of a laser beam incident on a suspended mirror (cf. Sec. 3.2.4), where the measurement is additionally subject to (white) classical force and sensing noise. We first assume that the laser is still turned on after the preparation stage, i.e. when $\tau > 0$, but we are stopping the conditioning process by not taking into account the measurement results. Therefore, in this non-conditioning stage, the mirror is still not only driven by the classical force but also by radiation pressure. In the free-mass limit which is the limit of small oscillator eigenfrequency and damping rate with $\omega_m, \gamma_m \ll \Omega_q$, the increase in the second-order moments simply becomes a truncated power series in τ

$$V_{xx}^{\text{on}}(\tau) = V_{xx}^{\text{cond}} + \frac{\hbar}{2m\Omega_q} \left(2\sqrt{1+2\xi_F^2} \sqrt{1+2\xi_x^2} \Omega_q \tau + \sqrt{2} (1+2\xi_F^2)^{3/4} (1+2\xi_x^2)^{1/4} (\Omega_q \tau)^2 + (1+2\xi_F^2) \frac{(\Omega_q \tau)^3}{3} \right), \quad (3.104)$$

$$V_{pp}^{\text{on}}(\tau) = V_{pp}^{\text{cond}} + \frac{\hbar m \Omega_q}{2} (1+2\xi_F^2) \Omega_q \tau, \quad (3.105)$$

$$V_{xp}^{\text{on}}(\tau) = V_{xp}^{\text{cond}} + \frac{\hbar}{2} \left(\sqrt{2} (1+2\xi_F^2)^{3/4} (1+2\xi_x^2)^{1/4} \Omega_q \tau + (1+2\xi_F^2) \frac{(\Omega_q \tau)^2}{2} \right). \quad (3.106)$$

Note that Eqs. (3.104)–(3.106) are also a well-defined approximation for an oscillator and are then valid for $\tau \ll 1/\omega_m$. Furthermore, in the case where the laser gets turned off when $\tau > 0$ we have

$$V_{xx}^{\text{off}}(\tau) = V_{xx}^{\text{on}}(\tau) - \frac{\hbar}{2m\Omega_q} \frac{(\Omega_q \tau)^3}{3} \quad (3.107)$$

$$V_{pp}^{\text{off}}(\tau) = V_{pp}^{\text{on}}(\tau) - \frac{\hbar m \Omega_q}{2} \Omega_q \tau, \quad (3.108)$$

$$V_{xp}^{\text{off}}(\tau) = V_{xp}^{\text{on}}(\tau) - \frac{\hbar}{2} \frac{(\Omega_q \tau)^2}{2}. \quad (3.109)$$

Note that this situation is only interesting from the theoretical point of view: turning out the carrier laser field in a real experimental set-up is totally infeasible because this would mean that the radiation pressure force at DC vanishes which then highly perturbs the motion of the test-mass.

It is advisable to go into the test-mass rotating frame – it would actually be a rotation with ω_m which is zero in our approximation – given by $V_{xx}^{\text{rot}}(\tau) = V_{xx}(\tau) + \tau^2/m^2 V_{pp}(\tau) - 2\tau/m V_{xp}(\tau)$, $V_{pp}^{\text{rot}}(\tau) = V_{pp}(\tau)$ and $V_{xp}^{\text{rot}}(\tau) = V_{xp}(\tau) - \tau/m V_{pp}^{\text{off}}(\tau)$. Note that the uncertainty product is conserved, i.e. $V_{xx}^{\text{rot}} V_{pp}^{\text{rot}} - (V_{xp}^{\text{rot}})^2 = V_{xx} V_{pp} - V_{xp}^2$. Then Eqs. (3.104)–(3.106) get transformed to

$$V_{xx}^{\text{on}}(\tau) \rightarrow V_{xx}^{\text{cond}} + \frac{\hbar}{2m\Omega_q} (1 + 2\xi_F^2) \frac{(\Omega_q \tau)^3}{3}, \quad (3.110)$$

$$V_{pp}^{\text{on}}(\tau) \rightarrow V_{pp}^{\text{cond}} + \frac{\hbar m \Omega_q}{2} (1 + 2\xi_F^2) \Omega_q \tau, \quad (3.111)$$

$$V_{xp}^{\text{on}}(\tau) \rightarrow V_{xp}^{\text{cond}} - \frac{\hbar}{2} (1 + 2\xi_F^2) \frac{(\Omega_q \tau)^2}{2}, \quad (3.112)$$

if the laser remains turned on after the preparation stage. Here one should pay attention to the fact that the cross-variance decreases and therefore approaches an unconditional state with no correlations in \hat{x} and \hat{p} . Remember that this decrease in V_{xp}^{cond} results in an increase in the uncertainty product $V_{xx}^{\text{on}} V_{pp}^{\text{on}} - (V_{xp}^{\text{on}})^2$. Furthermore, only in the rotating frame we can see that the change in the second-order moments is not caused by the sensing noise. The increase in the uncertainty product reads

$$V_{xx}^{\text{on}}(\tau_q) V_{pp}^{\text{on}}(\tau_q) - (V_{xp}^{\text{on}}(\tau_q))^2 = (V_{xx}^{\text{cond}} V_{pp}^{\text{cond}} - (V_{xp}^{\text{cond}})^2) \times \left(1 + \sqrt{2} \tau_q + \tau_q^2 + \frac{\sqrt{2}}{3} \tau_q^3 + \frac{1}{12} \tau_q^4 \right), \quad (3.113)$$

when using a measurement frequency of $\Omega_q = \sqrt{\Omega_x \Omega_F}$ which minimizes the state's uncertainty product within the preparation stage, and if the laser remains turned on, where $\tau_q \equiv \Omega_q \tau = \sqrt{\Omega_F \Omega_x} \tau$. For this scenario, Fig. 37 shows the washing out of the purity. Remarkable, after $\tau = 1/(2\Omega_q)$, the uncertainty product increases only by a factor of two.

The conditional variances with the laser turned off for $\tau > 0$ from Eqs. (3.107)–(3.109)

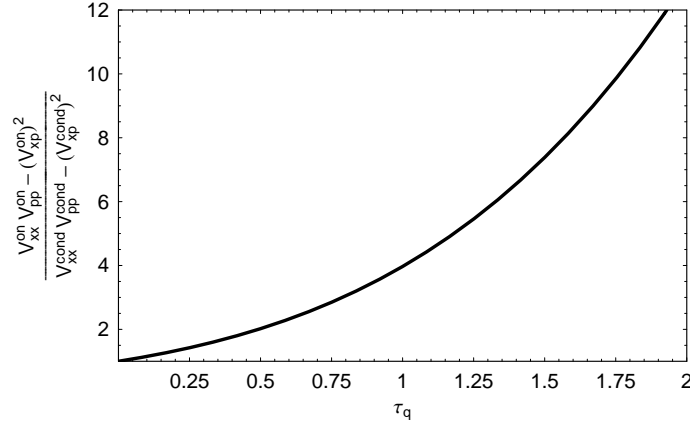


Figure 37: Lifetime of conditional state when the laser is still turned on after the preparation and a measurement frequency of $\Omega_q = \sqrt{\Omega_x \Omega_F}$ is used.

in the rotating frame are given by

$$V_{xx}^{\text{off}}(\tau) \rightarrow V_{xx}^{\text{cond}} + \frac{\hbar}{m} \Omega_F^2 \frac{\tau^3}{3}, \quad (3.114)$$

$$V_{pp}^{\text{rot}}(\tau) \rightarrow V_{pp}^{\text{cond}} + \hbar m \Omega_F^2 \tau, \quad (3.115)$$

$$V_{xp}^{\text{rot}}(\tau) \rightarrow V_{xp}^{\text{cond}} - \hbar \Omega_F^2 \frac{\tau^2}{2}. \quad (3.116)$$

Note that the second-order moments remain constant in absence of any decoherence, i.e. when the laser is turned off for $\tau > 0$ and without any classical noise $\Omega_F \rightarrow 0$.

3.3.2 Verification stage using back-action-noise evasion

During the verification stage, it is inevitable to evade the back-action noise [41] in order to have a free view on the prepared quantum state. It is not necessary to avoid the back action itself because the quantity we want to observe is the prepared state at the time right after the preparation or the optional free-evolution stage. It is sufficient to remove the back-action noise from the measurement output. A back-action evasion technique, variational measurement, was invented by Vyatchanin and Zubova [127], which only suits signals with known arrival times. Note that in the context of gravitational-wave detection, one would prefer frequency-domain variational techniques, as those proposed in e.g. Ref. [78]. For the variational measurement method, a local oscillator with a certain modulation is used for the homodyne detection. Integrating the resulting photocurrent for a time interval τ , we obtain the measurement output

$$\hat{y} = \int_0^\tau dt \left(g_1(t) \hat{b}_1(t) + g_2(t) \hat{b}_2(t) \right). \quad (3.117)$$

In order to evade the back-action noise, it turns out that we need to require

$$g_1(t) + \int_t^\tau dt' \chi_x(t' - t) g_2(t') = 0, \quad (3.118)$$

where $\chi_x(t' - t)$ is the response function of the test mass to external forces. Eq. (3.118) can be understood as the back-action evasion condition and fixes the local oscillator modulation

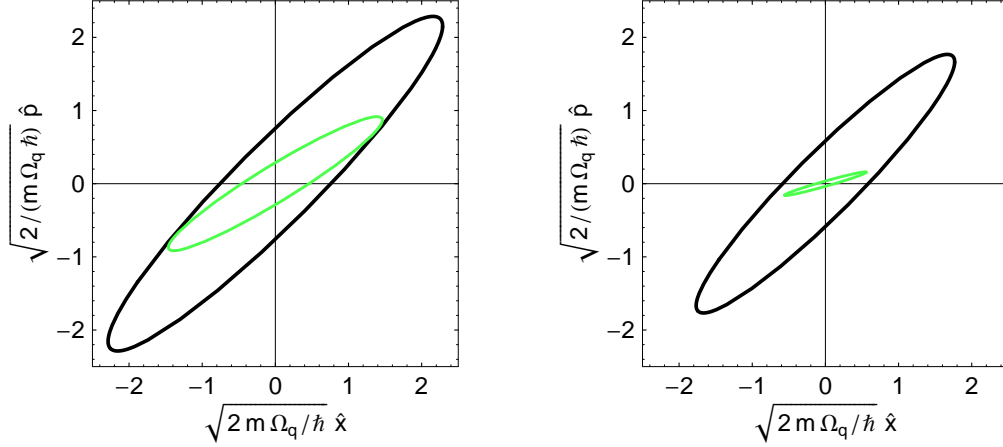


Figure 38: Test-mass squeezing ellipse of the conditional state (black ellipse) and the additional verification noise (green ellipse) in the free-mass limit. We have used ground-state normalized coordinates with respect to a harmonic oscillator with eigenfrequency Ω_q . The optimal measurement frequency is used and the classical noise satisfies $\xi_F = \xi_x = 0.4$ (left panel) and $\xi_F = \xi_x = 0.1$ (right panel).

function $g_1(t)$. Optimizing the additional noise arising within the verification stage over $g_2(t)$ which can be performed analytically (see the appendices of Ref. [41]), we obtain the variances

$$V_{xx}^{\text{add}} = 2 \frac{\hbar}{\sqrt{2} m \Omega_q} (2 \xi_F^2)^{1/4} (1 + 2 \xi_x^2)^{3/4}, \quad (3.119)$$

$$V_{pp}^{\text{add}} = 2 \frac{\hbar m \Omega_q}{\sqrt{2}} (2 \xi_F^2)^{3/4} (1 + 2 \xi_x^2)^{1/4}, \quad (3.120)$$

$$V_{xp}^{\text{add}} = 2 \frac{\hbar}{2} (2 \xi_F^2)^{1/2} (1 + 2 \xi_x^2)^{1/2}, \quad (3.121)$$

which are interestingly equal to twice the conditional variances from Eqs. (3.72)–(3.74) at phase-quadrature readout and with removed back-action.

Now we have to ensure that the fluctuations from the verification process do not cover the fluctuations which we want to measure, i.e. the conditional variances. Fig. 38 shows the squeezing ellipse of the conditional state and the one of the additional verification noise in two scenarios of classical noise.

3.4 Preparation of feedback-controlled macroscopic quantum states

Position and momentum of an object in a conditional quantum state are far away from being frozen. Quite the contrary: their first-order moments follow a stochastic process, a random walk in time. But since the quantum measurement enables us to follow the object's path in phase-space, the conditional state can nevertheless be very pure for the observer. Linearly feeding back the measurement result could really freeze the motion and trap the object into the quantum state. That may be the reason why preparing a quantum state via feedback

control is also known as *cold damping* [83]. Some people are also tempted to call this process ‘cooling’ which is quite misleading because on the one hand we consider only one degree of freedom of the test-mass motion and on the other hand the test mass is not in a thermal equilibrium. In the illustrative picture from Fig. 25, using feedback could fix the controlled state’s squeezing ellipse at the origin of the coordinate system by suppressing the path in phase-space.

Note that in general the control scheme will strongly determine the dynamics of the test mass, but the system could in a certain frequency band behave as a harmonic oscillator with an effective eigenfrequency. Recently, the classical noise budget of the Hanford LIGO detector has allowed a feedback control system to create a 2.5 kg oscillator with such an effective eigenfrequency of around 150 Hz shifted up from the pendulum eigenfrequency of 1 Hz and with an occupation number below 300 [49]. A similar investigation is currently performed at the GEO600 detector. Furthermore, there is a number of such cold-damping experiments considering different smaller-scale mechanical structures [34, 38, 68, 79, 88, 124]. All of them try to reach the oscillator’s ground state but are still some orders of magnitude away from their goal. As a real pure quantum state is approached, the semiclassical model as used in the above references will certainly break down and the quantum noise effects in the measurement process have to be included. In that regime it also becomes important to use an optimal control filter. Using the semiclassical model for the states as they are obtained in present cold-damping experiments, is totally adequate.

3.4.1 Optimal controller

In general, a conditional state does not change under any linear feedback control what we will show amongst others in the following. This is the reason why it only makes sense to consider an unconditional feedback-controlled state if we want to learn anything new. Moreover, almost all cold damping experiments deal with the unconditional state of the test mass anyway. In Ref. [42], we have generally obtained the unconditional variances in position and momentum of a test mass with the minimal uncertainty product – namely, among all those variances which are produced by a system under linear feedback control. Furthermore, in that reference, an optimal controller has been derived for a general linear Markovian measurement process. This controller is optimal in the sense that it allows to produce an unconditional linear feedback controlled state which is closest to a pure state. We will recall this derivation in the following.

Let us suppose that we filter the measurement output operator of a quantum measure-

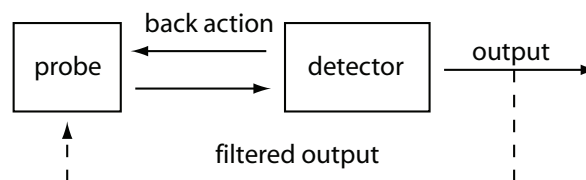


Figure 39: Schematic block diagram of a linear feedback control scheme in its simplest form. The detector’s output is first filtered and then feed back onto the probe.

ment process with the function $\mathcal{C}(t)$, and then apply it as a force $\int_{-\infty}^t dt' \mathcal{C}(t-t') \hat{y}^{\text{cl}}(t')$ onto

the measured object as depicted in Fig. 39. In the frequency domain we then obtain the controlled Heisenberg equations of motion given by

$$\hat{y}^{\text{cl}}(\Omega) = \hat{y}^{\text{ol}}(\Omega) + R_{YF}(\Omega) (\hat{x}^{\text{cl}}(\Omega) - \hat{x}^{\text{ol}}(\Omega)) , \quad (3.122)$$

$$\hat{x}^{\text{cl}}(\Omega) = \hat{x}^{\text{ol}}(\Omega) - R_{xx}(\Omega) \mathcal{C}(\Omega) \hat{y}^{\text{cl}}(\Omega) , \quad (3.123)$$

where the superscript 'cl' marks the closed-loop operators and 'ol' the open-loop operators. Defining the control kernel as

$$K_C(\Omega) = \frac{R_{xx}(\Omega) \mathcal{C}(\Omega)}{1 + R_{xx}(\Omega) \mathcal{C}(\Omega) R_{YF}(\Omega)} , \quad (3.124)$$

we can deduce whether the closed-loop system is stable and the feedback \mathcal{C} is proper, which is namely the case if and only if $K_C(\Omega)$ is a causal function and vanishes at infinity faster than at first order. Then we can – again in the time domain – write down the following relation between closed-loop and open-loop operators

$$\hat{x}^{\text{cl}}(t) = \hat{x}^{\text{ol}}(t) - \int_{-\infty}^t dt' K_C(t-t') \hat{y}^{\text{ol}}(t') , \quad (3.125)$$

$$\hat{p}^{\text{cl}}(t) = \hat{p}^{\text{ol}}(t) - \int_{-\infty}^t dt' \dot{K}_C(t-t') \hat{y}^{\text{ol}}(t') . \quad (3.126)$$

We also find that $\hat{y}^{\text{cl}}(t)$ is just equal to the convolution of a kernel function – similar to the one from Eq. (3.124) – and $\hat{y}^{\text{ol}}(t)$. If we use our knowledge about conditional states by considering Eq. (3.17) as well as its analog for \hat{p} , we can derive the relations

$$V_{xx}^{\text{ctrl}} = V_{xx}^{\text{cond}} + \int_0^{\infty} \frac{d\Omega}{2\pi} |K_x(\Omega) - K_C(\Omega)|^2 S_{yy}(\Omega) , \quad (3.127)$$

$$V_{pp}^{\text{ctrl}} = V_{pp}^{\text{cond}} + \int_0^{\infty} \frac{d\Omega}{2\pi} |K_p(\Omega) + i\Omega K_C(\Omega)|^2 S_{yy}(\Omega) , \quad (3.128)$$

$$V_{xp}^{\text{ctrl}} = 0 , \quad (3.129)$$

where $K_x(\Omega)$ is the frequency-domain Wiener filter for the position as given in Eq. (3.21) and $K_p(\Omega)$ its analog for the momentum. Furthermore, we find that the close loop output operator does not have any correlation with the quantity $\hat{R}_x(t)$ as defined in Eq. (3.17), i.e. $\langle \hat{R}_x(t) \hat{y}^{\text{cl}}(t') \rangle = 0$ for all $t' < t$, since $\hat{y}^{\text{cl}}(t')$ depends only on $\hat{y}^{\text{ol}}(t'')$ for all $t'' \leq t'$. The same applies to the close loop output operator and $\hat{R}_p(t)$. Since $\hat{R}_x(t)$ and $\hat{R}_p(t)$ totally determine the conditional state, this rigorously proves that the conditional state does not change under any linear feedback control as we have stated above.

From Eqs. (3.127)–(3.129) we learn that the controlled unconditional variances V_{xx}^{ctrl} and V_{pp}^{ctrl} are always larger than their conditional counterparts while the cross-variance is zero as it is required for an unconditional state. This leads us to the following relation

$$V_{xx}^{\text{ctrl}} V_{pp}^{\text{ctrl}} \geq V_{xx}^{\text{cond}} V_{xx}^{\text{cond}} \geq \frac{\hbar^2}{4} + (V_{xp}^{\text{cond}})^2 , \quad (3.130)$$

which shows that the unconditional uncertainty product of a controlled state can only reach the Heisenberg minimum if simultaneously $V_{xp}^{\text{cond}} = 0$ and $V_{xx}^{\text{cond}} V_{xx}^{\text{cond}} = \hbar^2/4$. Remarkably,

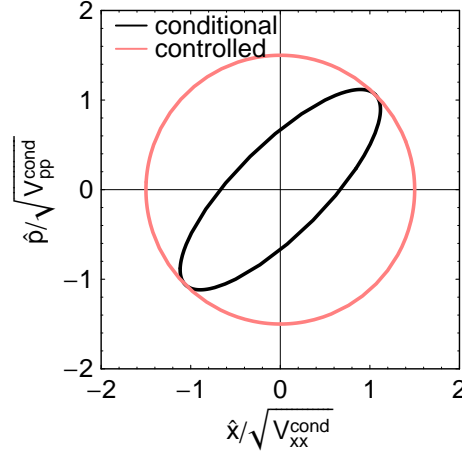


Figure 40: Test-mass squeezing ellipse of the conditional state compared to the one of the controlled state in normalized coordinates and with $V_{xp}^{\text{cond}} = 1/2 \sqrt{V_{xx}^{\text{cond}} V_{pp}^{\text{cond}}}$.

even for a perfect Markovian quantum measurement process with no correlation in its shot and its back-action noise, for which the conditional state is pure, these two conditions are impossible to fulfil (cf. Sec. 3.2.1). Therefore, one cannot apply any controller to create an unconditional perfectly pure state when using a Markovian measurement which has no correlation in shot and back-action noise.

Generally, if minimizing the Heisenberg uncertainty product of any controlled state given by $(V_{xx}^{\text{ctrl}} V_{pp}^{\text{ctrl}})$ using variational calculus, we find the optimal controlled state with the unconditional variances given by [42]

$$V_{xx}^{\text{ctrl}} = V_{xx}^{\text{cond}} + \sqrt{\frac{V_{xx}^{\text{cond}}}{V_{pp}^{\text{cond}}}} V_{xp}^{\text{cond}}, \quad (3.131)$$

$$V_{pp}^{\text{ctrl}} = V_{pp}^{\text{cond}} + \sqrt{\frac{V_{pp}^{\text{cond}}}{V_{xx}^{\text{cond}}}} V_{xp}^{\text{cond}}, \quad (3.132)$$

where the conditional variances are those which would originate from the same measurement process as used for the control scheme. Here it is worth to mention that the ratio between position and momentum fluctuations is the same in the conditional and the unconditional controlled state, i.e. $V_{xx}^{\text{ctrl}}/V_{pp}^{\text{ctrl}} = V_{xx}^{\text{cond}}/V_{pp}^{\text{cond}}$. If we re-scale the operators \hat{x} and \hat{p} in a way such that $V_{x'x'}^{\text{cond}} = V_{p'p'}^{\text{cond}} = 1$, the squeezing ellipse of the controlled state becomes a circle and we have $V_{x'x'}^{\text{ctrl}} = V_{p'p'}^{\text{ctrl}} = 1 + V_{x'p'}^{\text{cond}}$ which is in turn equal to the larger eigenvalue of the re-scaled conditional covariance matrix (compare also Fig. 40). In general, this fact provides us with a simple geometric construction for the unconditional optimal controlled state's squeezing ellipse: first draw a circle that totally encompasses the conditional state's squeezing ellipse in normalized coordinates. Then squeeze or stretch the circle in the position direction by V_{xx}^{cond} and in the momentum direction by V_{pp}^{cond} .

Note that the optimal controller producing the variances in Eqs. (3.131) and (3.132) is unique. For any Markovian measurement process the optimal controller reads

$$\mathcal{C}(\Omega) = \mathcal{C}_0 \frac{\Omega - \mathcal{C}_1}{\Omega - \mathcal{C}_2}, \quad (3.133)$$

where we have defined $\mathcal{C}_0 = -(\omega_m^2 + \Omega_4 \Omega_5)$, $\mathcal{C}_1 = (\Omega_5^3 + \omega_m^2 \Omega_4)/(\omega_m^2 + \Omega_4 \Omega_5)$, $\mathcal{C}_2 = \Omega_4$ with the control frequencies $\Omega_{4,5}$ that are purely imaginary and given by

$$\Omega_4 = -i[\sqrt{q_2} + \sqrt{2(q_2 - q_1)}], \quad \Omega_5 = -i\sqrt{q_2}. \quad (3.134)$$

The coefficients q_1 and q_2 are defined in Eqs. (3.41) and (3.42), respectively. It turns out that the optimal controller in Eq. (3.133) can be motivated simply from a constant feedback plus a linear damping and a simple band limiting, which justifies the more or less educated guesses as done in many previous publications – see e.g. Refs. [34, 39, 83, 126]. The optimal controller changes the dynamics of the system and provides an effective susceptibility which is the closed-loop response function of the oscillator's location to external forces and is given by

$$R_{xx}^{\text{eff}} = -\frac{\Omega - \Omega_4}{(\Omega - \Omega_1)(\Omega - \Omega_2)(\Omega - \Omega_5)}, \quad (3.135)$$

where $\Omega_{1,2}$ are the zeros of the measurement output spectrum and given right after Eq. (3.53). Interestingly, we find that we have the relation

$$|\Omega_1| = |\Omega_2| = |\Omega_5| = \sqrt{q_2} = 1/m \sqrt{V_{pp}^{\text{cond}}/V_{xx}^{\text{cond}}} = 1/m \sqrt{V_{pp}^{\text{ctrl}}/V_{xx}^{\text{ctrl}}} = \omega_{\text{eff}}, \quad (3.136)$$

where ω_{eff} , as given in Eq. (1.8), minimizes the occupation number as it is shown in Eq. (1.7). Furthermore, recall from Sec. 3.2.1 that $\sqrt{q_2}$ actually gives the new eigenfrequency of the conditional state.

Since a low uncertainty product of a controlled state requires a small V_{xp}^{cond} , we recall from Sec. 3.2.1 that in a Markovian measurement process having $V_{xp}^{\text{cond}} \sim 0$ is equivalent to having $q_1 \sim q_2$. In that regime we obtain $\Omega_4 \sim \Omega_5$ and R_{xx}^{eff} becomes equal to a susceptibility of a harmonic oscillator with poles equal to $\Omega_{1,2} \sim \pm i\omega_{\text{eff}}$. In this way it becomes really motivated to use the frequency ω_{eff} as the eigenfrequency of the controlled system and the effective occupation number from Eq. (1.6) as the occupation number of the controlled state.

3.4.2 Very low finesse cavity with vacuum input and classical noise

Now we can take the specific conditional variances as derived in Sec. 3.2 and use them to evaluate the controlled variances. Let us consider a weakly damped mechanical oscillator with the eigenfrequency ω_m as a test mass which is monitored by a linear Markovian quantum measurement process with spectral densities as given in Eq. (3.59). The measurement output is fed back onto the test mass as described above. If we then assume that the test mass is only additionally subjected to Markovian classical force noise, it has been shown in Ref. [42] that we can find a kind of phase transition: if the classical force noise intersects the standard quantum limit below the eigenfrequency of the oscillator, i.e. $\Omega_F < \omega_m$, there is a well-defined finite measurement frequency minimizing the uncertainty product, and therefore the effective occupation number (cf. Fig. 41). On the other hand, if the classical force noise becomes so high that $\Omega_F > \omega_m$, the uncertainty product reaches its minimum at an infinitely large optical power (cf. also Fig. 41). Independent from the level of classical noise, the values of the uncertainty product's minimum are then given by $\hbar^2/4(1 + \sqrt{2})^2$ which correspond to an effective occupation number of $\mathcal{N}_{\text{eff}} = 1/\sqrt{2}$.

In order to investigate a test-mass which would be a free mass without the control scheme, which is monitored by a quantum measurement process consisting of a balanced homodyne

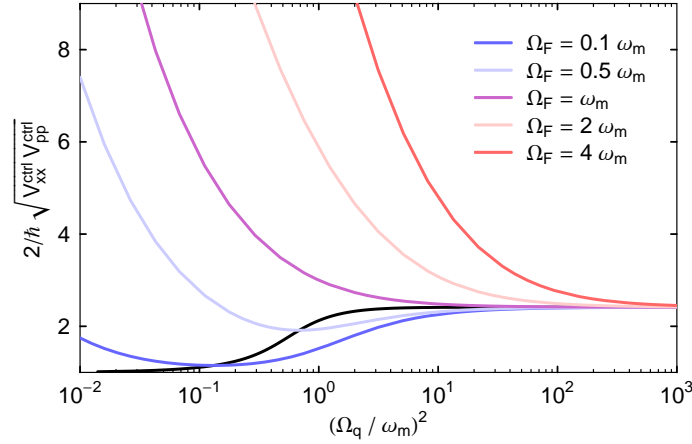


Figure 41: Controlled test-mass uncertainty product for a mechanical oscillator versus measurement frequency. Examples for different levels of classical force noise are given. The black curve represents the minimal achievable uncertainty product at a given level of classical force noise.

detection and which is subject to classical force as well as classical sensing noise, we need to insert Eqs. (3.72)–(3.74) into Eqs. (3.131) and (3.132). In the case of phase quadrature readout, i.e. with $\zeta = 0$, we obtain

$$\begin{aligned} V_{xx}^{\text{ctrl}} V_{pp}^{\text{ctrl}} &= (1 + \sqrt{2})^2 \underbrace{\frac{\hbar^2}{4} (1 + 2\xi_F^2) (1 + 2\xi_x^2)}_{\text{compare to Eq. (3.75) with } \zeta = 0} \\ &\geq (1 + \sqrt{2})^2 \frac{\hbar^2}{4} (1 + 2\xi_F \xi_x)^2. \end{aligned} \quad (3.137)$$

Therefore, allowing only a phase quadrature detection we find that the controlled uncertainty product is always a factor of $(1 + \sqrt{2})^2$ larger than the conditional uncertainty product. That means that even in the quantum noise limit, i.e. with $\xi_F = \xi_x = 0$, the optimal controlled test-mass is not in a pure state. This is simply due to the fact that measuring the output field at the phase quadrature does not introduce correlation into shot and back-action noise. And as we have mentioned above such a measurement cannot produce a pure controlled state.

With a flexible homodyne detection angle ζ and a moderate level of classical noise, there is still an optimal choice of the measurement frequency, which is in turn determined for instance by the optical power, but different from the one producing $\xi_F = \xi_x$. This is shown in Fig. 42. We can also see that for such a moderate level of classical noise, the most pure state at a fixed measurement frequency is usually produced at a homodyne detection angle close to the amplitude quadrature, where the controller can compensate the back-action noise. The higher the measurement frequency, the more back-action compensation is needed. As it is also shown in Fig. 42, the minimum of the controlled unconditional uncertainty product can then approach the conditional uncertainty product much closer than a factor of $(1 + \sqrt{2})^2 \approx 5.8$. For a classical noise frequency ratio of $\Omega_x/\Omega_F = 10$ as assumed in Fig. 42, the controlled uncertainty product with optimal measurement frequency and optimal homodyne detection angle satisfies already $V_{xx}^{\text{ctrl}} V_{pp}^{\text{ctrl}} / (V_{xx}^{\text{cond}} V_{pp}^{\text{cond}} - (V_{xp}^{\text{cond}})^2) \approx 2.5$.

Fig. 43 shows that the more the classical noise is below the standard quantum limit, which

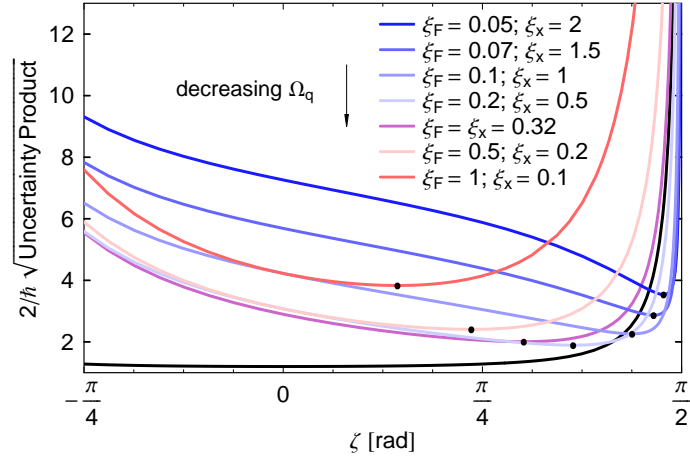


Figure 42: Controlled test-mass uncertainty product in the free-mass limit versus homodyne detection angle. Here the classical noise frequency ratio is fixed to $\Omega_x/\Omega_F = 10$. Examples for different ξ_F - ξ_x -combinations are given, which correspond to tuning the measurement frequency at a fixed classical noise. Each dot corresponds to the minimized uncertainty product with respect to the homodyne detection angle. The black curve represents the conditional state with $\xi_F = \xi_x$, i.e. at the optimal measurement frequency.

corresponds to a higher classical noise frequency ratio, the closer the controlled unconditional uncertainty product can approach the conditional uncertainty product. In the quantum noise limit the optimal controlled test-mass state can become even equal to a pure state but in the theoretical limit of an amplitude quadrature detection, i.e. with $\tan \zeta \rightarrow \infty$.

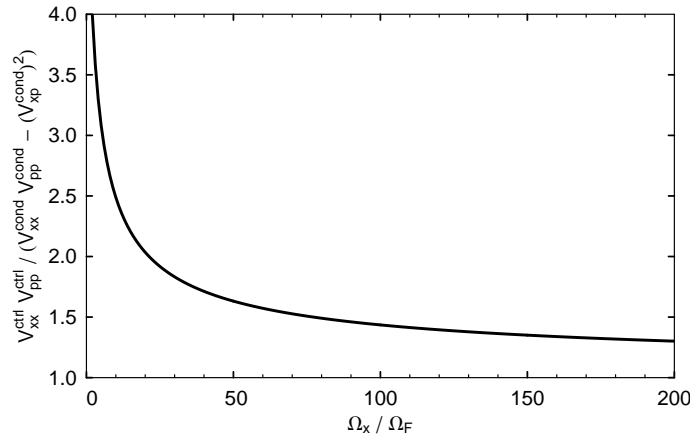


Figure 43: Minimal controlled test-mass uncertainty product in the free-mass limit versus the classical noise frequency ratio. For each level of classical noise an optimal measurement frequency and an optimal homodyne detection angle is used.

Other quantum measurement strategies – such as a non-Markovian measurement with a frequency dependent homodyne detection angle – may allow the controlled uncertainty product to become even closer to the conditional one at a higher level of classical noise. That means that we could find a curve which is below the curve plotted in Fig. 43. We can say that it is therefore not at all hopeless to reach a pure quantum state in cold damping experiments.

3.5 Macroscopic entanglement

In the world of microscopic particles, quantum entanglement has become a common observation. It can be found in discrete variables, such as the polarization of single photons, as well as in continuous variables, such as the amplitude and the phase quadrature of a coherent laser beam. In principle this phenomenon should not be restricted by the size and the weight of an object. It has turned out that a perfect Michelson interferometer seems to be the ideal device to produce entanglement between macroscopic and heavy objects [90, 91, 108]. In this section, we want to show that a Michelson interferometer at its standard quantum limit indeed produces entanglement between the conditional states of its otherwise free test-mass mirrors, if both common- and differential-mode test-mass motion are measured, but with different quantum-measurement processes. Considering position and momentum of two mirrors is in direct analogy to the Einstein, Podolsky and Rosen's gedanken experiment [47].

3.5.1 Michelson interferometer produces test-mass entanglement

Let us consider an equal-arm Michelson interferometer as in Fig. 44 with the carrier laser light injected from the left. As usual, the two beams split at the beam splitter and are

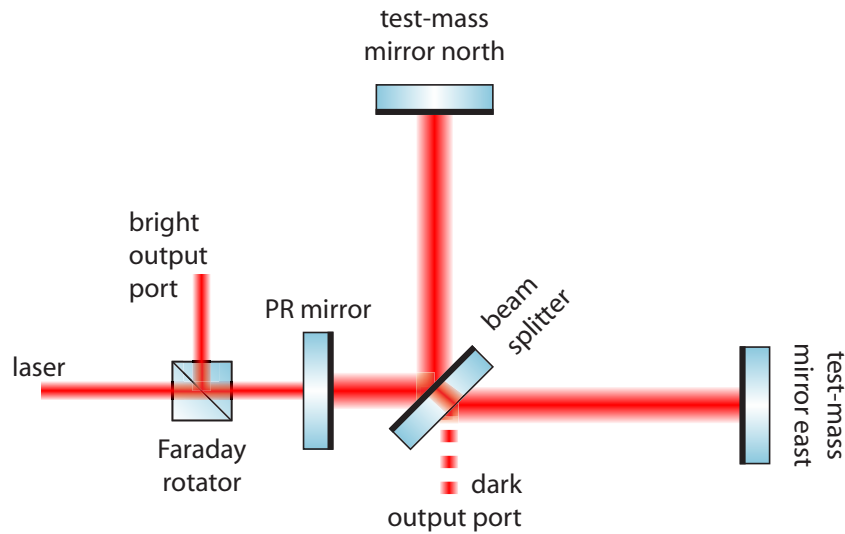


Figure 44: Schematic plot of a power-recycled Michelson interferometer. The suspended test-mass mirrors are supposed to be much lighter than the other suspended optics. The differential motion of the test-mass mirrors is detected at the dark (south) port and the common motion at the bright (west) port. A Faraday rotator might be used to access all of the back reflected light.

reflected by identical suspended test-mass mirrors in the north (n) and east (e) arms before being recombined at the beam splitter. The south port is kept dark at the zero point, with all light reflected to the bright port. A power-recycling mirror is positioned in such a way that it forms a resonant but relatively low finesse cavity for the carrier light with the test-mass mirrors. If the Michelson interferometer is perfectly balanced in arm length as well as in end mirror weight, eigenfrequency and loss, a differential arm-length change induces phase-modulation fields that only emerge at the dark port. Correspondingly, fluctuating vacuum

fields that enter the interferometer from the dark port only interact with test-mass mirror displacements in the differential mode. Similarly, an arm-length change in the common mode induces phase-modulation fields that only emerge at the bright port, while fluctuating modulation fields that enter the interferometer from the bright port only interact with the test-masses' common mode of motion. Note that throughout this section we will assume that the test-mass mirrors at the end of the interferometer arms are much lighter than all the other optical components. Especially the motion of the beam splitter is neglected in all following calculations. Furthermore, we will assume a very low eigenfrequency of the pendulum created by the suspension of the end mirrors and treat them as free masses.

Contrary to usual interferometric experiments, we assume that perfect balanced homodyne detections are made at both the dark and the bright port each with a certain frequency-independent quadrature phase. In this way, we have two independent measurement processes in our interferometer, one monitoring $\hat{x}^d \equiv (\hat{x}^e - \hat{x}^n)$ and the other monitoring $\hat{x}^c \equiv (\hat{x}^e + \hat{x}^n)$. Note that these two measurement processes are different in terms of their signal storage time due to the power-recycling cavity and they can be made further different in terms of the homodyne phase. Defining $\hat{p}^{c,d} \equiv (\hat{p}^e \pm \hat{p}^n)/2$, we have $[\hat{x}^c, \hat{p}^c] = [\hat{x}^d, \hat{p}^d] = i\hbar$ (cf. Eq. (1.1)). If both the common and the differential modes are in different but well-prepared quantum states, which are ideally pure states, such that the wave functions ψ^c and ψ^d are different, then the joint wave function

$$\Psi(x^e, x^n) = \psi^c(x^e + x^n) \psi^d(x^e - x^n) \neq \psi^n(x^n) \psi^e(x^e) \quad (3.138)$$

must be non-separable.

We have to note that such an entanglement in position and momentum between the two end mirrors of the Michelson interferometer is a very special kind of entanglement. When we assemble the individual test-mass common- and differential-mode states, they result in the state of the entire system: this system is described by the combined (4×4) covariance matrix among (x^e, p^e, x^n, p^n) which reads

$$\mathbf{V}_{\text{total}} = \begin{pmatrix} \mathbf{V}^e & \mathbf{V}^{\text{en}} \\ \mathbf{V}^{\text{ne}} & \mathbf{V}^n \end{pmatrix} \quad (3.139)$$

with the (2×2) entry matrices given by

$$\mathbf{V}^n = \mathbf{V}^e = \begin{pmatrix} (V_{xx}^c + V_{xx}^d)/4 & (V_{xp}^c + V_{xp}^d)/2 \\ (V_{xp}^c + V_{xp}^d)/2 & V_{pp}^c + V_{pp}^d \end{pmatrix}, \quad (3.140)$$

$$\mathbf{V}^{\text{en}} = \mathbf{V}^{\text{ne}} = \begin{pmatrix} (V_{xx}^c - V_{xx}^d)/4 & (V_{xp}^c - V_{xp}^d)/2 \\ (V_{xp}^c - V_{xp}^d)/2 & V_{pp}^c - V_{pp}^d \end{pmatrix}. \quad (3.141)$$

If the individual common- and differential mode quantum states are squeezed, the combined state is usually called a *two-mode squeezed state*. The combined covariance matrix from Eqs. (3.139) obtained together with Eqs. (3.140) and (3.141) is very similar to the covariance matrix for the amplitude and the phase quadrature of two output light beams which have been created by overlapping two continuous Gaussian light beams on a beam splitter as depicted in Fig. 45. Note that overlapping two light beams which are differently squeezed in amplitude and phase quadrature on a beam splitter is a very common way of how continuous variable entanglement is created in optics [11, 55]. For the test-mass mirrors we can say that the common and the differential mode of motion are superposed, resulting in the motion of

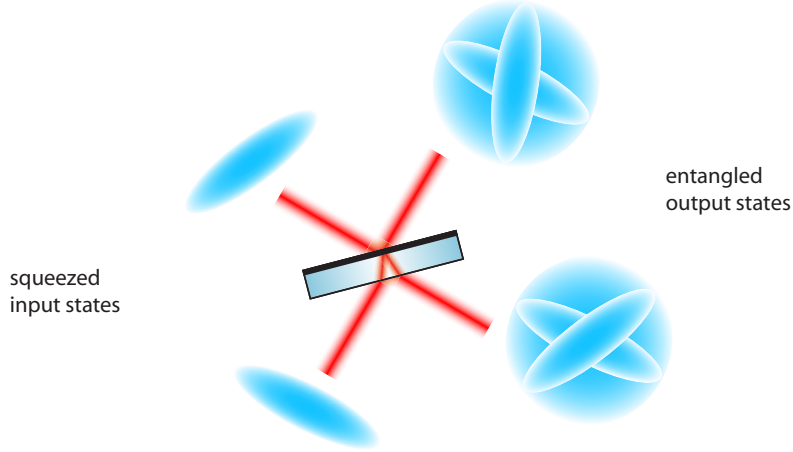


Figure 45: Illustrative picture of a two-mode squeezed state as created in optics. Two differently squeezed beams (in amplitude and phase quadrature) are overlapped on a beam splitter giving a pair of entangled output beams.

each individual test-mass mirror (cf. Fig. 46). For our two-mode squeezed state, Eq. (1.90) reduces to

$$\Sigma_+ = \underbrace{(V_{xx}^c V_{pp}^c - (V_{xp}^c)^2)}_{\det \mathbf{V}^c} + \underbrace{(V_{xx}^d V_{pp}^d - (V_{xp}^d)^2)}_{\det \mathbf{V}^d}, \quad (3.142)$$

$$\begin{aligned} \Sigma_- &= V_{xx}^c V_{pp}^d + V_{pp}^c V_{xx}^d - 2V_{xp}^c V_{xp}^d \\ &= 2 \sqrt{(V_{xx}^c V_{pp}^c - (V_{xp}^c)^2) (V_{xx}^d V_{pp}^d - (V_{xp}^d)^2)} \times \\ &\quad (\cosh r^c \cosh r^d - \sinh r^c \sinh r^d \cos 2(\varphi^c - \varphi^d)). \end{aligned} \quad (3.143)$$

Furthermore, we obtain

$$\det \mathbf{V}_{\text{total}} = \underbrace{(V_{xx}^c V_{pp}^c - (V_{xp}^c)^2)}_{\det \mathbf{V}^c} \underbrace{(V_{xx}^d V_{pp}^d - (V_{xp}^d)^2)}_{\det \mathbf{V}^d}. \quad (3.144)$$

Now all quantities in Eqs. (3.143) and (3.144) are given in terms of the Heisenberg uncertainty products ($\det \mathbf{V}^c$, $\det \mathbf{V}^d$) as well as the squeezing factors (r^c , r^d) and the squeezing angles (φ^c , φ^d) – each of common and differential mode. Then together with Eqs. (3.143) and (3.144), the separability condition as given in Eq. (1.91) becomes

$$\frac{2 \sqrt{\det \mathbf{V}_{\text{total}}}}{\hbar^2} + \frac{\hbar^2}{8 \sqrt{\det \mathbf{V}_{\text{total}}}} \geq \cosh r^c \cosh r^d - \sinh r^c \sinh r^d \cos 2(\varphi^c - \varphi^d). \quad (3.145)$$

The left hand side of Eq. (3.145) is always larger or equal to one and becomes equal to one if and only if the total state is pure, i.e. $\det \mathbf{V}_{\text{total}} = \hbar^4/16$. Suppose that the common and the differential mode are both in a pure state, i.e. $V_{xx}^c V_{pp}^c - (V_{xp}^c)^2 = V_{xx}^d V_{pp}^d - (V_{xp}^d)^2 = \hbar^2/4$, it is easy to verify that the separability condition from Eq. (3.145) is violated if and only if common and differential mode are differently squeezed. This is true if they have a different squeezing factor ($r^c \neq r^d$) or a different squeezing angle ($\varphi^c \neq \varphi^d$). On the other hand, when the common and the differential mode are both not squeezed, i.e. $r^c = r^d = 0$, the state is definitely separable, because the right hand side of Eq. (3.145) becomes equal to one

and therefore the inequality is fulfilled. In general, using the logarithmic negativity from Eq. (1.92), we have found that as long as $\cos 2(\varphi^c - \varphi^d) < 0$, we have that the higher r^c and r^d , the stronger the two test-mass mirrors are entangled.

3.5.2 Test-mass entanglement using conditional states

The homodyne detections on the out-going modulation fields at the dark and the bright port, respectively, collapse the quantum state of the corresponding mode (common and differential) of the test-mass mirror's motion. In the absence of classical noise, each mode will reach a pure state which is squeezed in position and momentum (cf. Sec. 3.2.3). Therefore, as long as the measurement processes for the common and differential mode are different, the test-mass mirrors are entangled. However, in the presence of classical noise, entanglement becomes less significant or even disappears.

The variances of a conditional state of the differential motion between the two (free-mass) end mirrors of a Michelson interferometer including a simple classical noise model are given in Sec. 3.2.4. For the common mode they have to be slightly modified since the power-recycling cavity – here with a high bandwidth and therefore adiabatically eliminated cavity mode – with transmissivity τ_{PR} enhances the measurement strength given by $\alpha^c = 2/\tau_{\text{PR}} \alpha > \alpha$ which is therefore larger than the one associated with the differential mode given by $(\alpha^d)^2 = \alpha^2 = 8 P \omega_0 \hbar / c^2$, where P refers to the circulating laser power in one arm. Furthermore, the common mode will suffer additionally to the classical force noise and the

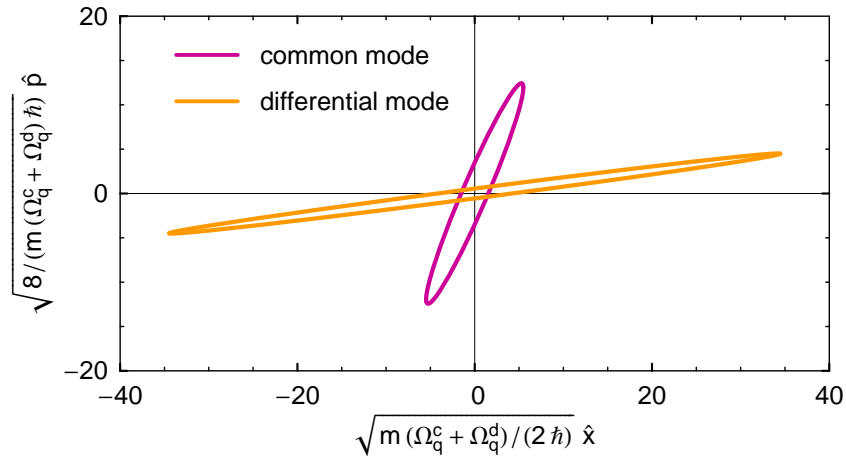


Figure 46: Squeezing ellipses in position and momentum for the common test-mass mode with $\Omega_q^c = 3\Omega_x$ and for the differential test-mass mode $\Omega_q^d = \Omega_F/3$. Ground-state normalized coordinates with respect to a harmonic oscillator with eigenfrequency $(\Omega_q^c + \Omega_q^d)/4$ are used. Classical noise satisfies $\Omega_x/\Omega_F = 5$ and no laser noise is assumed. Corresponding noise spectral densities can be found in Fig. 27.

classical sensing noise – we suppose that the strength of these two classical noise sources are equally distributed into common and differential mode – from laser noise. Therefore, while we can copy Eqs. (3.72)–(3.74) for the differential mode, we have to make some small replacements in Eqs. (3.72)–(3.74) in order to obtain the conditional variances of the common

mode as

$$V_{xx}^c = \frac{\hbar \sqrt{S_{l_2} + S_{l_1} \tan^2 \zeta^c + 2 \left(\frac{\Omega_q^c}{\Omega_x} \right)^2}}{\sqrt{2} m \Omega_q^c} \left(\sqrt{\left(S_{l_1} + 2 \left(\frac{\Omega_F}{\Omega_q^c} \right)^2 \right) \left(S_{l_2} + S_{l_1} \tan^2 \zeta^c + 2 \left(\frac{\Omega_q^c}{\Omega_x} \right)^2 \right)} - S_{l_1} \tan \zeta^c \right)^{\frac{1}{2}}, \quad (3.146)$$

$$V_{pp}^c = \frac{\hbar m \Omega_q^c \sqrt{S_{l_1} + 2 \left(\frac{\Omega_F}{\Omega_q^c} \right)^2}}{\sqrt{2}} \left(\sqrt{\left(S_{l_1} + 2 \left(\frac{\Omega_F}{\Omega_q^c} \right)^2 \right) \left(S_{l_2} + S_{l_1} \tan^2 \zeta^c + 2 \left(\frac{\Omega_q^c}{\Omega_x} \right)^2 \right)} - S_{l_1} \tan \zeta^c \right)^{\frac{1}{2}}, \quad (3.147)$$

$$V_{xp}^c = \frac{\hbar}{2} \left(\sqrt{\left(S_{l_1} + 2 \left(\frac{\Omega_F}{\Omega_q^c} \right)^2 \right) \left(S_{l_2} + S_{l_1} \tan^2 \zeta^c + 2 \left(\frac{\Omega_q^c}{\Omega_x} \right)^2 \right)} - S_{l_1} \tan \zeta^c \right). \quad (3.148)$$

Here $S_{l_{1,2}}$ are the (frequency-independent) spectra of amplitude and phase laser noise.

If we insert Eqs. (3.72)–(3.74) for the differential and Eqs. (3.146)–(3.148) for the common mode into Eqs. (3.143) and (3.144) and suppose phase quadrature readout at both output ports, only three frequency ratios remain: $\Omega_q^{c,d}/\Omega_F$ for common and differential mode, respectively, and Ω_x/Ω_F . The latter turns out to be the crucial factor for the existence of test-mass entanglement. Recall that there exists a frequency window with classical noise

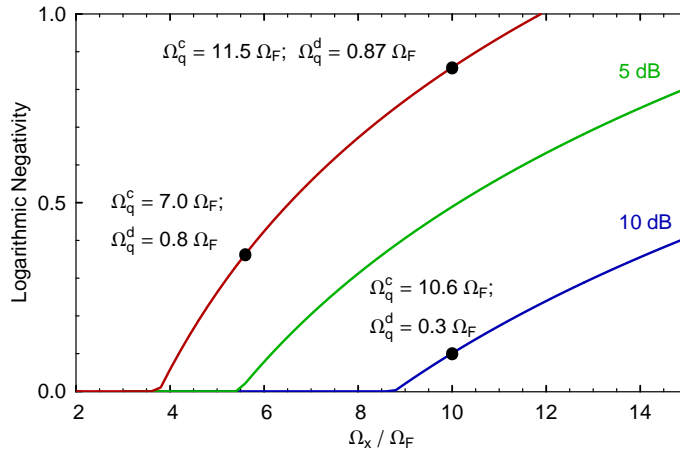


Figure 47: Logarithmic negativity versus Ω_x/Ω_F ; maximized with respect to Ω_q^c and Ω_q^d (example values marked in the plot) for: no laser noise (red line); 5 dB (green line) and 10 dB (blue line) technical laser noise above the vacuum level, in both, amplitude and phase quadrature. Phase quadrature detection ($\zeta = 0$) is used.

completely below the free-mass standard quantum limit if and only if $\Omega_x/\Omega_F > 2$. However, we have found that the existence of entanglement sets a slightly higher threshold value for the classical noise frequency ratio [91]. In Fig. 47, we have plotted the maximum achievable logarithmic negativity $E_{\mathcal{N}}$ which we have introduced in Sec. 1.4 as a function of Ω_x/Ω_F for different strengths of technical laser noise. Therefor we have numerically optimized $E_{\mathcal{N}}$ by varying the measurement frequencies Ω_q^c and Ω_q^d for a given classical noise frequency ratio

and for a given strength of laser noise. We have given some example values of Ω_q^c and Ω_q^d in Fig. 47 as used for this optimization: usually the common mode measurement frequency needs to be above the frequency window in which the classical noise beats the standard quantum limit, while the differential mode measurement frequency needs to be below that window as we have depicted in Fig. 27. Remarkably, even if the laser noise excites a value of 10 dB above the vacuum noise, the generation of entanglement is still possible with a moderate level of classical noise beating the standard quantum limit, namely for $\Omega_x/\Omega_F \gtrsim 9$. Fig. 48 shows the achievable test-mass entanglement at the fixed classical noise frequency

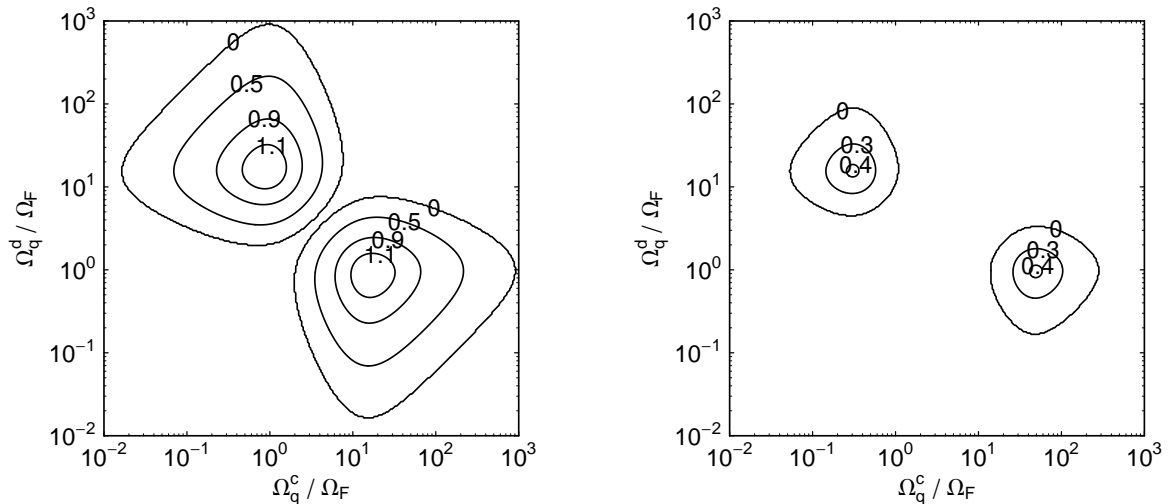


Figure 48: Regions of entangled test-mass states in the plane of common-differential mode measurement frequencies for a classical noise frequency ratio of $\Omega_x/\Omega_F = 14$. No laser noise (left panel) and 10 dB (right panel) technical laser noise above the vacuum level, in both, amplitude and phase quadrature are assumed. Phase quadrature detection is used.

ratio of $\Omega_x/\Omega_F = 14$ and using phase quadrature detection. Although these plots are plotted symmetric in common and differential mode measurement frequency, the common mode measurement frequency is always larger than the one of the differential mode due to the power-recycling. With lower classical noise frequency ratio or higher technical laser noise the allowed region of test-mass entanglement always shrinks.

The entanglement between the two test-mass mirrors – created by overlapping two modes – increases with the squeezing factor of the individual modes (common and differential) and with the angle separating the squeezed quadrature of these two modes. Then it is obvious that one should not observe common and differential mode via phase quadrature detection [90] but that there is a certain value for each the common and the differential mode of $\Omega_q^{c,d}$ and $-\pi/2 < \zeta^{c,d} < 0$ which is optimal for the entanglement and maximizes the logarithmic negativity (cf. Fig. 49). These optimal parameters depend of course on the classical noise, but are usually given by high power and detection close to $-\pi/2$ (cf. the example values as given in Fig. 49). That means that the states are totally dominated by radiation-pressure noise. But the conditioning is able to cure this disprofit if reading out close to amplitude quadrature which contains the radiation-pressure noise.

The ultimate limit of entanglement generation with a flexible but frequency-independent homodyne detection angle and no restriction on the optical power is given by the classical noise frequency ratio satisfying $\Omega_x/\Omega_F \gtrsim 3$. We conjecture that if we modify our quantum

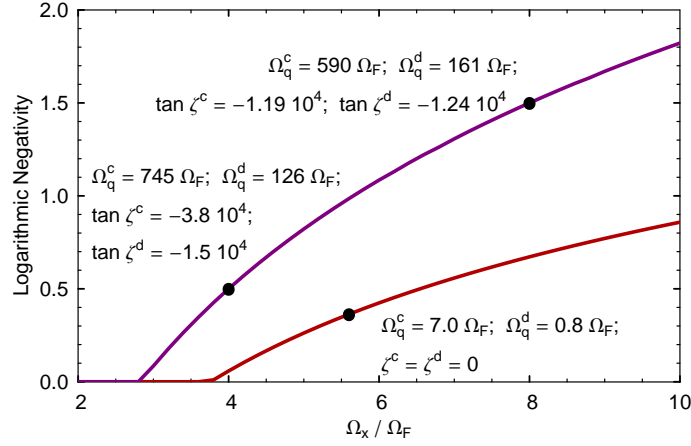


Figure 49: Logarithmic negativity versus Ω_x/Ω_F . Again maximized with respect to Ω_q^c and Ω_q^d using phase quadrature detection (red line) as well as additionally maximized with respect to ζ^c and ζ^d (purple line). In both cases no laser noise is assumed. At some positions optimal parameter values for Ω_q^c , Ω_q^d , ζ^c and ζ^d are given in the plot.

measurement process in the right way, the threshold value for the classical noise frequency ratio regarding the generation of entanglement will coincide with the one regarding the standard quantum limit beating, i.e. $\Omega_x/\Omega_F > 2$. But we have to leave the proof for this presumption and the discovery of how 'in the right way' actually has to be, open for future research. An educated guess is that the right way could be to perform a non-Markovian quantum non-demolition measurement which does not only remove the back-action noise from the measurement output but really circumvents the back action force onto the test mass.

Recall from Sec. 3.2 that the variances of a state prepared with input-squeezing can be mapped onto the variances of a state prepared with a flexible homodyne detection angle. Therefore, injecting squeezed vacuum states into the interferometer's dark port can help with the preparation of test-mass entanglement in the same way as the flexible homodyne detection angle does (cf. Fig. 49). But optical input squeezing lowers the required optical power and will therefore become essential in the preparation of macroscopic entanglement not only for this technical reason!

The laser noise – entering at the bright port and only affecting the common mode – can theoretically be almost suppressed with the optimal high optical power and optimal homodyne detection angle: if we take a look at the conditional common mode variances in the high power limit, i.e. at the highest order of Ω_q^c ,

$$V_{xx}^c \sim \hbar \sqrt{\frac{\sqrt{2} S_{l_1} \Omega_q^c}{m^2 \Omega_x^3}}, \quad (3.149)$$

$$V_{pp}^c \sim \frac{\sqrt{\sqrt{2} S_{l_1} \Omega_q^c} \hbar m \Omega_x}{4} \left(\sqrt{2} S_{l_1} \frac{2 \Omega_q^c}{\Omega_x} - S_{l_1} \tan \zeta^c \right), \quad (3.150)$$

$$V_{xp}^c \sim \frac{\hbar}{2} \left(\sqrt{2} S_{l_1} \frac{\Omega_q^c}{\Omega_x} - S_{l_1} \tan \zeta^c \right), \quad (3.151)$$

we can see that they depend only on amplitude laser noise and we can always re-scale Ω_q^c

and $\tan \zeta^c$ in order to make them independent of laser noise. Therefore, with laser noise not too high, the solid curve in Fig. 49 can always be reached. It is peculiar that a higher laser noise slightly lowers the required measurement frequency again.

Please note that the parameter values for the optical power corresponding to such a high measurement frequency as well as the fine-tuning of the homodyne detection angle – as they are both required in order to reach the maximal entanglement – are far away from any realistic experimental situation. The numerical optimization is more intended to give a theoretical limit on the possible entanglement generation.

3.5.3 Lifetime of test-mass entanglement after preparation

As we have learned in Sec. 3.3, the uncertainty product of a state increases when we stop using the measurement results for the conditioning process. With a higher uncertainty

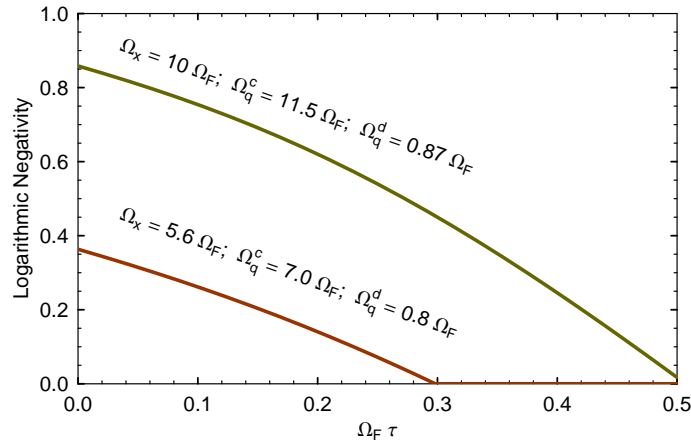


Figure 50: Logarithmic negativity versus $\Omega_x \tau$ for two different classical noise frequency ratios. We assume phase quadrature detection and no laser noise. All other parameters are listed in the plot.

product for the common and the differential mode, the entanglement becomes less and can totally vanish. This raises the question of how long the entanglement between the two end mirrors will survive when having finished the preparation stage. Fig. 50 shows for two different examples of classical noise frequency ratios, where the exact level of classical noise is still arbitrary, how the entanglement dies out in time τ after the preparation – here the preparation has stopped at $\tau = 0$. We have assumed that the laser is even turned off at $\tau > 0$. Furthermore, we have assumed optimal measurement frequencies (as given in Fig. 50) with phase quadrature detection of the common and the differential mode during the preparation. The prepared system with the small classical noise frequency ratio $\Omega_x/\Omega_F = 5.6$ remains roughly entangled for $\tau = 0.3/\Omega_F$, which, as an example for $\Omega_F/(2\pi) = 40$ Hz, corresponds to a lifetime of about a millisecond.

Some more research needs to be done in this direction – also about the verification stage. One thing we especially have to think about is whether we want to verify the entanglement via observing common and differential mode or even via some additional measurement at each test-mass mirror.

3.5.4 Test-mass Einstein-Podolsky-Rosen entanglement

A Michelson interferometer can even produce Einstein-Podolsky-Rosen entanglement in posi-

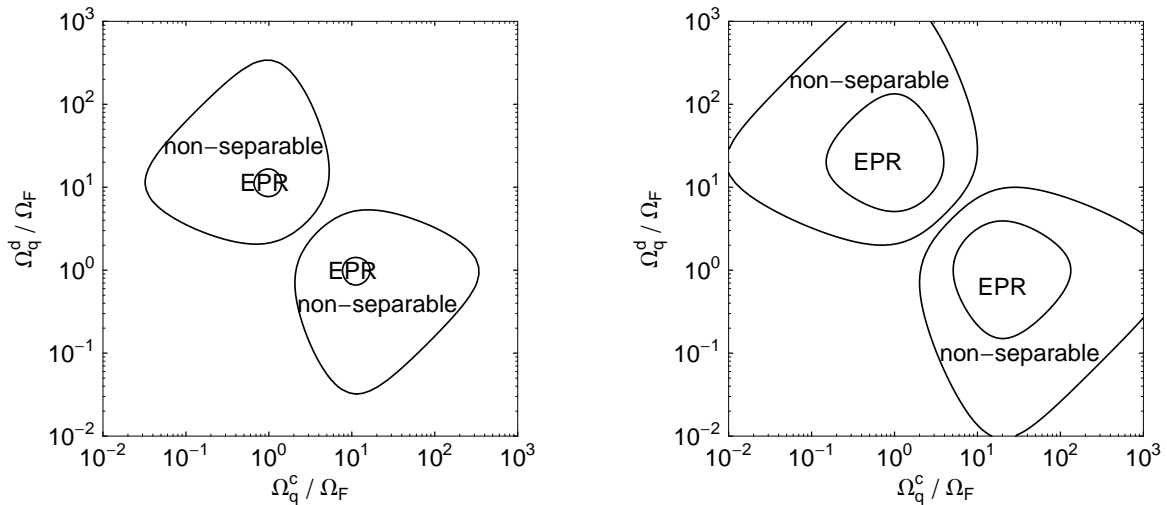


Figure 51: Regions of non-separable and Einstein-Podolsky-Rosen entangled test-mass states in the plane of common-differential mode measurement frequencies for two different classical noise frequency ratios: $\Omega_x/\Omega_F = 11$ (left panel) and $\Omega_x/\Omega_F = 20$ (right panel). Phase quadrature readout and no laser noise are assumed.

tion and momentum of its test-mass mirrors in the same way it produces non-separable states. This is exciting since two macroscopic and heavy objects satisfying Eq. (1.94) would exactly be what Einstein, Podolsky and Rosen had in mind in their Ref. [47]. But for Einstein-Podolsky-Rosen entanglement, the requirements on the classical noise is even stronger: assuming phase quadrature readout and no laser noise, the classical noise has to beat the standard quantum limit with a classical noise frequency ratio satisfying $\Omega_x/\Omega_F \gtrsim 10.5$. Fig. 51 compares the allowed region in the plane spanned by the common and the differential mode measurement frequency of non-separable with Einstein-Podolsky-Rosen entangled test-mass states for two different classical noise frequency ratios. As expected, the region in which the test-masses are Einstein-Podolsky-Rosen entangled is embedded into the region where the test-masses are non-separable.

3.5.5 Test-mass entanglement using controlled states

A different idea is to make use of feedback quantum controlled – or cold damped – common and differential test-mass modes in order to produce entanglement between the two test-mass mirrors. Suppose that we use the measurement results of the homodyne detections at the bright and the dark port of the Michelson interferometer to feed them back with optimal filter functions (cf. Sec. 3.4) onto the mirrors.

Since the unconditional controlled uncertainty product is always larger than the one of a conditional state – recall that for phase quadrature readout this factor is equal to $(1 + \sqrt{2})^2$, we expect that the generation of entanglement is also more difficult with controlled states. And indeed we have found that the classical noise has to beat the standard quantum limit with a classical noise frequency ratio satisfying $\Omega_x/\Omega_F \gtrsim 17$ (cf. Fig. 52). Interestingly,

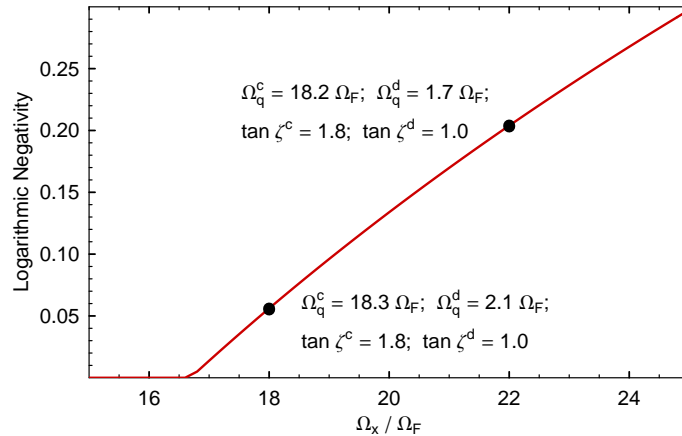


Figure 52: Logarithmic negativity versus Ω_x/Ω_F and maximized with respect to Ω_q^c and Ω_q^d as well as ζ^c and ζ^d . Here the entanglement is produced by controlled states and no laser noise is assumed. At some positions optimal parameter values for Ω_q^c , Ω_q^d , ζ^c and ζ^d are given in the plot.

even with the flexible homodyne detection angle, the optimal measurement frequencies at a given classical noise frequency ratio are not unreasonable high (cf. Fig. 52). It seems that here the strategy of producing back-action dominated common and differential modes plus back-action compensation is not the optimal way of generating entangled test masses by means of controlled common and differential mode states.

Furthermore, within the concept of controlled states we do not find the theoretical laser noise suppression as in the case of entanglement produced by conditional states. With laser noise the entanglement generation using controlled states becomes even more difficult. But also here the jury is still out and more research will hopefully reveal a better understanding and new ideas to circumvent the problems.

4 Summary and conclusion

In the first part of this thesis we have investigated several possibilities in order to increase the sensitivity of quantum-noise limited gravitational-wave detectors further. Based on the work carried out in Ref. [31], we have started with a special version of a Sagnac interferometer in Sec. 2.2 which can be used as a gravitational-wave detector. Here the Sagnac interferometer should be regarded as one representative of the group of optical speed-meter topologies. We have found out that applying the technique of detuned signal-recycling to such a speed meter does not have the same optomechanical effect as applying this technique to a position meter as it was investigated in Refs. [22–24]: the mirrors do not become subject to an optical spring but their dynamical mass becomes modified. This fact has led us to call this the optical inertia effect [92]. Note that we have been the first ones having theoretically investigated the quantum noise in an optical speed meter with detuned signal-recycling. Even though there is this big difference in the optomechanical structure, we have found that the quantum noise spectral density of a detuned signal-recycled Sagnac interferometer can become equal to the one of a detuned signal-recycled Michelson interferometer in a certain limit, the well-separated resonance case. We have explored the sensitivity performance of a Sagnac interferometer of Advanced LIGO scale on the signal-recycling parameter space – assuming a standard and a more optimistic classical noise budget – with respect to neutron star binary inspirals as a gravitational-wave source. We have compared this to the sensitivity performance of the planned Advanced LIGO detector. It has turned out that especially assuming the more optimistic classical noise budget, the detuned signal-recycled Sagnac interferometer can significantly improve the sensitivity in the low frequency regime. This makes the signal-recycled Sagnac interferometer a real candidate design for third-generation gravitational-wave detectors.

Another idea which we have investigated in Sec. 2.3 is to use an interferometer with detuned signal-recycling but a closed output port as a transducer which was suggested for a Michelson topology in Ref. [13]. We have compared the standard-quantum-limit-beating ability of the quantum noise in an ideal local meter [92] which either reads out the motion of a transducer consisting of a speed meter in the form of the Sagnac interferometer or the motion of a transducer consisting of a position meter in the form of the Michelson interferometer. Here we have theoretically pointed out several new interesting transducer effects. We have shown in which frequency regimes those effects can be realized by the two different transducer topologies. A practicable local meter design combined with a Michelson transducer is the local readout scheme [104] which has turned out to be an advisable low-cost add-on for the Advanced LIGO detector. A more detailed discussion of the local readout scheme can be found in Ref. [101,104]. Furthermore, we have motivated to investigate a local readout scheme based on a speed meter topology which could be an even more promising design for a third-generation gravitational-wave detector.

Finally, in Sec. 2.4 we have theoretically investigated the ponderomotive output-squeezing of a stable double-optical-spring cavity [89] as it is already installed at the Massachusetts Institute of Technology (cf. Ref. [35]). Such a squeezing could be used to increase the sensitivity of a laser interferometer gravitational-wave detector by injecting it into the dark port of this detector [27]. The output-squeezing of a single optical spring was considered in the theoretical work of Refs. [36,37], where the instability effect was cured with a feedback

control system. The effect of the control system was included into the calculations as control noise. We have shown that the stable double optical spring can produce more output-squeezing if the subcarrier output is conditioned onto the carrier output – even more output-squeezing than an uncontrolled and therefore unstable single optical spring with the same optomechanical eigenfrequency. Note that a stable double optical spring implemented in a laser interferometer gravitational-wave detector itself [103] can already help to increase the sensitivity. A very detailed discussion about our theoretical sensitivity optimization regarding such a scheme can be also found in Ref. [101].

The second part of this thesis has been devoted in great detail to a survey of the first principles in the preparation of macroscopic Gaussian quantum state of non-massless objects [90]. We have motivated and introduced the Wiener filter method in this context – as an advantage over the stochastic master equations [86] – and have given a simple analytical expression for the covariance matrix of a system under any continuous linear Markovian measurement process in Sec. 3.2.1. We have shown that in absence of any additional noise, the conditional state is totally determined by the measurement noise. The purity of the conditional state becomes even equal to the purity of the underlying measurement process. This provides an important insight into the understanding of conditional states which was probably not communicated before. In a more realistic quantum measurement process the conditional uncertainty product is further determined by the additional noise, the so-called classical noise. In Sec. 3.2.4, we have shown that if there is a non-zero frequency band in which the classical noise is completely below the standard quantum limit, the uncertainty product is just a factor of 2^2 away from the condition for producing a pure state. The wider the frequency band and the strength of this sub-standard-quantum-limit behavior is, the less mixed and therefore the more quantum the Gaussian state becomes. We have shown that a balanced homodyne detection as well as input-squeezing incorporated into the measurement process both do not help to get a more pure state but can significantly steer the test-mass squeezing. In Sec. 3.2.6, we have shown that a measurement process including a cavity with finite bandwidth contaminates the conditional test-mass purity due to the entanglement between the test mass and the cavity mode. But we have also shown that with sufficiently high bandwidth it is always justified to adiabatically eliminate the cavity mode. We have briefly considered test-mass state preparation with the help of a single or a double optical spring. The optical spring can moderate the effect of the cavity mode and increase the purity again. The optical spring also suppresses classical noise and increases the purity of a test mass further due to this fact which is reported elsewhere [90,101]. We have found a characteristic in the state preparation using a speed-meter topology: the uncertainty product diverges in the free-mass limit. Then we have investigated the free evolution of a conditional state and have also briefly thrown light on a possibility of how to verify [41] the conditional states in Sec. 3.3.

In Sec. 3.4, we have investigated a state preparation method which uses the help of a linear feedback control to produce unconditional states, the cold damping technique [83]. We have generally expressed the controlled variances in terms of the conditional variances which has allowed us to obtain the optimal controlled covariance matrix [42]. From this relation we have also been able to show that the optimal controlled uncertainty product is always larger or equal to the conditional one. Furthermore, we have obtained the expression for the optimal control filter in the case of an arbitrary linear continuous Markovian measurement process. We have shown that using a simple balanced homodyne detection allows this controller

to produce an uncertainty product which can already get quite close at the conditional uncertainty product. This fact suggests that cold dampening experiments are in principle able to prepare the unconditional ground state of the test mass.

Furthermore, in Sec. 3.5 we have motivated that a simple power-recycled Michelson interferometer is the ideal device to prepare macroscopic entanglement [91, 108]. We have shown that the existence of entanglement in position and momentum between the two end mirrors is closely related to the factor at which the classical noise beats the standard quantum limit: a quantum measurement with a flexible but frequency-independent homodyne detection angle and no restriction to the optical power as an example, theoretically requires the classical noise to be at least a factor of 1.5 below the free-mass standard quantum limit at a certain sideband frequency. A significantly lower level of classical noise will further allow to prepare the test masses in an Einstein-Podolsky-Rosen entangled state.

In order to really perform experiments towards macroscopic quantum mechanics, the crucial factor will be the level of classical noise. Using simple models, we have given several estimations of how low the classical noise floor has to be in order to perform certain experiments. Please note, that we have also carried out calculations assuming more realistic frequency-dependent noise models which will be reported elsewhere [101]. It is obvious that the gravitational-wave community provides the ideal facilities and a lot of knowledge which will help to prepare macroscopic quantum states. Even though the classical noise budget in current gravitational-wave detectors is still away from the requirements to see macroscopic quantum states. Nevertheless, this fact is not at all discouraging: there is a lot of on-going research in, for example, testing new mirror materials or mirror designs as well as in cryogenic techniques which will allow to press the thermal noise significantly down – even below the standard quantum limit. Note that several experiments – small scale as well as large-scale – aim at reaching the standard quantum limit. One very promising large-scale facility which could allow the classical noise to beat the standard quantum limit for the first time is provided by the 10 m prototype interferometer which will be set up at the Albert-Einstein-Institute in Hannover, Germany. There is an on-going debate about the mirror masses. Light mirrors raise the standard quantum limit but also raise the classical noise. We strongly believe that the preparation and verification of entangled test masses will experimentally be possible within the next decade! But as we have also seen, there is still a lot of experimental as well as even more theoretical research necessary in this interesting field of physics.

In the end we must come to the conclusion that the research towards gravitational-wave detectors with highly improved classical noise budgets kills two birds with one stone: It will on the one hand open the window to a totally new kind of astronomy and on the other hand provide ideal facilities to study macroscopic quantum mechanics.

References

- [1] Advanced ligo reference design. <http://www.ligo.caltech.edu/docs/M/M060056-07/M060056-07.pdf>.
- [2] Advanced ligo webpage. <http://www.ligo.caltech.edu/advLIGO/scripts/summary.shtml>.
- [3] Bench webpage. <http://www.ligo.mit.edu/bench/bench.html>.
- [4] R. Adhikari. *Private communication*, 2007.
- [5] M. Ando and *the TAMA collaboration*. Stable operation of a 300-m laser interferometer with sufficient sensitivity to detect gravitational-wave events within our galaxy. *Phys. Rev. Lett.*, 86:3950, 2001.
- [6] A. Barchielli. Stochastic differential equations and a posteriori states in quantum mechanics. *Int. J. Theor. Phys.*, 32:2221, 1992.
- [7] N. Bishop and S. D. Maharaj. *Proceedings of the 16th international conference on general relativity and gravitation*. World Scientific, 2001.
- [8] D. Bohm. A suggested interpretation of the quantum theory in terms of hidden variables. i. *Phys. Rev.*, 85:166, 1952.
- [9] D. Bohm. A suggested interpretation of the quantum theory in terms of hidden variables. ii. *Phys. Rev.*, 85:180, 1952.
- [10] M. Bondarescu and K. S. Thorne. New family of light beams and mirror shapes for future ligo interferometers. *Phys. Rev. D*, 74:082003, 2006.
- [11] W. P. Bowen, R. Schnabel, P. K. Lam, and T. C. Ralph. Experimental investigation of criteria for continuous variable entanglement. *Phys. Rev. Lett.*, 90:043601, 2003.
- [12] V. B. Braginsky. Classical and quantum restrictions on detection of weak distributions of a macroscopic oscillator. *Sov. Phys. JETP*, 26:831, 1968.
- [13] V. B. Braginsky, M. L. Gorodetsky, and F. Ya. Khalili. Optical bars in gravitational wave antennas. *Phys. Lett. A*, 232:340, 1997.
- [14] V. B. Braginsky and F. Ya. Khalili. Gravitational wave antenna with qnd speed meter. *Phys. Lett. A*, 147:251, 1990.
- [15] V. B. Braginsky and F. Ya. Khalili. Nonlinear meter for the gravitational wave antenna. *Phys. Lett. A*, 218:167, 1996.
- [16] V. B. Braginsky and F. Ya. Khalili. Quantum nondemolition measurements: the route from toys to tools. *Rev. Mod. Phys.*, 68:1, 1996.
- [17] V. B. Braginsky and F. Ya. Khalili. Low noise rigidity in quantum measurements. *Phys. Lett. A*, 257:241, 1999.
- [18] V. B. Braginsky and F. Ya. Khalili. *Quantum measurement*. Cambridge University Press, 1999.

-
- [19] V. B. Braginsky, Y. I. Vorontsov, and F. Ya. Khalili. *Sov. Phys. JETP Lett.*, 33:405, 1978.
- [20] V. B. Braginsky, Y. I. Vorontsov, and K. S. Thorne. Quantum nondemolition measurements. *Science*, 209:547, 1980.
- [21] A. Bunkowski, O. Burmeister, D. Friedrich, K. Danzmann, and R. Schnabel. High reflectivity grating waveguide coatings for 1064 nm. *Class. Quantum Grav.*, 23:7297, 2006.
- [22] A. Buonanno and Y. Chen. Quantum noise in second generation, signal-recycled laser interferometric gravitational-wave detectors. *Phys. Rev. D*, 64:042006, 2001.
- [23] A. Buonanno and Y. Chen. Signal recycled laser-interferometer gravitational-wave detectors as optical springs. *Phys. Rev. D*, 65:042001, 2002.
- [24] A. Buonanno and Y. Chen. Scaling law in signal recycled laser-interferometer gravitational-wave detectors. *Phys. Rev. D*, 67:062002, 2003.
- [25] A. O. Caldeira, H. A. Cerdeira, and R. Ramaswamy. Limits of weak damping of a quantum harmonic oscillator. *Phys. Rev. A*, 40:3438, 1989.
- [26] A. O. Caldeira and A. J. Leggett. Path integral approach to quantum brownian motion. *Physica A*, 121:587, 1983.
- [27] C. M. Caves. Quantum-mechanical noise in an interferometer. *Phys. Rev. D*, 23:1693, 1980.
- [28] C. M. Caves. Defense of the standard quantum limit for free-mass position. *Phys. Rev. Lett.*, 54:2465, 1985.
- [29] C. M. Caves and B. L. Schumaker. New formalism for two-photon quantum optics. *Phys. Rev. A*, 31:3068, 1985.
- [30] S. Chelkowski, H. Vahlbruch, K. Danzmann, and R. Schnabel. Coherent control of broadband vacuum squeezing. *Phys. Rev. A*, 75:043814, 2007.
- [31] Y. Chen. Sagnac interferometer as a speed-meter-type, quantum-nondemolition gravitational-wave detector. *Phys. Rev. D*, 67:122004, 2003.
- [32] Y. Chen and S. Kawamura. Displacement- and timing-noise-free gravitational-wave detection. *Phys. Rev. Lett.*, 96:231102, 2006.
- [33] Y. Chen, A. Pai, K. Somiya, S. Kawamura, S. Sato, K. Kokeyama, R. L. Ward, K. Goda, and E. E. Mikhailov. Interferometers for displacement-noise-free gravitational-wave detection. *Phys. Rev. Lett.*, 97:151103, 2006.
- [34] P. F. Cohadon, A. Heidmann, and M. Pinard. Cooling of a mirror by radiation pressure. *Phys. Rev. Lett.*, 83:3174, 1999.
- [35] T. Corbitt, Y. Chen, E. Innerhofer, H. Mueller-Ebhardt, D. Ottaway, H. Rehbein, D. Sigg, S. Whitcomb, C. Wipf, and N. Mavalvala. An all-optical trap for a gram-scale mirror. *Phys. Rev. Lett.*, 98:150802, 2007.

- [36] T. Corbitt, Y. Chen, F. Ya. Khalili, D. Ottaway, S. Vyatchanin, S. Whitcomb, and N. Mavalvala. Squeezed-state source using radiation-pressure-induced rigidity. *Phys. Rev. A*, 73:023801, 2006.
- [37] T. Corbitt, Y. Chen, and N. Mavalvala. Mathematical framework for simulation of quantum fields in complex interferometers using the two-photon formalism. *Phys. Rev. A*, 72:013818, 2005.
- [38] T. Corbitt, C. Wipf, T. Bodiya, D. Ottaway, D. Sigg, N. Smith, S. Whitcomb, and N. Mavalvala. Optical dilution and feedback cooling of a gram-scale oscillator to 6.9 mk. *Phys. Rev. Lett.*, 99:160801, 2007.
- [39] J.-M. Courty, A. Heidmann, and M. Pinard. Quantum limits of cold damping with optomechanical coupling. *Eur. Phys. J. D*, 17:399, 2001.
- [40] T. Damour, B. R. Iyer, and B. S. Sathyaprakash. Frequency-domain p-approximant filters for time-truncated inspiral gravitational wave signals from compact binaries. *Phys. Rev. D*, 62:084036, 2000.
- [41] S. Danilishin, H. Miao, H. Mueller-Ebhardt, H. Rehbein, K. Somiya, R. Schnabel, K. Danzmann, and Y. Chen. Probing heisenberg uncertainty with gravitational-wave detectors. *In preparation*, 2008.
- [42] S. Danilishin, H. Mueller-Ebhardt, H. Rehbein, K. Somiya, R. Schnabel, K. Danzmann, T. Corbitt, C. Wipf, N. Mavalvala, and Y. Chen. Creation of a quantum oscillator by classical control. *Submitted to Phys. Rev. Lett.*, 2008.
- [43] S. L. Danilishin. Sensitivity limitations in optical speed meter topology of gravitational-wave antennas. *Phys. Rev. D*, 69:102003, 2004.
- [44] M. C. Davis. Factoring the spectral matrix. *IEEE Trans. Autom. Control*, 8:296, 1963.
- [45] A. C. Doherty, S. M. Tan, A. S. Parkins, and D. F. Walls. State determination in continuous measurement. *Phys. Rev. A*, 60:2380, 1999.
- [46] L.-M. Duan, G. Giedke, J. I. Cirac, and P. Zoller. Inseparability criterion for continuous variable systems. *Phys. Rev. Lett.*, 84:2722, 2000.
- [47] A. Einstein, Podolsky, and Rosen. Can quantum-mechanical description of physical reality be considered complete? *Phys. Rev.*, 47:777, 1935.
- [48] B. Abbott *et al.* Detector description and performance for the first coincidence observations between ligo and geo. *Nucl. Inst. and Meth. A*, 517:154, 2004.
- [49] B. Abbott *et al.* Observation of a kilogram-scale oscillator near its quantum ground state. *Submitted to Nature*, 2008.
- [50] B. Willke *et al.* The geo 600 gravitational wave detector. *Class. Quantum Grav.*, 19:1377, 2002.
- [51] H. Everett. Relative state formulation of quantum mechanics. *Rev. Mod. Phys.*, 29:454, 1957.

- [52] L. Di Fiore and *the VIRGO collaboration*. The present status of the virgo central interferometer. *Class. Quant. Grav.*, 19:1421, 2002.
- [53] E. E. Flanagan and S. A. Hughes. Measuring gravitational waves from binary black hole coalescences. i. signal to noise for inspiral, merger, and ringdown. *Phys. Rev. D*, 57:4535, 1998.
- [54] A. Freise, G. Heinzel, K. A. Strain, J. Mizuno, K. D. Skeldon, H. Lueck, B. Willke, R. Schilling, A. Ruediger, W. Winkler, and K. Danzmann. Demonstration of detuned dual recycling at the garching 30m laser interferometer. *Phys. Rev. A*, 277:135, 2000.
- [55] Furusawa, Soerensen, Braunstein, Fuchs, Kimble, and Polzik. Unconditional quantum teleportation. *Science*, 282:706, 1998.
- [56] C. W. Gardiner and M. J. Collett. Input and output in damped quantum systems: Quantum stochastic differential equations and the master equation. *Phys. Rev. A*, 31:3761, 1985.
- [57] C. W. Gardiner and P. Zoller. *Quantum noise*. Springer-Verlag, Berlin, third edition, 2004.
- [58] M. E. Gertenshtein and V. I. Pustovoit. On the detection of low frequency gravitational waves. *Sov. Phys. JETP*, 16:433, 1963.
- [59] G. C. Ghirardi, A. Rimini, and T. Weber. Unified dynamics for microscopic and macroscopic systems. *Phys. Rev. D*, 34:470, 1986.
- [60] V. Giovannetti and D. Vitali. Phase-noise measurement in a cavity with a movable mirror undergoing quantum brownian motion. *Phys. Rev. A*, 63:023812, 2001.
- [61] S. Groeblacher, T. Paterek, R. Kaltenbaek, C. Brukner, M. Zukowski, M. Aspelmeyer, and A. Zeilinger. An experimental test of non-local realism. *Nature*, 446:871, 2007.
- [62] E. Gustafson, D. Shoemaker, K. Strain, and R. Weiss. Lsc white paper on detector research and development. <http://www.ligo.caltech.edu/docs/T/T990080-00.pdf>.
- [63] J. Harms, Y. Chen, S. Chelkowski, A. Franzen, H. Vahlbruch, K. Danzmann, and R. Schnabel. Squeezed-input, optical-spring, signal-recycled gravitational-wave detectors. *Phys. Rev. D*, 68:042001, 2003.
- [64] J. Harms, R. Schnabel, and K. Danzmann. Finite mass beam splitter in high power interferometers. *Phys. Rev. D*, 70:102001, 2004.
- [65] S. W. Hawking and G. F. R. Ellis. *The large scale structure of space-time*. Cambridge University Press, 1973.
- [66] G. Heinzel, K. A. Strain, J. Mizuno, K. D. Skeldon, B. Willke, W. Winkler, R. Schilling, A. Ruediger, and K. Danzmann. Experimental demonstration of a suspended dual recycling interferometer for gravitational wave detection. *Phys. Rev. Lett.*, 81:5493, 1998.

- [67] W. Heisenberg. Ueber den anschaulichen inhalt der quantentheoretischen kinematik und mechanik. *Zeitschrift fuer Physik*, 43:172, 1927.
- [68] A. Hopkins, K. Jacobs, S. Habib, and K. Schwab. Feedback cooling of nanomechanical resonator. *Phys. Rev. B*, 68:235328, 2003.
- [69] M. Horodecki, P. Horodecki, and R. Horodecki. Separability of mixed states: necessary and sufficient conditions. *Phys. Lett. A*, 223:1, 1996.
- [70] S. A. Hughes and K. S. Thorne. Seismic gravity-gradient noise in interferometric gravitational-wave detectors. *Phys. Rev. D*, 58:122002, 1998.
- [71] R. A. Hulse. The discovery of the binary pulsar (psr 1913+16). *Rev. Mod. Phys.*, 66:699, 1994.
- [72] M.T. Jaekel and S. Reynaud. Quantum limits in interferometric measurements. *Europhys. Lett.*, 13:301, 1990.
- [73] S. J. Jones, H. M. Wiseman, and A. C. Doherty. Entanglement, einstein-podolsky-rosen correlations, bell nonlocality, and steering. *Phys. Rev. A*, 76:052116, 2007.
- [74] S. Kawamura and Y. Chen. Displacement-noise-free gravitational-wave detection. *Phys. Rev. Lett.*, 93:211103, 2004.
- [75] F. Ya. Khalili. Quantum speedmeter and laser interferometric gravitational-wave antennae. <http://arxiv.org/abs/gr-qc/0211088>.
- [76] F. Ya. Khalili. The optical lever intracavity readout scheme for gravitational-wave antennae. *Phys. Lett. A*, 298:308, 2002.
- [77] F. Ya. Khalili and Yu. Levin. Speed meter as a quantum nondemolition measuring device for force. *Phys. Rev. D*, 54:4735, 1996.
- [78] H. J. Kimble, Y. Levin, A. B. Matsko, K. S. Thorne, and S. P. Vyatchanin. Conversion of conventional gravitational-wave interferometers into quantum nondemolition interferometers by modifying their input and/or output optics. *Phys. Rev. D*, 65:022002, 2001.
- [79] D. Kleckner and D. Bouwmeester. Sub-kelvin optical cooling of a micromechanical resonator. *Nature*, 444:75, 2006.
- [80] I. S. Kondrashov, D. A. Simakov, F. Ya. Khalili, and S. L. Danilishin. Optimizing the regimes of advanced ligo gravitational wave detector for multiple source types. <http://arxiv.org/abs/0806.1505>, 2008.
- [81] V. I. Lazebny and S. P. Vyatchanin. Displacement transformer in laser gravitational-wave detectors. *In preparation*, 2008.
- [82] H. Luetkepohl. *Introduction to multiple time series analysis*. Springer, 1993.
- [83] S. Mancini, D. Vitali, and P. Tombesi. Optomechanical cooling of a macroscopic oscillator by homodyne feedback. *Phys. Rev. Lett.*, 80:688, 1998.

- [84] K. McKenzie. *Private communication*, 2008.
- [85] B. J. Meers. Recycling in laser-interferometric gravitational-wave detectors. *Phys. Rev. D*, 38:2317, 1988.
- [86] G. J. Milburn. Classical and quantum conditional statistical dynamics. *Quantum Semi-class. Opt.*, 8:269, 1996.
- [87] O. Miyakawa, R. Ward, R. Adhikari, M. Evans, B. Abbott, R. Bork, D. Busby, J. Heefner, A. Ivanov, M. Smith, R. Taylor, S. Vass, A. Weinstein, M. Varvella, S. Kawamura, F. Kawazoe, S. Sakata, and C. Mow-Lowry. Measurement of optical response of a detuned resonant sideband extraction gravitational wave detector. *Phys. Rev. D*, 74:022001, 2006.
- [88] C. M. Mow-Lowry, A. J. Mullavey, S. Gossler, M. B. Gray, and D. E. McClelland. Cooling of a gram-scale cantilever flexure to 70 mk with a servo-modified optical spring. *Phys. Rev. Lett.*, 100:010801, 2008.
- [89] H. Mueller-Ebhardt, H. Rehbein, T. Corbitt, C. Wipf, N. Mavalvala, R. Schnabel, K. Danzmann, and Y. Chen. A double optical spring ponderomotive squeezer. *In preparation*, 2008.
- [90] H. Mueller-Ebhardt, H. Rehbein, C. Li, Y. Mino, K. Somiya, R. Schnabel, K. Danzmann, and Yanbei Chen. State preparation and macroscopic entanglement in gravitational-wave detectors. *In preparation*, 2008.
- [91] H. Mueller-Ebhardt, H. Rehbein, R. Schnabel, K. Danzmann, and Y. Chen. Entanglement of macroscopic test masses and the standard quantum limit in laser interferometry. *Phys. Rev. Lett.*, 100:013601, 2008.
- [92] H. Mueller-Ebhardt, K. Somiya, R. Schnabel, K. Danzmann, and Y. Chen. Signal-recycled sagnac interferometer. *Unpublished manuscript*, 2005.
- [93] A. F. Pace, M. J. Collett, and D. F. Walls. Quantum limits in interferometric detection of gravitational radiation. *Phys. Rev. A*, 47:3173, 1993.
- [94] A. Papoulis. *Signal analysis*. McGraw-Hill, 1977.
- [95] R. Penrose. Wavefunction collapse as a real gravitational effect. In A. S. Fokas, A. Grigoryan, T. Kibble, and B. Zegarlinski, editors, *Mathematical physics 2000: proceedings of the XIII international congress on mathematical physics*, page 266. Imperial College Press, 2000.
- [96] A. Peres. Separability criterion for density matrices. *Phys. Rev. Lett.*, 77:1413, 1996.
- [97] V. Poor. *An introduction to signal detection and estimation*. Springer-Verlag, 1994.
- [98] M. B. Priestley. *Spectral analysis and time series*. Academic Press, 2001.
- [99] P. Purdue. Analysis of a quantum nondemolition speed-meter interferometer. *Phys. Rev. D*, 66:022001, 2002.

- [100] P. Purdue and Y. Chen. Practical speed meter designs for quantum nondemolition gravitational-wave interferometers. *Phys. Rev. D*, 66:122004, 2002.
- [101] H. Rehbein. PhD thesis, Leibniz Universität Hannover, *in preparation*, 2008.
- [102] H. Rehbein, J. Harms, R. Schnabel, and K. Danzmann. Optical transfer functions of kerr nonlinear cavities and interferometers. *Phys. Rev. Lett.*, 95:193001, 2005.
- [103] H. Rehbein, H. Mueller-Ebhardt, K. Somiya, S. L. Danilishin, R. Schnabel, K. Danzmann, and Y. Chen. Double optical spring enhancement for gravitational wave detectors. *Phys. Rev. D*, 78:062003, 2008.
- [104] H. Rehbein, H. Mueller-Ebhardt, K. Somiya, C. Li, R. Schnabel, K. Danzmann, and Y. Chen. Local readout enhancement for detuned signal-recycling interferometers. *Phys. Rev. D*, 76:062002, 2007.
- [105] M. D. Reid. Demonstration of the einstein-podolsky-rosen paradox using nondegenerate parametric amplification. *Phys. Rev. A*, 40:913, 1989.
- [106] G. Sagnac. *C. R. Acad. Sci. III*, 95:1410, 1913.
- [107] A. Schliesser, P. Del’Haye, N. Nooshi, K. J. Vahala, and T. J. Kippenberg. Radiation pressure cooling of a micromechanical oscillator using dynamical backaction. *Phys. Rev. Lett.*, 97:243905, 2006.
- [108] R. Schnabel, H. Mueller-Ebhardt, and H. Rehbein. Verschraenkte spiegel. *Physik in unserer Zeit*, 40:234, 2008.
- [109] E. Schroedinger. Die gegenwaertige situation in der quantenmechanik. *Naturwissenschaften*, 48:823, 1935.
- [110] B. L. Schumaker and C. M. Caves. New formalism for two-photon quantum optics. *Phys. Rev. A*, 31:3093, 1985.
- [111] B. F. Schutz. *A first course in general relativity*. Cambridge University Press, 1985.
- [112] D. Sigg and *the LIGO Science Collaboration*. Status of the ligo detectors. *Class. Quantum Grav.*, 23:51, 2006.
- [113] R. Simon. Peres-horodecki separability criterion for continuous variable systems. *Phys. Rev. Lett.*, 84:2726, 2000.
- [114] K. Somiya, P. Beyersdorf, K. Arai, S. Sato, S. Kawamura, O. Miyakawa, F. Kawazoe, S. Sakata, A. Sekido, and N. Mio. Development of a frequency-detuned interferometer as a prototype experiment for next-generation gravitational-wave detectors. *Appl. Opt.*, 44:3179, 2005.
- [115] K.-X. Sun, M. M. Fejer, E. Gustafson, and R. L. Byer. Sagnac interferometer for gravitational-wave detection. *Phys. Rev. Lett.*, 76:3053, 1996.
- [116] J. H. Taylor. Binary pulsars and relativistic gravity. *Rev. Mod. Phys.*, 66:711, 1994.

- [117] K. S. Thorne, R. W. P. Drever, C. M. Caves, M. Zimmermann, and V. D. Sandberg. Quantum nondemolition measurements of harmonic oscillators. *Phys. Rev. Lett.*, 40:667, 1978.
- [118] T. Uchiyama, D. Tatsumi, T. Tomaru, M. E. Tobar, K. Kuroda, T. Suzuki, N. Sato, A. Yamamoto, T. Haruyama, and T. Shintomi. Cryogenic cooling of a sapphire mirror-suspension for interferometric gravitational wave detectors. *Phys. Lett. A*, 242:211, 1998.
- [119] T. Uchiyama, T. Tomaru, M. E. Tobar, D. Tatsumi, S. Miyoki, M. Ohashi, K. Kuroda, T. Suzuki, N. Sato, T. Haruyama, A. Yamamoto, and T. Shintomi. Mechanical quality factor of a cryogenic sapphire test mass for gravitational wave detectors. *Phys. Lett. A*, 261:5, 1999.
- [120] W. G. Unruh. *Quantum optics, experimental gravitation, and measurement theory*. Plenum, 1982.
- [121] H. Vahlbruch, S. Chelkowski, B. Hage, A. Franzen, K. Danzmann, and R. Schnabel. Demonstration of a squeezed-light-enhanced power- and signal-recycled michelson interferometer. *Phys. Rev. Lett.*, 95:211102, 2005.
- [122] H. Vahlbruch, S. Chelkowski, B. Hage, A. Franzen, K. Danzmann, and R. Schnabel. Coherent control of vacuum squeezing in the gravitational-wave detection band. *Phys. Rev. Lett.*, 97:011101, 2006.
- [123] G. Vidal and R. F. Werner. Computable measure of entanglement. *Phys. Rev. A*, 65:032314, 2002.
- [124] A. Vinante, M. Bignotto, M. Bonaldi, M. Cerdonio, L. Conti, P. Falferi, N. Liguori, S. Longo, R. Mezzena, A. Ortolan, G. A. Prodi, F. Salemi, L. Taffarello, G. Vedovato, S. Vitale, and J.-P. Zendri. Feedback cooling of the normal modes of a massive electromechanical system to submillikelvin temperature. *Phys. Rev. Lett.*, 101:033601, 2008.
- [125] D. Vitali, S. Mancini, L. Ribichini, and P. Tombesi. Mirror quiescence and high-sensitivity position measurements with feedback. *Phys. Rev. A*, 65:063803, 2002.
- [126] D. Vitali, S. Mancini, L. Ribichini, and P. Tombesi. Macroscopic mechanical oscillators at the quantum limit through optomechanical cooling. *J. Opt. Soc. Am. B*, 20:1054, 2003.
- [127] S. P. Vyatchanin and E. A. Zubova. Quantum variation measurement of a force. *Phys. Lett. A*, 201:269, 1995.
- [128] J. Weber. Evidence for discovery of gravitational radiation. *Phys. Rev. Lett.*, 25:180, 1970.
- [129] S. Weinberg. *Gravitation and cosmology: principles and applications of the general theory of relativity*. 1972, Wiley.
- [130] S. E. Whitcomb. Ground-based gravitational-wave detection: now and future. *Class. Quantum Grav.*, 25:114013, 2008.

-
- [131] N. Wiener. *Extrapolation, interpolation, and smoothing of stationary time series*. The MIT Press, 1949.
- [132] C. Wipf, T. Corbitt, Y. Chen, and N. Mavalvala. A route to observing ponderomotive entanglement with optically trapped mirrors. <http://arxiv.org/abs/0803.4001>, 2008.
- [133] A. Zeilinger. On the interpretation and philosophical foundation of quantum mechanics. In U. Ketvel et al., editor, *Festschrift for K. V. Laurikainen*. Helsinki University Press, 1996.
- [134] W. H. Zurek, S. Habib, and J. P. Paz. Coherent states via decoherence. *Phys. Rev. Lett.*, 70:1187, 1993.

Acknowledgements

I would like to specially thank Prof. Dr. Yanbei Chen and Prof. Dr. Roman Schnabel for excellently team-supervising my studies and for many useful discussions and advices. I have learned a lot from you in the time of my PhD studies! I would also like to express my thanks to the Director of our institute, Prof. Dr. Karsten Danzmann, for accommodation at the Albert-Einstein-Institut in Hannover.

Futhermore, I would like to thank especially Henning Rehbein for a very good cooperation in all our studies, but also Kentaro Somiya, Stefan Danilishin, Haixing Miao, Yasushi Mino, Chao Li, Thomas Corbitt, Christopher Wipf, Prof. Dr. Nergis Mavalvala, Prof. Dr. Farid Ya. Khalili, Prof. Dr. Kip S. Thorne and all the other members of the AEI-Caltech-MIT-MSU MQM discussion group for many useful discussions.

I would also like to thank all members of the Albert-Einstein-Institut for advices on theory as well as on what is actually experimentally realizable. Here I thank especially those members of the Institute in the quantum interferometry group of Prof. Dr. R. Schnabel for a very good commutation in questions related to squeezing and entanglement.

I really need to express my thanks to James DiGuglielmo for carefully reading the manuscript and very useful comments and advices. Thanks for finding the time to do so!

Furthermore, I would like to thank the Alexander von Humboldt Foundation's Sofja Kovalevskaja Programme for financial support.

Last but not least, I would like to thank my partner Dorothee Herzog for all her support as well as my parents Holger and Rosemarie Müller-Ebhardt for making my studies possible.

Curriculum Vitae

Name: Helge Müller-Ebhardt

Date of birth: 16.05.1979

Place of birth: Hannover, Germany

Nationality: German

Address: Am Graswege 8, 30169 Hannover, Germany

Email: h.muellerebhardt@gmx.de

1985–1989	Grundschule Grasdorf
1989–1991	Orientierungsstufe der KGS Laatzen
1991–1998	Gymnasium Laatzen, Abitur
1998–1999	Civil service at the Dr. med. E. A. Wilkening Pflegeheim Hannover Waldheim
1999–2002	Leibniz Universität Hannover (physics and mathematics)
2002–2003	University of Manchester (SOKRATES scholarship) (physics and mathematics)
2003–2004	Diploma thesis at the Institut für Theoretische Physik der Leibniz Universität Hannover
2005–2008	PhD thesis at the Institut für Gravitationsphysik der Leibniz Universität Hannover und des Max-Planck-Instituts

Publications

T. A. Ivanova, O. Lechtenfeld and H. Müller-Ebhardt, "Noncommutative moduli for multi-instantons", *Mod. Phys. Lett. A* **19**, 2419 (2004)

[hep-th/0404127].

H. Müller-Ebhardt, "On multi-instanton and multi-monopole configurations in Yang-Mills theory", Diploma thesis (2004)

[www.itp.uni-hannover.de/~lechtenf/theses.html].

T. Corbitt, Y. Chen, E. Innerhofer, H. Müller-Ebhardt, D. Ottaway, H. Rehbein, D. Sigg, S. Whitcomb, C. Wipf and N. Mavalvala, "An all-optical trap for a gram-scale mirror", *Phys. Rev. Lett.* **98**, 150802 (2007)

[quant-ph/0612188].

H. Rehbein, H. Müller-Ebhardt, K. Somiya, C. Li, R. Schnabel, K. Danzmann and Y. Chen, "Local readout enhancement for detuned signal-recycling interferometers", *Phys. Rev. D* **76**, 062002 (2007)

[gr-qc/0705.2987].

H. Müller-Ebhardt, H. Rehbein, R. Schnabel, K. Danzmann and Y. Chen, "Entanglement of macroscopic test masses and the standard quantum limit in laser interferometry", *Phys. Rev. Lett.* **100**, 013601 (2008)

[quant-ph/0702258].

H. Rehbein, H. Müller-Ebhardt, K. Somiya, S. L. Danilishin, R. Schnabel, K. Danzmann and Y. Chen, "Double optical spring enhancement for gravitational wave detectors", *Phys. Rev. D* **78**, 062003 (2008)

[gr-qc/0805.3096].

S. Danilishin, H. Müller-Ebhardt, H. Rehbein, K. Somiya, R. Schnabel, K. Danzmann, T. Corbitt, C. Wipf, N. Mavalvala and Y. Chen, "Creation of a quantum oscillator by classical control", submitted to *Phys. Rev. Lett.* (2008)

[quant-ph/0809.2024].

R. Schnabel, H. Müller-Ebhardt and H. Rehbein, "Verschränkte Spiegel", *Physik in unserer Zeit* **40**, 234 (2008).